UNIVERSITÀ DEGLI STUDI DI TRIESTE

UNIVERSITÀ DEGLI STUDI DI TRIESTE

XXXV CICLO DEL DOTTORATO DI RICERCA IN CHIMICA

FLUOROPHORE-GOLD NANOPARTICLE CONSTRUCTS AS SENSING PROBES FOR BACTERIA IDENTIFICATION

Settore scientifico-disciplinare: **CHIM/06 CHIMICA ORGANICA**

DOTTORANDA

CLAUDIA MARIA CAFIERO

COORDINATORE

PROF. ENZO ALESSIO

SUPERVISORE DI TESI

PROF. PAOLO PENGO

CO-SUPERVISORE DI TESI

PROF. PAOLO TECILLA

ANNO ACCADEMICO 2021/2022

Table of Contents

Abstract

The research activity of this PhD thesis was carried out as part of the collaborative research project BacHounds: Supramolecular nanostructures for bacteria detection (PRIN 2017). Currently, bacterial antimicrobial resistance (AMR) has emerged as one of the leading public health threats of the 21st century, and the World Health Organization (WHO) has identified AMR as one of the major global public health threats facing mankind. Among the main causes of antimicrobial resistance, the misuse and overuse of antimicrobials and poor access to quality, affordable medicines and diagnostics are the most relevant. Diagnostic techniques may contribute to the rapid identification of emerging resistant bacterial strains, allowing improved antibiotic stewardship and enhancing the cure rate. Indeed, it has been shown that the optimization of antibiotic therapy during the first 6-12 hours of infection is crucial for the treatment of life-threatening infections. Although novel sequencing-based approaches to pathogen identification have shown considerable progress in bacteria identification, to date these conventional techniques are still too slow, expensive, labour intensive, and challenging for clinical use. Thus, an urgent need exists to improve the current methods for the rapid detection of bacteria. In this context, gold nanoparticles (AuNPs) have aroused considerable interest in the development of viable options for the diagnosis and treatment of bacterial infections capable to meet this need, due to their biocompatibility, their optical and electronic properties, and their relatively simple production and modification.

This thesis proposes an alternative approach to bacteria detection; our proposed strategy primarily aims at the recognition of negative charges and hydrophobic patterns of the bacterial cell wall by using a library of positively charged gold nanoparticles (AuNPs) interacting non covalently with a specific fluorophore. The innovation of this approach is based on the use of mixed-monolayer AuNPs featuring fluorinated ligands in the protective shell which allow to modulate the hydrophobicity of the AuNPs outer surface providing an additional recognition mechanism. The first part of the project has been focused on the design and preparation of a library of cationic homoligand AuNPs and heteroligand AuNPs bearing hydrogenated (H-) and fluorinated (F-) ligands on their mixed monolayer. For both nanoparticles, the positive charges are provided by the H- ligands possessing a

permanent quaternary ammonium group as end-group, which allows no-specific electrostatic interactions with the negatively charged groups present on the bacterial outer membrane. Regarding the homoligand AuNPs, ultrasmall (~2 nm) and small (~5 nm) AuNPs have been prepared to increase diversity in the AuNP library via different size-dependent membrane association constants. On the other hand, diverse H-/F- ratios have been used to prepare water-soluble heteroligand AuNPs aiming to modulate the hydrophobic properties of the AuNP surface. The development of a transduction mechanism to detect the AuNPs-bacteria recognition event has been carried out, exploiting the peculiar property of the AuNPs to act as a quencher towards numerous fluorophores. For this purpose, the AuNPs quenching efficiency has been tested toward two organic dyes and an anionic fluorescent polymer (PPP-OSO_3) by fluorescence titrations, whose results have underlined the higher quenching efficacy of all AuNPs toward PPP-OSO_3.

The fluorescence quenching of the polymer by the nanoparticles has been studied in depth, including the estimation of the AuNP/PPP-OSO_3 association constant in collaboration with the group of Prof. Marco Montalti. Subsequently, the activities have been focused on the interaction studies between the AuNPs-polymer constructs and anionic liposomes, whose purpose is to act as bacterial membrane models. Two different anionic liposomes composed of POPG and a mixture of POPC/POPG have been prepared to achieve different surface charges. By fluorescence titrations of liposome-AuNPs solution with PPP-OSO_3, it has been observed that the quenching ability of the cationic AuNPs towards PPP-OSO_3 is markedly reduced in the presence of anionic liposomes, indicating an interaction of the nanoparticles with these systems, especially in case of AuNPs bearing fluorinated ligands. Within the time span of this PhD thesis, preliminary biological tests have been performed in collaboration with the group of Prof.ssa Cristina Airoldi and Prof. Alessandro Palmioli of Università of Milano-Bicocca, to analyse the quenching efficiency of the AuNPs toward PPP-OSO_3 in the presence of different bacterial strains encompassing Gram positive, Gram negative and mycobacteria.

The second part of the project has been focused on the development of a new type of activated gold nanoparticles (AuNPs) and their functionalization with bio-inspired peptide-based cationic ligands, exploring other synthetic strategies for AuNP preparation. In detail, peptide-decorated AuNPs have been designed to improve the specific-site interactions with the elements present on the bacterial membranes and to increase the diversity in the gold nanoparticles library. For the preparation of these AuNPs, an innovative approach based on the Staudinger-Bertozzi click chemistry reaction has been

pursued in order to optimize the AuNP functionalization. The proposed strategy is based on the preparation of activated AuNPs, whose surface is decorated with an appropriately substituted triarylphosphine, and on the synthesis of azide-containing peptides. Both homoligand and heteroligand activated-AuNPs have been synthesised to evaluate and optimize the stability of these systems. For the preparation of both homoligand and heteroligand activated-AuNPs, a novel ligand containing a methyl-2-(diphenylphosphino)benzoate motif has been synthetised.

Riassunto

L'attività di ricerca di questa tesi di dottorato è stata svolta nell'ambito del progetto di ricerca collaborativo BacHounds: Supramolecular nanostructures for bacteria detection (PRIN 2017).

Negli ultimi decenni, l'aumento allarmante dei casi di antibiotico resistenza (AMR, *antimicrobial resistance*) ha indotto l'Organizzazione mondiale della sanità (OMS) ad inserire l'AMR tra le principali minacce per la salute pubblica a livello mondiale. L'uso improprio e/o eccessivo di antibiotici, insieme ad una limitata diffusione di strumenti diagnostici atti ad una rapida identificazione dei ceppi patogeni, sono tra le principali cause del fenomeno AMR. In merito alle tecnologie diagnostiche, è stato dimostrato quanto l'ottimizzazione della terapia antibiotica durante le prime 6-12 ore di infezione sia cruciale per il trattamento delle infezioni potenzialmente letali, sottolineando l'importanza e la necessità di una tecnologia che permetta di identificare rapidamente il ceppo batterico in esame. Sebbene i nuovi approcci basati sul sequenziamento abbiano mostrato notevoli progressi nell'identificazione dei batteri, ad oggi queste tecniche risultano essere ancora troppo lente, costose, e laboriose per permettere una loro applicazione globale, soprattutto nei paesi in via di sviluppo dove il fenomeno AMR è particolarmente diffuso. Nell'ottica di sviluppare un metodo diagnostico rapido e di facile utilizzo e diffusione, le nanoparticelle d'oro (AuNPs) hanno suscitato notevole interesse nella progettazione di valide opzioni per la diagnosi e il trattamento delle infezioni batteriche, grazie alla loro biocompatibilità, alle loro proprietà ottiche ed elettroniche e alla loro semplice preparazione e funzionalizzazione.

In questo contesto si inserisce questo lavoro di tesi volto allo sviluppo di un approccio alternativo per la discriminazione di diversi ceppi batterici; in particolare, la strategia da noi proposta mira all'utilizzo di nanoparticelle d'oro (AuNPs) per il riconoscimento della parete batterica attraverso una combinazione di interazioni elettrostatiche ed idrofobiche. Infatti, le superficie esterne delle pareti batteriche espongono cariche negative ma anche unità strutturali come acidi teicoici e lipidi che le conferiscono una certa idrofobicità. Le AuNPs possono essere preparate in modo da esporre sulla loro superficie esterna sia cariche positive, garantendo quindi la complementarità di carica con la parete batterica, ma anche domini idrofobici. L'innovazione di tale approccio si basa sulla scelta di introdurre nella libreria di nanoparticelle AuNPs protette da monostrati misti, composti da miscele di ligandi

idrogenati (H-) cationici e ligandi fluorurati (F-). La presenza di quest'ultimi permette di modulare l'idrofobicità della superficie esterna delle AuNPs, fornendo un ulteriore meccanismo di riconoscimento. La prima parte del progetto è stata quindi incentrata sulla progettazione e preparazione della libreria di AuNPs cationiche omoleganti ed eteroleganti. Per entrambe le tipologie di nanoparticelle le cariche positive sono fornite da leganti idrogenato contenenti come gruppo di testa uno ione ammonio quaternario, che consente interazioni elettrostatiche non specifiche con gli elementi carichi negativamente presenti sulla membrana batterica esterna. Per quanto riguarda le AuNPs omoleganti, sono state preparate nanoparticelle con nucleo di oro di diversa dimensione (~ 2 nm e ~ 5 nm) al fine di aumentare la diversità nella libreria, sfruttando la dipendenza della densità di carica della superficie dalla dimensione della nanoparticella. D'altra parte, sono state preparate diverse nanoparticelle eteroleganti utilizzando miscele con diverso rapporto tra leganti idrogenati e fluorurati capaci comunque di produrre nanoparticelle solubili in soluzione acquose. La diversa percentuale di leganti fluorurati nei loro monostrati misti conferisce a queste nanoparticelle differenti idrofobicità. Una volta caratterizzate le AuNPs, le attività di ricerca sono state focalizzate allo sviluppo di un meccanismo di trasduzione capace di segnalare l'associazione AuNPs/batteri. A tal scopo, si è deciso di sfruttare la proprietà di quenching fi fluorescenza delle AuNPs nei confronti di numerosi fluorofori, testandone l'efficienza rispetto a due fluorofori organici a basso peso molecolare (carbossifluoresceina e piranina) e ad un polimero fluorescente anionico (PPP-OSO_3) mediante titolazioni di fluorescenza. I risultati di questi esperimenti hanno evidenziato la maggiore efficacia di quenching nei confronti del polimero PPP-OSO_3 da parte di tutte le nanoparticelle della libreria. Il quenching di fluorescenza delle AuNPs nei confronti del polimero scelto è stato studiato in collaborazione con il gruppo del Prof. Marco Montalti dell'Università di Bologna stabilendo che questo ha luogo con un meccanismo statico sul polimero ancorato alla superficie esterna delle nanoparticelle. La potenziale capacità delle AuNPs di legare la parete batterica attraverso una combinazione di interazioni elettrostatiche ed idrofobiche e la possibilità che questa interazione potesse essere evidenziata mediante la variazione delle proprietà di fluorescenza del PPP-OSO_3 sono state valutate ricorrendo a dei sistemi modello. A tal fine sono stati preparati due diversi liposomi anionici a diversa densità di cariche negative, composti rispettivamente dal lipide anionico POPG e da una miscela di POPG e il lipide zwitterionico POPC. Le titolazioni di fluorescenza ottenute aggiungendo quantità crescenti di PPP-OSO_3 a soluzioni contenenti il liposoma in esame e ciascun membro della libreria di nanoparticelle hanno consentito di evidenziare una generale riduzione del quenching. Questi risultati suggeriscono la presenza di interazioni preferenziali tra le nanoparticelle

e lo strato fosfolipidico del liposoma che impedisce una efficace interazione con il PPP-OSO_3, specialmente nel caso delle AuNPs con monostrato misto idrogenato/fluorurato. Analizzando la risposta di fluorescenza di tutte le AuNPs nella libreria per i due liposomi è stato possibile evidenziare delle differenze significative che consentono, in linea di principio, la discriminazione dei due diversi liposomi.

L'interazione del sistema AuNPs/ PPP-OSO_3 con diversi ceppi batterici è stata studiata, in modo preliminare, in collaborazione con il gruppo della Prof.ssa Cristina Airoldi dell'Università di Milano-Bicocca considerando due batteri Gram negativi: *E. coli* e *P. putida*; un batterio Gram positivo: *S. epidermidis* ed il micobatterio *M. smegmatis*. I risultati ottenuti hanno permesso di evidenziare che la libreria di AuNPs utilizzata in questi esperimenti è in grado di generare profili di fluorescenza significativamente differenti a seconda di quale ceppo batterico viene considerato, consentendo la distinzione tra batteri Gram negativi, Gram positivi e micobatteri su base qualitativa.

Contemporaneamente allo studio delle interazioni AuNPs/PPP-OSO_3, una seconda parte del progetto si è concentrata sullo sviluppo di un nuovo tipo di nanoparticelle d'oro e sulla loro funzionalizzazione con leganti cationici basati su peptidi. Questa attività è stata intrapresa allo scopo di verificare se l'introduzione di piccoli peptidi carichi positivamente a pH fisiologico permettesse di migliorare la selettività delle interazioni AuNPs-batteri e di aumentare la diversità della libreria. Per la preparazione di queste AuNPs decorate da peptidi è stato scelto un approccio innovativo basato sulla reazione di *click chemistry* nota come ligazione di Staudinger-Bertozzi, al fine di ottimizzare e facilitare la funzionalizzazione delle nanoparticelle con ligandi contenenti una porzione peptidica. La strategia proposta si basa sulla preparazione di nanoparticelle "attivate", la cui superficie è funzionalizzata da ligandi tiolici contenenti una triarilfosfina opportunamente sostituita, e sulla sintesi di peptidi contenenti un gruppo azide tale da permettere la reazione di ligazione. Per la sintesi delle AuNPs attivate, si è scelto di preparare AuNPs eteroleganti per valutarne la stabilità e condurre degli studi preliminare di ligazione.

Chapter 1

1. General introduction:

Why gold nanoparticles are popular in nanotechnology?

Many authors state that the idea of nanotechnology appeared for the first time in the famous talk "*There is plenty of room at the bottom*" given by the physicist Richard Feynman at the American Physical Society meeting at Caltech on December 29th, 1959.[1] At the nanoscale, the properties of a bulk material would change and the phenomena we are used to would become less important whereas surface effects would become dramatically more significant. Furthermore, at the nanoscale level, the fraction of surface exposed atoms is much higher than at the macroscale and consequently, the properties of a material are strongly dependent on its size, shape, and structure. The fascination with nanomaterials (NMs) is explained by their uncommon properties, markedly different from those of bulk materials due to the appearance of quantum confinement effects. Therefore, NMs are effectively a bridge between bulk materials and atomic or molecular structures (Figure 1).[2]

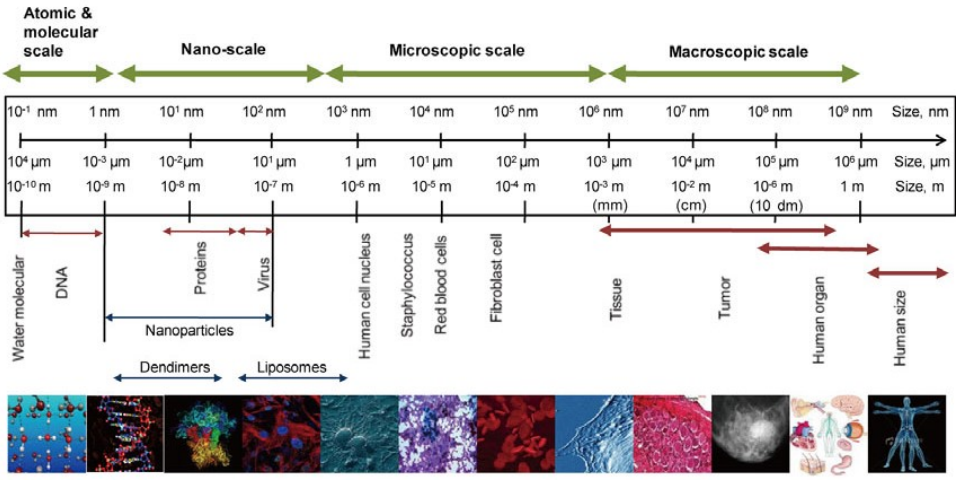

Figure 1.1. Size scale from atomic structures to biological systems. From Kim, E.-S. et al. Mol. Cells 2013, 36 (6), 477–484.

For these reasons, nanomaterial research has experienced an exponential growth over the past three decades, promoting impressive technological advancement and the synthesis of a variety of novel materials. Nanomaterials are defined as all those materials whose at least one dimension is confined between 1 and 100 nm and are usually categorized depending on their size, composition, shape, and origin. Among them, core-shell nanoparticles (CSNs) have been intensively investigated for their great potential in various fields, like catalysts, medical and analytical applications.[3–5] They are composed of an inner material (core) and an outer layer material (shell); depending on the core and shell nature, CSNs are classified into various categories.[6,7] Recently, much attention has been focused on the promising properties of metal nanoparticles (NPs) based on gold, platinum, palladium and silver because of their quantum-size effects and suitability for high added values applications such as in catalysis and the biomedical field, some of which are summarised in Table 1.1.[8–13]

Table 1.1. Properties, ligands, and some biological applications of noble metal-based nanoparticles. Adapted from De, M. et al. 2008, 20 (22), 4225–4241.

Core materials	Characteristics	Ligand(s)	Biological Applications
Au	Optical absorption, fluorescence, and fluorescence quenching	Thiol, disulfide, phosphine, amine	Biomolecular recognition, delivery, sensing
Ag	Surface-enhanced fluorescence	Thiol	sensing
Pt	Catalytic property	Thiol, phosphine, amine, isocyanide	Bio-catalyst, sensing

The chemical stability of NPs is paramount to avoid degradation processes and to promote the implementation of these nanomaterials. In this context, gold plays a special role in nanoscience and nanotechnology thanks to its properties. These include its chemically inert nature that allows to handle and manipulate samples under standard conditions but also making it biocompatible and therefore suitable for potential medical applications. However, all this cannot explain the incredible variety and number of research works concerning gold NPs and its applications in nanoscience.

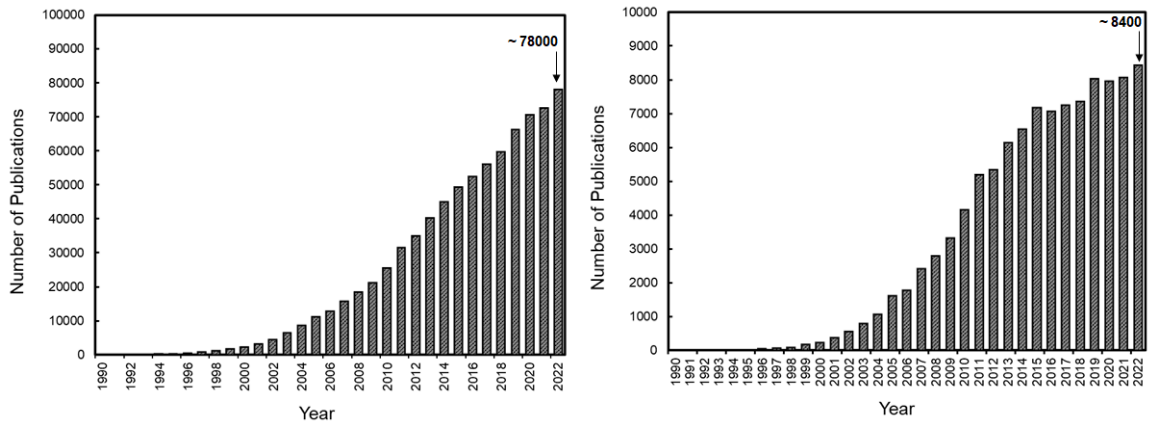

Figure 1.2. Annual record of the total number of scientific publications included in Scopus database using "nanoparticles" (left) or "gold nanoparticles" (right) as search keywords. All values were obtained from Scopus.

Over 160 years ago Michael Faraday presented to the Royal Society of London the first systematic study of the nature of gold and other metals "*in a state of extreme division*"; this event defines the birth of modern colloid chemistry.[14–17] Along the years the number of scientific publications about gold NPs increased steadily and in 2022 it represented about 10% of the total publications concerning nanoparticles, Figure 1.2. A boost in the interest on gold NPs is marked by the discovery of their preparation in the presence of alkanethiols[18–22] that delivers hybrid organic-inorganic systems in which an organic monolayer is covalently grafted to the gold surface. This discovery brought together two apparently different areas of scientific research: The functionalization of metal surfaces by formation of self-assembled monolayers (SAMs) and colloid chemistry.

1.1 Self-assembled monolayers in two and three dimensions

The physicochemical properties of nanostructures are highly dependent on their surface and interfacial environment. Some metals, including gold and silver, tend to adsorb spontaneously certain types of molecules because the adsorption event lowers the free energy of the interface between the metal and its surrounding environment.[23–27] This spontaneous adsorption of molecules leads to the formation of a molecular monolayer, a so-called self-assembled monolayer. The ability to organize matter on the nanometer scale is one of the major enabling principles in the field of nanotechnology. In this context, SAMs on flat surfaces are an example of a convenient and relatively simple way of surface coating exploiting intermolecular self-assembly. In a typical SAM, the molecules adsorbed consist of three units, as illustrated in Figure 1.3.

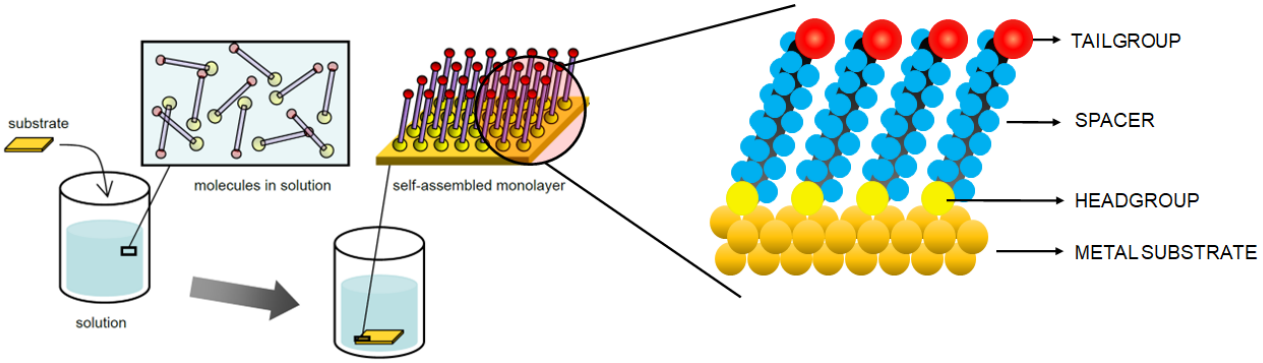

Figure 1.3. Schematic preparation of SAM and an illustration of SAM constituents. Adapted from Reed, M. A. et al. Sci. Am. 2000, 282 (6), 86–93, and Love, J. C. et al. Chem. Rev. 2005, 105 (4), 1103–1170.

The adsorbed molecules are immobilized on the solid substrate by a reactive headgroup that provides a strong molecule–substrate interaction. Such a favourable interaction is the primary driving force for the self-assembly process. A spacer moiety (or backbone) influences the molecular orientation via intermolecular van der Waals forces and stabilizes the supramolecular assembly, introducing long-range or short-range ordering. At last, it is possible to insert a specific terminal group (tailgroup or end-group) on the adsorbed molecule, which provides chemical functionality to the SAM. Therefore, the end-group can be used to tailor the physicochemical properties of the SAM surface such as solvation, wetting, and charge interactions. Additionally, the SAM surface can be used as an intermediate platform for further modification, such as functionalization with new molecules, biomolecules, or nanostructures either by weak interactions or covalent bonds. In this way, it is possible to explore plenty of applications, in fields such as biology, catalysis, sensing, etc.[28–31] (Figure 1.4).[32–36]

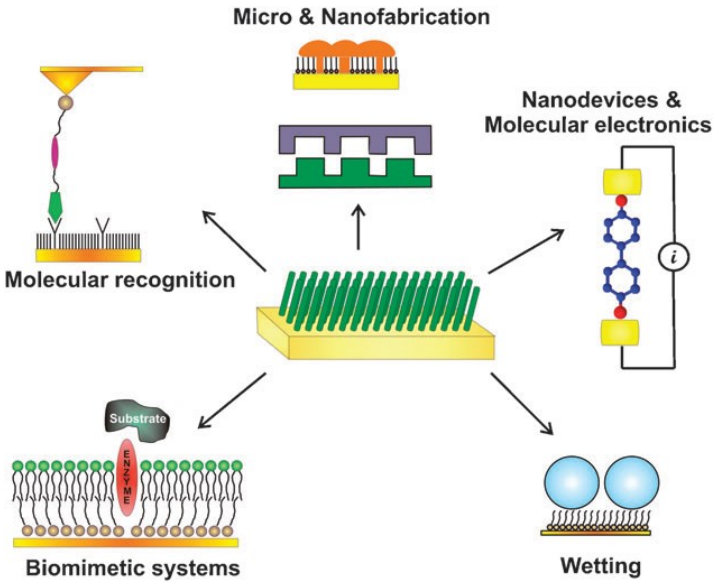

Figure 1.4. Possible applications of SAMs exploiting their tailorable properties. From Vericat, C. et al. *Chem. Soc. Rev.* **2010**, *39* (5), 1805–1834.

The most widely studied SAMs are those formed by the adsorption of thiols on gold (111) surfaces driven by the high mutual chemical affinity between gold and sulfur. These SAMs are easily prepared due to the formation of a strong gold-sulfur (Au-S) bond, and the stability of these systems is enhanced by the van der Waals interactions between the alkyl chains.[37–46] The nature of the Au-S bond has been the subject of numerous studies, as is the fate of the hydrogen atom originally bound to the sulfur atom. Nowadays, consensus exists on the fact that the thiol moieties –SH are chemisorbed to gold surfaces, with hydrogen loss during the bond formation.[47–50] However, under some conditions there has been evidence of thiols physisorption on gold surfaces preserving the S–H bond in SAMs prepared via solution deposition under ambient conditions.[51,52] The study of the structure of SAMs formed by alkanethiols on Au(111) pinpointed that upon adsorption of thiols the Au surface is highly reconstructed with gold adatoms bridging two different thiolate ligands.[53]

SAMs can also be formed on nanosized metal particles giving rise to supramolecular assemblies defined as monolayer-protected metal nanoparticles (MPMNs).

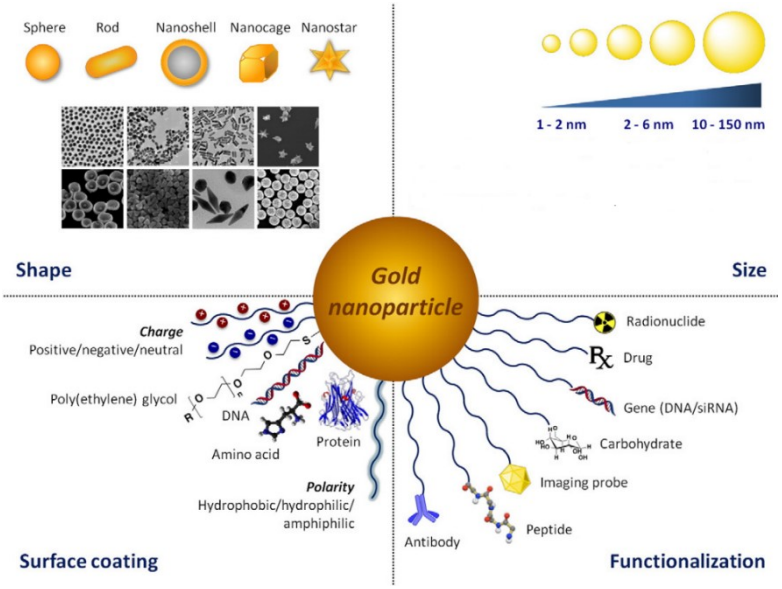

Figure 1.5. The synthetic versatility of AuNPs enables fine tailoring of the particle size, shape, and surface properties. From Her, S. et al. *Adv. Drug Deliv. Rev.* **2017**, *109*, 84–101.

The popularity and the increased attention towards gold nanoparticles stemmed from numerous features such as their facile methods of synthesis, and the high degree of control over shape and size. Furthermore, thanks to their conducive nature toward surface modification, AuNPs can be functionalized with a variety of ligands (Figure 1.5) tailoring their interfacial properties. This property of AuNPs has emerged as a crucial and promising tool to engineer AuNP surfaces, allowing the attachment of multiple types of ligands, and the development of multifunctional gold nanoparticles with multiple capabilities and enormous potential in many fields.[54–59]

1.1.1 Mixed self-assembled monolayers in two and three dimensions

SAMs composed of a mixture of different ligands are defined as mixed-SAMs. They can be easily produced both by a one-step procedure, consisting of simultaneous absorption from a solution of different ligands, or alternatively, by using a two-step procedure that requires exposing a preformed ligand-protected monolayer to a solution containing another ligand. Contrary to one-component SAMs, mixed-SAMs showed unusual nanoscale phase-separated domains. Indeed, there are several examples in which Au{111} surfaces covered by mixed-SAMs of alkanethiols showed a phase segregation and the formation of nanometer-scale domains. [60,61]

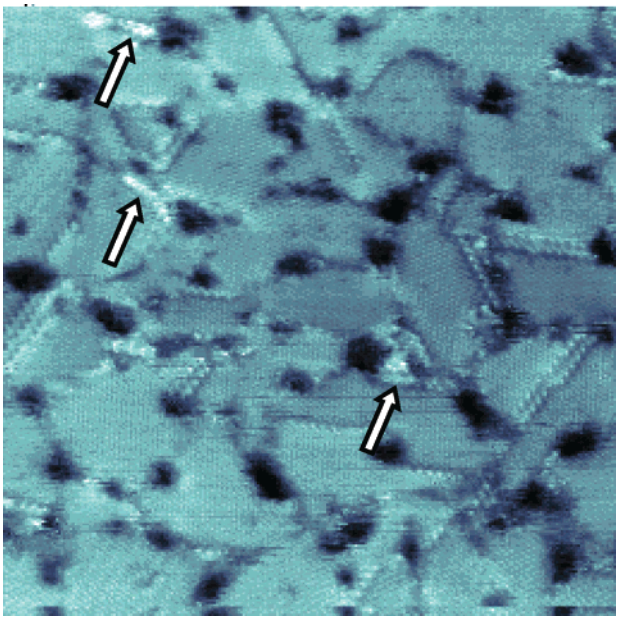

Figure 1.6. STM image of a 580 Å x 580 Å area of a monolayer formed from a 1:3 mole ratio (adsorption solution) of 1ATC9 and *n*-decanethiol. The arrows point to areas of 1ATC9 adsorption in the *n*-decanethiolate matrix. From Smith, R. K. et al. *J. Phys. Chem. B* **2001**, *105* (6), 1119–1122.

In Figure 1.6 an STM image of binary SAMs on Au{111} composed of an amide-containing alkanethiol and a straight chain alkanethiol is shown.[62] In this study, it was observed that in the *n*-decanethiolate matrix, the 1ATC9 (3-mercapto-*N*-nonylpropionamide) molecules bind to the substrate surface at the edge of vacancy islands and grain boundaries (areas with a circular shape and characteristic height) of the gold substrate. This segregation of the 1ATC9 molecules in the SAM was rationalized considering that it would be energetically unfavorable for the polar amide moiety to be buried within the crystalline matrix of the nonpolar *n*-decanethiolate molecules. Therefore, adsorption may occur to minimize the contact sites from the surrounding molecules. The formation of these phase-separated domains has been investigated in numerous scanning tunneling microscopy (STM) studies of mixed-SAMs on flat Au{111} substrates and, it has been established that the phase segregation on flat surfaces is a thermodynamically driven process. Randomly dispersed domains are observed in all cases with no general tendency to the formation of long-range ordered features. without a particular order.

Mixed-SAMs can also be formed on curved surfaces and in recent years, important discoveries unveiled the rich diversity of subnanometer structures that can be obtained by self-sorting of a mixture of unlike thiols grafted on the AuNP.

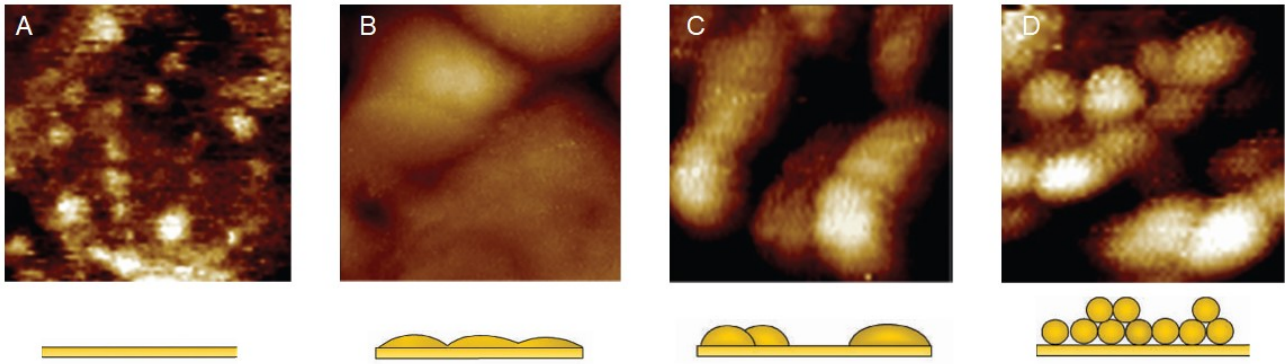

Figure 1.7. STM images of mixed SAMs on surfaces of different curvatures: flat Au{111} (**A**), Au film deposited on a silicon wafer showing hemispheres of < 20 nm diameter (**B**), Au film containing Au crystals of < 10 nm diameter (**C**), and Au film showing Au crystals of 5 nm diameter (**D**). Scale bar 10 nm. From Jackson, A. M. *Nat. Mater.* **2004**, *3* (5), 330–336.

The first observation of ligand self-sorting on AuNPs surface leading to domains of well well-defined morphology was reported by Stellacci and co-workers[61]. In details, these authors discovered the formation of stripe-like domains in the monolayer of AuNP prepared using a 2/1 mixture of octanethiol (OT) and mercaptopropionic acid (MPA) and studied the influence of the gold nanoparticles size, and therefore curvatures on this self-sorting behaviour, (Figure 1.7A-D). Ordered stripe-like domains have been observed only for nanoparticle surfaces with high curvature such as those of 10 nm or 5 nm in diameter Figure 1.7C and Figure 1.7D respectively. These features were instead missing for mixed-SAMs grafted on flat Au surfaces (Figure 1.7A) and 20 nm diameter hemispheres deposited on Au film (Figure 1.7B) where only randomly dispersed domains could be observed. Stellacci and co-workers concluded that the curvature of the substrates was one of the triggers for this organization. Another parameter investigated was the nature of the metallic core, so mixed-SAM silver nanoparticles (AgNPs) were prepared and analysed by STM, showing similar stripe-like domains. Consequently, the authors concluded that the surface curvature is the possible driving force of this well-defined phase segregation.[63] Besides, elucidating the mechanisms that govern phase separation and the intermolecular interactions between of adsorbates has been essential for the design of systems with well-defined and controlled morphologies.

One of the most attractive consequences of these nanometer-defined domains is that the monolayer morphology as a whole can be easily tailored. Indeed, by using two different ligands and varying their ratio it is possible to control and change both the spacing and the shape of the phase-separated domains, and thus the resulting global domain morphology (Figure 1.8).

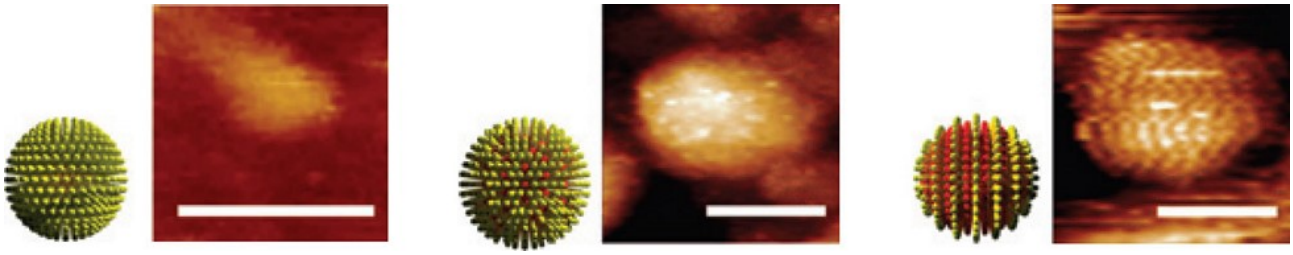

Figure 1.8. Schematic illustration of AuNPs shell structure and their respective STM images (scale bar 5 nm). From left to right homoligand monolayer (octanethiol as ligand), random and striped heteroligand monolayer (octanethiol/mercaptopropionic acid) as a consequence of ligand ration varying. From Pengo, P. et al. *Eur. Biophys. J.* **2017**, *46* (8), 749–771.

Specifically, three limiting 3D patterns are possible on the AuNP surface coated by two unlike ligands: Janus-like, stripe-like, and mixed random domains (Figure 1.9).[64,65]

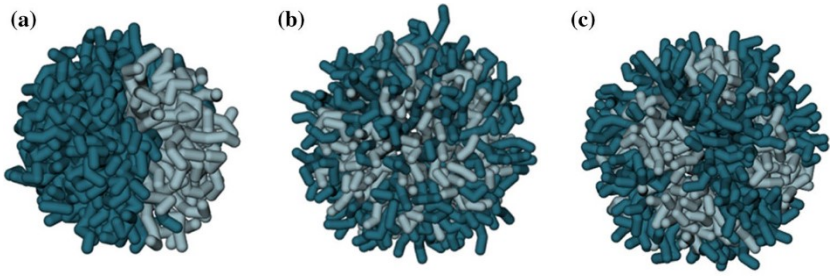

Figure 1.9. 3D SAM organization using binary mixture to coat AuNPs: Janus-like (**a**), stripe-like (**b**), and random (**c**) domains. Adapted from Pengo, P. et al. *Eur. Biophys. J.* **2017**, *46* (8), 749–771.

Glotzer and co-workers have confirmed the crucial role of curvature in stripe-like organization by computational investigations.[66] As a result of their study, both NP size core and length of ligands were identified as critical parameters in the microphase-separated domain formation. The final NP monolayer morphology was found to be affected by the balance of enthalpy contributions (driving macrophase separation) and conformational entropy (leading to increased ligand–ligand interface surface area). Considering ligands with equal length (Figure 1.10a and Figure 1.10b), on small enough NP the tails of all ligand chains have sufficient free volume, and therefore favourable conformational entropy term (Figure 1.10b), arranging radially outward from the NP core. In this case, the gain in entropy by creating additional interfaces (and thus stripes) is not significant, so the ligands tend to separate into two distinct phases resulting in a Janus arrangement. Increasing the NP radius, both the curvature and the available free volume decrease, while the entropic gain due to interface formation (elongated domains) increased (Figure 1.10a). As result, the ligands tend to assemble into stripe-like domains. Continuing to increase the NP radius, disordered patchy and not aligned stipe-like domains are expected to dominate.

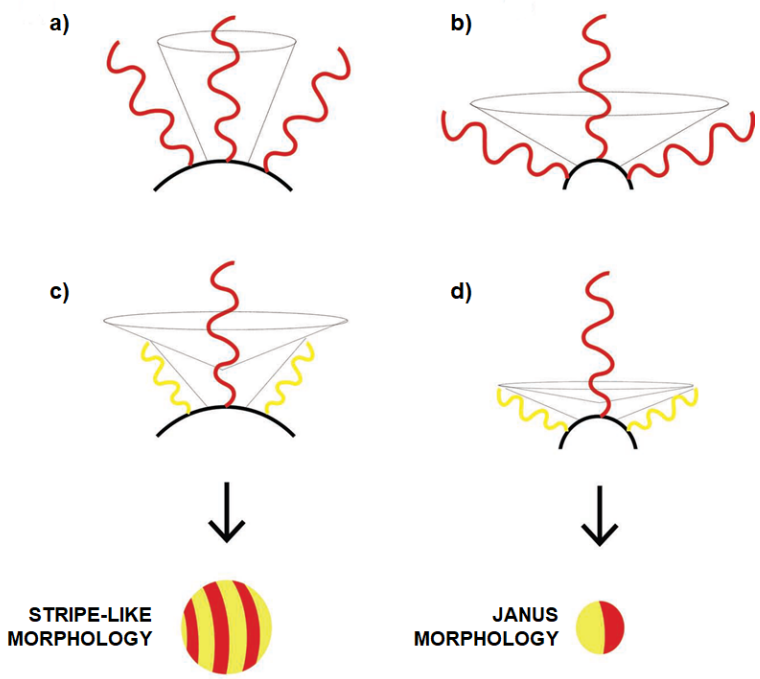

Figure 1.10. Schematic representation of the free volume (*grey cone*) of ligand tails on an NP surface when they were surrounded by other types of surfactant chains of the same (**a, b**) or different lengths (**c, d**) on larger (left column) and smaller (right column) NPs. Adapted from [66]Kim, H. et al. *Adv. Mater.* **2012**, *24* (28), 3857–3863.

On the other hand, considering a mixture of long or bulky ligands and shorter or less bulky ligands (Figure 1.10c and Figure 1.10d), the system tends to gain additional conformational entropy by creating interfaces at which the longer/bulky ligands are adjacent to shorter/less bulky ones. In this way, the bulky tails have an extra free volume available that is sufficient to overcome the enthalpic loss, then the system evolves forming microphase separated stripes.

As a result of this fine enthalpy–entropy interplay, the surface curvature and the nature of the unlike ligands guide the system at the final equilibrium morphology that best balances all contributions. So, mixtures of immiscible ligands may adopt a Janus morphology when the entropy contributions are small, a random mixed arrangement when enthalpy is small, or when an ordered arrangement is hindered (e.g., a branched ligand structure), and a stipe-like arrangement when the two components are balanced.

Based on these studies, it can be concluded that the different arrangements are observable in certain core size regimes, even by considering the nature of the ligands. Kim *et al.*[67] have synthesized and analysed diverse Janus AuNPs varying the ligands combination, concluding that the Janus arrangement is stable and can be observed when the core sizes are smaller than 1.5 nm. Instead, for the stripe-like arrangement, Carney *et al.*[68] have identified 2.5-8 nm as the core sizes range in which

this assembly occurs. So, the transition from Janus to stripe-like morphologies was predicted to exist when the gold core size is between 1.5–3 nm.

Therefore, stripe-like domains were possible using mixture of immiscible ligands of different chain lengths and/or bulkiness, proposing that the entropy contribution was the driving force of these arrangements on the NPs surface. Further studies carried out by *Ge et al.*[69] highlighted that formation of striped domain takes place on NP surfaces, but only for a subset of molecular systems. Indeed, beyond the entropic contributions, they suggested the striped pattern formation also depended upon the interligand interaction dictated by ligand physicochemical characteristics. For their study, two binary mixed monolayer systems were analysed by molecular simulations. Specifically, they compared the mixed monolayer systems composed by a mixture of octanethiol (OT, hydrophobic) and 3-mercaptopropionic acid (MPA, charged), and the one formed by hexanethiol (S-C6, hydrophobic) and polyethylene functionalised hexanethiol (S-C6-$[OCC]_n$-OH, neutral, polar). Starting from the concept that ligands with different chain length (or steric hindrance) tend to assume the conformation with the largest free conformational volume, the random morphology possess the maximum available volume for longer ligand that usually has the smaller ligands as its neighbours. Therefore, the Janus morphology has the smaller available volume, and the stripe-like state is placed as intermediate, concluding that $S_{random} > S_{stripe\text{-}like} > S_{janus}$ (where S is the system entropy) (Figure 1.11a). Assuming the potential energy (U) and S of a given state did not change with the temperature (T), Ge *et al.* have obtained a linear dependence of the system free energy (F) to T (Figure 1.11b), in which the equilibrium state corresponds to the state with the lower F.

Since the two ligands of each mixed-SAM are immiscible, both the Janus and the stripe-like arrangement are expected to have a lower internal energy U than the random morphology, so $U_{random} > U_{janus}$ and $U_{random} > U_{stripe\text{-}like}$. The relationship between $U_{stripe\text{-}like}$ and U_{janus} was analysed for both systems computing the respective U values at low temperatures of each morphology. Curiously, they found that for the first system (OT/MPA) $U_{stripe\text{-}like} < U_{janus}$, while for the second bSAM system (S-C6/ S-C6-$[OCC]_n$-OH) $U_{stripe\text{-}like} > U_{janus}$. Based on these results, Ge *et al.* proposed the existence of three types of mixed-SAM systems (Figure 1.11b).

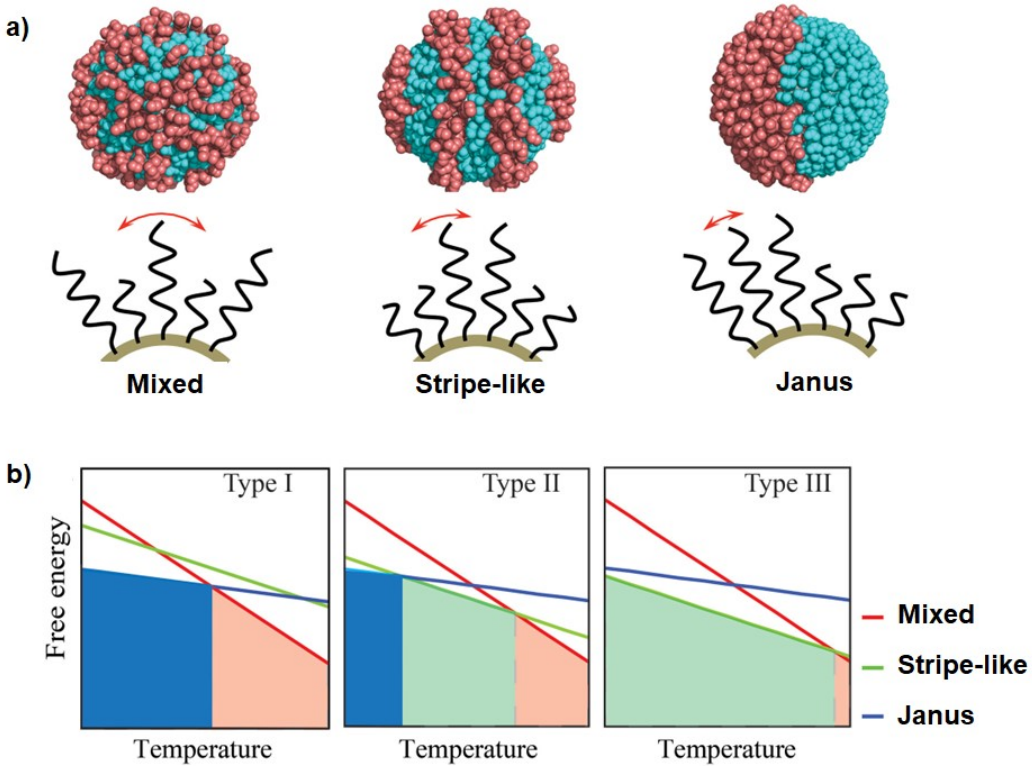

Figure 1.11. (**a**) 3D structures (top) and corresponding schematic diagrams (bottom) illustrate the difference in available volume for each of the three arrangements; (**b**) Free energy as a function of temperature. From Ge, X.et al. *Small* **2015**, *11* (37), 4894–4899.

Another strategy that could be exploited to trigger the formation of well-defined morphologies on the surface of thiolate protected gold nanoparticles is the "super hydrophobic" effect of a specific class of compounds: the fluorinated thiolate ligands (F-ligands). It is indeed well established that fluorinated compounds are largely immiscible with hydrogenated organic compounds and polar media.[70,71] This property has been exploited at the nano- and meso-scale to achieve self-sorting in supramolecular objects which is also favoured by the rigid-rod character of fluoroalkyl chains that promotes ordered packing.[72–74]

Following this line, Pasquato and co-workers were the first to pinpoint that the reciprocal phobicity of F/H ligands was an effective driving force triggering the formation of phase separated domains on the surface of gold nanoparticles. These authors displayed that using mixtures of amphiphilic F- and amphiphilic H- thiols bearing terminal polyethylene glycol units of different lengths, clustering of the F-ligands was favoured even when the fraction of the F-ligands was very small.[75–78] These studies have also demonstrated the formation of phase-separated/stripe-like and Janus domains depending on the nanoparticle size, in keeping with the work of Stellacci.[79] Further studies from the same group lead to the development of nanoparticle systems with a complete array of monolayer morphologies.[80]

This was achieved by systematically varying the structure, relative length, steric bulk, and molar ratio of *F*- to *H*- ligands mixtures.

In addition to ligand immiscibility and length differences, this study point out that the steric hindrance and rigidity of the *F*-chains are further key parameters that affected the final layer morphology. So that Janus monolayers formed when *H*- and *F*- ligands had the same length and were at least 12 carbon atoms long (Figure 1.12a). Indeed, reducing the chain length of both ligands to eight carbons tended to create no defined morphologies (Figure 1.12b), probably because of the large footprint of *F*-chains. For the same reason, branched ligands disfavoured phase segregation and promoted random monolayers (Figure 1.12c). Finally, only when the mismatch of ligand length is equal to eight carbon atoms, stripe-like domains are formed (Figure 1.12d), while a four-carbon mismatch tended to form patchy morphologies.

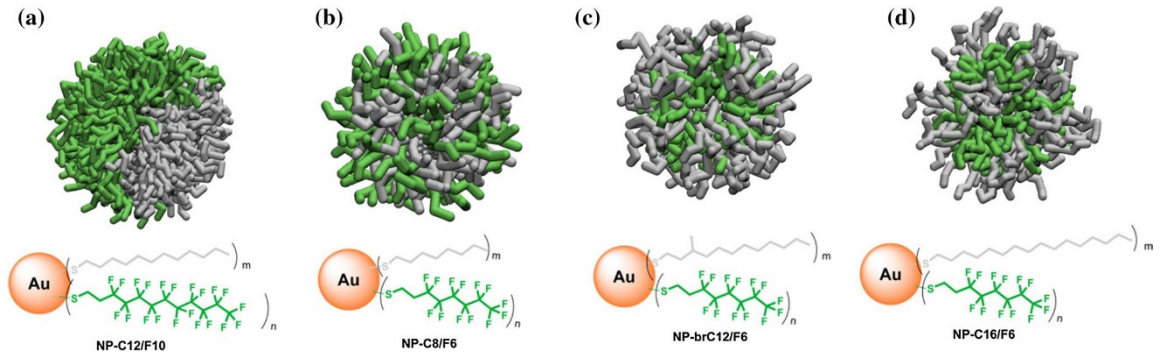

Figure 1.12. Equilibrium morphologies were predicted from CG simulations. Note that C8, C12, and C16 refer to the full length of *H*- chains (*m*), while F6 and F10 refer only to the number of fluorinated carbons in *F*-chains (*n*). The solvent was omitted for clarity. Color code: gray for *H*- ligands, and green for *F*- ligands. From Şologan, M. et al. *ACS Nano* **2016**, *10* (10), 9316–9325.

The design principles arising from these studies are currently employed by Pasquato's group in synthesizing and characterizing more complex nanoparticle systems for practical applications.

1.2 Nanoparticles synthesis and surface functionalization

The selection of proper synthetic methods is crucial to optimize the size and shape of the gold nanoparticles and therefore tuning their properties for a given specific application. Numerous preparative methods for AuNPs have been reported, including both the "top-down" (physical manipulation), and the "bottom-up" (chemical transformation) approaches which generates AuNPs from individual molecules via a chemical or biological reduction approach. The bottom-up approach offers a more versatile strategy in terms of size control, size range, and functionalization. By virtue

of this, only the methodologies belonging to this approach will be discussed in detail, focusing on the Turkevich (Figure 1.13a) and Brust-Schiffrin (Figure 1.13b) methods .[81–83]

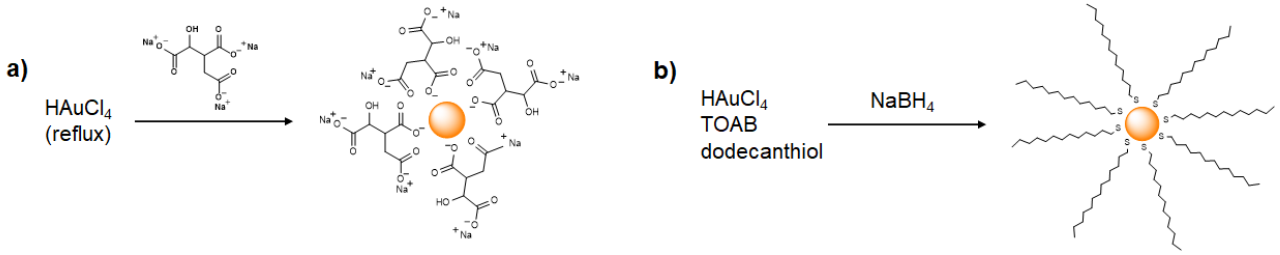

Figure 1.13. The most famous AuNP synthetic methods: the one-phaseTurkevich synthesis (**a**) in which the citrate acts both as a stabilizer and reducing agent, and the two-phase Brust-Schriffrin synthesis (**b**) where $NaBH_4$ is used as a reducing agent and dodecanethiol as a stabilizer.

1.2.1 Synthesis of hydrophilic AuNPs: Turkevich method

The first synthesis of hydrophilic nanoparticles was performed by Turkevich *et al.*[84] in 1951, the synthesis is based on the use of sodium citrate as both a reducing agent and stabilizer of the nanoparticles and further studies have improved the Turkevich method to control particle sizes.[85,86] Although very common, this approach suffers from several limitations and issues, especially in cases where a post-synthesis functionalization of the nanoparticles is required. Indeed, the citrate stabilizers can be displaced by ligands, such as thiols, that establish with the gold surface a stronger interaction, however, displacement may not be complete with the pre-adsorbed citrates remaining alongside thiols in a mixed layer of ill-defined composition..[87] The remaining citrate molecules can affect the AuNP surface chemistry due to the hydroxyl/carboxyl functionality and influence AuNP properties such as pH-dependent surface charge, intracellular activity, and toxicity. The incomplete ligand exchange is probably due to the stable network of hydrogen-bonded dihydrogen citrate species (Figure 1.14). Despite the Au-$O_{(COO-)}$ bond is much weaker than the Au-S bond, the intermolecular interactions and consequent steric and chelating effects of the entire citrate layer make the complete thiol-functionalization harder.

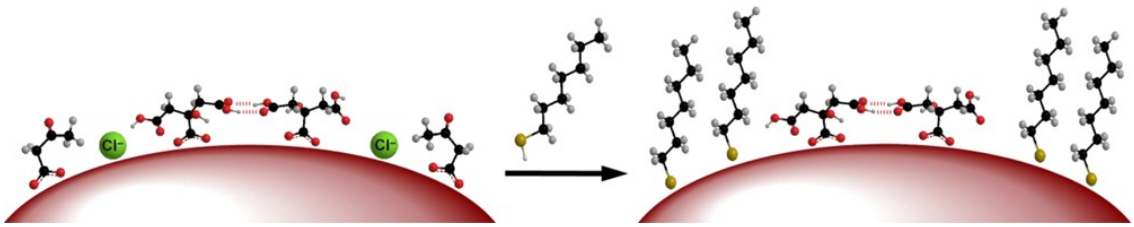

Figure 1.14. Representative AuNP surface displaying hydrogen-bonded citrate layers. From Park, J.-W. et al. *ACS Nano* **2015**, *9* (2), 1665–1682.

Several strategies have been developed to conquer this problem including using a surfactant.[88–95]

1.2.2 Synthesis of hydrophobic AuNPs: Brust-Schiffrin method

Brust and Schiffrin published in 1994 a breakthrough in AuNP synthesis, allowing the facile preparation of thermally stable organic soluble AuNPs.[96] They prepared alkanethiol-stabilized AuNPs through a biphasic reduction protocol using tetraoctylammonium bromide (TOAB) as the phase transfer reagent, and sodium borohydride ($NaBH_4$) as the reducing agent. This methodology was studied in detail by the Murray group providing protocols to achieve control over AuNP size and size dispersion enabling the preparation of AuNPs with sizes from 1.5 to 5 nm by varying the reaction conditions, such as gold/thiol ratio, reduction rate, and reaction temperature.[97] In this method, $AuCl_4^-$ is transferred from the aqueous phase to toluene using TOAB. During this process, the colorless toluene phase turned into a deep orange color, while the starting aqueous phase turned from yellow to colorless. Then, the aqueous phase was discarded, and dodecanethiol was added to the organic solution; The presence of alkanethiols induced a color change from orange (Au (III)) to colorless (Au (I)). Then, upon the addition of $NaBH_4$, the solution rapidly changed from colorless (Au (I)) to dark brown (Au (0)), indicating the formation of AuNPs (Figure 1.15).

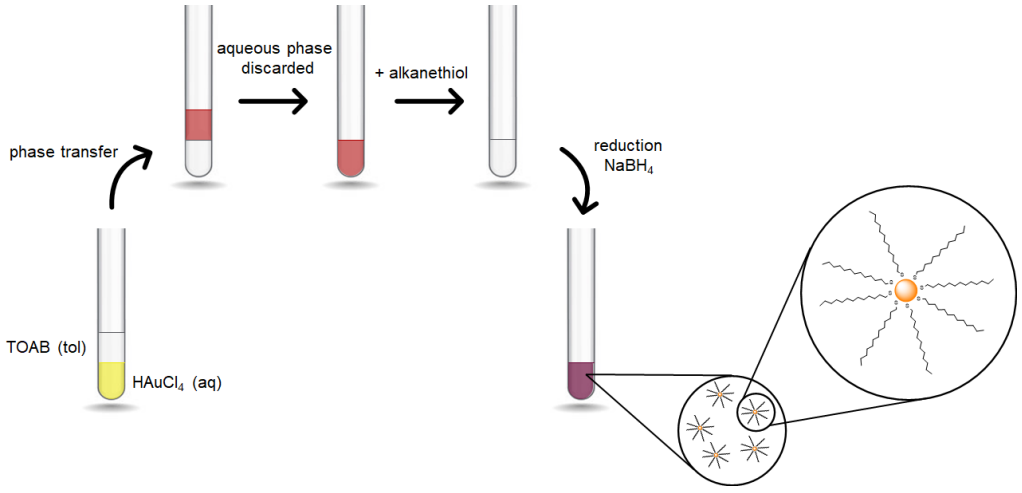

Figure 1.15. Schematic representation of Brust-Schiffrin synthesis of AuNPs.

Modified Brust-Schiffrin methods with different protecting ligands and reducing reagents have been successfully used for the synthesis of AuNPs with different sizes.[98,99] Compared to most other AuNPs, these alkanethiol-protected AuNPs display higher stability due to the synergic effect of the strong thiol-gold bond and van der Waals interactions between the neighboring ligand alkyl chains. Indeed,

these AuNPs can be repeatedly dried and redissolved in common organic solvents without irreversible aggregation or decomposition, making them excellent precursors for further functionalization.

1.2.3 Post-functionalization of AuNPs: Place exchange reaction

The synthetic procedure of Brust *et al.* paved the way to the development of several versatile strategies to functionalize alkanethiol-protected AuNPs, leading to their use as multifunctional reagents, catalysts, chemical sensors, etc. One of the most relevant reactions developed to this end is the place-exchange reaction, regarded as an important synthetic route to functionalized AuNPs.[100,101] This strategy offers a practical route for the post-functionalization of AuNPs, introducing novel functionalities on the AuNPs. Briefly, in the place exchange reaction, the initial thiol ligands (RS) adsorbed on AuNPs are exchanged by new free thiol ligands (R'S) leading to mixed monolayer nanoparticles. Recently, the mechanism of SAM morphology evolution in thiol-for-thiol exchange reaction has been studied in detail by the Stellacci group.[102] These authors found that the final morphology is largely dependent on thermodynamic equilibrium, and so on the chemical nature of the ligands. For unlike ligands (different chain lengths or/and end-groups), the incoming ligand randomly adds to nanoparticle surfaces at first, while patchy domains slowly grow as the reaction proceeds. Also, numerous kinetics studies on the place exchange reaction have been performed, aiming at assessing whether this process can be associative (S_N2-Like), dissociative (S_N1-like), or a combination thereof, the general conclusion is that the place exchange reaction takes place with an associative mechanism.[103–107] Under certain conditions, the thiol-for-thiol exchange reaction presents some limitations and issues, such as the etching of the gold cores if a large excess of incoming thiols is used that leads to unexpected size reduction.[108] In addition, the process may be time-consuming especially when sterically hindered incoming thiols are used or the initial nanoparticle monolayer masks efficiently the Au-S interface of the nanoparticles. [109]

The place exchange reaction has been widely employed because it allows to obtain functionalised nanoparticles avoiding the use of the strong reducing conditions of the direct Brust-Schiffrin synthesis in the case of reduction-sensitive functional thiols, and remains a standard procedure for the post synthetic AuNPs functionalization.[110–120] The exchange reaction also allows to introduce more than two different functional ligands enabling to achieve a rich variety of multivalent monolayer-protected AuNPs.[121]

1.3 Characterization of Self-Assembled Monolayer AuNPs

As mentioned above, the ligand structure, their density, and ultimately the monolayer composition, and morphology contribute significantly to the chemical, biological, and interfacial behavior of AuNPs. However, also the AuNP core is crucial in determining the overall structure of the AuNP monolayer and therefore of their properties. Hence, it can be deduced that the structure characterization of AuNPs is a key-factor in the development of AuNPs applications. Suitable methods for the characterization of AuNPs must provide reliable information on both the organic coating (composition/structure of the monolayer) and inorganic core. Although many examples of the potential emerging applications of these nanosystems can be found in the literature, characterisation of the structure of both the inorganic core and the protecting monolayer is often difficult. These issues arise because dealing with the task of characterizing systems whose nature is intrinsically statistical is challenging. Consequently, adequate characterization of these nanomaterials is a fundamental prerequisite to guarantee data reproducibility and build knowledge of predictable properties for the engineering of nano-objects with well-defined physicochemical and structural features.

The most significant characterization techniques used to analyse the core and the monolayers of AuNPs can be grouped into different categories. Among these, the most common are microscopy analyses (e.g., AFM, STM, SEM, TEM), spectroscopic analyses (e.g., ESR, XPS, UV-vis, NMR, MS, FTIR, etc), light scattering (e.g. DLS, zeta potential) and thermal gravimetric (TGA) analysis.[79,122,123] Furthermore, these techniques can be divided into those that analyse the monolayer-protected AuNPs as such and those that can be applied to a decomposed sample of the nanoparticles for assessing, for instance, the monolayer composition. (Figure 1.16).

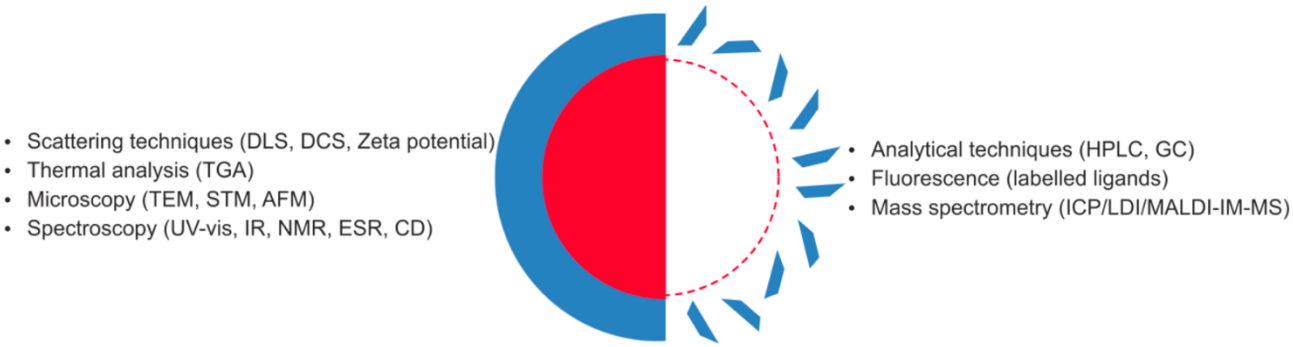

Figure 1.16. Some techniques for AuNP characterization divided according to whether the monolayer decomposition is required (right) or not (left). From Colangelo, E. et al. *Bioconjug. Chem.* **2017**, *28* (1), 11–22.

In the following paragraphs, only the techniques used during the thesis activity will be discussed in more detail, which are TEM, TGA, DLS, NMR, and UV-vis.

1.3.1 Transmission Electron Microscopy (TEM)

Transmission electron microscopy (TEM) is a versatile physical characterization method, that provides a direct measure of the size and shape of the cores of hybrid organic-inorganic NPs In a typical TEM image, the inorganic cores appear with high contrast respect to organic layers because of the strong electron-scattering properties of the material. By processing the TEM micrographs, it is possible to assess the size distribution of the population of NPs imaged. From the statistical distribution of the core sizes, it is possible to determine (histogram) the average core size and its dispersion about the average core size. On the other hand, since the low electron scattering character of the organic monolayer, is not possible to have a sufficient contrast to make it visible in regular TEM images. However, negative staining can be employed to visualize the NP monolayer. This method involves the use of heavily electron-scattering compounds (e.g., uranyl acetate, ammonium molybdate, or osmium tetroxide) to stain the background of TEM grids. Ideally, the negative staining produces a homogeneous dark background in which organic monolayers appear as bright corona around the dark inorganic cores (Figure 1.17).

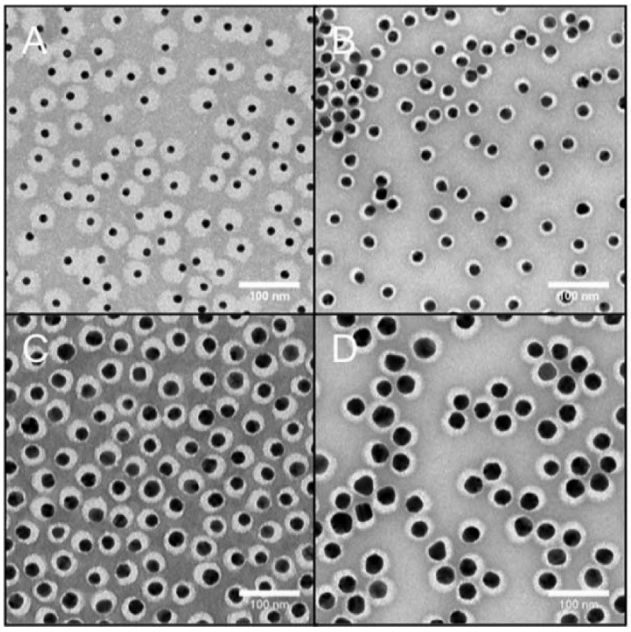

Figure 1.17. TEM image of PEG-protected AuNPs of different sizes. The negative staining allows for visualization of the PEG monolayer around the NPs. From Hühn, J. et al. *Chem. Mater.* **2017**, *29* (1), 399–461.

The NPs are deposited from a dilute solution onto carbon coated TEM grids usually made of copper, and the solvent is evaporated at room temperature. During the evaporation, a drying-induced clustering on the TEM grids can occur, avoidable by depositing diluted NP suspensions on the TEM grids or optimizing the rate of drying. For much higher magnification, HR-TEM (high-resolution TEM) is used for its capability of achieving resolution even at the atomic level. Thanks to this technique is it possible to visualize the atomic layers within a single core, allowing the measurement of interatomic distances, gathering information on how the gold atoms are arranged.

1.3.2 Thermal Gravimetric Analysis (TGA)

Thermogravimetric analysis (TGA) measures the changes in the sample mass (g) as the sample is treated at increasing temperatures in a controlled manner. This analysis provides important information about physical (phase transitions, absorption, and desorption) and chemical phenomena including thermal decomposition. In the case of monolayer protected AuNPs, the TGA allows monitoring changes in weight over a temperature ramp, due to the loss of the organic coating Indeed, the continuous temperature increase induces firstly evaporation of residual solvent, and then the decomposition of the organic monolayer grafted on the nanoparticle core (in the range of 150-400 °C). By the deconvolution of the TGA curve is possible to calculate the percent by weight of the organic coating to the NP total weight.

The major disadvantages of TGA analysis are its destructive nature and the relatively large amount of sample needed. In a typical TGA experiment, two or more milligrams of material are required, making TGA a “consuming technique” in case of expensive or limited-quantity samples, especially when frequent and multiple experiments need to be made.

1.3.3 Dynamic Light Scattering (DLS)

Dynamic light scattering (DLS) is an analytical tool used routinely for NPs characterization, able to directly measures the particle size from nanoparticle dispersions. DLS analysis permits measuring the hydrodynamic diameter of NPs with its corresponding polydispersity index (PDI). This technique exploits the Brownian motion of NPs and its relationship with the particle size. Briefly, the Brownian motion is the movement of particles due to the random collision with the solvent molecules that surrounds the particles. This movement is related to the particle size by the Stokes-Einstein equation:

$$D = \frac{k_b T}{6\pi\eta r_H}$$

where D is the diffusion coefficient, k_b is the Boltzmann constant, T is the absolute temperature, η is the viscosity of the medium, r_H is the hydrodynamic radius of the spherical particle, and the term $1/6\pi\eta r$ indicated the mobility μ of the particle. So, small particles move quickly, and large particles move more slowly. The DLS instrumentation records the temporal fluctuations of scattered light given by the Brownian motion of the NPs in solution (Figure 1.18).

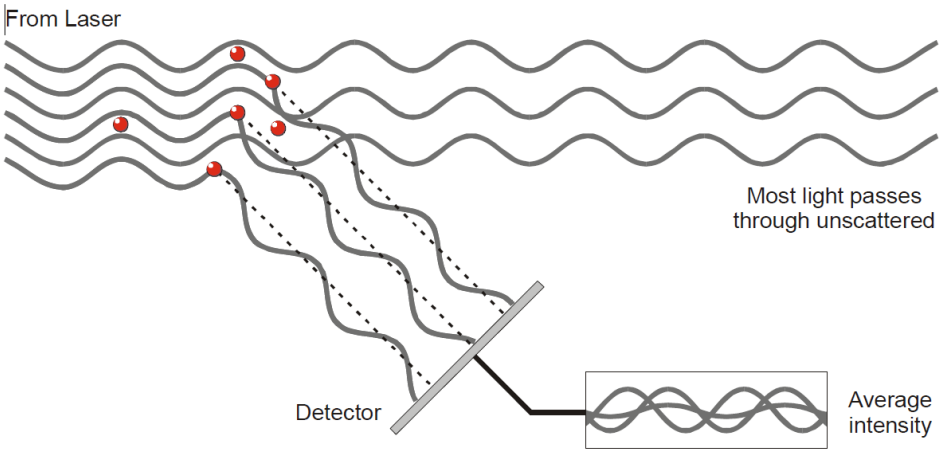

Figure 1.18. The scattered light falling on the detector.

Using a correlation function and the Einstein-Stokes relation, it is possible to determine the size distribution of NPs. The obtained distributions of hydrodynamic diameters are generated by DLS as an intensity distribution. Applying Mie's theory and assuming that all NPs are spherical and homogeneous, the intensity distribution can be converted to a volume distribution, which can be further converted to a number distribution. The intensity distribution considers the scattering intensity of each NP population. Hence, even in the case of low aggregation, the intensity distribution can provide overestimated values of hydrodynamic diameter since the intensity of scattering is proportional to the sixth power of particle diameter (Rayleigh's approximation). On the other hand, volume and number distributions need several assumptions. In particular, the number distribution is of limited use because small errors in gathering data for the correlation function could lead to large errors in this calculation.

1.3.4 Nuclear Magnetic Resonance (NMR)

Nuclear Magnetic Resonance has been demonstrated to be a universal and versatile method for the characterization of nanomaterials. Also, it has been regarded as one of the most powerful techniques for the characterization of AuNP, offering many possibilities for the study of the monolayer, composition, dynamics and morphology (Figure 1.19).

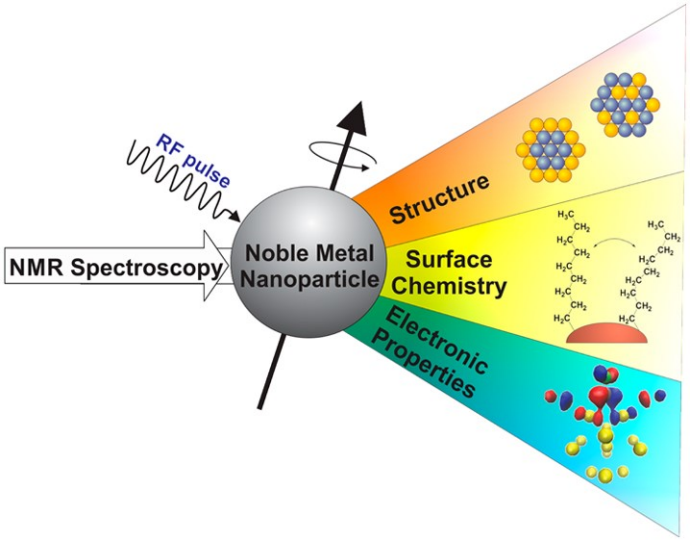

Figure 1.19. Important information obtainable by NMR analysis of the nanoparticles. From Marbella, L. E. et al. *Chem. Mater.* **2015**, *27* (8), 2721–2739.

The NMR spectra of nanoparticles show a characteristic line broadening of the resonances, an altering in the chemical shift, and the disappearance of some resonances compared to the NMR spectra of the pertinent free ligands (Figure 1.20).[46,97,124–127]

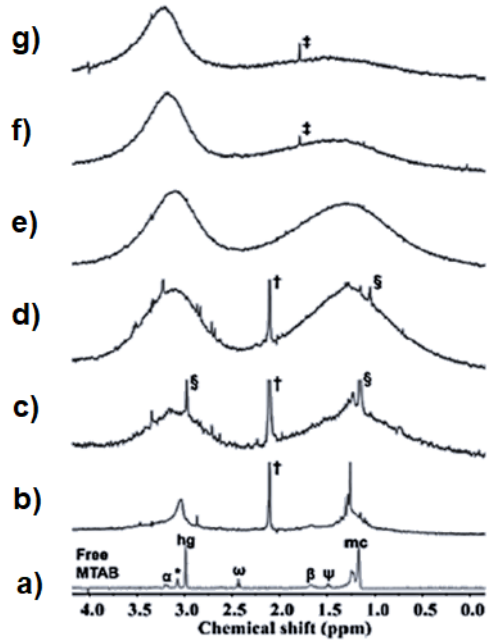

Figure 1.20. ^{1}H NMR spectra of free MTAB (**a**) and MTAB-AuNPs in D_2O (**b-g**). The traces from bottom to top corresponded to the particle size of 1.2 ± 0.3 nm (**b**), 4.8 ± 1.1 nm (**c**), 6.4 ± 1.1 nm (**d**), 8.2 ± 0.9 nm (**e**), 10.8 ± 0.8 nm (**f**), 13.4 ± 1.2 nm (**g**). Adapted from Wu, M. et al. *J. Am. Chem. Soc.* **2019**, *141* (10), 4316–4327.

When ligand molecules are adsorbed to the AuNP surface, their molecular tumbling is severely reduced. In this situation chemical shift anisotropy (CSA), dipole-dipole spin coupling interactions and the distribution of chemical environments lead to signal line broadening. The broadening is more marked for the nuclei closer to the gold core because they are densely packed and more solid-like than the nuclei far apart from the core surface. Grafting of ligands leads also to a change in the spin transverse relaxation time T2 that in turns directly influences the NMR linewidth. The resonances of the nuclei close to the gold core are also affected by a further line broaden mechanism due to the quadrupolar moment of the gold nuclei (I=3/2). The signal line broadening becomes more and more severe as the size of the nanoparticles increase NMR spectroscopy is very useful to understand the structure of the nanoparticle monolayer, this is particularly relevant in the case of mixed ligand-protected AuNPs; indeed, it has been shown that the chemical shifts of the ligand nuclei forming the monolayer are affected by the neighbouring ligand species in a morphology dependent manner. This dependence can be used as an important indication of the neighbouring environment of the ligands and, therefore, it may allow retrieving information on the monolayer morphology. Indeed, some studies[79,128] have demonstrated that by assessing the dependence of the chemical shifts of diagnostic peaks as a function of the monolayer composition it is possible to define characteristic trends that are specific of the monolayer morphology. For random arrangements, the chemical shift shows a linear dependence on the monolayer composition due to the coincidence between global and local

compositions. In the Janus arrangements, this equivalence is removed, and the shift is proportional to the inverse of the composition. While for stripe-like arrangements, the dependence is more complex leading to a sigmoidal trend depending on the evolution of the shape of domains. The study of chemical shift dependence on monolayer morphologies has also been applied to mixed-SAM AuNPs coated with hydrocarbon and fluorinated ligands (Figure 1.21).[80] By ^{19}F NMR the trends of random, Janus, and stripe-like AuNPs were determined and it is found to be consistent with the other studies.

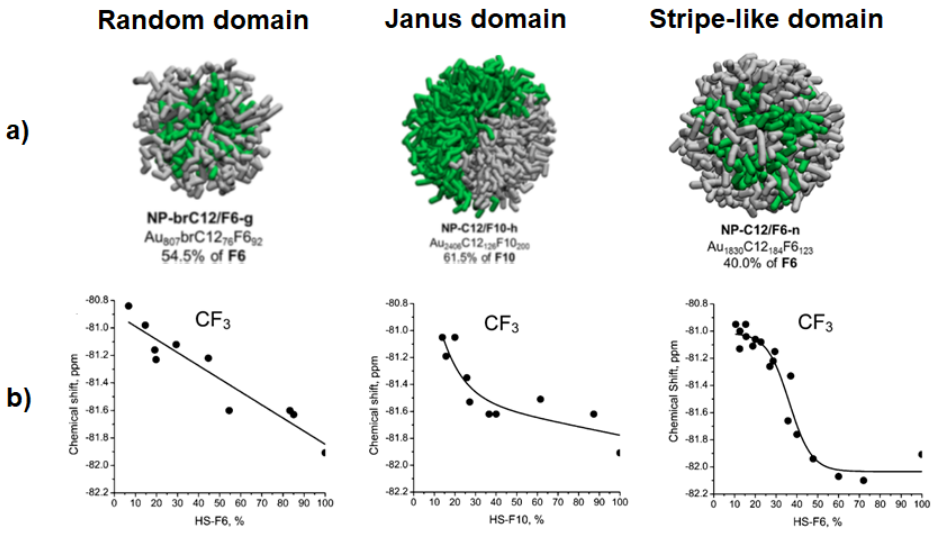

Figure 1.21. (**a**) Equilibrium morphologies of NP-brC12/F6, NP-C12/F10, and NP-C12/F6 (color code: gray, H-chains; green, F-chains) as obtained by the mesoscale simulations. The solvent is omitted for clarity. (**b**) Chemical shift (δ) variation of -CF_3 groups increasing the percentage of the fluorinated ligand in the monolayer of NP-brC12/F6, NP-C12/F10, and NP-C12/F6. The solid line serves as a guide for the eyes only. Adapted from Şologan, M. et al. *ACS Nano* **2016**, *10* (10), 9316–9325.

Additionally, the NMR techniques that exploit the Nuclear Overhauser effect (NOE), namely the 2D NMR Nuclear Overhauser Effect Spectroscopy (NOESY) and the Heteronuclear Overhauser Effect Spectroscopy (HOESY), can be employed for an in-depth analysis of the morphology of the monolayer in mixed SAM AuNPs. Indeed, when the nuclear spins are close enough (<0.5 nm), these techniques allow detecting cross-correlation peaks between these nuclear spins. The intensity of the cross-peaks depends on the number of contacts between the ligands. Therefore, in the case of ligands confined in different domains of the monolayer, the intensity of the cross-peaks depends on the extension of the interface between the domains. Hence, in the case of small domains, stripe-like domains or a random arrangement of the ligands, the number of interface surfaces is high, and intense cross peaks are observable. Instead, the absence of cross-peaks may be an indication of a Janus morphology in which the number of ligands at the interface between the domains is small number respect to the overall number of ligands in the domain.

Another crucial feature of the AuNP monolayer that can be extrapolated by NMR is the ligand chain packing. Indeed, the T_2 (spin-spin) relaxation is affected by molecular mobility, and it can be measured by NMR experiments (Carr-Purcell-Meiboom-Gill pulse sequence). For bound ligands on the AuNPs, their mobility depends on the size of the AuNP and the relative chains packing of the monolayer. As the AuNP size increases, both the ligand mobility and its T_2 decrease. In the case of a homogeneous system, T_2 is inversely proportional to the peak width and the resulting value (defined as T_2^*) is the same obtained by the CPMG pulse sequence. However, for AuNPs with a diameter below ~ 14 nm, Murphy and co-workers have found that T_2^* is often higher than T_2 calculated by CPMG experiments, attributing this difference to a heterogeneous environment of the ligand headgroups due to the high surface curvature of small AuNPs.[127] As the AuNP size increase, as the difference between T_2 and T_2^* decreases. In addition, NMR analysis also permits to calculate of the ligand ratio on mixed-SAM AuNPs by decomposition of the monolayer using oxidizing agents. In detail, by choosing and then integrating the characteristic peaks of the diverse ligands is possible to find the ratio between the ligands by calculating the corresponding peak areas.

Besides the characterization of the monolayer, the combination of the NMR technique and monolayer-protected AuNPs has raised considerable interest in the field of chemosensing. In this contest, Mancin and co-workers have designed and developed novel NMR experiments to detect and quantify small analytes that are able to interact with the nanoparticle monolayer. Their strategy is based on both the slow diffusion of AuNPs in solution, compared to that of organic molecules, and on the possibility of exploiting intermolecular dipolar interactions to transfer magnetization between two interacting species.[129–132] So, their approach exploit a NMR sequence composed of the magnetization dephasing of all rapid diffusing species and the subsequent magnetization transfer from the AuNPs to the molecules interacting with the AuNP monolayer (the analytes). The result is the full NMR spectrum of the analyte.

1.3.5 UV-Vis Spectroscopy

Some nanoparticles including the AuNPs display size- and shape-dependant optical properties. In this context, UV-vis spectroscopy is a common and simple method to characterize AuNPs that may be used to retrieve information on the average core sizes and shapes of the nanoparticles. Moreover, UV-vis spectroscopy can be used to determine the concentration of NPs and to follow colloidal growth and stability. Clearly, this technique does not possess the accuracy of TEM analyses, since the

absorption is not very sensitive to the relatively small changes in core size as ones typically encountered in polydisperse gold nanoparticles preparations, furthermore UV-Vis analyses cannot pinpoint the presence of small nanoparticles accompanying larger ones because of the much stronger absorption of the latter. However, UV-vis spectroscopy remains a useful technique because it allows to perform a fast and simple preliminary analysis of a nanoparticle sample without sophisticated sample preparations. The AuNPs property that make UV-Vis analysis useful is their localised surface plasmon resonance (LSPR), due to the collective oscillations of AuNP conduction electrons induced by the absorption of photons.[133] This phenomenon occurs in a precise range of the electromagnetic spectrum between the visible and the infrared regions. The consequence of light absorption by AuNPs is the appearance of the surface plasmon band (SPB), in a range from 500 to 550 nm and is absent in both small nanoparticles ($d < 2$ nm). The spectral position and shape of the SPB depend on numerous parameters, such as the core size, size-distribution, shape, surface chemistry, medium, etc (Figure 1.22). For instance, the LSPR can change dramatically upon aggregation, resulting in significant red-shifting of LSPR wavelength due to the interparticle plasmon coupling. This phenomenon can be clearly perceived by the naked eye as a colour change from red to blue and has been extensively exploited in the development of bioanalytical devices and colorimetric sensors.[134–137]

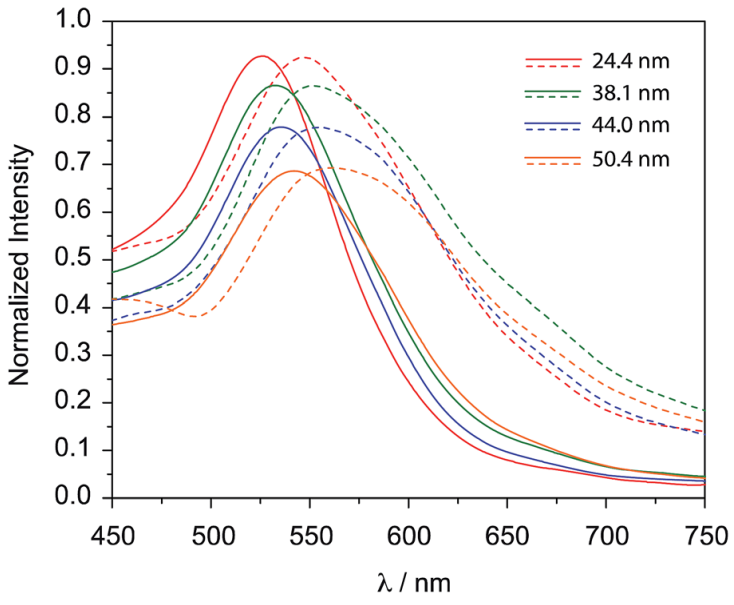

Figure 1.22. Surface plasmon absorption spectra of gold nanoparticles of varying size in aqueous solution (solid lines) and silk films (dotted lines). From Guo, C. et al. *RSC Adv.* **2014**, *5* (3), 1937–1942.

1.4 Physical properties of AuNPs

Gold nanoparticles show interesting optical properties depending on their size and shape that are significantly different from those of the bulk state. Moving to the nanoscale, the properties of a material like electrical, magnetic, optical, and chemical properties that are independent of its size and shape in the bulk state, become sensitive to these features. The reason for this change is related to the quantum size effects, due to the electron confinement and energy quantization. As the size decreases, the electrons become more confined, and this leads to an increase in the band gap energy. Spherical AuNPs of adequate size exhibit a range of colors (e.g., brown, orange, red, and purple) and this phenomenon is due to the collective oscillation of the conduction electrons producing the LSPR (Figure 1.23). The wavelength at the maximum for the plasmon resonance of AuNPs is usually in the visible region. In detail, the oscillating electromagnetic field of light causes the conduction electrons oscillations of AuNPs, inducing the polarization of the electron density of the nanoparticle core. When the frequency of the electromagnetic field becomes resonant with the electron oscillations, a strong absorption occurs. [138,139]

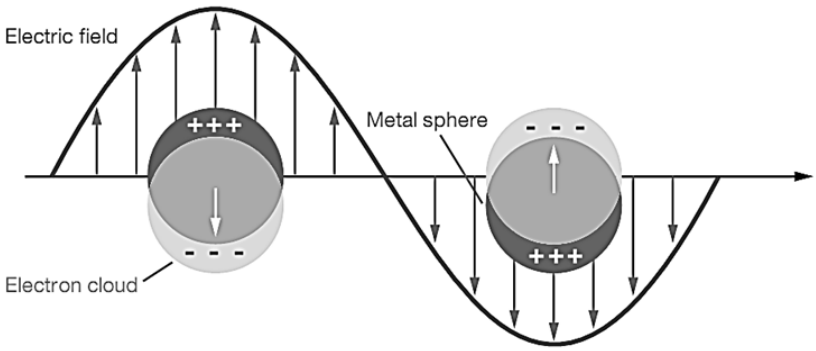

Figure 1.23. The oscillations of the AuNP conduction electrons with the electromagnetic field. When the frequency of the incident light matches the intrinsic frequency of AuNP, resonance occurs. Adapted from Willets, K. A. et al. *Annu. Rev. Phys. Chem.* **2007**, *58* (1), 267–297.

This feature manifests itself when the size of the AuNPs is larger than about 3 nm whilst AuNPs with a size around 2 nm do not show plasmon UV-vis resonances. Moreover, molecularly precise gold nanoclusters (AuNCs) are characterized by discreet absorption bands due to well-defined transitions among energy levels resembling those of typical organic chromophores. AuNCs and small gold nanoparticles may also display luminescence in the near-infrared (NIR) region, which makes them promising candidates for in vivo optical imaging and analysis because this spectral range matches the biological transparency window.[140,141]

1.4.1 Near Infrared (NIR) Emission

AuNCs are ultra-small nanoparticles (diameter < 2 nm) composed of a few tens to a few hundred gold atoms coated by a protecting monolayer. The optical properties showed by AuNCs are fundamentally different from those exhibited by AuNPs. Indeed, while the latter are dominated by the collective oscillation of conductions electrons giving rise to their LSPR, for AuNCs molecular-like properties emerge and the absorption spectra are dominated by single-electron transitions This is the result of their reduced size, and therefore their reduced number of atoms, giving rise to a discrete electronic structure and molecular-like properties, such as HOMO-LUMO electronic transitions, near-infrared (NIR) photoluminescence, and many others.[142] Moreover, the unique optical properties of this type of nanostructure are closely related to their precise composition and structure of the metal core (Figure 1.24).[143]

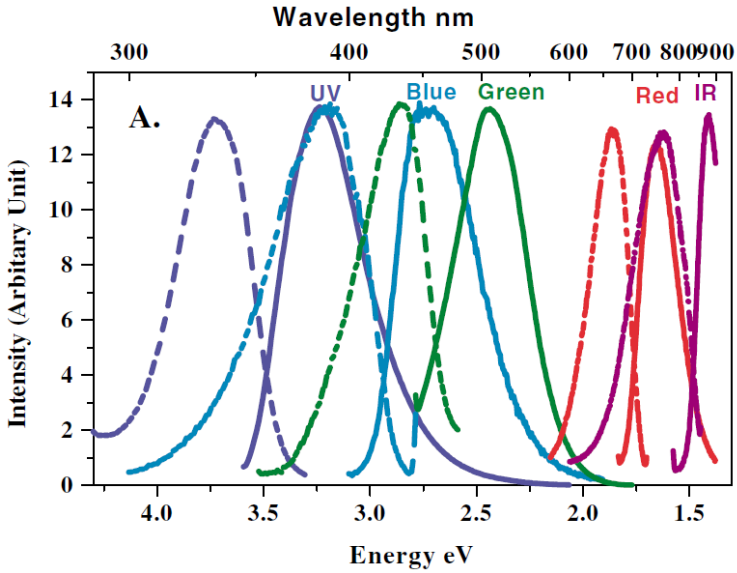

Figure 1.24. Excitation (dashed line) and emission (solid line) spectra of AuNCs of different sizes. The increase in AuNC size produces the excitation and emission maxima shift to longer wavelength. From Zheng, J. et al. *Phys. Rev. Lett.* **2004**, *93* (7).

Furthermore, the functionalization of the monolayer strongly influences the optical and electronic properties of the AuNCs. Indeed, ligands have been shown to not only significantly influence the shape and geometric structures of AuNCs, but also the energy of HOMO-LUMO orbitals through energy transfer behaviors. For instance, Zhu, M. *et al*. have analysed the structure of a precise alkanethiol-protected AuNC, in which eighteen molecules of phenylethanethiol (SR) coat the cluster Au_{25} (formula $Au_{25}SR_{18}^{-}$). In this study, they also have performed time-dependent density functional theory (TDDFT) calculations to correlate the electronic structure with the optical absorption spectrum

of a simplified model cluster: $Au_{25}(SH)_{18}^-$. This computational approach has allowed to establish a correlation between the AuNCs structure with the optical properties (Figure 1.25).[144]

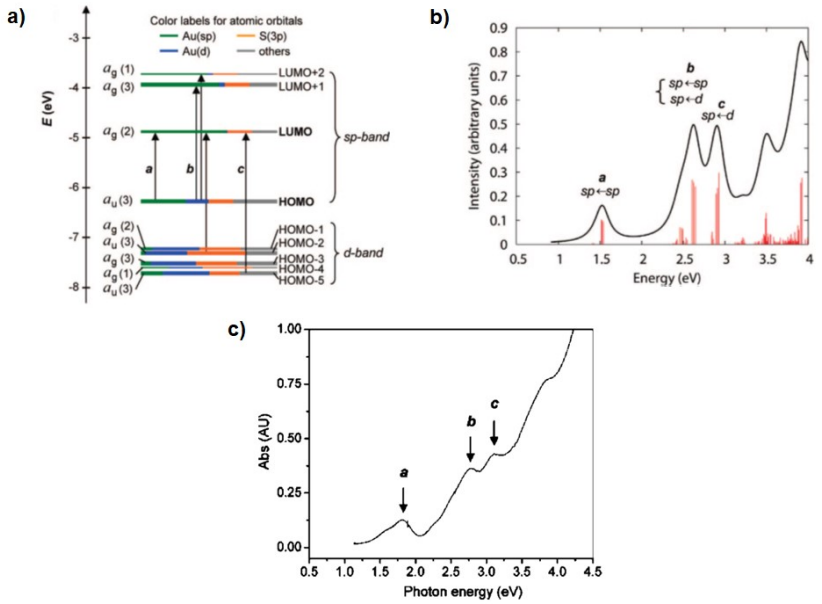

Figure 1.25. (**a**) Kohn-Sham orbital energy level diagram for a model compound $Au_{25}(SH)_{18}^-$. The energy is expressed in eV. Each KS orbital is drawn to indicate the relative contributions (line length with color labels) of the atomic orbitals of Au (6sp) in green, Au (5d) in blue, S (3p) in yellow, and others in gray. (**b**) The theoretical absorption spectrum of $Au_{25}(SH)_{18}^-$. Peak assignments (**a**, **b**): peak *a* corresponds to 1.8 eV (observed), peak *b* corresponds to 2.75 eV (observed), and peak *c* corresponds to 3.1 eV (observed). (**c**) The UV-vis spectrum of $Au_{25}(SR)_{18}^-$ clusters. Adapted from Zhu, M. et al. *J. Am. Chem. Soc.* **2008**, *130* (18), 5883–588.

Their results have shown that both sets of HOMO and LUMO orbitals of the model nanocluster of $Au_{25}(SH)_{18}^-$ have a significant degree of 3p ligand character (coloured in orange in Figure 1.25a), underlying how the ligand can significantly influence the electronic structure of the nanocluster, and so its properties. It should be noted that the theoretical spectrum for $Au_{25}(SH)_{18}^-$ (Figure 1.25b) agrees quite well with the UV-vis spectrum of $Au_{25}(SR)_{18}^-$ (Figure 1.25c). A noticeable blue shift observed in the latter with respect to the theoretical absorption spectrum of $Au_{25}(SH)_{18}^-$, was explained on the basis of the electron-donating effect of the SCH_2CH_2Ph moiety.[145,146] This study is useful to illustrate the quantum size effect on the optical properties of AuNCs. Unlike AuNPs in which the collective excitation of conduction electrons (LSPR) commands their optical properties, these nanoclusters ($Au_{25}(SR)_{18}^-$) show one-electron transitions, on which their absorption and emission features depend.[147–149] Currently, the role of ligands in AuNC luminescence remains an object of intense investigation; recent studies suggest increasing the electron-donating capability of ligands enhances the fluorescence intensity of the AuNCs through the so-called ligand-to-metal charge transfer (LMCT), or by the ligand-to-metal-metal charge transfer (LMMCT) which is associated with the presence of aurophilic (Au−Au) interaction.[150–153] Moreover, it was demonstrated that using ligands

with electron-rich moieties such as atoms (e.g., N, O) or groups, the fluorescence of the cluster is largely enhanced.[154] On the other hand, since the vibrational and rotational motions of ligand chains cause energy loss through nonradiative pathways, the introduction of a certain rigidity by functionalization of AuNCs with bulky moieties was exploited to significantly enhance the luminescence quantum yield.[155,156] In contrast to the LMCT, Pramanik *et al*. showed that metal-to-ligand charge transfer (MLCT) can be exploited to greatly enhance the fluorescence of gold nanoclusters.[157] They have noted that the emission of AuNCs coating by thioctic acid (TA) and polyethylene glycol (PEG) is dramatically enhanced by introducing the triphenylphosphonium cation moiety in the monolayer. Based on these results, the surface engineering of AuNCs is a promising strategy for achieving tailored optical properties.[158,159]

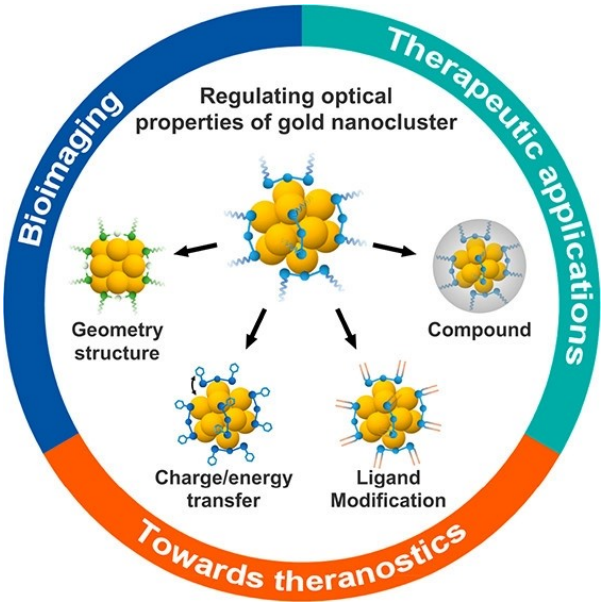

Figure 1.26. The possible strategies to tune and modulate the optical properties of AuNCs. From Zhu, S. et al. *ACS Omega* **2020**, *5* (36), 22702–22707.

1.4.2 Fluorescence quenching

Among the optical properties of AuNPs, their extraordinarily fluorescence quenching ability has received increased attention during the last decades. It was demonstrated that AuNPs can be used as excellent quenchers of molecular excitation energy in dye-AuNP hybrids, exceeding the quenching efficiency of the common organic acceptor molecules.[160] Several experimental and computational investigations about dye molecule-AuNC systems have established that both radiative (R_{rad}) and nonradiative (R_{nonrad}) effects are responsible for the fluorescence quenching by AuNPs.[161] About the nonradiative effects, various theoretical models describing the fluorophore-AuNP quenching

mechanism have been proposed, and both FRET (Förster resonance energy transfer) and NSET (nanosurface energy transfer) have been accepted as applicable theories.[162] In FRET theory, both donor and acceptor are considered as point dipoles; the efficiency of this process is inversely proportional to the sixth power of the donor-acceptor distance. In NSET, the acceptor is a nanosized surface modelled as a collection of many point dipoles. Unlike the FRET, its efficiency is inversely proportional to the fourth power of the distance between the donor molecule and the acceptor surface. Consequently, NSET can overcome FRET distance-dependent energy transfer limit, allowing the monitoring of many other events.

The quenching efficiency of AuNPs depends on both some AuNP features, such as size and shape,[163] as the proximity of the fluorophore to the gold core and the possible overlap between the emission spectrum of the dye molecule and the SPR of the AuNPs.

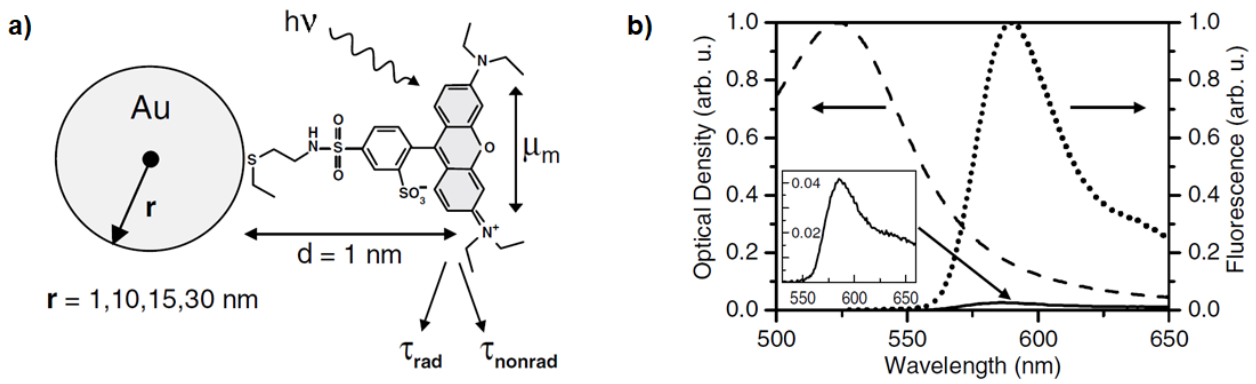

Figure 1.27. (**a**) Lissamine-AuNP system, where AuNPs of different sized are synthesized (1-30 nm) and functionalized with lissamine molecules through a thioether group; (**b**) optical density spectrum of a 15 nm AuNPs (dashed curve), fluorescence spectra of a 0:37 μM aqueous solution of lisammine dye molecules before (dotted curve) and after interaction with AuNPs (solid curve and inset). A drastic fluorescence quenching is observed. Adapted from Dulkeith, E. et al. *Phys. Rev. Lett.* **2002**, *89* (20), 203002.

Dulkeith *et al*. have investigated in depth the role of the Au core size in quenching efficiency. The system they have analysed for this purpose is composed of lisammine molecules as donors, and AuNPs of varying sizes as acceptors (Figure 1.27a). Through analysis by time-resolved photoluminescence (PL) spectroscopy, they have determined the changes in the radiative and non-radiative rates as a function of the radius *r* of the AuNPs (Figure 1.28).[164–166]

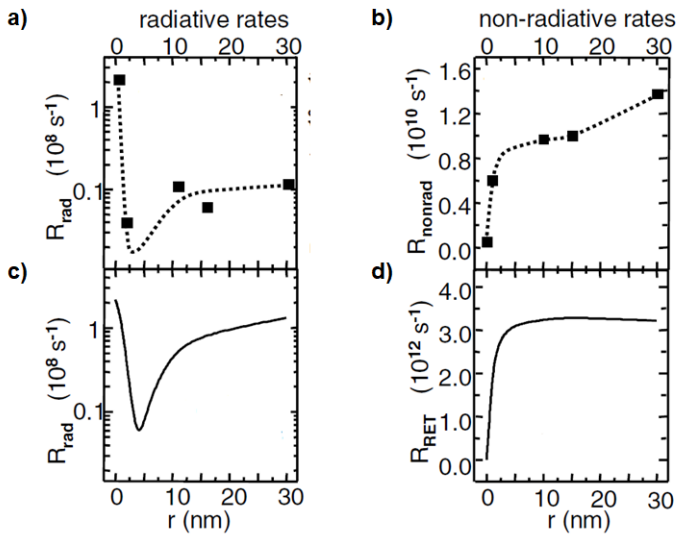

Figure 1.28. The radiative and nonradiative rates as a function of AuNP radius (*r*), determined by experimental analysis (**a, b**) and by theoretical models (**c, d**). At *r* = 0, the measurement is referred to the free fluorophore. The distance between the fluorophore and the AuNP remained constant at 1 nm. Adapted from Dulkeith, E. et al. *Phys. Rev. Lett.* **2002**, *89* (20), 203002.

As shown in Figure 1.28, both the experimental and the computational data have confirmed the dependence of the fluorescence quenching on the Au core size, showing a decrease in the radiative rate and an increase in the nonradiative rate by increasing the AuNPs size. Overall, the exceptional quenching ability of AuNPs makes them excellent candidates for fluorescence-based sensors, which will be dealt with in more detail in the second chapter.[161,167–171]

1.5 AuNPs in biosensing: an overview of the major opportunities and recent advances

It is therefore evident that AuNPs display many chemical and physical properties that make them fascinating and promising tools in a wide range of fields. Among them, AuNPs have recently gathered considerable attention from bionanotechnology.[172–174] The ease of AuNPs functionalization make them versatile platforms for the conjugation with a rich variety of biomoieties such as peptides, oligonucleotides, antibodies, nucleic acids, and proteins (Figure 1.29).[175] Thanks to their tailorable optical properties, low cytotoxicity, and biocompatibility, bioconjugate-AuNPs have become valuable candidates for the design of novel biomaterials for *in vitro* and *in vivo* applications.[176–178] Currently, the potential of AuNPs is being actively exploited for devising numerous novel strategies

in the biomedical field, addressing, for instance, bioimaging, cancer therapy, and drug delivery and biosensing.

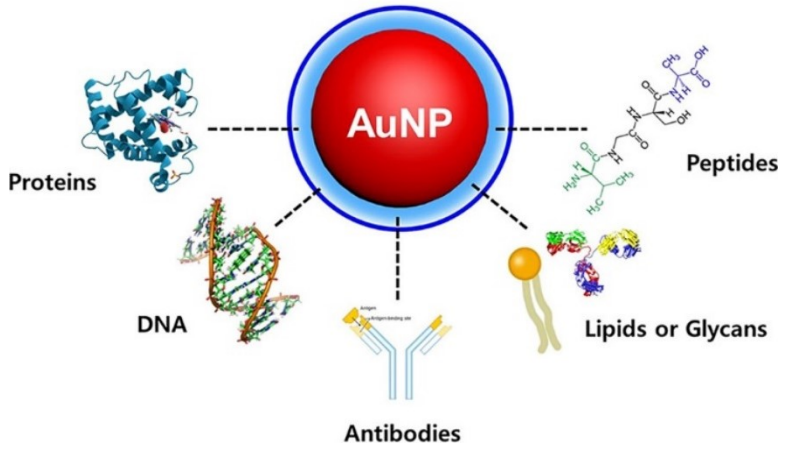

Figure 1.29. The facile surface functionalization of AuNPs allows the introduction of diverse bioelements, such as peptides, nucleic acids, antibodies, etc. From Lee, J. W. et al. *ACS Appl. Mater. Interfaces* **2021**, *13* (36), 42311–42328.

In general, a sensor is composed of two distinct components: a recognition element that interacts and binds specifically the target analyte, and a transducer mechanism or component that provides a read-out to signal te binding event. An efficient sensor provides high selectivity, reduced response times, low limits of detection (LOD), and high S/N ratio. In this context, nanomaterials offer an optimal choice, both for their unique physicochemical characteristics and because the optimization of their S/N ratio can benefit from the miniaturization of the sensor elements.[179]

The possibilities to easily engineer the AuNP make them suitable platforms for the selective binding and detection of molecules, anions, metal ions, proteins, and biological targets. Their high surface-to-volume ratio provides dense loading of functional groups, enabling multivalent recognition possibly ensuring enhanced interactions with the target. Moreover, by exploiting the optical and electronic properties of AuNPs as transducing mechanisms, diverse sensing strategies have been developed and implemented.

1.5.1 Colorimetric sensing

Colorimetric sensing by AuNPs typically exploits the SPR giving rise to an intense absorption band from 500 to 550 nm. The extinction coefficients (ε) at the maximum of the surface plasmon band for gold nanoparticles can be orders of magnitude higher than typical organic dyes with the ε values depending on the third power of the nanoparticle diameter.[180] This feature makes AuNPs ideal when

compliance with the detection, even on a qualitative basis, of small amount of analyte is mandatory such as in biomolecular sensing. One of the most common analytical applications of AuNPs taking advantage of the SPR band is as reporters providing the optical readout in lateral flow assays.[181–183] Another strategy for colorimetric sensing using AuNPs consists in exploiting the plasmonic coupling, between AuNPs causing a sizable red-shift and broadening of the plasmon band because of the AuNP aggregation. This phenomenon leads to a visible color change from red to blue of the AuNP preparation, providing a practical, fast, and low-price absorption-based method for the detection of several analytes, such as organic molecules and metal ions. Additionally, the target-induced AuNP aggregation strategy is widely used in biosensing by the conjugation of specific recognition elements, such as antibodies, aptamers, and proteins on the AuNPs surface.[184–189]

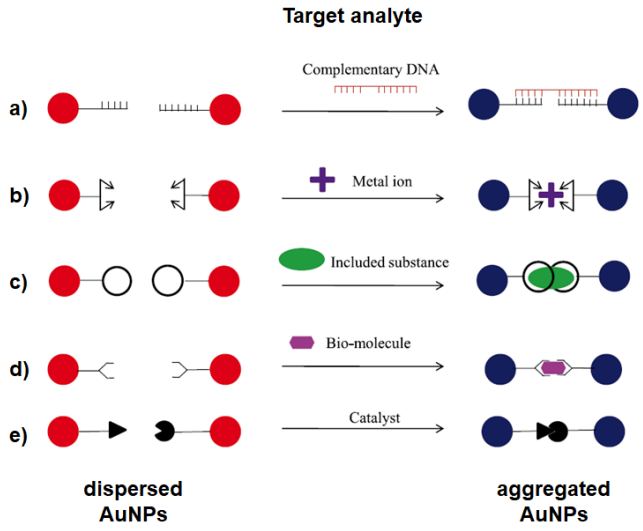

Figure 1.30. Some examples of target-induced AuNP aggregation. Adapted from Uehara, N. *Anal. Sci.* **2010**, *26* (12), 1219–1228.

Regarding the recent AuNP-based colorimetric strategies for bacteria detection and/or discrimination, Mou *et al.*[190] have successfully developed a rapid and simple detection strategy for pathogenic bacteria, exploiting a specific pathway of bacteria metabolism and the optical properties of AuNPs. When the bacteria are exposed to a copper-rich environment a defence mechanism consisting in copper-binding systems and redox enzyme cascades is triggered to remove the toxic Cu^{2+} by reduction to Cu^{+}. Inspired by this process, Mou *et al*. devised a click chemistry-assisted system for bacteria detection by using two batches of AuNPs, functionalised respectively with azide and alkyne-containing molecules. Indeed, it is well known that Cu^{+} catalyse the azide-alkyne coupling. So, their strategy is based on the reduction of Cu^{2+} to Cu^{+} by the targets (pathogenic bacteria), and then Cu^{+} acts as catalyst to trigger the click chemistry reaction between azide-AuNPs and alkyne-AuNPs. The

reaction promotes the AuNP aggregation and so the colour change of the analysed sample from red to blue (Figure 1.31a). Moreover, the authors have implemented a bacterial separation system using iron oxide magnetic NPs functionalized with bacterial species-identifiable aptamers (single-stranded oligonucleic acids) in samples containing multiple bacteria strains. After the magnetic separation, the isolated bacteria were released and treated with the two batches of azide- and alkyne- AuNPs. The combination of aptamer-based magnetic separation and the click chemistry-induced AuNP aggregation allowed to identify and quantify the bacteria strains.

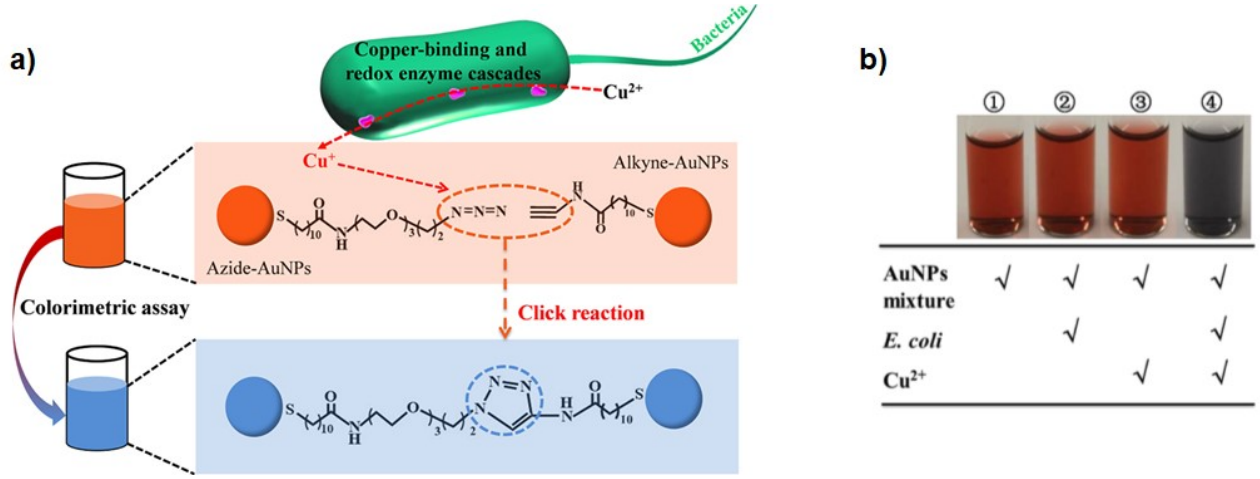

Figure 1.31. (**a**) Scheme of Mou *et al.* strategy for pathogenic bacteria detection using modified azide- and alkyne-AuNPs. (b) Photographs of solutions containing the system components: azide- and alkyne-AuNPs (1), azide- and alkyne-AuNPs in presence of *E. coli* (2), and azide- and alkyne-AuNPs in presence of Cu^{+} (3). The last solution (4) contains all components, and it is the only one to show a colour change. Adapted from Mou, X.-Z. *ACS Appl. Mater. Interfaces* **2019**, *11* (26), 23093–23101.

Another attractive colorimetric strategy involves the use of aptamers to functionalise the AuNPs. This strategy permits to combine the high affinity and specificity of the aptamers with the LSPR of the AuNPs.[137,191] Without the conjugation of complex biomolecules, the optical properties of the AuNPs still allow to get good results in the field of biosensing. Amornwairat and Pissuwan have reported an interesting example of colorimetric strategy for bacteria detection and discrimination, using AuNPs functionalised with 4-mercaptophenylboronic acid (4-MPBA).[192] The units of 4-MPBA displayed on the AuNPs surface can interact with the *cis*-diol groups in saccharides and glycosylated biomolecules, present on both Gram-positive and Gram-negative cell walls forming boronate esters. In the authors approach, the detection mechanism is based on the inhibition of the NaOH induced aggregation of 4-MPBA@AuNPs in the presence of bacteria. In the absence of bacteria, the AuNPs aggregation is triggered by the addition of high concentration of sodium hydroxide. Instead, if bacteria are present 4-MPBA@AuNPs bind to the to the saccharides present on the bacterial wall, escaping aggregation

(Figure 1.32). Based on the number of interactions between the AuNPs and the binding sites present on the bacteria envelope it is possible to obtain solutions of different colors thus discriminating different bacteria strains. To confirm this strategy, the authors have chosen two bacteria strains, *E. coli* K-12 and *S. aureus*, that were incubated with 4-MPBA@AuNPs. As shown in Figure 1.32, the color of the solution appeared red for *E. coli* K-12, and deep purple for *S. aureus*, indicating that *S. aureus* interacts less with the nanoparticles than *E. coli* K-12.

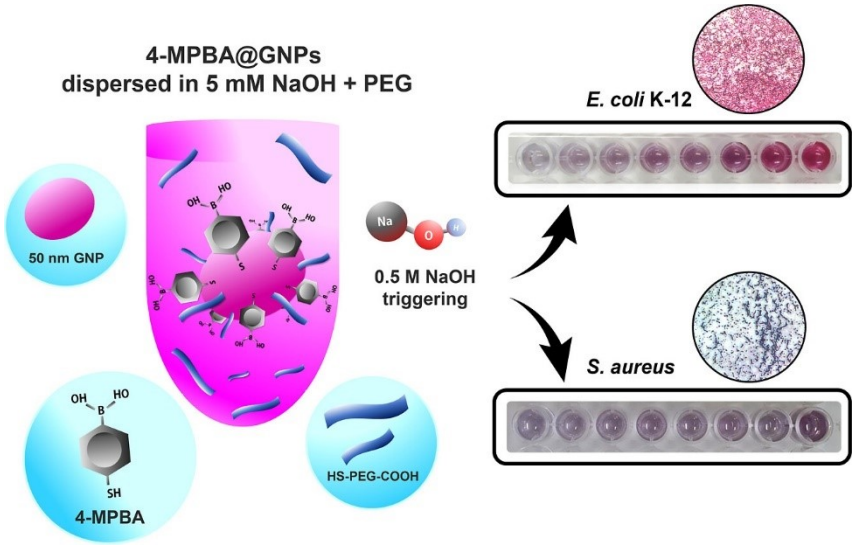

Figure 1.32. The colorimetric strategy of bacteria by using 4-MPBA@AuNPs, PEG and NaOH triggering. From Amornwairat, P.; Pissuwan, D. *ACS Omega* **2023**.

In these examples the AuNPs were functionalised with relatively simple and synthetic ligands; resorting to the use of more complex and selective recognition units, the aggregation of plasmonic AuNPs has been widely used in the development of 'naked eye' detection systems for biomolecules. An example can be found in the context of the recent outbreak of SARS-CoV-2. Indeed, this approach has been applied for the detection of either different viral proteins such as the spike protein[193], the nucleocapsid (N) proteins[194]; anti SARS-CoV-2 IgG antibodies[195] or for detecting the presence of viral RNA.[196,197]

1.5.2 Fluorescence sensing

The excellent quenching ability of AuNPs towards numerous fluorophores, such as organic dyes and fluorescent proteins, makes them optimal materials for the engineering of fluorescence-based assays involving nanoparticle-fluorophore complexes. This approach can exploit either the turn-off or the turn-on of fluorescence and require a close proximity of the fluorophore to the AuNPs surface; under

these conditions the most efficient quenching can take place. The approach that is more pertinent to this thesis is the one that leads to fluorescence turn-on upon recognition of the analyte. To insert a fluorophore close to the outer surface of gold nanoparticles both covalent and non-covalent approaches can be pursued. In the case of non-covalent interactions between the AuNPs and the fluorophore the nanoparticles act as exo-receptors; in the presence of an analyte displaying some affinity for the nanoparticle surface, the fluorophore can be partly or totally displaced from the nanoparticle surface recovering its fluorescence properties. Therefore the analyte recognition results in a fluorescence turn-on For the self-assembly of organic molecules, not necessarily fluorophores, on the nanoparticles surface, the electrostatic interactions between cationic nanoparticles and anionic molecules proved to be particularly useful and was extensively exploited in seminal works by Rotello[198,199] and Prins.[200–203] This approach has been extended to anionic fluorophores with formation of AuNPs-fluorophore constructs to be used as platforms for the detection of biomolecules.[204]

Fan *et al*. reported that the fluorescence quenching efficiency of anionic AuNPs towards a cationic, water-soluble polyfluorene was much higher than both any previously reported conjugated polymer-quencher pair, and typical small organic dye-quencher pairs.[205] They explained that this peculiar quenching ability was due to several factors, including the contribution of electrostatic interactions between the polymer and the AuNPs. According to their results, such interactions provided an optimal driving force for the binding, ensuring an efficient static quenching.

Based on this study, Rotello and co-workers have investigated in depth the binding between charged conjugated polymers and charged AuNPs, focusing their attention on the parameters influencing the recognition event.[206] In their investigations the authors choose two distinct anionic fluorescent polymers to study their interaction with cationic AuNPs of varying hydrophobicity (Figure 1.33a), and the corresponding binding affinity k_a was calculated in aqueous solutions with or without added NaCl.

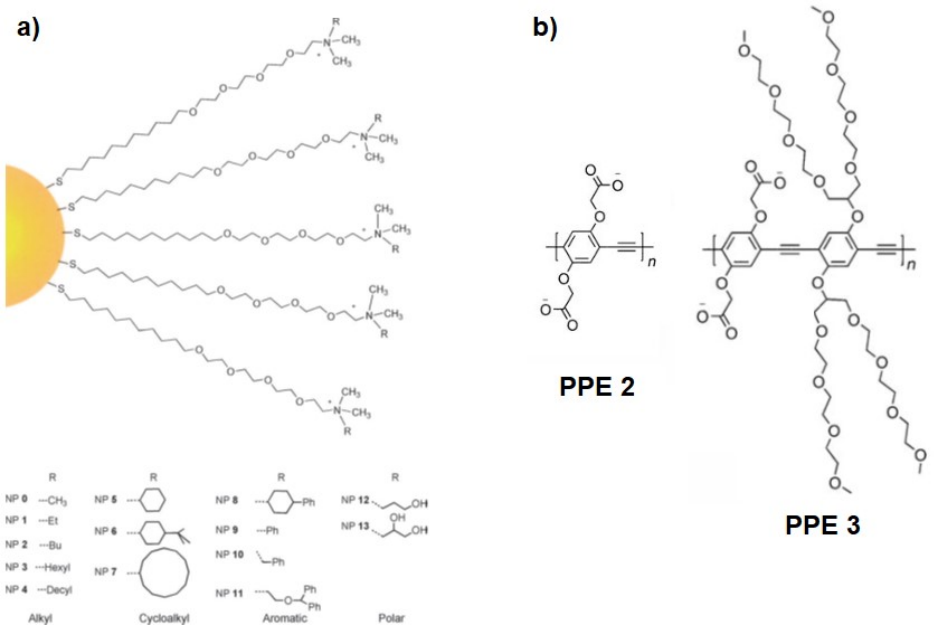

Figure 1.33. Evaluation of the binding affinity between different functionalised cationic AuNPs (**a**) and anionic polymers (**b**). Adapted from Bunz, U. H. F.; Rotello, V. M. *Angew. Chem. Int. Ed.* **2010**, *49* (19), 3268–3279.

Considering the analyses carried out using the **PPE3** polymer (Figure 1.33b) in aqueous media, the authors have found that AuNPs featuring aromatic end-groups showed a higher quenching efficiency, and therefore a higher binding affinity to the conjugated polymer than AuNPs displaying aliphatic end-groups on their outer surface. This result is consistent with the multivalent π-π interactions between AuNPs and **PPE3**. Since many of the biological processes take place in environment with high ionic strength, Rotello and co-workers also analysed how the binding of **PPE3** to the AuNPs could be influenced by the presence of salts. In this case, the AuNPs with aromatic end-groups have shown a high sensibility to the ionic strength that decreased the corresponding k_a. The authors also attempted a correlation study between the hydrophobicity of the ligands and the AuNPs-**PPE3** binding constants (k_a). Interestingly, it was possible to pinpoint that the hydrophobicity does not play a crucial role for the binding in the case of aliphatic AuNPs, while it was more important in the case of aromatic AuNPs. These results lead to the conclusion that the binding event is strongly dependent on electrostatic interactions, whose contribution is a crucial component for the assembly of stable polymer-AuNPs constructs, especially in environments with high ionic strength.

A promising approach in the sensing field regards the use of nanoparticle libraries. According to the nanoparticle functionalization their interaction with the target can be tuned, each member of the library can therefore be designed to provide a different response. The array of the responses represents a ‘signature’ which should selectively identify the target. Indeed, several studies have focused on

fluorescence-based sensing, exploiting fluorescent sensor arrays consisting of AuNPs with different surface chemistry. Rotello and co-workers have pioneered this field extensively exploring this approach based on arrays of engineered AuNPs as fluorescent quenching agents, for the discrimination of a variety of biological samples. Their approach is based on the noncovalent conjugation of fluorescent molecules (proteins or polymers) to the AuNPs, obtaining quenched fluorophore-AuNP constructs. The target analyte competitively binds to AuNPs, promoting the release of the fluorescent molecule from the nanoparticle surface restoring its fluorescence (Figure 1.34).[207–209] Briefly, gold nanoparticles bearing positively charged headgroups electrostatically interact with negative fluorescent protein (FP), promoting FP fluorescence quenching. With the addition of another negatively charged protein (e.g., serum albumin, transferrin, or fibrinogen), the FP can be displaced and released, restoring its fluorescence. By varying the functionalities of the AuNP surface, the affinity of the AuNPs towards FP and the anionic analyte can be varied, creating a sensor array.

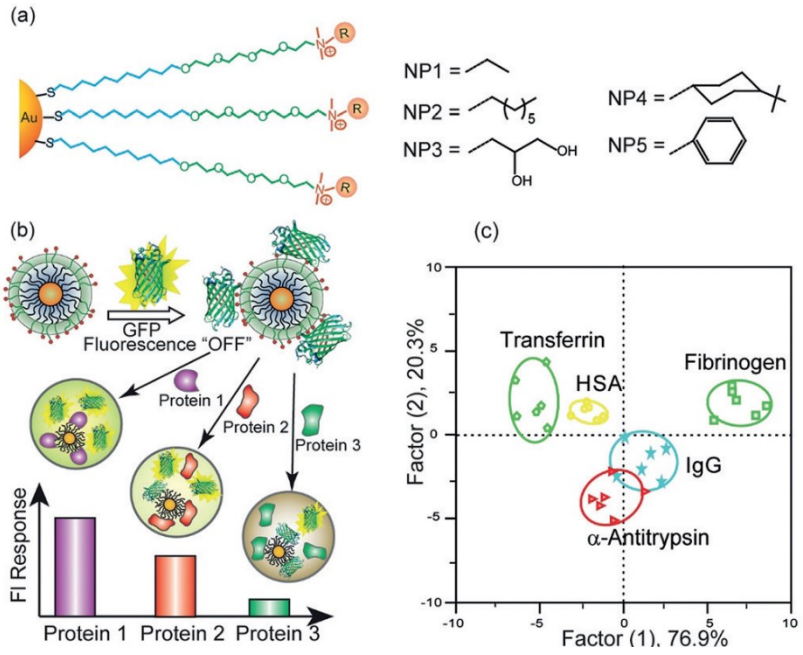

Figure 1.34. Protein detection by AuNPs-fluorophore sensor array. (a) Structure of cationic Au-NPs. (b) Sensing scheme of AuNP-FP (fluorescent protein) array in which positively charged AuNPs electrostatically interact with a negative green fluorescent protein (GFP) and quenched its fluorescence. The addition of other proteins causes differential release of FP. (c) Differentiation of five major serum proteins in spiked human serum samples. From Geng, Y. *Angew. Chem. Int. Ed.* **2019**, *58* (16), 5190–5200.

This approach has been further extended moving from recognition of biomolecules to the recognition of extended bio-interfaces; this topic will be further discussed in the next chapter.

Chapter 2

2. Gold nanoparticles for in vitro diagnostics: bacteria sensing

After the widespread use of advanced antibiotics from the 1930s to the 1960s, antibiotic resistant bacteria appeared almost immediately. Currently, the bacterial antimicrobial resistance (AMR) has emerged as one of the leading public health threats of the 21st century. In fact, both the U.S. Centers for Disease Control and Prevention (CDC) and the World Health Organization (WHO) have identified the AMR as one of the major global public health threats facing mankind. Recent projections indicate that AMR will result in 10 million annual deaths by 2050, more than those caused by cancer presently.[210] Another factor contributing to aggravate the current situation is the appearance of ESKAPE (*Enterococcus faecium, Staphylococcus aureus (S. aureus), Klebsiella pneumoniae, Acinetobacter baumannii, Pseudomonas aeruginosa, and Enterobacter* species) super bacteria. Among the possible interventions for addressing the challenge of bacterial AMR, the development of sensing strategies able to obtain an accurate and rapid detection of bacteria is an urgent priority. In this way it would be possible to minimize the use of antibiotics when they are not needed to improve human health (such as treating viral infections). Moreover, timely diagnostic testing allows to both guide patient treatment and reduce or suspend antimicrobial use when appropriate, as well as giving important support on preventing hospital infections.

In vitro diagnostic devices (IVDs) are tests that can detect diseases or infections and can also be used to monitor the evolution of health conditions. IVD devices include pregnancy tests, COVID-19 tests, and HIV tests and many others. Currently, according to the World Health Organization over 40 000 products are available for IVD testing, and they continue to receive much public attention because of their distinct features.[211]

The IVD tests are non-invasive products, and usually do not require any interaction with the human body directly. In this way possible biological safety problems on patients are avoided, compared to *in vivo* diagnostics. An added value is that the IVD devices are affordable and accessible. Moreover, one of the major aspects of IVD tests is the possibility of rapidly providing valuable information on the patient health conditions. Thereby, physicians or patients can make a timely decision for the cure or treatment of the problem. Globally, all these features are even more relevant in remote settings in which the managing outbreaks of acute infectious diseases need effective but simple diagnostic systems.[212] Furthermore, IVD devices can also be implemented as Point of Care Devices (POC) that can be used directly at the patient bedside reducing the costs of diagnostic procedures.

Currently, the major limitation of the commonly used IVD systems is their moderate detection sensitivity, compared to the standard diagnostic techniques as ELISA and PCR typical of laboratory settings. In turn, these techniques require sophisticated processes, costly equipment, and reagents, and most importantly are time consuming making them not appropriate for rapid diagnostics. Therefore, the development of simple but more sensitive IVD devices is highly desirable for the healthcare systems. To overcome these issues, many studies have aimed at devising high-sensitivity nanomaterials-based IVD systems. In this context, the AuNP-based IVDs have attracted a remarkable interest at the research level because the optical properties of AuNPs such as LSPR, FRET, surface enhanced Raman scattering (SERS) are well-suited to develop robust and simple-to-use assays. As mentioned in the previous chapter, these properties make AuNPs optimal scaffolds for the fabrication of biosensors for a variety of biotargets. Furthermore, AuNPs show several practical advantages compared to the other nanomaterials (facile and reproducible synthesis in common conditions, easy functionalization) that make them particularly suitable for IVDs development. Indeed, in the last decade, there has been a considerable increase in the development of AuNP-based IVD systems for a variety of applications, from electrochemical, to fluorometric assays. In particular, this chapter will deal to the use of AuNPs in bacteria detection, focusing on the sensor array strategy combined with fluorescence-based sensing.

2.1 AuNPs-based sensor array as chemical nose

Ideally, a specific sensor should be able to recognize a single analyte. However, specificity is hard to get, especially when the sensing element is a relatively simplified receptor like the ones that can be achieved by conventional design methods and synthetic procedures. Furthermore, in complex media

such as biological samples, matrix effects and cross-reactivity can be a source of performance deterioration. To overcome these issues and increase selectivity, the concept of "chemical nose" has been developed inspired by the mammalian olfactory system. A "chemical nose" consists of an array-based system that uses synthetic molecules and/or materials as chemical receptors. Then, unlike specific recognition by a single receptor, the chemical nose sensing exploits the binding between an analyte and a whole array of recognition elements, each of which display some selectivity, but no one needs to be necessarily truly specific. The result of this approach is a set of responses, one for each element in the sensing array, that is selective for each analyte, that can be read out and associate to the analyte through a recognition pattern. Significantly, even chemical nose composed by a relatively small number of recognition elements can provide distinctive recognition patterns.[213]

The sensing and biosensing involve two distinct processes: the analyte recognition, and the signal transduction upon binding event. The recognition event between analyte and each recognition elements of the array must be transduced into a measurable result, such as an electric, fluorescent, or colorimetric signal. In this context, the unique features of AuNPs can be used for both recognition and transduction processes. About the first process, the AuNPs functionalization provides multiple interaction sites on AuNP surface, allowing to use small amounts of sensing material while increasing sensitivity. An example of chemical nose sensor based on AuNPs was reported by Rotello and co-workers, in which an enzyme-nanoparticle array was developed using a set of different functionalised cationic AuNPs as receptors (Figure 2.1a).[214] In this example, the cationic AuNPs are electrostatically bound to the anionic β-Galactosidase (β-Gal). The AuNPs/β-Gal interaction inhibits the enzyme activity toward a fluorogenic substrate (Figure 2.1b), 4-methylumbelliferyl-β-D-galactopyranoside (MUG). The addition of target proteins (such as α-Amylase, bovine serum albumin (BSA), cytochrome C (CytC), and others) that competed with β-Gal for the nanoparticle surface was found to promote the release β-Gal and restore of its enzymatic activity, permitting the reaction with MUG and the generation of a fluorescence signal (Figure 2.1c).

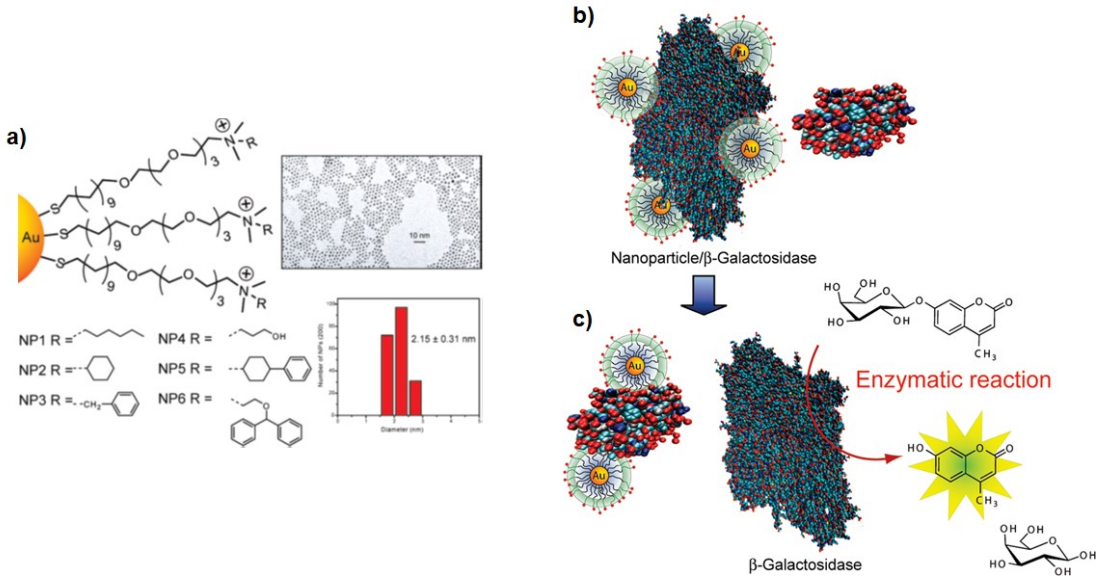

Figure 2.1. Schematic representation of Rotello et al. sensor comprised of *β*-Gal and cationic AuNPs. Adapted from Miranda, O. R. et al. *J. Am. Chem. Soc.* **2010**, *132* (14), 5285–5289.

Furthermore, the optical properties of AuNPs can be exploited as transduction system, including the LSPR red-shift upon nanoparticle aggregation, and the AuNPs activity as fluorescence quencher (Figure 34). As far as the latter is concerned, the quenching activity of AuNPs has been the subject of several studies, some of which have addressed the application of this property in the field of sensing. In fact, it has been shown that when the fluorophore is a polymer, the quenching activity of the AuNPs is much higher and also can be modulated by the type of interaction established between the AuNPs and the polymer.

2.2 AuNPs-conjugated polymer sensor array for bacteria sensing

As mentioned at the beginning of this chapter, a simple and rapid device that could detect and identify most prevalent pathogens would be of high added value in the context of bacteria sensing thus mitigating the antibiotic misuse and limit the worsening of antibiotic resistance. Through an appropriate tuning of size and shape-dependent properties and functionalization of the AuNPs, different sensing systems can be achieved, including the detection of Gram-negative and Gram-positive bacteria (Figure 2.2).[215] As far as the bacteria detection is concerned, often a spectrophotometer can meet the requirement for analysis, without the need to expensive tools or skilled labor.

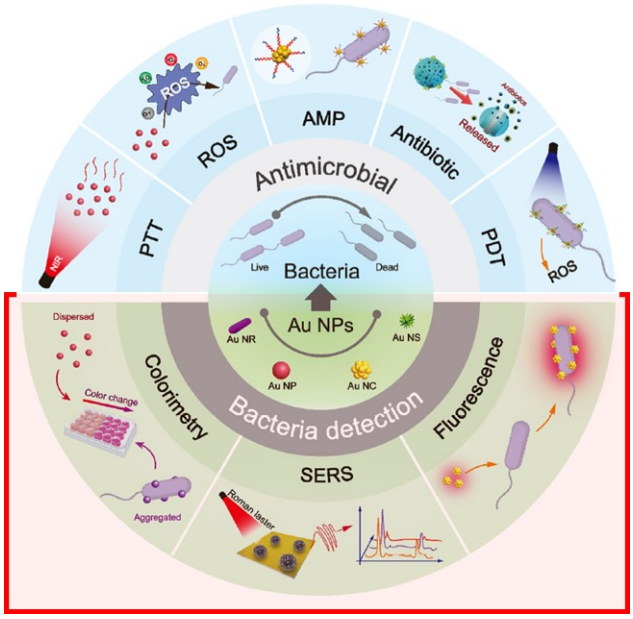

Figure 2.2. Scheme of possible AuNPs-based strategies for bacteria detection and antimicrobial. Adapted from Ge, P. et al. *ACS Mater. Lett.* **2023**, *5* (3), 638–655.

Regarding the fluorescence-based sensing approaches, AuNPs-conjugated polymer constructs have pioneered the development of a novel array-based strategy, in which AuNPs act as both selective recognition elements and quenchers. The presence of an analyte able to competitively interact with the AuNPs set promotes restoring the fluorescence signal due to the release of the polymer. As a result, the diverse affinity of the analyte to each AuNPs provides a specific fluorescence response pattern. Along this line, Rotello and co-workers have developed a sensitive and fast procedure for bacteria sensing.[216] The core of this approach is the common feature of Gram-positive and Gram-negative bacteria of having a negatively charged cell membrane. The presence of diverse anionic elements on the bacteria wall provides a multivalent environment suitable for interaction with cationic AuNPs.

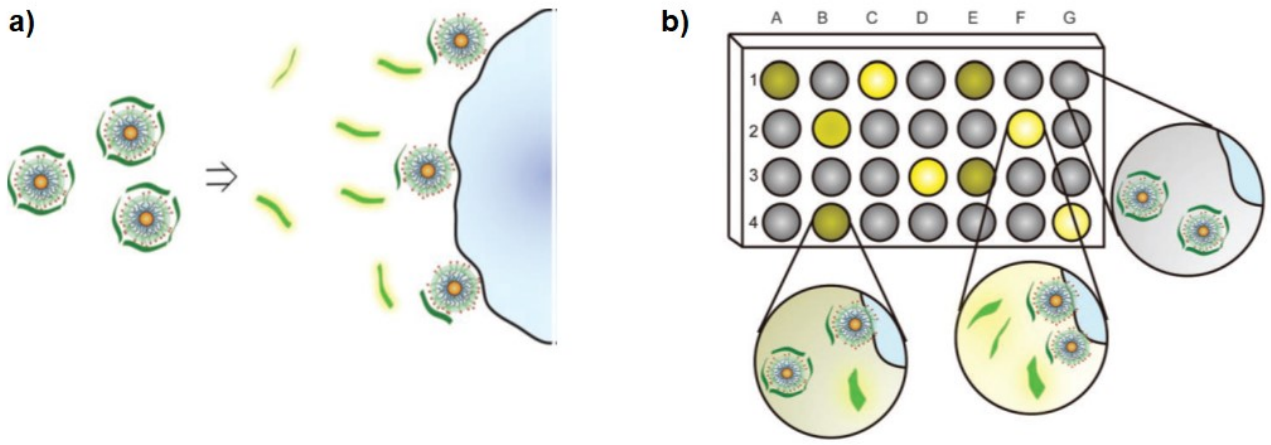

Figure 2.3. Scheme of the Rotello and co-workers strategy for bacteria identification based on the different affinity between the AuNPs-PPE constructs and bacterial cell wall (**a**). As high is the binding of AuNPs to the elements present on the bacteria cell wall, as high is the fluorescence recovery of the polymer (**b**). Adapted from Phillips, R. L. et al. *Angew. Chem. Int. Ed.* **2008**, *47* (14), 2590–2594.

As shown in Figure 2.3, these authors first prepared fluorescence-quenched constructs through the association of anionic PPE with cationic hydrophobic and hydrophilic AuNPs. Then, they investigated how the addition of different bacteria strains influenced the binding of AuNPs to the anionic polymer, studying the corresponding fluorescence response due to the release of a certain amount of PPE. The authors have noted that the fluorescence changes are reproducible, and especially depend on the bacteria strains studied; by this approach Rotello and co-workers were able to differentiate twelve different bacteria strains. In addition, the authors found that the higher fluorescence recovery was observed for hydrophobic AuNPs. This observation is in keeping with the stronger AuNPs-bacteria binding expected when, in addition to electrostatic interaction, the hydrophobic effect involving the hydrophobic moieties on the AuNPs outer surface, and the hydrophobic regions of the bacteria cell wall comes into play. This study demonstrated the great potential of AuNPs-polymer constructs for bacteria sensing and underlined the crucial role of both electrostatic and hydrophobic interactions in the binding of these AuNPs with bacteria.

A more recent study reported the use of AuNPs-polymer constructs for a different application, but exploiting the same strategy.[217] In detail, two types of cationic AuNPs have been prepared and functionalized with a cationic cysteine-terminated oligopeptide (CysHHC10), and a thiol-capped α-poly(L)lysine (PLL). These AuNPs are identified as AuH and AuL, respectively in Figure 2.4a. These nanoparticle systems were used for the electrostatic assembly, on their outer surface, of two anionic polymers, PPE and PPEG (Figure 2.4b), and upon the interaction with the cationic AuNPs the fluorescence of the PPE or PPEG was efficiently quenched.

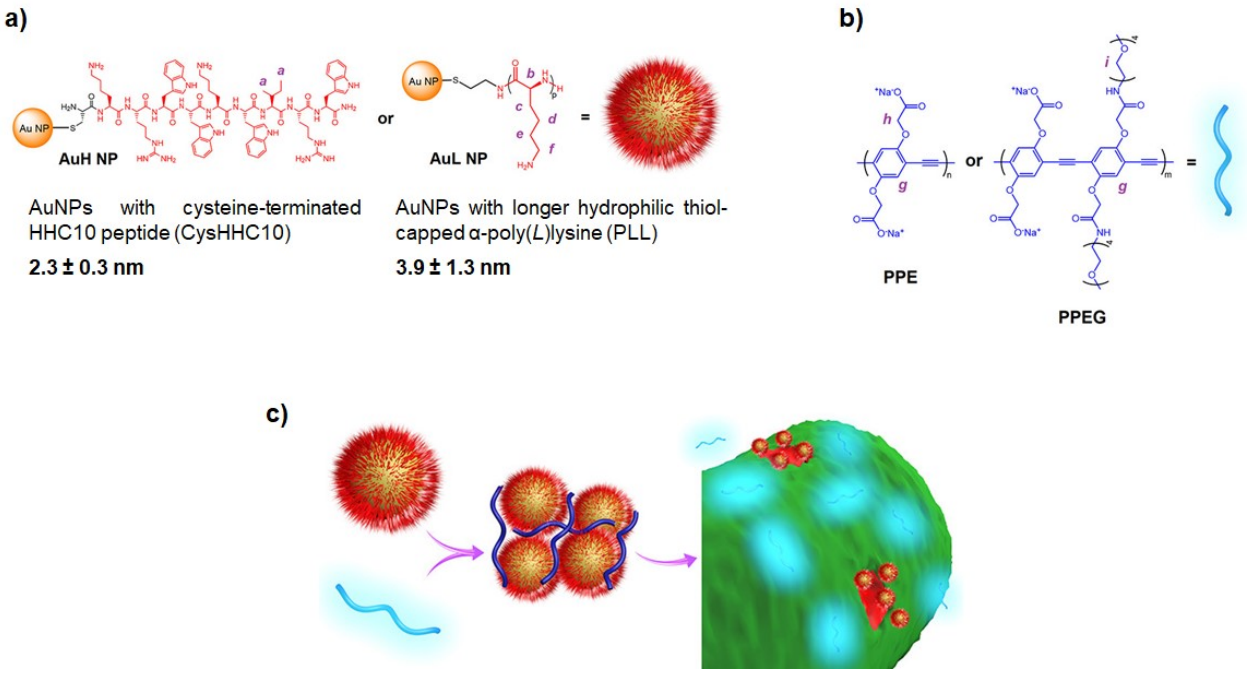

Figure 2.4. Illustration of the functionalised cationic AuNPs, AuH and AuL (**a**) and the anionic conjugated polymers, PPE and PPEG (**b**). Scheme AuNPs-polymers assembly and displacement of the anionic polymeric upon contact with bacteria (**c**). Adapted from Pranantyo, D. et al. *Nano Lett.* **2021**, *21* (2), 899–906.

In this study a wide range of Gram-positive and Gram-negative bacteria were tested, analysing the recovery of fluorescence intensity upon the microorganism addition (Figure 2.4c). The authors have first prepared a quenched AuNP-polymer construct monitoring the gradual decreasing in the fluorescence intensity of the conjugated polymers upon the addition of the Au NPs, until reaching a plateau (Figure 2.5a). Next, the quenched AuNP-polymer constructs have been incubated with different bacteria strains, to evaluate the competitive displacement of the anionic polymeric counterion by bacteria. The results have highlighted that the fluorescence recovery of the nano-constructs depends on the bacteria species, obtaining different fluorescent profiles (Figure 2.5b-e).

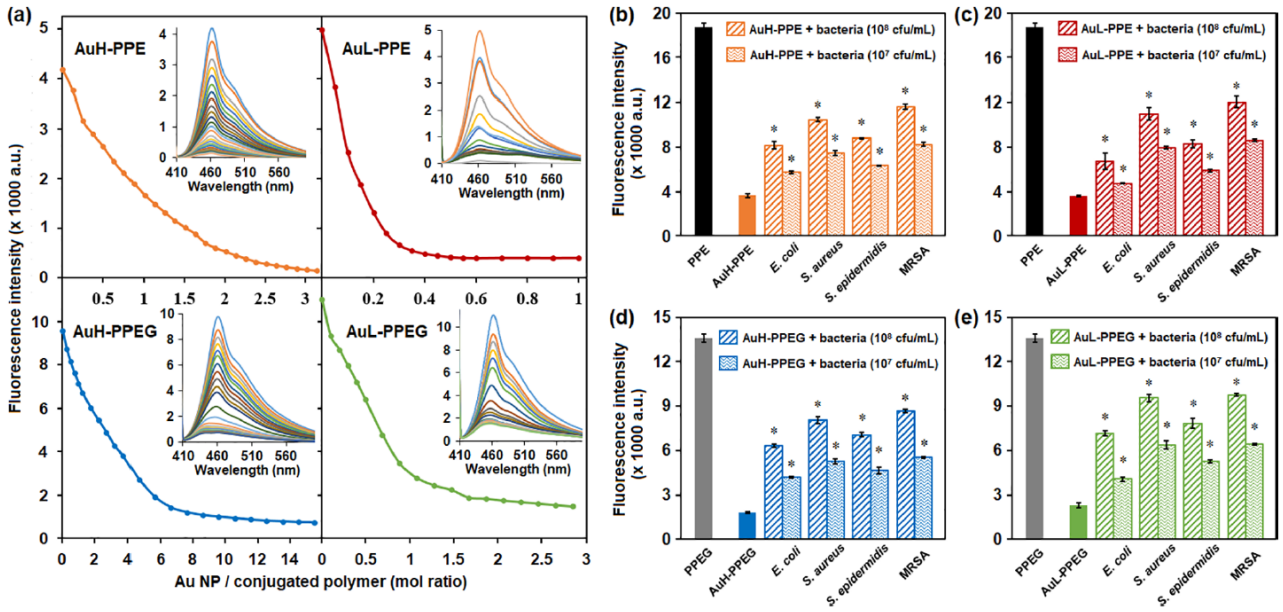

Figure 2.5. (**a**) Fluorescence titration of the anionic conjugated polymers with the cationic AuNPs, and the corresponding fluorescence spectra upon gradual titration. Fluorescence recovery of the polymers from the (**b**) AuHPPE, (**c**) AuL-PPE, (**d**) AuH-PPEG, and (**e**) AuL-PPEG nanoconstructs upon contact with various bacteria.

In summary, the AuNPs-polymer constructs have paved the way to the design of AuNPs-based sensor array for bacteria detection and identification. Future research could be focused on the exploration of various combinations of cationic AuNPs and anionic polymers, aiming to the development of highly sensitive and selective systems for bacteria sensing.

References

(1) Guisbiers, G.; Mejía-Rosales, S.; Leonard Deepak, F. Nanomaterial Properties: Size and Shape Dependencies. *J. Nanomater.* **2012**, *2012*, 1–2. https://doi.org/10.1155/2012/180976.

(2) Kim, E.-S.; Ahn, E. H.; Chung, E.; Kim, D.-H. Recent Advances in Nanobiotechnology and High-Throughput Molecular Techniques for Systems Biomedicine. *Mol. Cells* **2013**, *36* (6), 477–484. https://doi.org/10.1007/s10059-013-0304-6.

(3) Kamat, P. V. Photophysical, Photochemical and Photocatalytic Aspects of Metal Nanoparticles. *J. Phys. Chem. B* **2002**, *106* (32), 7729–7744. https://doi.org/10.1021/jp0209289.

(4) Burda, C.; Chen, X.; Narayanan, R.; El-Sayed, M. A. Chemistry and Properties of Nanocrystals of Different Shapes. *Chem. Rev.* **2005**, *105* (4), 1025–1102. https://doi.org/10.1021/cr030063a.

(5) Frederix, F.; Friedt, J.-M.; Choi, K.-H.; Laureyn, W.; Campitelli, A.; Mondelaers, D.; Maes, G.; Borghs, G. Biosensing Based on Light Absorption of Nanoscaled Gold and Silver Particles. *Anal. Chem.* **2003**, *75* (24), 6894–6900. https://doi.org/10.1021/ac0346609.

(6) Feng, H.; Tang, L.; Zeng, G.; Zhou, Y.; Deng, Y.; Ren, X.; Song, B.; Liang, C.; Wei, M.; Yu, J. Core-Shell Nanomaterials: Applications in Energy Storage and Conversion. *Adv. Colloid Interface Sci.* **2019**, *267*, 26–46. https://doi.org/10.1016/j.cis.2019.03.001.

(7) Kumar, K. S.; Kumar, V. B.; Paik, P. Recent Advancement in Functional Core-Shell Nanoparticles of Polymers: Synthesis, Physical Properties, and Applications in Medical Biotechnology. *J. Nanoparticles* **2013**, *2013*, 1–24. https://doi.org/10.1155/2013/672059.

(8) Rosi, N. L.; Mirkin, C. A. Nanostructures in Biodiagnostics. *Chem. Rev.* **2005**, *105* (4), 1547–1562. https://doi.org/10.1021/cr030067f.

(9) Cao, Y. C.; Jin, R.; Mirkin, C. A. Nanoparticles with Raman Spectroscopic Fingerprints for DNA and RNA Detection. *Science* **2002**, *297* (5586), 1536–1540. https://doi.org/10.1126/science.297.5586.1536.

(10) De, M.; Ghosh, P. S.; Rotello, V. M. Applications of Nanoparticles in Biology. *Adv. Mater.* **2008**, *20* (22), 4225–4241. https://doi.org/10.1002/adma.200703183.

(11) Ghosh, P.; Han, G.; De, M.; Kim, C.; Rotello, V. Gold Nanoparticles in Delivery Applications☆. *Adv. Drug Deliv. Rev.* **2008**, *60* (11), 1307–1315. https://doi.org/10.1016/j.addr.2008.03.016.

(12) Kreibig, U.; Vollmer, M. Theoretical Considerations. In *Optical Properties of Metal Clusters*; Toennies, J. P., Gonser, U., Osgood, R. M., Panish, M. B., Sakaki, H., Lotsch, H. K. V., Series Eds.; Springer Series in Materials Science; Springer Berlin Heidelberg: Berlin, Heidelberg, 1995; Vol. 25, pp 13–201. https://doi.org/10.1007/978-3-662-09109-8_2.

(13) Daniel, M.-C.; Astruc, D. Gold Nanoparticles: Assembly, Supramolecular Chemistry, Quantum-Size-Related Properties, and Applications toward Biology, Catalysis, and Nanotechnology. *Chem. Rev.* **2004**, *104* (1), 293–346. https://doi.org/10.1021/cr030698+.

(14) X. The Bakerian Lecture. —Experimental Relations of Gold (and Other Metals) to Light. *Philos. Trans. R. Soc. Lond.* **1857**, *147*, 145–181. https://doi.org/10.1098/rstl.1857.0011.

(15) Yaqoob, S. B.; Adnan, R.; Rameez Khan, R. M.; Rashid, M. Gold, Silver, and Palladium Nanoparticles: A Chemical Tool for Biomedical Applications. *Front. Chem.* **2020**, *8*.

(16) Shan, J.; Tenhu, H. Recent Advances in Polymer Protected Gold Nanoparticles: Synthesis, Properties and Applications. *Chem. Commun.* **2007**, No. 44, 4580. https://doi.org/10.1039/b707740h.

(17) Edwards, P. P.; Thomas, J. M. Gold in a Metallic Divided State—From Faraday to Present-Day Nanoscience. *Angew. Chem. Int. Ed.* **2007**, *46* (29), 5480–5486. https://doi.org/10.1002/anie.200700428.

(18) Weisbecker, C. S.; Merritt, M. V.; Whitesides, G. M. Molecular Self-Assembly of Aliphatic Thiols on Gold Colloids. *Langmuir* **1996**, *12* (16), 3763–3772. https://doi.org/10.1021/la950776r.

(19) Bethell, D.; Brust, M.; Schiffrin, D. J.; Kiely, C. From Monolayers to Nanostructured Materials: An Organic Chemist's View of Self-Assembly. *J. Electroanal. Chem.* **1996**, *409* (1), 137–143. https://doi.org/10.1016/0022-0728(96)04533-0.

(20) Kiely, C. J.; Fink, J.; Brust, M.; Bethell, D.; Schiffrin, D. J. Spontaneous Ordering of Bimodal Ensembles of Nanoscopic Gold Clusters. *Nature* **1998**, *396* (6710), 444–446. https://doi.org/10.1038/24808.

(21) Martin, J. E.; Wilcoxon, J. P.; Odinek, J.; Provencio, P. Control of the Interparticle Spacing in Gold Nanoparticle Superlattices. *J. Phys. Chem. B* **2000**, *104* (40), 9475–9486. https://doi.org/10.1021/jp001292t.

(22) Terrill, R. H.; Postlethwaite, T. A.; Chen, C.; Poon, C.-D.; Terzis, A.; Chen, A.; Hutchison, J. E.; Clark, M. R.; Wignall, G. Monolayers in Three Dimensions: NMR, SAXS, Thermal, and Electron Hopping Studies of Alkanethiol Stabilized Gold Clusters. *J. Am. Chem. Soc.* **1995**, *117* (50), 12537–12548. https://doi.org/10.1021/ja00155a017.

(23) Vericat, C.; Vela, M. E.; Corthey, G.; Pensa, E.; Cortés, E.; Fonticelli, M. H.; Ibañez, F.; Benitez, G. E.; Carro, P.; Salvarezza, R. C. Self-Assembled Monolayers of Thiolates on Metals: A Review Article on Sulfur-Metal Chemistry and Surface Structures. *RSC Adv.* **2014**, *4* (53), 27730–27754. https://doi.org/10.1039/C4RA04659E.

(24) Ulman, A. Formation and Structure of Self-Assembled Monolayers. *Chem. Rev.* **1996**, *96* (4), 1533–1554. https://doi.org/10.1021/cr9502357.

(25) Schreiber, F. Structure and Growth of Self-Assembling Monolayers. *Prog. Surf. Sci.* **2000**, *65* (5), 151–257. https://doi.org/10.1016/S0079-6816(00)00024-1.

(26) Dubois, L. H.; Nuzzo, R. G. Synthesis, Structure, and Properties of Model Organic Surfaces. *Annu. Rev. Phys. Chem.* **1992**, *43* (1), 437–463. https://doi.org/10.1146/annurev.pc.43.100192.002253.

(27) Hughes, B. R.; Dahman, Y. Chapter 14 - Control, Design, and Understanding of Molecular Self-Assembly. In *Fabrication and Self-Assembly of Nanobiomaterials*; Grumezescu, A. M., Ed.; William Andrew Publishing, 2016; pp 431–458. https://doi.org/10.1016/B978-0-323-41533-0.00014-3.

(28) Bain, C. D.; Evall, J.; Whitesides, G. M. Formation of Monolayers by the Coadsorption of Thiols on Gold: Variation in the Head Group, Tail Group, and Solvent. *J. Am. Chem. Soc.* **1989**, *111* (18), 7155–7164. https://doi.org/10.1021/ja00200a039.

(29) Singh, M.; Kaur, N.; Comini, E. The Role of Self-Assembled Monolayers in Electronic Devices. *J. Mater. Chem. C* **2020**, *8* (12), 3938–3955. https://doi.org/10.1039/D0TC00388C.

(30) Drzazgowska, J.; Schmid, B.; Süssmuth, R. D.; Altintas, Z. Self-Assembled Monolayer Epitope Bridges for Molecular Imprinting and Cancer Biomarker Sensing. *Anal. Chem.* **2020**, *92* (7), 4798–4806. https://doi.org/10.1021/acs.analchem.9b03813.

(31) Lin, S.; Lin, X.; Shang, Y.; Han, S.; Hasi, W.; Wang, L. Self-Assembly of Faceted Gold Nanocrystals for Surface-Enhanced Raman Scattering Application. *J. Phys. Chem. C* **2019**, *123* (40), 24714–24722. https://doi.org/10.1021/acs.jpcc.9b06686.

(32) Love, J. C.; Estroff, L. A.; Kriebel, J. K.; Nuzzo, R. G.; Whitesides, G. M. Self-Assembled Monolayers of Thiolates on Metals as a Form of Nanotechnology. *Chem. Rev.* **2005**, *105* (4), 1103–1170. https://doi.org/10.1021/cr0300789.

(33) Krämer, S.; Fuierer, R. R.; Gorman, C. B. Scanning Probe Lithography Using Self-Assembled Monolayers. *Chem. Rev.* **2003**, *103* (11), 4367–4418. https://doi.org/10.1021/cr020704m.

(34) Dubois, L. H.; Zegarski, B. R.; Nuzzo, R. G. Fundamental Studies of Microscopic Wetting on Organic Surfaces. 2. Interaction of Secondary Adsorbates with Chemically Textured Organic Monolayers. *J. Am. Chem. Soc.* **1990**, *112* (2), 570–579. https://doi.org/10.1021/ja00158a013.

(35) Reed, M. A.; Tour, J. M. Computing with molecules. *Sci. Am.* **2000**, *282* (6), 86–93.

(36) Vericat, C.; Vela, M. E.; Benitez, G.; Carro, P.; Salvarezza, R. C. Self-Assembled Monolayers of Thiols and Dithiols on Gold: New Challenges for a Well-Known System. *Chem. Soc. Rev.* **2010**, *39* (5), 1805–1834. https://doi.org/10.1039/B907301A.

(37) Badia, A.; Singh, S.; Demers, L.; Cuccia, L.; Brown, G. R.; Lennox, R. B. Self-Assembled Monolayers on Gold Nanoparticles. *Chem. – Eur. J.* **1996**, *2* (3), 359–363. https://doi.org/10.1002/chem.19960020318.

(38) Ghorai, P. Kr.; Glotzer, S. C. Molecular Dynamics Simulation Study of Self-Assembled Monolayers of Alkanethiol Surfactants on Spherical Gold Nanoparticles. *J. Phys. Chem. C* **2007**, *111* (43), 15857–15862. https://doi.org/10.1021/jp0746289.

(39) Otálvaro, D.; Veening, T.; Brocks, G. Self-Assembled Monolayer Induced Au(111) and Ag(111) Reconstructions: Work Functions and Interface Dipole Formation. *J. Phys. Chem. C* **2012**, *116* (14), 7826–7837. https://doi.org/10.1021/jp300512k.

(40) Poirier, G. E. Characterization of Organosulfur Molecular Monolayers on Au(111) Using Scanning Tunneling Microscopy. *Chem. Rev.* **1997**, *97* (4), 1117–1128. https://doi.org/10.1021/cr960074m.

(41) Delamarche, Emmanuel.; Michel, Bruno.; Biebuyck, H. A.; Gerber, C. Golden Interfaces: The Surface of Self-Assembled Monolayers. *Adv. Mater.* **1996**, *8* (9), 719–729. https://doi.org/10.1002/adma.19960080903.

(42) Badia, A.; Demers, L.; Dickinson, L.; Morin, F. G.; Lennox, R. B.; Reven, L. Gold−Sulfur Interactions in Alkylthiol Self-Assembled Monolayers Formed on Gold Nanoparticles Studied by Solid-State NMR. *J. Am. Chem. Soc.* **1997**, *119* (45), 11104–11105. https://doi.org/10.1021/ja9726163.

(43) Bain, C. D.; Whitesides, G. M. Molecular-Level Control over Surface Order in Self-Assembled Monolayer Films of Thiols on Gold. *Science* **1988**, *240* (4848), 62–63. https://doi.org/10.1126/science.240.4848.62.

(44) Bain, C. D.; Biebuyck, H. A.; Whitesides, G. M. Comparison of Self-Assembled Monolayers on Gold: Coadsorption of Thiols and Disulfides. *Langmuir* **1989**, *5* (3), 723–727. https://doi.org/10.1021/la00087a027.

(45) Badia, A.; Cuccia, L.; Demers, L.; Morin, F.; Lennox, R. B. Structure and Dynamics in Alkanethiolate Monolayers Self-Assembled on Gold Nanoparticles: A DSC, FT-IR, and Deuterium NMR Study. *J. Am. Chem. Soc.* **1997**, *119* (11), 2682–2692. https://doi.org/10.1021/ja963571t.

(46) Badia, A.; Gao, W.; Singh, S.; Demers, L.; Cuccia, L.; Reven, L. Structure and Chain Dynamics of Alkanethiol-Capped Gold Colloids. *Langmuir* **1996**, *12* (5), 1262–1269. https://doi.org/10.1021/la9510487.

(47) Chi, Q.; Ford, M. J.; Halder, A.; Hush, N. S.; Reimers, J. R.; Ulstrup, J. Sulfur Ligand Mediated Electrochemistry of Gold Surfaces and Nanoparticles: What, How, and Why. *Curr. Opin. Electrochem.* **2017**, *1* (1), 7–15. https://doi.org/10.1016/j.coelec.2016.12.004.

(48) Marchi, D.; Cara, E.; Lupi, F. F.; Hönicke, P.; Kayser, Y.; Beckhof, B.; Castellino, M.; Klapetek, P.; Zoccante, A.; Laus, M.; Cossi, M. Structure and Stability of 7-Mercapto-4-Methylcoumarin Self-Assembled Monolayers on Gold: An Experimental and Computational

Analysis. *Phys. Chem. Chem. Phys.* **2022**, *24* (36), 22083–22090. https://doi.org/10.1039/D2CP03103E.

(49) Ferretti, S.; Paynter, S.; Russell, D. A.; Sapsford, K. E.; Richardson, D. J. Self-Assembled Monolayers: A Versatile Tool for the Formulation of Bio-Surfaces. *TrAC Trends Anal. Chem.* **2000**, *19* (9), 530–540. https://doi.org/10.1016/S0165-9936(00)00032-7.

(50) Bourg, M.-C.; Badia, A.; Lennox, R. B. Gold−Sulfur Bonding in 2D and 3D Self-Assembled Monolayers: XPS Characterization. *J. Phys. Chem. B* **2000**, *104* (28), 6562–6567. https://doi.org/10.1021/jp9935337.

(51) Inkpen, M. S.; Liu, Z.-F.; Li, H.; Campos, L. M.; Neaton, J. B.; Venkataraman, L. Non-Chemisorbed Gold–Sulfur Binding Prevails in Self-Assembled Monolayers. *Nat. Chem.* **2019**, *11* (4), 351–358. https://doi.org/10.1038/s41557-019-0216-y.

(52) Hasan, M.; Bethell, D.; Brust, M. The Fate of Sulfur-Bound Hydrogen on Formation of Self-Assembled Thiol Monolayers on Gold: ^{1}H NMR Spectroscopic Evidence from Solutions of Gold Clusters. *J. Am. Chem. Soc.* **2002**, *124* (7), 1132–1133. https://doi.org/10.1021/ja0120577.

(53) Cossaro, A.; Mazzarello, R.; Rousseau, R.; Casalis, L.; Verdini, A.; Kohlmeyer, A.; Floreano, L.; Scandolo, S.; Morgante, A.; Klein, M. L.; Scoles, G. X-Ray Diffraction and Computation Yield the Structure of Alkanethiols on Gold(111). *Science* **2008**, *321* (5891), 943–946. https://doi.org/10.1126/science.1158532.

(54) Aminabad, N. S.; Farshbaf, M.; Akbarzadeh, A. Recent Advances of Gold Nanoparticles in Biomedical Applications: State of the Art. *Cell Biochem. Biophys.* **2019**, *77* (2), 123–137. https://doi.org/10.1007/s12013-018-0863-4.

(55) Bansal, S. A.; Kumar, V.; Karimi, J.; Singh, A. P.; Kumar, S. Role of Gold Nanoparticles in Advanced Biomedical Applications. *Nanoscale Adv.* **2020**, *2* (9), 3764–3787. https://doi.org/10.1039/D0NA00472C.

(56) Alex, S.; Tiwari, A. Functionalized Gold Nanoparticles: Synthesis, Properties and Applications—A Review. *J. Nanosci. Nanotechnol.* **2015**, *15* (3), 1869–1894. https://doi.org/10.1166/jnn.2015.9718.

(57) Her, S.; Jaffray, D. A.; Allen, C. Gold Nanoparticles for Applications in Cancer Radiotherapy: Mechanisms and Recent Advancements. *Adv. Drug Deliv. Rev.* **2017**, *109*, 84–101. https://doi.org/10.1016/j.addr.2015.12.012.

(58) Hu, X.; Zhang, Y.; Ding, T.; Liu, J.; Zhao, H. Multifunctional Gold Nanoparticles: A Novel Nanomaterial for Various Medical Applications and Biological Activities. *Front. Bioeng. Biotechnol.* **2020**, *8*.

(59) Lucarini, M.; Pasquato, L. ESR Spectroscopy as a Tool to Investigate the Properties of Self-Assembled Monolayers Protecting Gold Nanoparticles. *Nanoscale* **2010**, *2* (5), 668–676. https://doi.org/10.1039/B9NR00384C.

(60) Stranick, S. J.; Atre, S. V.; Parikh, A. N.; Wood, M. C.; Allara, D. L.; Winograd, N.; Weiss, P. S. Nanometer-Scale Phase Separation in Mixed Composition Self-Assembled Monolayers. *Nanotechnology* **1996**, *7* (4), 438. https://doi.org/10.1088/0957-4484/7/4/025.

(61) Folkers, J. P.; Laibinis, P. E.; Whitesides, G. M. Self-Assembled Monolayers of Alkanethiols on Gold: Comparisons of Monolayers Containing Mixtures of Short- and Long-Chain Constituents with Methyl and Hydroxymethyl Terminal Groups. *Langmuir* **1992**, *8* (5), 1330–1341. https://doi.org/10.1021/la00041a015.

(62) Smith, R. K.; Reed, S. M.; Lewis, P. A.; Monnell, J. D.; Clegg, R. S.; Kelly, K. F.; Bumm, L. A.; Hutchison, J. E.; Weiss, P. S. Phase Separation within a Binary Self-Assembled Monolayer on Au{111} Driven by an Amide-Containing Alkanethiol. *J. Phys. Chem. B* **2001**, *105* (6), 1119–1122. https://doi.org/10.1021/jp0035129.

(63) Jackson, A. M.; Hu, Y.; Silva, P. J.; Stellacci, F. From Homoligand- to Mixed-Ligand-Monolayer-Protected Metal Nanoparticles: A Scanning Tunneling Microscopy Investigation. *J. Am. Chem. Soc.* **2006**, *128* (34), 11135–11149. https://doi.org/10.1021/ja061545h.

(64) Gentilini, C.; Pasquato, L. Morphology of Mixed-Monolayers Protecting Metal Nanoparticles. *J Mater Chem* **2010**, *20* (8), 1403–1412. https://doi.org/10.1039/B912759C.

(65) Pengo, P.; Şologan, M.; Pasquato, L.; Guida, F.; Pacor, S.; Tossi, A.; Stellacci, F.; Marson, D.; Boccardo, S.; Pricl, S.; Posocco, P. Gold Nanoparticles with Patterned Surface Monolayers for Nanomedicine: Current Perspectives. *Eur. Biophys. J.* **2017**, *46* (8), 749–771. https://doi.org/10.1007/s00249-017-1250-6.

(66) Singh, C.; Ghorai, P. K.; Horsch, M. A.; Jackson, A. M.; Larson, R. G.; Stellacci, F.; Glotzer, S. C. Entropy-Mediated Patterning of Surfactant-Coated Nanoparticles and Surfaces. *Phys. Rev. Lett.* **2007**, *99* (22), 226106. https://doi.org/10.1103/PhysRevLett.99.226106.

(67) Kim, H.; Carney, R. P.; Reguera, J.; Ong, Q. K.; Liu, X.; Stellacci, F. Synthesis and Characterization of Janus Gold Nanoparticles. *Adv. Mater.* **2012**, *24* (28), 3857–3863. https://doi.org/10.1002/adma.201200926.

(68) Carney, R. P.; DeVries, G. A.; Dubois, C.; Kim, H.; Kim, J. Y.; Singh, C.; Ghorai, P. K.; Tracy, J. B.; Stiles, R. L.; Murray, R. W.; Glotzer, S. C.; Stellacci, F. Size Limitations for the Formation of Ordered Striped Nanoparticles. *J. Am. Chem. Soc.* **2008**, *130* (3), 798–799. https://doi.org/10.1021/ja077383m.

(69) Ge, X.; Ke, P. C.; Davis, T. P.; Ding, F. A Thermodynamics Model for the Emergence of a Stripe-like Binary SAM on a Nanoparticle Surface. *Small* **2015**, *11* (37), 4894–4899. https://doi.org/10.1002/smll.201501049.

(70) Krafft, M. P.; Riess, J. G. Chemistry, Physical Chemistry, and Uses of Molecular Fluorocarbon−Hydrocarbon Diblocks, Triblocks, and Related Compounds—Unique "Apolar" Components for Self-Assembled Colloid and Interface Engineering. *Chem. Rev.* **2009**, *109* (5), 1714–1792. https://doi.org/10.1021/cr800260k.

(71) Dalvi, V. H.; Rossky, P. J. Molecular Origins of Fluorocarbon Hydrophobicity. *Proc. Natl. Acad. Sci.* **2010**, *107* (31), 13603–13607. https://doi.org/10.1073/pnas.0915169107.

(72) Şologan, M.; Gentilini, C.; Bidoggia, S.; Boccalon, M.; Pace, A.; Pengo, P.; Pasquato, L. Gold Nanoparticles Protected by Mixed Hydrogenated/Fluorinated Monolayers: Controlling and Exploring the Surface Features. *J. Nanoparticle Res.* **2018**, *20* (6), 152. https://doi.org/10.1007/s11051-018-4231-5.

(73) Şologan, M.; Boccalon, M.; Bidoggia, S.; Gentilini, C.; Pasquato, L.; Pengo, P. Self-Sorting in Mixed Fluorinated/Hydrogenated Assemblies. *Supramol. Chem.* **2017**, *29* (11), 808–822. https://doi.org/10.1080/10610278.2017.1386307.

(74) Tirotta, I.; Calloni, A.; Pigliacelli, C.; Brambilla, A.; Bussetti, G.; Duò, L.; Metrangolo, P.; Baldelli Bombelli, F. Chemical Characterization of Fluorinated/Hydrogenated Mixed Monolayers

Grafted on Gold Nanoparticles. *J. Fluor. Chem.* **2018**, *206*, 99–107. https://doi.org/10.1016/j.jfluchem.2017.12.014.

(75) Bidoggia, S.; Milocco, F.; Polizzi, S.; Canton, P.; Saccani, A.; Sanavio, B.; Krol, S.; Stellacci, F.; Pengo, P.; Pasquato, L. Fluorinated and Charged Hydrogenated Alkanethiolates Grafted on Gold: Expanding the Diversity of Mixed-Monolayer Nanoparticles for Biological Applications. *Bioconjug. Chem.* **2017**, *28* (1), 43–52. https://doi.org/10.1021/acs.bioconjchem.6b00585.

(76) Gentilini, C.; Franchi, P.; Mileo, E.; Polizzi, S.; Lucarini, M.; Pasquato, L. Formation of Patches on 3D SAMs Driven by Thiols with Immiscible Chains Observed by ESR Spectroscopy. *Angew. Chem. Int. Ed.* **2009**, *48* (17), 3060–3064. https://doi.org/10.1002/anie.200805321.

(77) Pengo, P.; Pasquato, L. Gold Nanoparticles Protected by Fluorinated Ligands: Syntheses, Properties and Applications. *J. Fluor. Chem.* **2015**, *177*, 2–10. https://doi.org/10.1016/j.jfluchem.2015.03.005.

(78) Posocco, P.; Gentilini, C.; Bidoggia, S.; Pace, A.; Franchi, P.; Lucarini, M.; Fermeglia, M.; Pricl, S.; Pasquato, L. Self-Organization of Mixtures of Fluorocarbon and Hydrocarbon Amphiphilic Thiolates on the Surface of Gold Nanoparticles. *ACS Nano* **2012**, *6* (8), 7243–7253. https://doi.org/10.1021/nn302366q.

(79) Ong, Q.; Luo, Z.; Stellacci, F. Characterization of Ligand Shell for Mixed-Ligand Coated Gold Nanoparticles. *Acc. Chem. Res.* **2017**, *50* (8), 1911–1919. https://doi.org/10.1021/acs.accounts.7b00165.

(80) Şologan, M.; Marson, D.; Polizzi, S.; Pengo, P.; Boccardo, S.; Pricl, S.; Posocco, P.; Pasquato, L. Patchy and Janus Nanoparticles by Self-Organization of Mixtures of Fluorinated and Hydrogenated Alkanethiolates on the Surface of a Gold Core. *ACS Nano* **2016**, *10* (10), 9316–9325. https://doi.org/10.1021/acsnano.6b03931.

(81) Hühn, J.; Carrillo-Carrion, C.; Soliman, M. G.; Pfeiffer, C.; Valdeperez, D.; Masood, A.; Chakraborty, I.; Zhu, L.; Gallego, M.; Yue, Z.; Carril, M.; Feliu, N.; Escudero, A.; Alkilany, A. M.; Pelaz, B.; del Pino, P.; Parak, W. J. Selected Standard Protocols for the Synthesis, Phase Transfer, and Characterization of Inorganic Colloidal Nanoparticles. *Chem. Mater.* **2017**, *29* (1), 399–461. https://doi.org/10.1021/acs.chemmater.6b04738.

(82) Zhao, P.; Li, N.; Astruc, D. State of the Art in Gold Nanoparticle Synthesis. *Coord. Chem. Rev.* **2013**, *257* (3), 638–665. https://doi.org/10.1016/j.ccr.2012.09.002.

(83) Yeh, Y.-C.; Creran, B.; Rotello, V. M. Gold Nanoparticles: Preparation, Properties, and Applications in Bionanotechnology. *Nanoscale* **2012**, *4* (6), 1871–1880. https://doi.org/10.1039/C1NR11188D.

(84) Turkevich, J.; Stevenson, P. C.; Hillier, J. A Study of the Nucleation and Growth Processes in the Synthesis of Colloidal Gold. *Discuss. Faraday Soc.* **1951**, *11*, 55. https://doi.org/10.1039/df9511100055.

(85) Frens, G. Controlled Nucleation for the Regulation of the Particle Size in Monodisperse Gold Suspensions. *Nat. Phys. Sci.* **1973**, *241* (105), 20–22. https://doi.org/10.1038/physci241020a0.

(86) Chow, M. K.; Zukoski, C. F. Gold Sol Formation Mechanisms: Role of Colloidal Stability. *J. Colloid Interface Sci.* **1994**, *165* (1), 97–109. https://doi.org/10.1006/jcis.1994.1210.

(87) Park, J.-W.; Shumaker-Parry, J. S. Strong Resistance of Citrate Anions on Metal Nanoparticles to Desorption under Thiol Functionalization. *ACS Nano* **2015**, *9* (2), 1665–1682. https://doi.org/10.1021/nn506379m.

(88) Ji, X.; Song, X.; Li, J.; Bai, Y.; Yang, W.; Peng, X. Size Control of Gold Nanocrystals in Citrate Reduction: The Third Role of Citrate. *J. Am. Chem. Soc.* **2007**, *129* (45), 13939–13948. https://doi.org/10.1021/ja074447k.

(89) Kimling, J.; Maier, M.; Okenve, B.; Kotaidis, V.; Ballot, H.; Plech, A. Turkevich Method for Gold Nanoparticle Synthesis Revisited. *J. Phys. Chem. B* **2006**, *110* (32), 15700–15707. https://doi.org/10.1021/jp061667w.

(90) Nguyen, D. T.; Kim, D.-J.; So, M. G.; Kim, K.-S. Experimental Measurements of Gold Nanoparticle Nucleation and Growth by Citrate Reduction of HAuCl4. *Adv. Powder Technol.* **2010**, *21* (2), 111–118. https://doi.org/10.1016/j.apt.2009.11.005.

(91) Polte, J.; Ahner, T. T.; Delissen, F.; Sokolov, S.; Emmerling, F.; Thünemann, A. F.; Kraehnert, R. Mechanism of Gold Nanoparticle Formation in the Classical Citrate Synthesis Method Derived from Coupled In Situ XANES and SAXS Evaluation. *J. Am. Chem. Soc.* **2010**, *132* (4), 1296–1301. https://doi.org/10.1021/ja906506j.

(92) Uppal, M. A.; Kafizas, A.; Ewing, M. B.; Parkin, I. P. The Effect of Initiation Method on the Size, Monodispersity and Shape of Gold Nanoparticles Formed by the Turkevich Method. *New J. Chem.* **2010**, *34* (12), 2906–2914. https://doi.org/10.1039/C0NJ00505C.

(93) Uppal, M. A.; Kafizas, A.; Lim, T. H.; Parkin, I. P. The Extended Time Evolution Size Decrease of Gold Nanoparticles Formed by the Turkevich Method. *New J. Chem.* **2010**, *34* (7), 1401–1407. https://doi.org/10.1039/B9NJ00745H.

(94) Aslan, K.; Pérez-Luna, V. H. Surface Modification of Colloidal Gold by Chemisorption of Alkanethiols in the Presence of a Nonionic Surfactant. *Langmuir* **2002**, *18* (16), 6059–6065. https://doi.org/10.1021/la025795x.

(95) Lin, S.-Y.; Tsai, Y.-T.; Chen, C.-C.; Lin, C.-M.; Chen, C. Two-Step Functionalization of Neutral and Positively Charged Thiols onto Citrate-Stabilized Au Nanoparticles. *J. Phys. Chem. B* **2004**, *108* (7), 2134–2139. https://doi.org/10.1021/jp036310w.

(96) Brust, M.; Walker, M.; Bethell, D.; J. Schiffrin, D.; Whyman, R. Synthesis of Thiol-Derivatised Gold Nanoparticles in a Two-Phase Liquid–Liquid System. *J. Chem. Soc. Chem. Commun.* **1994**, *0* (7), 801–802. https://doi.org/10.1039/C39940000801.

(97) Hostetler, M. J.; Wingate, J. E.; Zhong, C.-J.; Harris, J. E.; Vachet, R. W.; Clark, M. R.; Londono, J. D.; Green, S. J.; Stokes, J. J.; Wignall, G. D.; Glish, G. L.; Porter, M. D.; Evans, N. D.; Murray, R. W. Alkanethiolate Gold Cluster Molecules with Core Diameters from 1.5 to 5.2 Nm: Core and Monolayer Properties as a Function of Core Size. *Langmuir* **1998**, *14* (1), 17–30. https://doi.org/10.1021/la970588w.

(98) Manea, F.; Bindoli, C.; Polizzi, S.; Lay, L.; Scrimin, P. Expeditious Synthesis of Water-Soluble, Monolayer-Protected Gold Nanoparticles of Controlled Size and Monolayer Composition. *Langmuir* **2008**, *24* (8), 4120–4124. https://doi.org/10.1021/la703558y.

(99) Jha, S.; Ramadori, F.; Quarta, S.; Biasiolo, A.; Fabris, E.; Baldan, P.; Guarino, G.; Ruvoletto, M.; Villano, G.; Turato, C.; Gatta, A.; Mancin, F.; Pontisso, P.; Scrimin, P. Binding and Uptake into Human Hepatocellular Carcinoma Cells of Peptide-Functionalized Gold Nanoparticles. *Bioconjug. Chem.* **2017**, *28* (1), 222–229. https://doi.org/10.1021/acs.bioconjchem.6b00441.

(100) Hostetler, M. J.; Green, S. J.; Stokes, J. J.; Murray, R. W. Monolayers in Three Dimensions: Synthesis and Electrochemistry of ω-Functionalized Alkanethiolate-Stabilized Gold Cluster Compounds. *J. Am. Chem. Soc.* **1996**, *118* (17), 4212–4213. https://doi.org/10.1021/ja960198g.

(101) Templeton, A. C.; Wuelfing, W. P.; Murray, R. W. Monolayer-Protected Cluster Molecules. *Acc. Chem. Res.* **2000**, *33* (1), 27–36. https://doi.org/10.1021/ar9602664.

(102) Luo, Z.; Hou, J.; Menin, L.; Ong, Q. K.; Stellacci, F. Evolution of the Ligand Shell Morphology during Ligand Exchange Reactions on Gold Nanoparticles. *Angew. Chem. Int. Ed.* **2017**, *56* (43), 13521–13525. https://doi.org/10.1002/anie.201708190.

(103) Montalti, M.; Prodi, L.; Zaccheroni, N.; Baxter, R.; Teobaldi, G.; Zerbetto, F. Kinetics of Place-Exchange Reactions of Thiols on Gold Nanoparticles. *Langmuir* **2003**, *19* (12), 5172–5174. https://doi.org/10.1021/la034581s.

(104) Hostetler, M. J.; Templeton, A. C.; Murray, R. W. Dynamics of Place-Exchange Reactions on Monolayer-Protected Gold Cluster Molecules. *Langmuir* **1999**, *15* (11), 3782–3789. https://doi.org/10.1021/la981598f.

(105) Song, Y.; Murray, R. W. Dynamics and Extent of Ligand Exchange Depend on Electronic Charge of Metal Nanoparticles. *J. Am. Chem. Soc.* **2002**, *124* (24), 7096–7102. https://doi.org/10.1021/ja0174985.

(106) Ionita, P.; Caragheorgheopol, A.; Gilbert, B. C.; Chechik, V. EPR Study of a Place-Exchange Reaction on Au Nanoparticles: Two Branches of a Disulfide Molecule Do Not Adsorb Adjacent to Each Other. *J. Am. Chem. Soc.* **2002**, *124* (31), 9048–9049. https://doi.org/10.1021/ja0265456.

(107) Kassam, A.; Bremner, G.; Clark, B.; Ulibarri, G.; Lennox, R. B. Place Exchange Reactions of Alkyl Thiols on Gold Nanoparticles. *J. Am. Chem. Soc.* **2006**, *128* (11), 3476–3477. https://doi.org/10.1021/ja057091q.

(108) Goldmann, C.; Ribot, F.; Peiretti, L. F.; Quaino, P.; Tielens, F.; Sanchez, C.; Chanéac, C.; Portehault, D. Quantified Binding Scale of Competing Ligands at the Surface of Gold Nanoparticles: The Role of Entropy and Intermolecular Forces. *Small* **2017**, *13* (20), 1604028. https://doi.org/10.1002/smll.201604028.

(109) Chapter 4 Modification and Passivation of Colloidal Particles. In *Studies in Interface Science*; Capek, I., Ed.; Nanocomposite Structures and Dispersions; Elsevier, 2006; Vol. 23, pp 225–292. https://doi.org/10.1016/S1383-7303(06)80005-0.

(110) Chen, Y.; Xianyu, Y.; Jiang, X. Surface Modification of Gold Nanoparticles with Small Molecules for Biochemical Analysis. *Acc. Chem. Res.* **2017**, *50* (2), 310–319. https://doi.org/10.1021/acs.accounts.6b00506.

(111) Simard, J.; Briggs, C.; Boal, A. K.; Rotello, V. M. Formation and PH-Controlled Assembly of Amphiphilic Gold Nanoparticles. *Chem. Commun.* **2000**, No. 19, 1943–1944. https://doi.org/10.1039/B004162I.

(112) Warner, M. G.; Reed, S. M.; Hutchison, J. E. Small, Water-Soluble, Ligand-Stabilized Gold Nanoparticles Synthesized by Interfacial Ligand Exchange Reactions. *Chem. Mater.* **2000**, *12* (11), 3316–3320. https://doi.org/10.1021/cm0003875.

(113) Huang, D.; Liu, X.; Lai, C.; Qin, L.; Zhang, C.; Yi, H.; Zeng, G.; Li, B.; Deng, R.; Liu, S.; Zhang, Y. Colorimetric Determination of Mercury(II) Using Gold Nanoparticles and Double Ligand Exchange. *Microchim. Acta* **2018**, *186* (1), 31. https://doi.org/10.1007/s00604-018-3126-6.

(114) Şologan, M.; Padelli, F.; Giachetti, I.; Aquino, D.; Boccalon, M.; Adami, G.; Pengo, P.; Pasquato, L. Functionalized Gold Nanoparticles as Contrast Agents for Proton and Dual Proton/Fluorine MRI. *Nanomaterials* **2019**, *9* (6), 879. https://doi.org/10.3390/nano9060879.

(115) Maus, L.; Dick, O.; Bading, H.; Spatz, J. P.; Fiammengo, R. Conjugation of Peptides to the Passivation Shell of Gold Nanoparticles for Targeting of Cell-Surface Receptors. *ACS Nano* **2010**, *4* (11), 6617–6628. https://doi.org/10.1021/nn101867w.

(116) Baranov, D.; Kadnikova, E. N. Synthesis and Characterization of Azidoalkyl-Functionalized Gold Nanoparticles as Scaffolds for “Click”-Chemistry Derivatization. *J. Mater. Chem.* **2011**, *21* (17), 6152–6157. https://doi.org/10.1039/C1JM10183H.

(117) Wang, Y.; Bürgi, T. Ligand Exchange Reactions on Thiolate-Protected Gold Nanoclusters. *Nanoscale Adv.* **2021**, *3* (10), 2710–2727. https://doi.org/10.1039/D1NA00178G.

(118) Gulati, S.; Singh, P.; Diwan, A.; Mongia, A.; Kumar, S. Functionalized Gold Nanoparticles: Promising and Efficient Diagnostic and Therapeutic Tools for HIV/AIDS. *RSC Med. Chem.* **2020**, *11* (11), 1252–1266. https://doi.org/10.1039/D0MD00298D.

(119) Pengo, P.; Baltzer, L.; Pasquato, L.; Scrimin, P. Substrate Modulation of the Activity of an Artificial Nanoesterase Made of Peptide-Functionalized Gold Nanoparticles. *Angew. Chem. Int. Ed.* **2007**, *46* (3), 400–404. https://doi.org/10.1002/anie.200602581.

(120) Franceschini, C.; Scrimin, P.; Prins, L. J. Light-Triggered Thiol-Exchange on Gold Nanoparticles at Low Micromolar Concentrations in Water. *Langmuir* **2014**, *30* (46), 13831–13836. https://doi.org/10.1021/la5034965.

(121) Boal, A. K.; Rotello, V. M. Fabrication and Self-Optimization of Multivalent Receptors on Nanoparticle Scaffolds. *J. Am. Chem. Soc.* **2000**, *122* (4), 734–735. https://doi.org/10.1021/ja993900s.

(122) Colangelo, E.; Comenge, J.; Paramelle, D.; Volk, M.; Chen, Q.; Lévy, R. Characterizing Self-Assembled Monolayers on Gold Nanoparticles. *Bioconjug. Chem.* **2017**, *28* (1), 11–22. https://doi.org/10.1021/acs.bioconjchem.6b00587.

(123) Ghosh Chaudhuri, R.; Paria, S. Core/Shell Nanoparticles: Classes, Properties, Synthesis Mechanisms, Characterization, and Applications. *Chem. Rev.* **2012**, *112* (4), 2373–2433. https://doi.org/10.1021/cr100449n.

(124) Marbella, L. E.; Millstone, J. E. NMR Techniques for Noble Metal Nanoparticles. *Chem. Mater.* **2015**, *27* (8), 2721–2739. https://doi.org/10.1021/cm504809c.

(125) Salassa, G.; Bürgi, T. NMR Spectroscopy: A Potent Tool for Studying Monolayer-Protected Metal Nanoclusters. *Nanoscale Horiz.* **2018**, *3* (5), 457–463. https://doi.org/10.1039/C8NH00058A.

(126) Jayawardena, H. S. N.; Liyanage, S. H.; Rathnayake, K.; Patel, U.; Yan, M. Analytical Methods for Characterization of Nanomaterial Surfaces. *Anal. Chem.* **2021**, *93* (4), 1889–1911. https://doi.org/10.1021/acs.analchem.0c05208.

(127) Wu, M.; Vartanian, A. M.; Chong, G.; Pandiakumar, A. K.; Hamers, R. J.; Hernandez, R.; Murphy, C. J. Solution NMR Analysis of Ligand Environment in Quaternary Ammonium-Terminated Self-Assembled Monolayers on Gold Nanoparticles: The Effect of Surface Curvature and Ligand Structure. *J. Am. Chem. Soc.* **2019**, *141* (10), 4316–4327. https://doi.org/10.1021/jacs.8b11445.

(128) Liu, X.; Yu, M.; Kim, H.; Mameli, M.; Stellacci, F. Determination of Monolayer-Protected Gold Nanoparticle Ligand–Shell Morphology Using NMR. *Nat. Commun.* **2012**, *3* (1), 1182. https://doi.org/10.1038/ncomms2155.

(129) Salvia, M.-V.; Salassa, G.; Rastrelli, F.; Mancin, F. Turning Supramolecular Receptors into Chemosensors by Nanoparticle-Assisted "NMR Chemosensing." *J. Am. Chem. Soc.* **2015**, *137* (35), 11399–11406. https://doi.org/10.1021/jacs.5b06300.

(130) Gabrielli, L.; Rosa-Gastaldo, D.; Salvia, M.-V.; Springhetti, S.; Rastrelli, F.; Mancin, F. Detection and Identification of Designer Drugs by Nanoparticle-Based NMR Chemosensing. *Chem. Sci.* **2018**, *9* (21), 4777–4784. https://doi.org/10.1039/C8SC01283K.

(131) De Biasi, F.; Rosa-Gastaldo, D.; Sun, X.; Mancin, F.; Rastrelli, F. Nanoparticle-Assisted NMR Spectroscopy: Enhanced Detection of Analytes by Water-Mediated Saturation Transfer. *J. Am. Chem. Soc.* **2019**, *141* (12), 4870–4877. https://doi.org/10.1021/jacs.8b13225.

(132) Biasi, F. D.; Rosa-Gastaldo, D.; Mancin, F.; Rastrelli, F. Hybrid Nanoreceptors for High Sensitivity Detection of Small Molecules by NMR Chemosensing. *Chem. Commun.* **2021**, *57* (24), 3002–3005. https://doi.org/10.1039/D0CC07559K.

(133) Huang, X.; El-Sayed, M. A. Gold Nanoparticles: Optical Properties and Implementations in Cancer Diagnosis and Photothermal Therapy. *J. Adv. Res.* **2010**, *1* (1), 13–28. https://doi.org/10.1016/j.jare.2010.02.002.

(134) Nath, N.; Chilkoti, A. A Colorimetric Gold Nanoparticle Sensor To Interrogate Biomolecular Interactions in Real Time on a Surface. *Anal. Chem.* **2002**, *74* (3), 504–509. https://doi.org/10.1021/ac015657x.

(135) Matsui, J.; Akamatsu, K.; Hara, N.; Miyoshi, D.; Nawafune, H.; Tamaki, K.; Sugimoto, N. SPR Sensor Chip for Detection of Small Molecules Using Molecularly Imprinted Polymer with Embedded Gold Nanoparticles. *Anal. Chem.* **2005**, *77* (13), 4282–4285. https://doi.org/10.1021/ac050227i.

(136) Akshaya, K.; Arthi, C.; Pavithra, A. J.; Poovizhi, P.; Antinate, S. S.; Hikku, G. S.; Jeyasubramanian, K.; Murugesan, R. Bioconjugated Gold Nanoparticles as an Efficient Colorimetric Sensor for Cancer Diagnostics. *Photodiagnosis Photodyn. Ther.* **2020**, *30*, 101699. https://doi.org/10.1016/j.pdpdt.2020.101699.

(137) Liu, X.; He, F.; Zhang, F.; Zhang, Z.; Huang, Z.; Liu, J. Dopamine and Melamine Binding to Gold Nanoparticles Dominates Their Aptamer-Based Label-Free Colorimetric Sensing. *Anal. Chem.* **2020**, *92* (13), 9370–9378. https://doi.org/10.1021/acs.analchem.0c01773.

(138) Willets, K. A.; Van Duyne, R. P. Localized Surface Plasmon Resonance Spectroscopy and Sensing. *Annu. Rev. Phys. Chem.* **2007**, *58* (1), 267–297. https://doi.org/10.1146/annurev.physchem.58.032806.104607.

(139) Eustis, S.; El-Sayed, M. A. Why Gold Nanoparticles Are More Precious than Pretty Gold: Noble Metal Surface Plasmon Resonance and Its Enhancement of the Radiative and Nonradiative Properties of Nanocrystals of Different Shapes. *Chem. Soc. Rev.* **2006**, *35* (3), 209–217. https://doi.org/10.1039/B514191E.

(140) Song, X.; Zhu, W.; Ge, X.; Li, R.; Li, S.; Chen, X.; Song, J.; Xie, J.; Chen, X.; Yang, H. A New Class of NIR-II Gold Nanocluster-Based Protein Biolabels for In Vivo Tumor-Targeted Imaging. *Angew. Chem. Int. Ed.* **2021**, *60* (3), 1306–1312. https://doi.org/10.1002/anie.202010870.

(141) Wang, W.; Kong, Y.; Jiang, J.; Xie, Q.; Huang, Y.; Li, G.; Wu, D.; Zheng, H.; Gao, M.; Xu, S.; Pan, Y.; Li, W.; Ma, R.; Wu, M. X.; Li, X.; Zuilhof, H.; Cai, X.; Li, R. Engineering the Protein Corona Structure on Gold Nanoclusters Enables Red-Shifted Emissions in the Second Near-Infrared Window for Gastrointestinal Imaging. *Angew. Chem. Int. Ed.* **2020**, *59* (50), 22431–22435. https://doi.org/10.1002/anie.202010089.

(142) Bigioni, T. P.; Whetten, R. L.; Dag, Ö. Near-Infrared Luminescence from Small Gold Nanocrystals. *J. Phys. Chem. B* **2000**, *104* (30), 6983–6986. https://doi.org/10.1021/jp993867w.

(143) Zheng, J.; Zhang, C.; Dickson, R. M. Highly Fluorescent, Water-Soluble, Size-Tunable Gold Quantum Dots. *Phys. Rev. Lett.* **2004**, *93* (7), 077402. https://doi.org/10.1103/PhysRevLett.93.077402.

(144) Zhu, M.; Aikens, C. M.; Hollander, F. J.; Schatz, G. C.; Jin, R. Correlating the Crystal Structure of A Thiol-Protected Au25 Cluster and Optical Properties. *J. Am. Chem. Soc.* **2008**, *130* (18), 5883–5885. https://doi.org/10.1021/ja801173r.

(145) Aikens, C. M.; Schatz, G. C. Time-Dependent Density Functional Theory Examination of the Effects of Ligand Adsorption on Metal Nanoparticles. In *Nanoparticles: Synthesis, Stabilization,*

Passivation, and Functionalization; ACS Symposium Series; American Chemical Society, 2008; Vol. 996, pp 108–121. https://doi.org/10.1021/bk-2008-0996.ch009.

(146) Jin, R. Quantum Sized, Thiolate-Protected Gold Nanoclusters. *Nanoscale* **2010**, *2* (3), 343–362. https://doi.org/10.1039/B9NR00160C.

(147) Wang, G.; Huang, T.; Murray, R. W.; Menard, L.; Nuzzo, R. G. Near-IR Luminescence of Monolayer-Protected Metal Clusters. *J. Am. Chem. Soc.* **2005**, *127* (3), 812–813. https://doi.org/10.1021/ja0452471.

(148) Schaeffer, N.; Tan, B.; Dickinson, C.; Rosseinsky, M. J.; Laromaine, A.; McComb, D. W.; Stevens, M. M.; Wang, Y.; Petit, L.; Barentin, C.; Spiller, D. G.; Cooper, A. I.; Lévy, R. Fluorescent or Not? Size-Dependent Fluorescence Switching for Polymer-Stabilized Gold Clusters in the 1.1–1.7 Nm Size Range. *Chem. Commun.* **2008**, No. 34, 3986–3988. https://doi.org/10.1039/B809876J.

(149) Link, S.; Beeby, A.; FitzGerald, S.; El-Sayed, M. A.; Schaaff, T. G.; Whetten, R. L. Visible to Infrared Luminescence from a 28-Atom Gold Cluster. *J. Phys. Chem. B* **2002**, *106* (13), 3410–3415. https://doi.org/10.1021/jp014259v.

(150) Lin, Y.; Charchar, P.; Christofferson, A. J.; Thomas, M. R.; Todorova, N.; Mazo, M. M.; Chen, Q.; Doutch, J.; Richardson, R.; Yarovsky, I.; Stevens, M. M. Surface Dynamics and Ligand–Core Interactions of Quantum Sized Photoluminescent Gold Nanoclusters. *J. Am. Chem. Soc.* **2018**, *140* (51), 18217–18226. https://doi.org/10.1021/jacs.8b04436.

(151) Chen, L.-Y.; Wang, C.-W.; Yuan, Z.; Chang, H.-T. Fluorescent Gold Nanoclusters: Recent Advances in Sensing and Imaging. *Anal. Chem.* **2015**, *87* (1), 216–229. https://doi.org/10.1021/ac503636j.

(152) Kundu, S.; Ghosh, B.; Nandi, S.; Ghosh, M.; Pyne, A.; Chatterjee, J.; Sarkar, N. Surface Ligand-Controlled Wavelength-Tunable Luminescence of Gold Nanoclusters: Cellular Imaging and Smart Fluorescent Probes for Amyloid Detection. *ACS Appl. Bio Mater.* **2020**, *3* (7), 4282–4293. https://doi.org/10.1021/acsabm.0c00337.

(153) Huang, C.-C.; Yang, Z.; Lee, K.-H.; Chang, H.-T. Synthesis of Highly Fluorescent Gold Nanoparticles for Sensing Mercury(II). *Angew. Chem.* **2007**, *119* (36), 6948–6952. https://doi.org/10.1002/ange.200700803.

(154) Wu, Z.; Jin, R. On the Ligand's Role in the Fluorescence of Gold Nanoclusters. *Nano Lett.* **2010**, *10* (7), 2568–2573. https://doi.org/10.1021/nl101225f.

(155) Obstarczyk, P.; Pniakowska, A.; Nonappa; Grzelczak, M. P.; Olesiak-Bańska, J. Crown Ether-Capped Gold Nanoclusters as a Multimodal Platform for Bioimaging. *ACS Omega* **2023**, *8* (12), 11503–11511. https://doi.org/10.1021/acsomega.3c00426.

(156) Kang, X.; Zhu, M. Tailoring the Photoluminescence of Atomically Precise Nanoclusters. *Chem. Soc. Rev.* **2019**, *48* (8), 2422–2457. https://doi.org/10.1039/C8CS00800K.

(157) Pramanik, G.; Humpolickova, J.; Valenta, J.; Kundu, P.; Bals, S.; Bour, P.; Dracinsky, M.; Cigler, P. Gold Nanoclusters with Bright Near-Infrared Photoluminescence. *Nanoscale* **2018**, *10* (8), 3792–3798. https://doi.org/10.1039/C7NR06050E.

(158) Kumar, A. S. K.; Tseng, W.-L. Perspective on Recent Developments of near Infrared-Emitting Gold Nanoclusters: Applications in Sensing and Bio-Imaging. *Anal. Methods* **2020**, *12* (14), 1809–1826. https://doi.org/10.1039/D0AY00157K.

(159) Zhu, S.; Wang, X.; Cong, Y.; Li, L. Regulating the Optical Properties of Gold Nanoclusters for Biological Applications. *ACS Omega* **2020**, *5* (36), 22702–22707. https://doi.org/10.1021/acsomega.0c03218.

(160) Bouché, M.; Hsu, J. C.; Dong, Y. C.; Kim, J.; Taing, K.; Cormode, D. P. Recent Advances in Molecular Imaging with Gold Nanoparticles. *Bioconjug. Chem.* **2020**, *31* (2), 303–314. https://doi.org/10.1021/acs.bioconjchem.9b00669.

(161) Swierczewska, M.; Lee, S.; Chen, X. The Design and Application of Fluorophore–Gold Nanoparticle Activatable Probes. *Phys. Chem. Chem. Phys.* **2011**, *13* (21), 9929–9941. https://doi.org/10.1039/C0CP02967J.

(162) Chen, C.; Hildebrandt, N. Resonance Energy Transfer to Gold Nanoparticles: NSET Defeats FRET. *TrAC Trends Anal. Chem.* **2020**, *123*, 115748. https://doi.org/10.1016/j.trac.2019.115748.

(163) Xue, C.; Xue, Y.; Dai, L.; Urbas, A.; Li, Q. Size- and Shape-Dependent Fluorescence Quenching of Gold Nanoparticles on Perylene Dye. *Adv. Opt. Mater.* **2013**, *1* (8), 581–587. https://doi.org/10.1002/adom.201300175.

(164) Dulkeith, E.; Morteani, A. C.; Niedereichholz, T.; Klar, T. A.; Feldmann, J.; Levi, S. A.; van Veggel, F. C. J. M.; Reinhoudt, D. N.; Möller, M.; Gittins, D. I. Fluorescence Quenching of Dye

Molecules near Gold Nanoparticles: Radiative and Nonradiative Effects. *Phys. Rev. Lett.* **2002**, *89* (20), 203002. https://doi.org/10.1103/PhysRevLett.89.203002.

(165) Dulkeith, E.; Ringler, M.; Klar, T. A.; Feldmann, J.; Muñoz Javier, A.; Parak, W. J. Gold Nanoparticles Quench Fluorescence by Phase Induced Radiative Rate Suppression. *Nano Lett.* **2005**, *5* (4), 585–589. https://doi.org/10.1021/nl0480969.

(166) Schneider, G.; Decher, G.; Nerambourg, N.; Praho, R.; Werts, M. H. V.; Blanchard-Desce, M. Distance-Dependent Fluorescence Quenching on Gold Nanoparticles Ensheathed with Layer-by-Layer Assembled Polyelectrolytes. *Nano Lett.* **2006**, *6* (3), 530–536. https://doi.org/10.1021/nl052441s.

(167) Thomas, K. G.; Kamat, P. V. Chromophore-Functionalized Gold Nanoparticles. *Acc. Chem. Res.* **2003**, *36* (12), 888–898. https://doi.org/10.1021/ar030030h.

(168) Lee, J.-H.; Cho, H.-Y.; Choi, H. K.; Lee, J.-Y.; Choi, J.-W. Application of Gold Nanoparticle to Plasmonic Biosensors. *Int. J. Mol. Sci.* **2018**, *19* (7), 2021. https://doi.org/10.3390/ijms19072021.

(169) Zhang, H.; Xu, P.; Zhang, X.; Cao, X.; Han, W.; Liu, M.; Liu, X.; Zeng, W. Au Nanoparticles Based Ultra-Fast "Turn-On" Fluorescent Sensor for Detection of Biothiols and Its Application in Living Cell Imaging. *Chin. Chem. Lett.* **2020**, *31* (5), 1083–1086. https://doi.org/10.1016/j.cclet.2019.10.005.

(170) Su, L.; Wang, S.; Wang, L.; Yan, Z.; Yi, H.; Zhang, D.; Shen, G.; Ma, Y. Fluorescent Aptasensor for Carbendazim Detection in Aqueous Samples Based on Gold Nanoparticles Quenching Rhodamine B. *Spectrochim. Acta. A. Mol. Biomol. Spectrosc.* **2020**, *225*, 117511. https://doi.org/10.1016/j.saa.2019.117511.

(171) Wu, Y.; Ali, M. R. K.; Chen, K.; Fang, N.; El-Sayed, M. A. Gold Nanoparticles in Biological Optical Imaging. *Nano Today* **2019**, *24*, 120–140. https://doi.org/10.1016/j.nantod.2018.12.006.

(172) Sperling, R. A.; Gil, P. R.; Zhang, F.; Zanella, M.; Parak, W. J. Biological Applications of Gold Nanoparticles. *Chem. Soc. Rev.* **2008**, *37* (9), 1896–1908. https://doi.org/10.1039/B712170A.

(173) Zhang, J.; Mou, L.; Jiang, X. Surface Chemistry of Gold Nanoparticles for Health-Related Applications. *Chem. Sci.* **2020**, *11* (4), 923–936. https://doi.org/10.1039/C9SC06497D.

(174) Anil Bansal, S.; Kumar, V.; Karimi, J.; Pal Singh, A.; Kumar, S. Role of Gold Nanoparticles in Advanced Biomedical Applications. *Nanoscale Adv.* **2020**, *2* (9), 3764–3787. https://doi.org/10.1039/D0NA00472C.

(175) Lee, J. W.; Choi, S.-R.; Heo, J. H. Simultaneous Stabilization and Functionalization of Gold Nanoparticles via Biomolecule Conjugation: Progress and Perspectives. *ACS Appl. Mater. Interfaces* **2021**, *13* (36), 42311–42328. https://doi.org/10.1021/acsami.1c10436.

(176) Lunnoo, T.; Assawakhajornsak, J.; Puangmali, T. In Silico Study of Gold Nanoparticle Uptake into a Mammalian Cell: Interplay of Size, Shape, Surface Charge, and Aggregation. *J. Phys. Chem. C* **2019**, *123* (6), 3801–3810. https://doi.org/10.1021/acs.jpcc.8b07616.

(177) van de Looij, S. M.; Hebels, E. R.; Viola, M.; Hembury, M.; Oliveira, S.; Vermonden, T. Gold Nanoclusters: Imaging, Therapy, and Theranostic Roles in Biomedical Applications. *Bioconjug. Chem.* **2022**, *33* (1), 4–23. https://doi.org/10.1021/acs.bioconjchem.1c00475.

(178) Patil, T.; Gambhir, R.; Vibhute, A.; Tiwari, A. P. Gold Nanoparticles: Synthesis Methods, Functionalization and Biological Applications. *J. Clust. Sci.* **2023**, *34* (2), 705–725. https://doi.org/10.1007/s10876-022-02287-6.

(179) Sheehan, P. E.; Whitman, L. J. Detection Limits for Nanoscale Biosensors. *Nano Lett.* **2005**, *5* (4), 803–807. https://doi.org/10.1021/nl050298x.

(180) Liu, X.; Atwater, M.; Wang, J.; Huo, Q. Extinction Coefficient of Gold Nanoparticles with Different Sizes and Different Capping Ligands. *Colloids Surf. B Biointerfaces* **2007**, *58* (1), 3–7. https://doi.org/10.1016/j.colsurfb.2006.08.005.

(181) Atta, S.; Canning, A. J.; Odion, R.; Wang, H.; Hau, D.; Devadhasan, J. P.; Summers, A. J.; Gates-Hollingsworth, M. A.; Pflughoeft, K. J.; Gu, J.; Montgomery, D. C.; AuCoin, D. P.; Zenhausern, F.; Vo-Dinh, T. Sharp Branched Gold Nanostar-Based Lateral-Flow Immunoassay for Detection of Yersinia Pestis. *ACS Appl. Nano Mater.* **2023**, *6* (5), 3884–3892. https://doi.org/10.1021/acsanm.2c05557.

(182) Nguyen, V.-T.; Song, S.; Park, S.; Joo, C. Recent Advances in High-Sensitivity Detection Methods for Paper-Based Lateral-Flow Assay. *Biosens. Bioelectron.* **2020**, *152*, 112015. https://doi.org/10.1016/j.bios.2020.112015.

(183) Parolo, C.; Sena-Torralba, A.; Bergua, J. F.; Calucho, E.; Fuentes-Chust, C.; Hu, L.; Rivas, L.; Álvarez-Diduk, R.; Nguyen, E. P.; Cinti, S.; Quesada-González, D.; Merkoçi, A. Tutorial: Design and Fabrication of Nanoparticle-Based Lateral-Flow Immunoassays. *Nat. Protoc.* **2020**, *15* (12), 3788–3816. https://doi.org/10.1038/s41596-020-0357-x.

(184) Priyadarshini, E.; Pradhan, N. Gold Nanoparticles as Efficient Sensors in Colorimetric Detection of Toxic Metal Ions: A Review. *Sens. Actuators B Chem.* **2017**, *238*, 888–902. https://doi.org/10.1016/j.snb.2016.06.081.

(185) Yang, J.; Wang, X.; Sun, Y.; Chen, B.; Hu, F.; Guo, C.; Yang, T. Recent Advances in Colorimetric Sensors Based on Gold Nanoparticles for Pathogen Detection. *Biosensors* **2023**, *13* (1), 29. https://doi.org/10.3390/bios13010029.

(186) Saha, K.; Agasti, S. S.; Kim, C.; Li, X.; Rotello, V. M. Gold Nanoparticles in Chemical and Biological Sensing. *Chem. Rev.* **2012**, *112* (5), 2739–2779. https://doi.org/10.1021/cr2001178.

(187) Zhang, F.; Liu, J. Label-Free Colorimetric Biosensors Based on Aptamers and Gold Nanoparticles: A Critical Review. *Anal. Sens.* **2021**, *1* (1), 30–43. https://doi.org/10.1002/anse.202000023.

(188) Uehara, N. Polymer-Functionalized Gold Nanoparticles as Versatile Sensing Materials. *Anal. Sci.* **2010**, *26* (12), 1219–1228. https://doi.org/10.2116/analsci.26.1219.

(189) Pezzato, C.; Maiti, S.; Chen, J. L.-Y.; Cazzolaro, A.; Gobbo, C.; Prins, L. J. Monolayer Protected Gold Nanoparticles with Metal-Ion Binding Sites: Functional Systems for Chemosensing Applications. *Chem. Commun.* **2015**, *51* (49), 9922–9931. https://doi.org/10.1039/C5CC00814J.

(190) Mou, X.-Z.; Chen, X.-Y.; Wang, J.; Zhang, Z.; Yang, Y.; Shou, Z.-X.; Tu, Y.-X.; Du, X.; Wu, C.; Zhao, Y.; Qiu, L.; Jiang, P.; Chen, C.; Huang, D.-S.; Li, Y.-Q. Bacteria-Instructed Click Chemistry between Functionalized Gold Nanoparticles for Point-of-Care Microbial Detection. *ACS Appl. Mater. Interfaces* **2019**, *11* (26), 23093–23101. https://doi.org/10.1021/acsami.9b09279.

(191) Kim, H.; Park, M.; Hwang, J.; Kim, J. H.; Chung, D.-R.; Lee, K.; Kang, M. Development of Label-Free Colorimetric Assay for MERS-CoV Using Gold Nanoparticles. *ACS Sens.* **2019**, *4* (5), 1306–1312. https://doi.org/10.1021/acssensors.9b00175.

(192) Amornwairat, P.; Pissuwan, D. Colorimetric Sensing of Gram-Negative and Gram-Positive Bacteria Using 4-Mercaptophenylboronic Acid-Functionalized Gold Nanoparticles in the Presence of Polyethylene Glycol. *ACS Omega* **2023**. https://doi.org/10.1021/acsomega.3c01205.

(193) Ferreira, A. L.; de Lima, L. F.; Torres, M. D. T.; de Araujo, W. R.; de la Fuente-Nunez, C. Low-Cost Optodiagnostic for Minute-Time Scale Detection of SARS-CoV-2. *ACS Nano* **2021**, *15* (11), 17453–17462. https://doi.org/10.1021/acsnano.1c03236.

(194) Behrouzi, K.; Lin, L. Gold Nanoparticle Based Plasmonic Sensing for the Detection of SARS-CoV-2 Nucleocapsid Proteins. *Biosens. Bioelectron.* **2022**, *195*, 113669. https://doi.org/10.1016/j.bios.2021.113669.

(195) Lew, T. T. S.; Aung, K. M. M.; Ow, S. Y.; Amrun, S. N.; Sutarlie, L.; Ng, L. F. P.; Su, X. Epitope-Functionalized Gold Nanoparticles for Rapid and Selective Detection of SARS-CoV-2 IgG Antibodies. *ACS Nano* **2021**, *15* (7), 12286–12297. https://doi.org/10.1021/acsnano.1c04091.

(196) Moitra, P.; Alafeef, M.; Dighe, K.; Frieman, M. B.; Pan, D. Selective Naked-Eye Detection of SARS-CoV-2 Mediated by N Gene Targeted Antisense Oligonucleotide Capped Plasmonic Nanoparticles. *ACS Nano* **2020**, *14* (6), 7617–7627. https://doi.org/10.1021/acsnano.0c03822.

(197) Cao, Y.; Wu, J.; Pang, B.; Zhang, H.; Chris Le, X. CRISPR/Cas12a-Mediated Gold Nanoparticle Aggregation for Colorimetric Detection of SARS-CoV-2. *Chem. Commun.* **2021**, *57* (56), 6871–6874. https://doi.org/10.1039/D1CC02546E.

(198) Fischer, N. O.; Verma, A.; Goodman, C. M.; Simard, J. M.; Rotello, V. M. Reversible "Irreversible" Inhibition of Chymotrypsin Using Nanoparticle Receptors. *J. Am. Chem. Soc.* **2003**, *125* (44), 13387–13391. https://doi.org/10.1021/ja0352505.

(199) Fischer, N. O.; McIntosh, C. M.; Simard, J. M.; Rotello, V. M. Inhibition of Chymotrypsin through Surface Binding Using Nanoparticle-Based Receptors. *Proc. Natl. Acad. Sci.* **2002**, *99* (8), 5018–5023. https://doi.org/10.1073/pnas.082644099.

(200) Martin, S. G.; Prins, L. J. Dynamic Nanoproteins: Self-Assembled Peptide Surfaces on Monolayer Protected Gold Nanoparticles. *Chem. Commun.* **2016**, *52* (60), 9387–9390. https://doi.org/10.1039/C6CC04786F.

(201) Pieters, G.; Pezzato, C.; Prins, L. J. Controlling Supramolecular Complex Formation on the Surface of a Monolayer-Protected Gold Nanoparticle in Water. *Langmuir* **2013**, *29* (24), 7180–7185. https://doi.org/10.1021/la304316z.

(202) Pezzato, C.; Lee, B.; Severin, K.; Prins, L. J. Pattern-Based Sensing of Nucleotides with Functionalized Gold Nanoparticles. *Chem. Commun.* **2012**, *49* (5), 469–471. https://doi.org/10.1039/C2CC38058G.

(203) Zaramella, D.; Scrimin, P.; Prins, L. J. Self-Assembly of a Catalytic Multivalent Peptide–Nanoparticle Complex. *J. Am. Chem. Soc.* **2012**, *134* (20), 8396–8399. https://doi.org/10.1021/ja302754h.

(204) Miranda, O. R.; You, C.-C.; Phillips, R.; Kim, I.-B.; Ghosh, P. S.; Bunz, U. H. F.; Rotello, V. M. Array-Based Sensing of Proteins Using Conjugated Polymers. *J. Am. Chem. Soc.* **2007**, *129* (32), 9856–9857. https://doi.org/10.1021/ja0737927.

(205) Fan, C.; Wang, S.; Hong, J. W.; Bazan, G. C.; Plaxco, K. W.; Heeger, A. J. Beyond Superquenching: Hyper-Efficient Energy Transfer from Conjugated Polymers to Gold Nanoparticles. *Proc. Natl. Acad. Sci.* **2003**, *100* (11), 6297–6301. https://doi.org/10.1073/pnas.1132025100.

(206) Bunz, U. H. F.; Rotello, V. M. Gold Nanoparticle–Fluorophore Complexes: Sensitive and Discerning "Noses" for Biosystems Sensing. *Angew. Chem. Int. Ed.* **2010**, *49* (19), 3268–3279. https://doi.org/10.1002/anie.200906928.

(207) Geng, Y.; Peveler, W. J.; Rotello, V. M. Array-Based "Chemical Nose" Sensing in Diagnostics and Drug Discovery. *Angew. Chem. Int. Ed.* **2019**, *58* (16), 5190–5200. https://doi.org/10.1002/anie.201809607.

(208) Rana, S.; Elci, S. G.; Mout, R.; Singla, A. K.; Yazdani, M.; Bender, M.; Bajaj, A.; Saha, K.; Bunz, U. H. F.; Jirik, F. R.; Rotello, V. M. Ratiometric Array of Conjugated Polymers–Fluorescent Protein Provides a Robust Mammalian Cell Sensor. *J. Am. Chem. Soc.* **2016**, *138* (13), 4522–4529. https://doi.org/10.1021/jacs.6b00067.

(209) Le, N. D. B.; Yesilbag Tonga, G.; Mout, R.; Kim, S.-T.; Wille, M. E.; Rana, S.; Dunphy, K. A.; Jerry, D. J.; Yazdani, M.; Ramanathan, R.; Rotello, C. M.; Rotello, V. M. Cancer Cell

Discrimination Using Host–Guest "Doubled" Arrays. *J. Am. Chem. Soc.* **2017**, *139* (23), 8008–8012. https://doi.org/10.1021/jacs.7b03657.

(210) Gupta, A.; Mumtaz, S.; Li, C.-H.; Hussain, I.; Rotello, V. M. Combatting Antibiotic-Resistant Bacteria Using Nanomaterials. *Chem. Soc. Rev.* **2019**, *48* (2), 415–427. https://doi.org/10.1039/C7CS00748E.

(211) Rohr, U.-P.; Binder, C.; Dieterle, T.; Giusti, F.; Messina, C. G. M.; Toerien, E.; Moch, H.; Schäfer, H. H. The Value of In Vitro Diagnostic Testing in Medical Practice: A Status Report. *PLoS ONE* **2016**, *11* (3), e0149856. https://doi.org/10.1371/journal.pone.0149856.

(212) Zhou, W.; Gao, X.; Liu, D.; Chen, X. Gold Nanoparticles for In Vitro Diagnostics. *Chem. Rev.* **2015**, *115* (19), 10575–10636. https://doi.org/10.1021/acs.chemrev.5b00100.

(213) De, M.; Rana, S.; Akpinar, H.; Miranda, O. R.; Arvizo, R. R.; Bunz, U. H. F.; Rotello, V. M. Sensing of Proteins in Human Serum Using Conjugates of Nanoparticles and Green Fluorescent Protein. *Nat. Chem.* **2009**, *1* (6), 461–465. https://doi.org/10.1038/nchem.334.

(214) Miranda, O. R.; Chen, H.-T.; You, C.-C.; Mortenson, D. E.; Yang, X.-C.; Bunz, U. H. F.; Rotello, V. M. Enzyme-Amplified Array Sensing of Proteins in Solution and in Biofluids. *J. Am. Chem. Soc.* **2010**, *132* (14), 5285–5289. https://doi.org/10.1021/ja1006756.

(215) Ge, P.; Zhang, J.; Ding, T.; Xianyu, Y. Surface Chemistry of Gold Nanoparticles for Bacterial Detection and Antimicrobial Applications. *ACS Mater. Lett.* **2023**, *5* (3), 638–655. https://doi.org/10.1021/acsmaterialslett.2c00923.

(216) Phillips, R. L.; Miranda, O. R.; You, C.-C.; Rotello, V. M.; Bunz, U. H. F. Rapid and Efficient Identification of Bacteria Using Gold-Nanoparticle–Poly(Para-Phenyleneethynylene) Constructs. *Angew. Chem. Int. Ed.* **2008**, *47* (14), 2590–2594. https://doi.org/10.1002/anie.200703369.

(217) Pranantyo, D.; Raju, C.; Si, Z.; Xu, X.; Pethe, K.; Kang, E.-T.; Chan-Park, M. B. Nontoxic Antimicrobial Cationic Peptide Nanoconstructs with Bacteria-Displaceable Polymeric Counteranions. *Nano Lett.* **2021**, *21* (2), 899–906. https://doi.org/10.1021/acs.nanolett.0c03261.

Chapter 3

3. Charged homoligand and heteroligand AuNPs

The first part of this chapter will discuss the preparation of a first array of cationic homo- and hetero-ligand AuNPs. In detail, two types of cationic hydrogenated (*H*-) thiols were needed, namely **HC12N** and **HC16N** (Figure 3.1a). In both thiols, the positive charge is conferred by a permanent quaternary ammonium group as an endgroup. The only structural difference is the different alkyl chain length. This feature does not imply significant differences in the homoligand AuNP properties but may have a crucial role in the monolayer arrangement of heteroligand AuNPs (also defined as mixed SAM-AuNPs). The preparation of heteroligand AuNPs has been achieved using the cationic *H*-thiol (**HC12N** or **HC16N**) in combination with a readily available *1H,1H,2H,2H*-perfluoro-alkanethiol as fluorinated (*F*-) component.

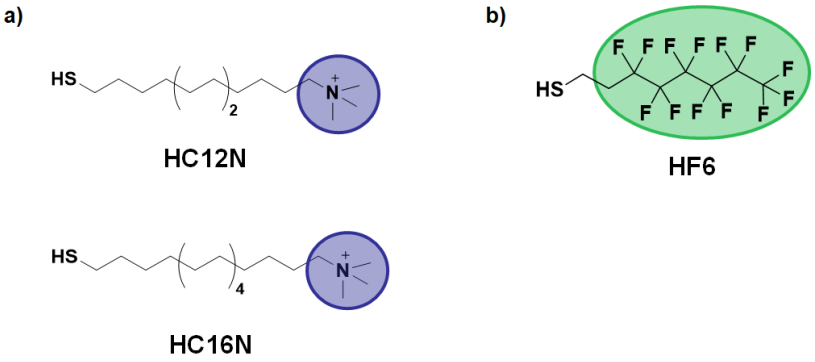

Figure 3.1. Structures of the two cationic ligands (**a**) used for the preparation of the first array of both homoligand AuNPs and heteroligand AuNPs. For the latter, **HC12N** and **HC16N** are in combination with the fluorinated ligand **HF6** (**b**).

Both **HC12N** and **HC16N** have already been synthesised by Pasquato and co-workers.[1] By using combinations of these cationic thiols with *1H,1H,2H,2H*-perfluoro-1-decanethiol (**HF8**) or *1H,1H,2H,2H*-perfluoro-1-octanethiol (**HF6**; Figure 3.1b), they have prepared several charged *H*-/*F*-mixed monolayer AuNPs varying the *H*-/*F*- ratio, and then evaluated their potential in medical and

biological applications. The solubility properties assessment of these systems has pinpointed the critical role of the length mismatch between the *H*- ligands and *F*- thiol in obtaining water-soluble mixed AuNPs. The length of the *F*- thiol has to allow the exposure of the hydrophobic domains to the external environment to trigger hydrophobic interactions with surrounding systems or targets, and at the same time ensuring good solubility in a polar environment. These authors data have demonstrated that the longest *F*- thiol **HF8** provides mixed monolayer AuNPs poorly soluble in polar solvents, whereas **HF6** gives AuNPs with improved solubility in the same media. Based on this study, in this thesis work **HF6** was selected as fluorinated component to achieve charged *H*-/*F*-mixed AuNPs. These nanoparticles together with the corresponding homoligand ones represent the first set of cationic AuNPs (Figure 3.2) prepared and analysed to validate the project strategy.

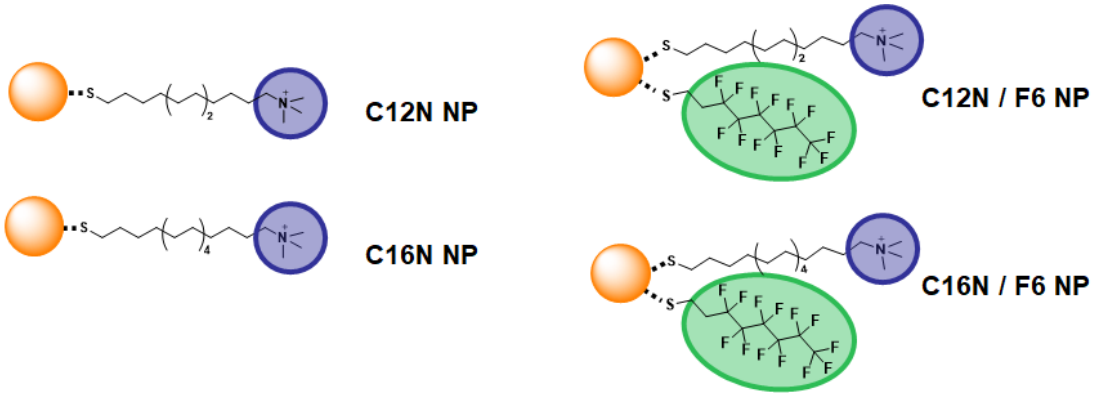

Figure 3.2. Schematic illustration of the first set of cationic AuNPs.

These nanoparticles were used to test their ability to quench the emission of negatively charged organic fluorophores considering both low molecular species and polymers. As expected, the fluorescence quenching properties were more pronounced towards the anionic polymer, because of the efficient binding of this species towards the AuNPs due to the multivalent interactions established between the quencher and the donor. The quenching studies were performed by titrations of the chosen fluorophore with the cationic AuNPs. These analyses have been initially performed in water, this allowed to whether or not the interaction with the fluorophore and the nanoparticles was taking place leading to quenching and to find the optimal AuNPs/fluorophore concentrations. The same experiments were afterwards carried out in phosphate buffered saline solutions to mimic biological conditions. After evaluation of the AuNPs quenching properties and identification of optimal experimental conditions, the AuNPs-fluorophore interactions were studied in the presence of liposomes as convenient models of biological membrane. To this end, two distinct anionic liposomes have been prepared by using zwitterionic and anionic lipids in order to achieve systems with different

surface charge. The liposomes have been incubated with the cationic AuNPs and then titrated with a fluorophore solution of known concentration. The resulting fluorescence experiments pinpointed promising differentiations in the fluorescence profiles, as a function of the liposome lipid composition, paving the way for the final studies on the interactions of these nanosystems with different bacterial strains.

3.1 Synthesis and characterization of cationic homoligand AuNPs

The preparation of the homoligand AuNPs, required the synthesis of the two cationic ligands **HC12N** and **HC16N**. The shorter **HC12N** ligand was synthesized following a procedure reported in the literature (Scheme 3.1a). Instead, for the **HC16N** synthesis an improved procedure, less laborious respect to that reported in the literature, was developed and optimized in this thesis work (Scheme 3.1b).[2]

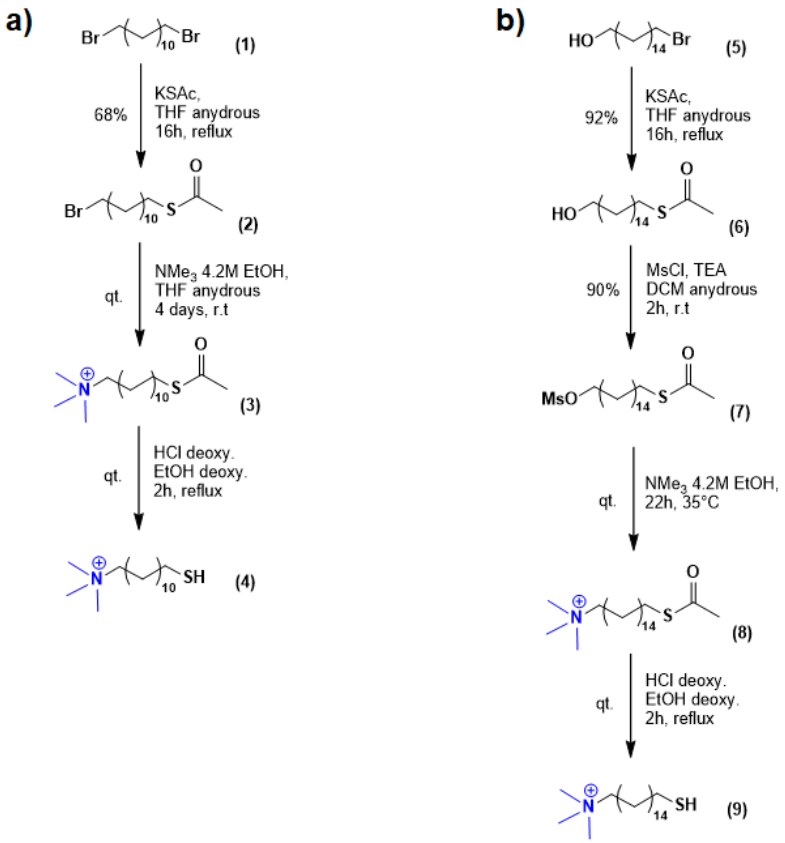

Scheme 3.1 Synthetic procedures for **HC12N** (**a**) previously used by Pasquato and co-workers, and **HC16N** (**b**).

As mentioned above the structure of these thiols is very similar since they differ solely for the length of the alkyl chain connecting the sulfur headgroup to the quaternary ammonium end-group. The alkyl chains of these ligands are required to provide the nanoparticle monolayer with sufficient stability because of the van der Waals interactions between neighbouring ligands. On the other hand, the cationic end-groups guarantee both good solubility in water and polar solvents, and are instrumental to endow the nanoparticles with a recognition element for anionic substrates. Regarding the nature of the ligand end group, the choice of trimethylammonium is not accidental. Indeed, the chemistry of these ligands significantly affects the structure and packing mode of the SAM monolayers, especially for small and ultra-small AuNPs (diameter below ~ 5 nm).[3] Indeed, Recent experimental electron spin resonance (ESR) studies combined with molecular dynamics (MD) simulations aiming at characterising the structure of the nanoparticles monolayer varying the ligands end-groups have displayed that bulky terminal groups, such as trimethylammonium, trigger a radial organization of the ligands within the nanoparticles monolayer. [4] This is an indication that the steric hindrance of the end groups exceeds, in this case, the stabilising interchain as van der Waals interactions, and solvophobic forces (Figure 3.3a). In contrast, less bulky end groups, such as the sulfonate group, allow the chains to approach and order themselves establishing further stabilizing interactions Figure 3.3b).

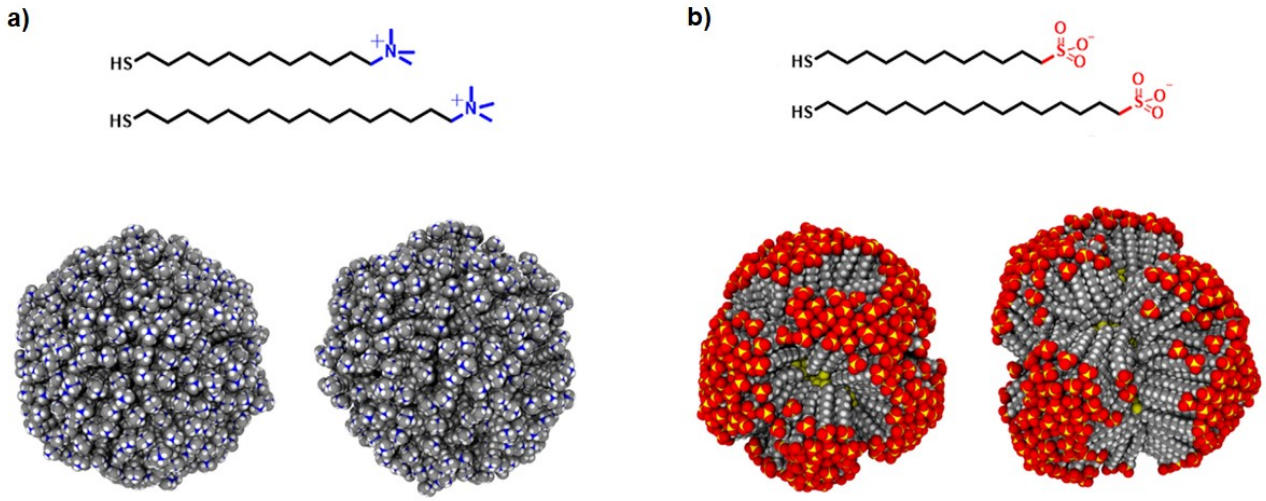

Figure 3.3. Some structures of bulky (**a**) and small (**b**) ligands used for the preparation of corresponding homoligand monolayer-protected AuNPs. The model of monolayer organization on the gold core of NPs is obtained from MD calculations. Color legend: carbon, grey; oxygen, red; sulfur, yellow; nitrogen, blue; hydrogen, white. Adapted from Pellizzoni, E. et al. J. Colloid Interface Sci. 2022, 607, 1373–1381.

The radial organization of the monolayer is a key element for the successful application of AuNPs in biological fields since this arrangement provides a homogeneous monolayer. In addition to providing uniform hydration both on and within the monolayer, this type of organization ensures multivalent interactions with the target, maintaining some ligand flexibility for possible conformational rearrangements upon target binding.

3.1.1 Synthesis of HC12N and HC16N

The beginning of the research activity was focused on the synthesis of the cationic ligands **HC12N** and **HC16N**. The synthesis of **HC12N** (Scheme 3.1a), starts from the commercially available 1,12-dibromodecane (**1**) which is desimetrized by a S_N2 nucleophilic substitution performed in the presence of potassium thioacetate (KSAc), to obtain compound **2**. The desimetrization required an excess of compound 1 to favour the obtaining of the monosubstituted product. Through this step, the thiol group is inserted into the structure protected as thioester that is stable under the conditions required for the further functionalization of **2**. The following step consists in another nucleophilic substitution in the presence of a large excess of trimethylamine using ethanol as solvent. The reaction was performed at room temperature and complete conversion of **2** to the desired product **3** was achieved after four days. Finally, the free thiol ligand **4** was obtained by acid-catalysed transesterification using deoxygenated ethanol as reagent and solvent, in the presence of concentrated aqueous HCl as the catalyst.

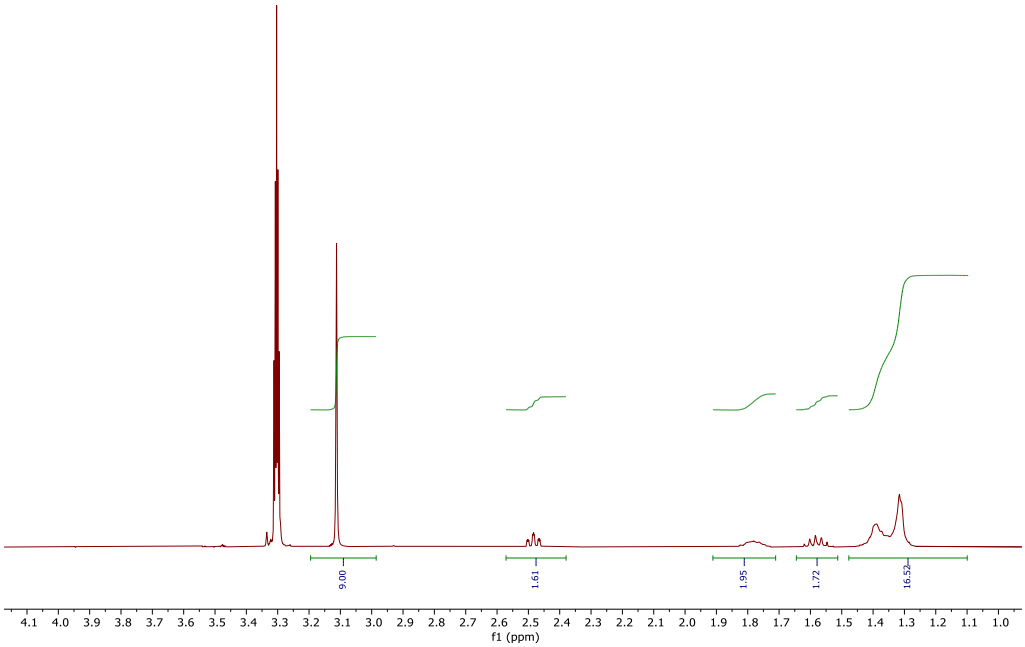

Figure 3.4. ^{1}H NMR (400 MHz, CD_3OD) of the ligand **HC12N**.

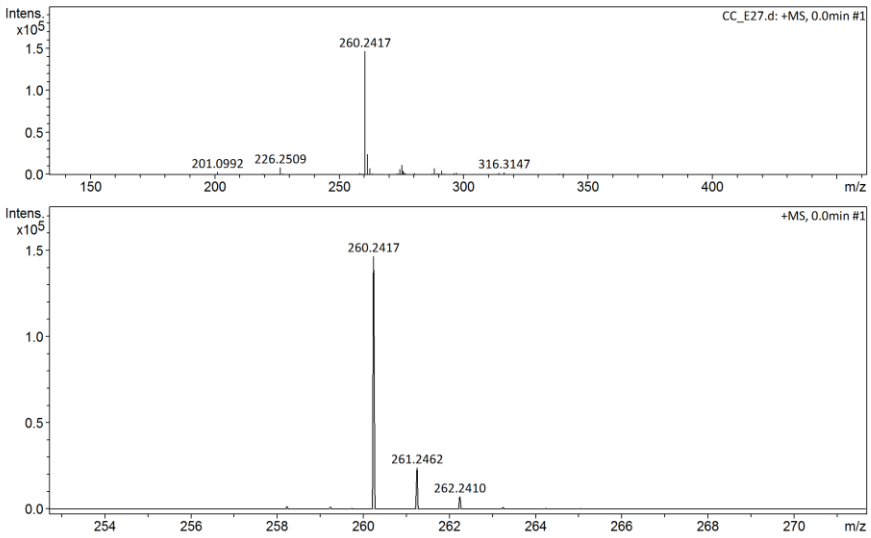

Figure 3.5. The observed (top) and magnified (bottom) exact mass spectrum of **HC12N**.

The product was obtained with an overall yield of 68% and the successful final deprotection could be confirmed by ^{1}H-NMR analysis (Figure 3.4), and accurate mass determination (Figure 3.5). In the ^{1}H-NMR spectrum, it is possible to observe the disappearance of the singlet at 2.32 ppm relative to the methyl protons of the thioester group, and the appearance of the characteristic peak at 2.5 ppm relative to the methylene protons in the alpha to thiol group.

The synthesis of **HC16N** (Scheme 3.1b) starts from the commercially available 16-Bromo-1-hexadecanol (**5**), this compound is reacted with KSAc in anhydrous THF under reflux to afford the protected thiol **6**. To reduce the reaction times compared to those required by the synthetic protocol previously used for the synthesis of this ligand[1], the next step involves the conversion of the terminal hydroxyl group of **6** into a better leaving group using mesyl chloride. A slight excess of triethylamine was used in this step to neutralize the hydrochloric acid released during the reaction, and the mesylate **7** was obtained with a yield of 90%. At this point, the following two reactions: introduction of the trimethylamonium group to achieve compound **8** and thiol deprotection to achieve the ligand **9** were carried out using the same conditions described for **HC12N**. The final product was obtained with an overall yield of 83%. The corresponding ^{1}H-NMR and high-resolution ESI-MS spectra are shown below (Figure 3.6, and Figure 3.7). The same considerations made for the ^{1}H-NMR spectrum of **HC12N** can be applied to that of **HC16N**, however, in this case, even after the acid catalysed thioester cleavage, the peak at 2.7 ppm due to the methyl protons of the mesylate anion is still present suggesting that mesylate is the actual counter anion of ligand **9**.

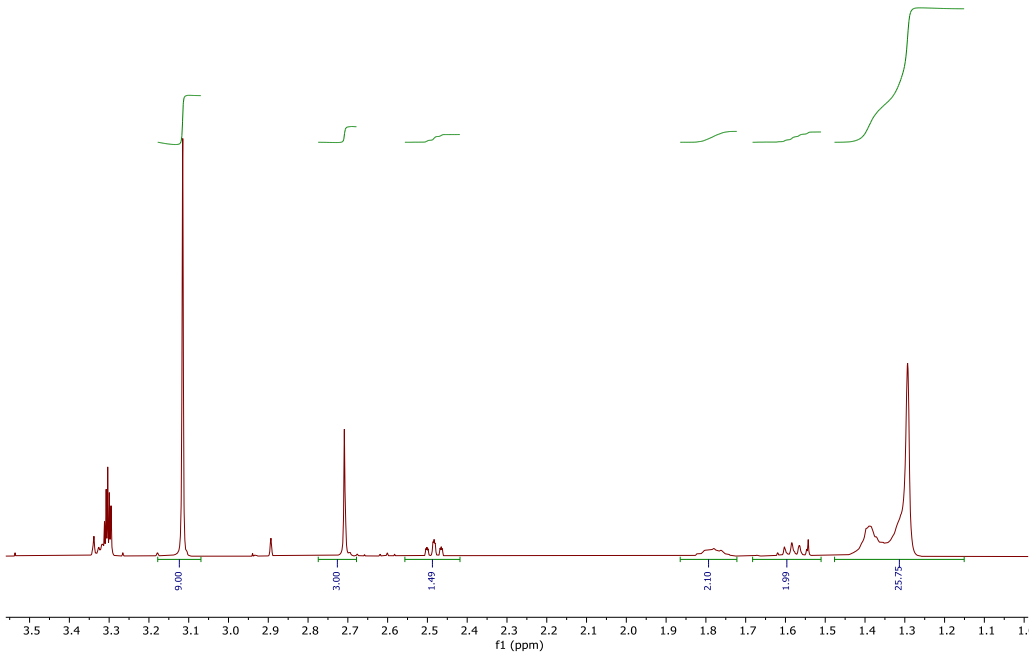

Figure 3.6. ^{1}H NMR (400 MHz, CD_3OD) of the ligand **HC16N**.

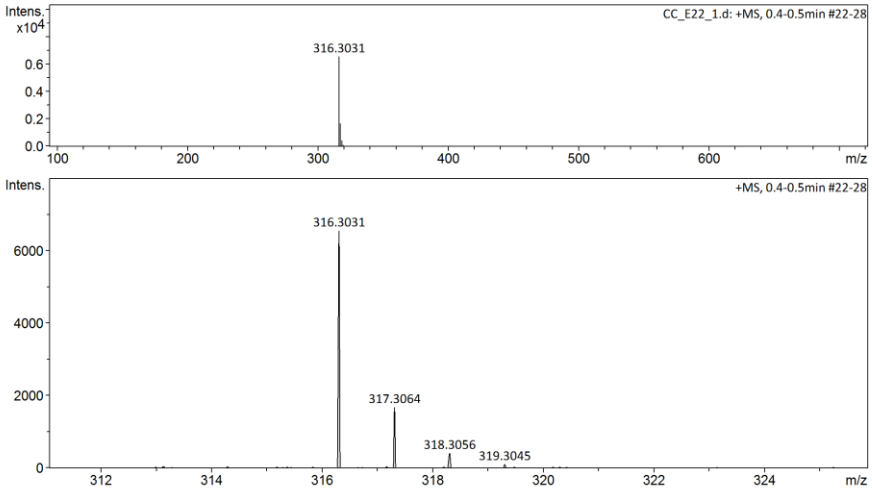

Figure 3.7. The observed (top) and magnified (bottom) exact mass spectrum of **HC16N**.

The ligands **4** and **9** were used to prepare the homoligand C12N AuNPs and C16N AuNPs. To this end, two different synthetic approaches were used to modulate the nanoparticles size, with target values of about 2 nm (ultra-small AuNPs) and about 5 (small AuNPs). The choice of preparing homoligand AuNPs of different sizes has the purpose to introduce a further element of diversity into the AuNP library. The AuNP size affects the curvature radius and so the number of interactions between the AuNP functionalised endgroups and the target surface, influencing the binding association constant, as well as the number of AuNPs adsorbed on the target surface.

3.1.2 usNP C12N and usNP C16N: synthesis and NMR and UV-vis analyses

The procedures for preparing ultra-small C12N and C16N AuNPs (usNP C12N and usNP C16N) will be described in this section. To date, most of the synthesis of AuNPs is inspired by the pioneering two-step Brust-Schiffrin method. Briefly, the gold precursor, usually hydrogen tetrachloroaurate is transferred from the aqueous solution to an organic phase (e.g., toluene) by tetraoctylammonium chloride as a phase transfer agent. The next reduction of $AuCl_4^-$ ions with $NaBH_4$ in the presence of the alkanethiols produces highly stable alkanethiol-protected AuNPs. Once prepared, the nanoparticles can be further functionalized by taking advantage of the place exchange reaction. In the case of water-soluble nanoparticles, the synthetic strategies can exploit thiol-to-thiol exchange reactions starting from alkanethiol protected-AuNPs, or direct methods that employ a charged thiol functionalised in the reduction step. Both approaches can involve some issues. The exchange reaction typically leads to mixed monolayers, while direct procedures require using functionalized thiols under

harsh reduction conditions that could induce their degradation. Thus, different strategies have been developed to overcome these problems, still enabling good size control, colloidal stability, and narrow particle size distribution.[5–8] Among them, Scrimin and co-workers[9] have proposed a well-controlled protocol for the preparation of functionalised AuNPs of varying sizes (Scheme 3.2), by exploiting the Peng synthesis protocol.[10] Compared to the Brust-Schiffrin synthesis, the major difference is that the nanoparticles core is prepared in the absence of the thiol ligand. This is possible because of the use of dioctylamine which is added to the organic phase prior the addition of the reducing agent. The dioctylamine acts as a weak stabilizer in the nanoparticles growing process and also as a mild reducing agent. The following addition of $NaBH_4$ completes the reduction process leading to nanoparticles stabilised by the dioctylamine ligands. After the synthesis is complete, these weakly stabilised nanoparticles can be exposed to a solution of thiols that displace the dioctylamine ligands leading to thiolate-stabilised AuNPs. This method shows several advantages due to the use of dioctylamine, namely the excellent size control of the AuNPs, the possibility to prepare AuNPs of different sizes by tuning the amount of dioctylamine present in the reaction mixture, and the avoidance to expose functionalised thiols to hard reducing conditions.

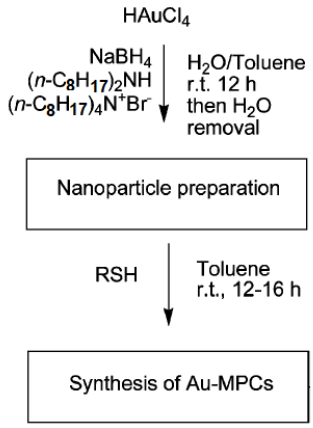

Scheme 3.2 Scheme of Scrimin and co-workers' synthesis protocol. Adapted from Manea, F. et al. Langmuir, 2008, 24 (8), 4120–4124.

This procedure was applied to the preparation of the usNP C12N and usNP C16N, with some modifications in the AuNPs purification process. In details, after the washing cycles of the aqueous phase containing the AuNPs with toluene, ethyl ether, and ethyl acetate reported in the protocol, the resulted AuNP solution was brought to dryness under reduced pressure. The solid was taken up with methanol, precipitated by ethyl ether addition, and centrifuged. This procedure was performed two times, then the AuNPs were collected and the absence of excess ligands and other impurities was assessed by ^{1}H-NMR analysis. Once the purity of the AuNPs solution was confirmed, both the

nanoparticle systems were characterised. The ^{1}H-NMR and UV-vis spectra of usNP C12N are displayed in Figure 3.8 and Figure 3.9 respectively. The UV-vis technique allows one to obtain a preliminary indication of the AuNPs size; given their ultra-small dimensions, the typical LSPR band in a range from 500 to 550 nm is just hinted, as their electrons exist in discrete energy levels. Regarding usNP C16N, the pertinent ^{1}H-NMR and UV-vis spectra are displayed Figure 3.10 and Figure 3.11.

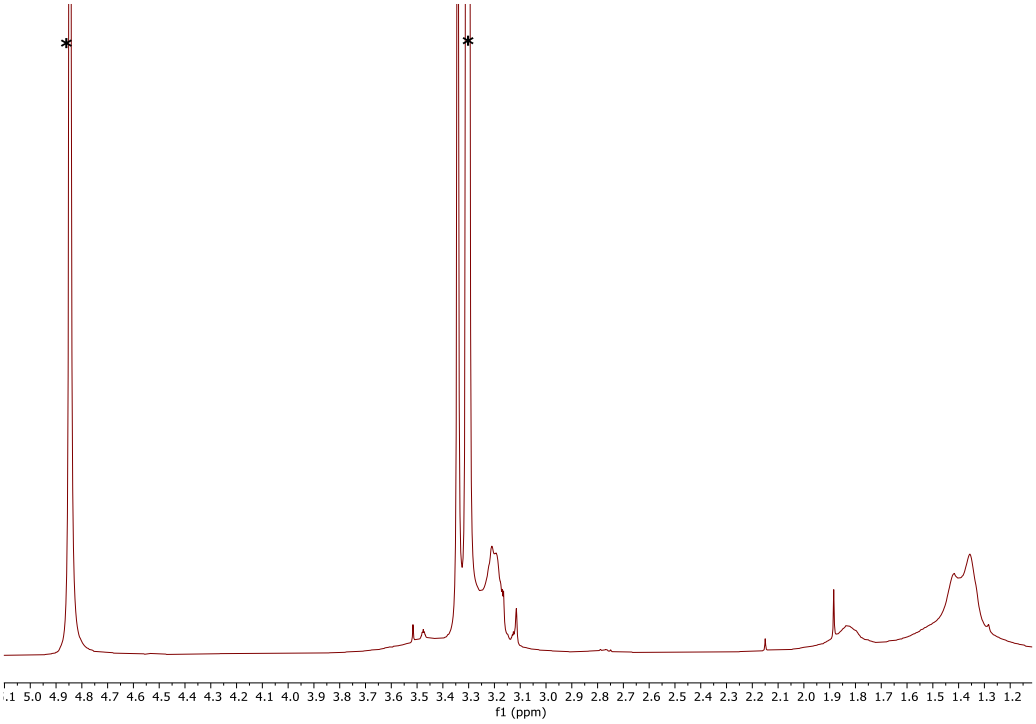

Figure 3.8. ^{1}H NMR (400 MHz, CD_3OD) of usNP C12N. The solvent peaks are indicated by an asterisk (methanol, water).

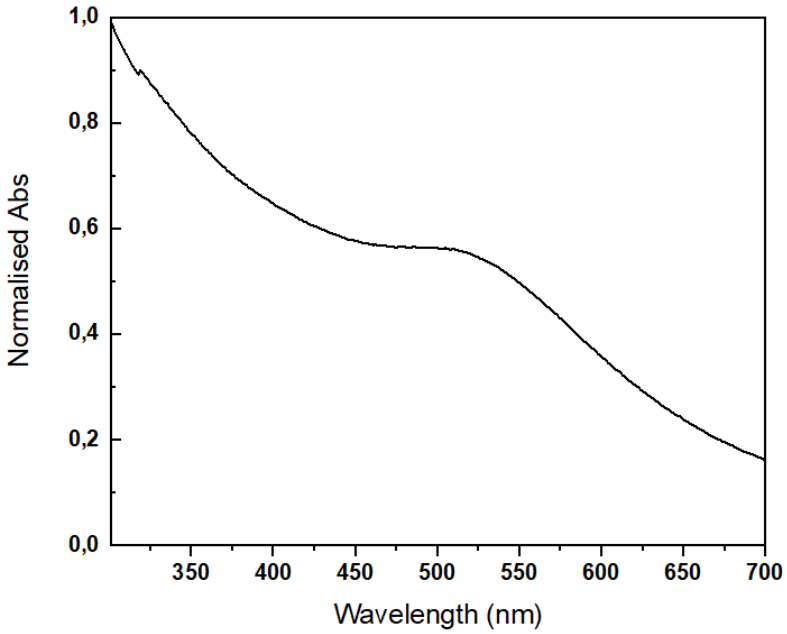

Figure 3.9. UV-vis spectrum of usNP C12N in milliQ water ([AuNPs] 0.1 mg/mL).

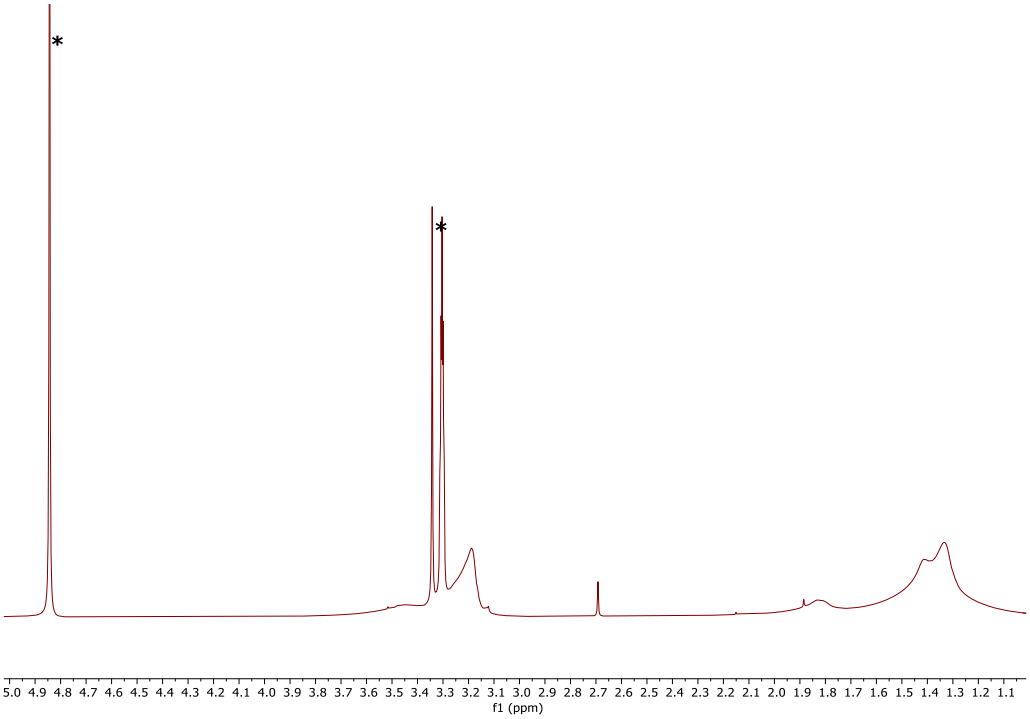

Figure 3.10. ^{1}H NMR (400 MHz, CD_3OD) of usNP C16N. The solvent peaks are indicated by an asterisk (methanol, water).

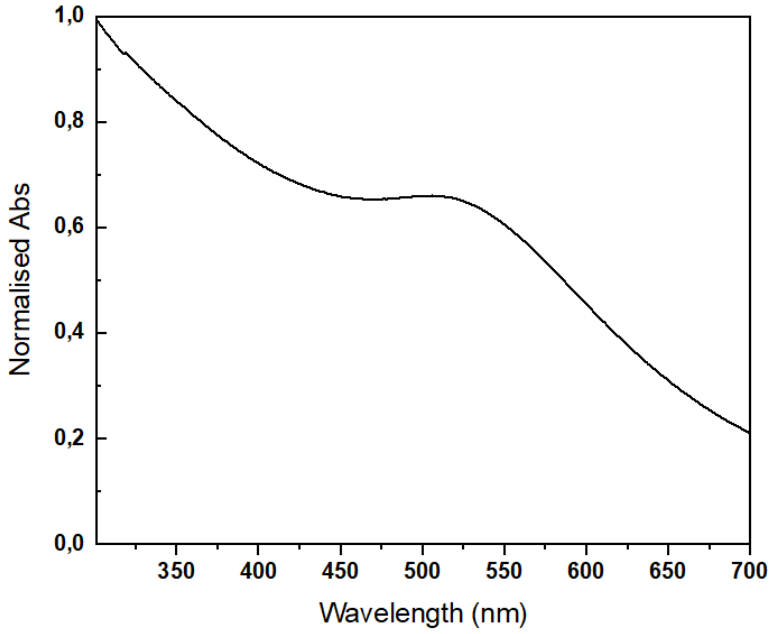

Figure 3.11. UV-vis spectrum of usNP C16N in milliQ water ([AuNPs] 0.1 mg/mL).

3.1.3 usNP C12N and usNP C16N: characterization

Detailed size analysis of these ultrasmall homoligand AuNPs could be achieved by TEM; Figure 3.12 displays a representative TEM image of usNP C12N, with the corresponding size distribution that allows to calculate an average core size of 1.9 ± 0.6 nm considering a set of 654 AuNPs. Regarding usNP C16N, the pertinent TEM image and size distribution are shown in Figure 3.13. In this case, the core diameter was determined to be 2.1 ± 0.7 nm considering a set of 1886 AuNPs.

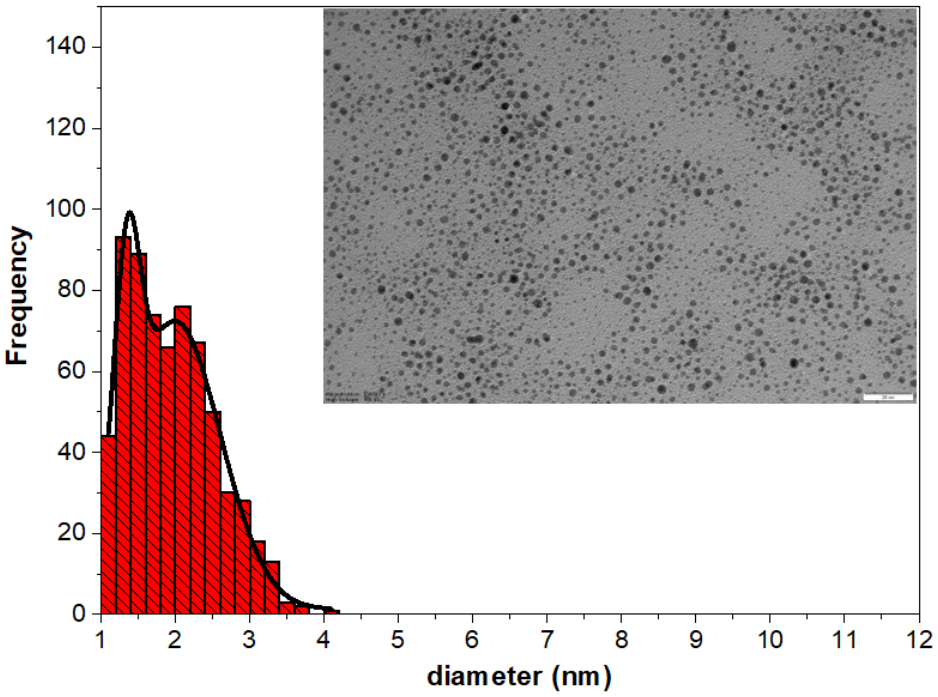

Figure 3.12. TEM and size distribution of usNP C12N. Scale bar 20 nm.

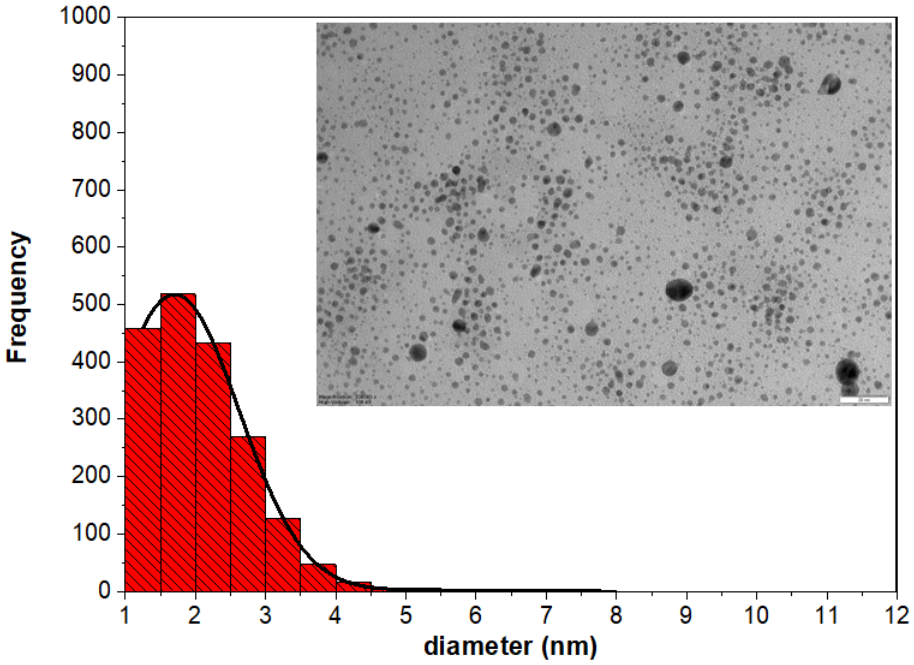

Figure 3.13. TEM and size distribution of usNP C16N. Scale bar 20 nm.

Moreover, TGA analyses are performed to quantify the percentage of organic coating present on the AuNPs surfaces. For both batches of AuNPs the TGA curve and its derivate are reported in Figure 3.14 and Figure 3.15, labelled in black and red respectively.

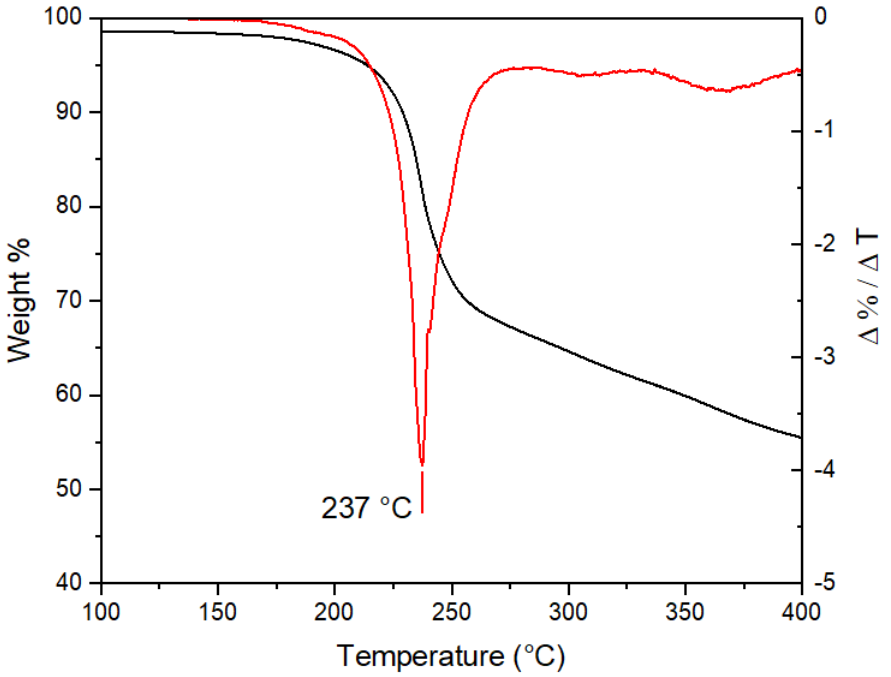

Figure 3.14. TGA curves of usNP C12N.

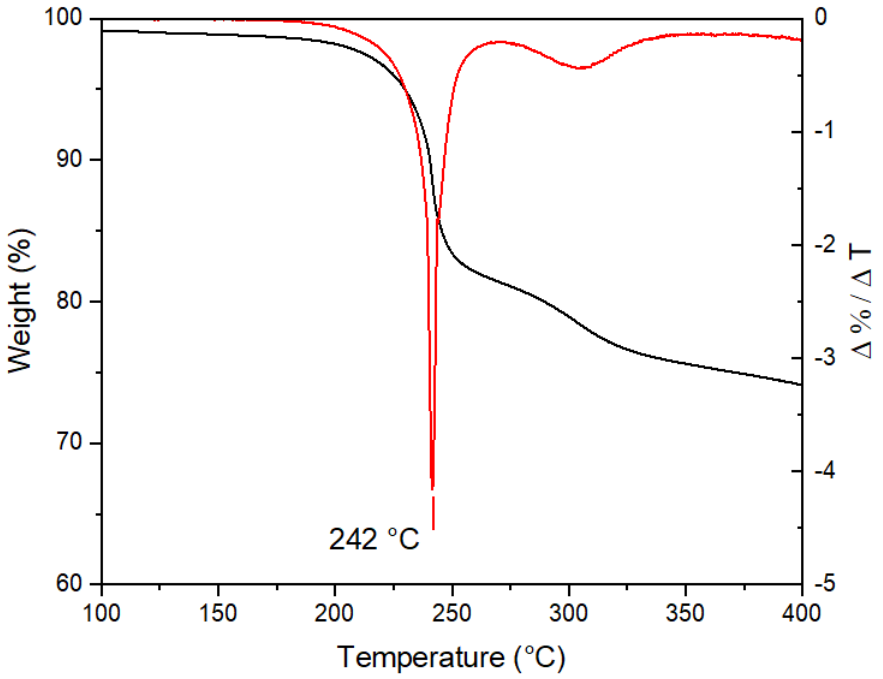

Figure 3.15. TGA curves of usNP C16N.

To assess the composition of the organic coating and the inorganic core of these AuNPs, I mainly relied on two studies. Precisely, I have chosen to exploit the math formulas described in the work of Hühn *et al.*[11] and the results of Murray and co-workers[12] to find the mathematical relationship between the number of Au atoms and the core diameter of a single AuNP.

For a spherical AuNP with a certain inorganic core mass (m_c) and volume (V_c), the number of Au atoms ($N_{Au\ atoms}$) present in the core have been calculated using the formula:

$$N_{Au\ atoms} = N_A \times n_{AuNP} \quad (1)$$

where N_A is the Avogadro number, and n_{Au} is the moles of Au present in one AuNP that can be expressed by the ratio between m_c and the Au atomic weight ($m_{a\ Au}$). Thus, the eq. 1 can be expressed as follows:

$$N_{Au\ atoms} = N_A \times \frac{m_c}{m_{a\ Au}} = N_A \times \frac{\rho \times V_c}{m_{a\ Au}} = (N_A \times \rho \times \frac{\pi}{6} \times \frac{1}{m_{a\ Au}}) \times d^3 = D \times d^3 \quad (2)$$

where d is the AuNP diameter and ρ is the Au density (19.3 g/cm^3). At the end, a cubic dependence of Au atoms on the diameter could obtained, in which the term D contains all constant terms. To test the validity of this approach, the number of Au atoms determined by Murray and co-workers were fitted to eq. 2 (Figure 3.16).

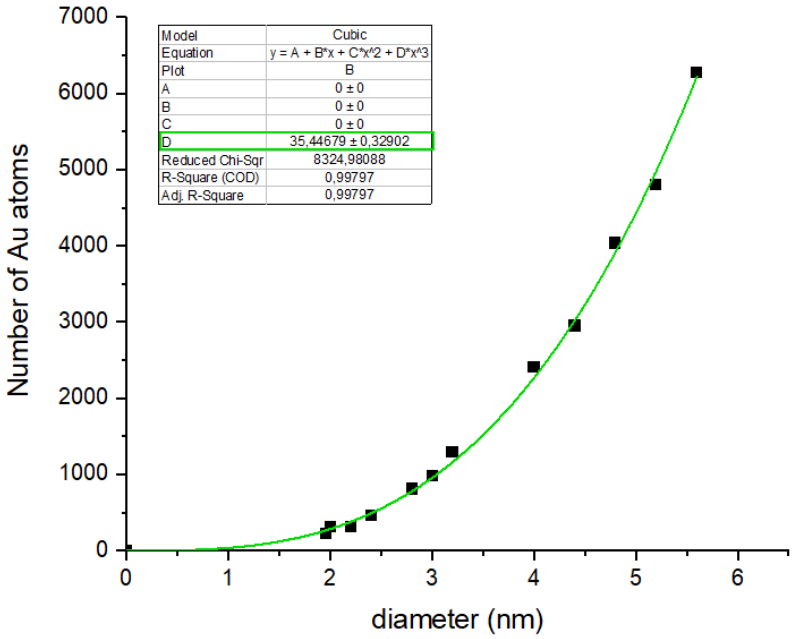

Figure 3.16. Plot of the number of Au atoms according to the AuNP diameters reported by Hostetler, M. J. *Langmuir* **1998**, *14* (1), 17–30.

For the data fit a cubic polynomial with the coefficients of the diameter powers of order zero to two set to zero. The model prediction is in good agreement with the experimental reference data reported by Murray and co-workers. This approach was used to calculate the number of gold atoms of the whole set of nanoparticles using the D coefficient (Table 3.1). The number of Au atoms was calculated disregarding the uncertainty on the AuNPs diameter.

Table 3.1 Core composition for the ultrasmall homoligand AuNPs.

	d(nm)	$N_{Au\ atoms\ for\ AuNP}$
usNP C12N	1.9 ± 0.6	263
usNP C16N	2.1 ± 0.7	324

By combining the TGA data and the nanoparticles size determined by TEM, it was possible to determine the composition of the nanoparticles, Table 3.2.

Table 3.2. Composition of the ultrasmall homoligand AuNPs

	Diameter (nm)	**TGA (% organic)**	**Composition**
usNP C12N	1.9 ± 0.6	32.0	$Au_{262}L_{80}$
usNP C16N	2.1 ± 0.7	26.0	$Au_{323}L_{70}$

Concerning the usNP C16N, the smaller ligand numbers than the usNP C12N could explained by the different spatial distribution of the endgroups. In detail, the ligand density of an AuNP monolayer derives from the compromise of two factors: (i) the chain packing and (ii) the free available volume per ligand. For ultrasmall AuNPs, the great curvature radius provides a large free volume available per ligand which can influenced the chain packing order of the AuNP monolayer. Indeed, an increase in the available free volume corresponds to a greater spatial distribution of the end groups which can lead to a decrease in the chain order and ligand density (Figure 3.17).[13]

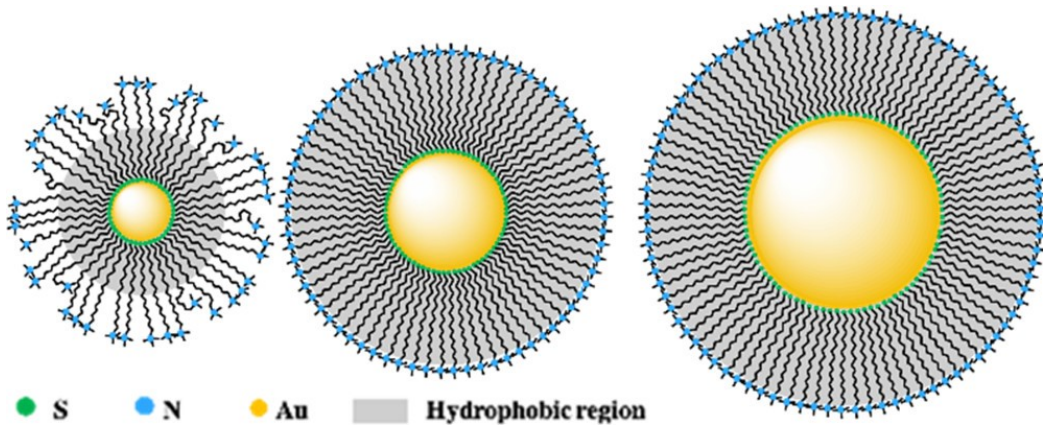

Figure 3.17. Ligand packing as a function of the AuNP size. From Wu, M. et al. *J. Am. Chem. Soc.* **2019**, *141* (10), 4316–4327.

Thus, for the same AuNP size, the greater the length of the chain, the greater the mobility of the endgroups, resulting in a lower ligand density.

Alongside the determination of the nanoparticle size and composition, the AuNPs were further characterised for their colloidal stability in solution. This characterization was performed by assessing the nanoparticles ζ-potential. When a particle is dispersed into a liquid, the groups present on its surface interact with the surrounding medium and may interact with other neutral or charged species in the solvent. In the case of charged AuNPs, this process results in the partial accumulation of counterions on the AuNP surface. Around the outer surface of charged AuNPs two layers of ions can be formed (Figure 3.18). The stern layer is the closest layer to the AuNPs surface, and it is composed of ions strongly bound, while the diffuse layer is the furthest layer to the AuNP surface formed by loosely bound ions. The boundary between the diffuse layer and the surrounding medium is called slipping plane.

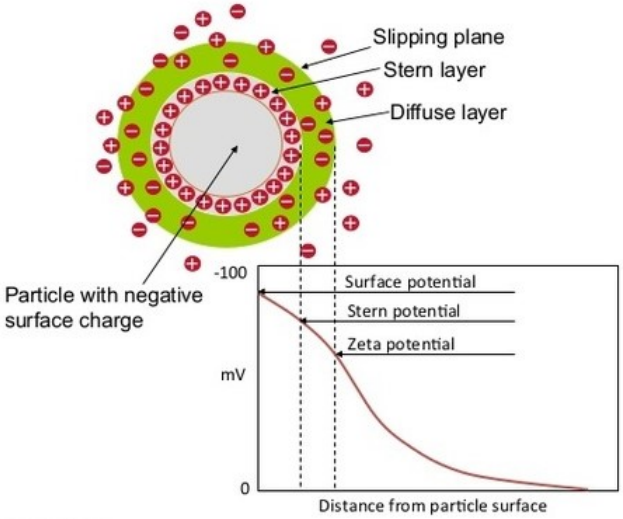

Figure 3.18. Schematic representation of zeta potential.

The ζ-potential is defined as the potential present at the slipping plane, and its magnitude determines the potential colloidal stability of the dispersed AuNPs. Indeed, small magnitudes of the ζ-potential are an indication of a possible tendency to aggregation of AuNPs because of the lack of strong repulsive inter-particles electrostatic forces. Both cationic homoligand AuNPs, displayed ζ-potentials that are compatible with colloidally moderate-stable systems.[14,15] In addition to ζ-potential analyses, the hydrodynamic diameters of the nanoparticles were also determined at the same concentration The corresponding results are collectively summarise in the Table 3.3.

Table 3.3. ζ-potential observed for the ultrasmall homoligand cationic AuNPs in aqueous medium

	[AuNPs] in mg/mL	ζ-potential in mV	Hydrodynamic diameter (nm)
usNP C12N	0.025	+24.5	6.3 ± 1.6
usNP C16N	0.025	+ 23.2	9.0 ± 2.5

3.1.4. usNP C12N and usNP C16N: IR emission characterization

Due to their ultrasmall size, these nanoparticles can display luminescence in the visible or near infrared region. This property is typical of small nanoparticles and discrete thiolate protected clusters that possess a rigid gold-sulfur interface. The rigidity in mainly due to the structural frameworks that are ultimately responsible for keeping together the gold core of the particles and the ligands comprised in the monolayer. Indeed, the ligand shell of the particles, especially in small ones is a complex structure in which the thiolate ligands and gold adatoms are bound together in motifs called staples of general formula $Au_n(SR)_{n+1}$. The terminal thiolates of the staples are those that directly bind to the gold core, and the gold adatoms in the staple interact with core gold atoms by aurophilic interactions. The structural characterization of a variety of atomically precise (*i.e.* strictly monodispersed) thiolate protected gold clusters has allowed to pinpoint that as the sizes of nanoclusters decreases, longer and more rigid $Au_n(SR)_{n+1}$ staple motif appears. Conversely for larger clusters simpler and less rigid $Au(SR)_2$ staples dominates alongside with bridging motifs of structure –RS– directly connected to two gold atoms in the core, the latter being extremely rare in smaller clusters.[16,17] This rigid interface is likely responsible of the suppression of nonradiative pathways leading to thermal reactivation of the excited states formed upon light absorption. The nature of the excited states that leading to photoluminescence in debated and strongly depends on the species under consideration, but consensus exists on the localization of these excited states at the level of the gold sulfur interface. From a general point of view, the emission of Au(I)-thiolate units arises from the ligand-to-metal charge transfer (LMCT) and the ligand-to-metal–metal charge transfer (LMMC) on the AuNCs surface, due to Au(I)-S bonds and aurophilic Au(I)-Au(I) interactions.[18–20] To analyse and evaluate this potential luminescence properties of usNP C12N and usNP C16N, several luminescence experiments were carried out in collaboration with the group of Prof. Montalti. These analyses comprised emission experiments performed by irradiation of an ultrasmall nanoparticle solution at 520 nm, using a cut-off filter at 580 nm. For both homoligand AuNPs an emission in the NIR region

has been observed however, this was much more pronounced in the case of usNP C12N with features two bands at around 900 and 1100 nm, while for the usNP C16N the emission was much smaller. The emission data for usNP C12N and usNP C16N are reported in Figure 3.19a and Figure 3.19b respectively.

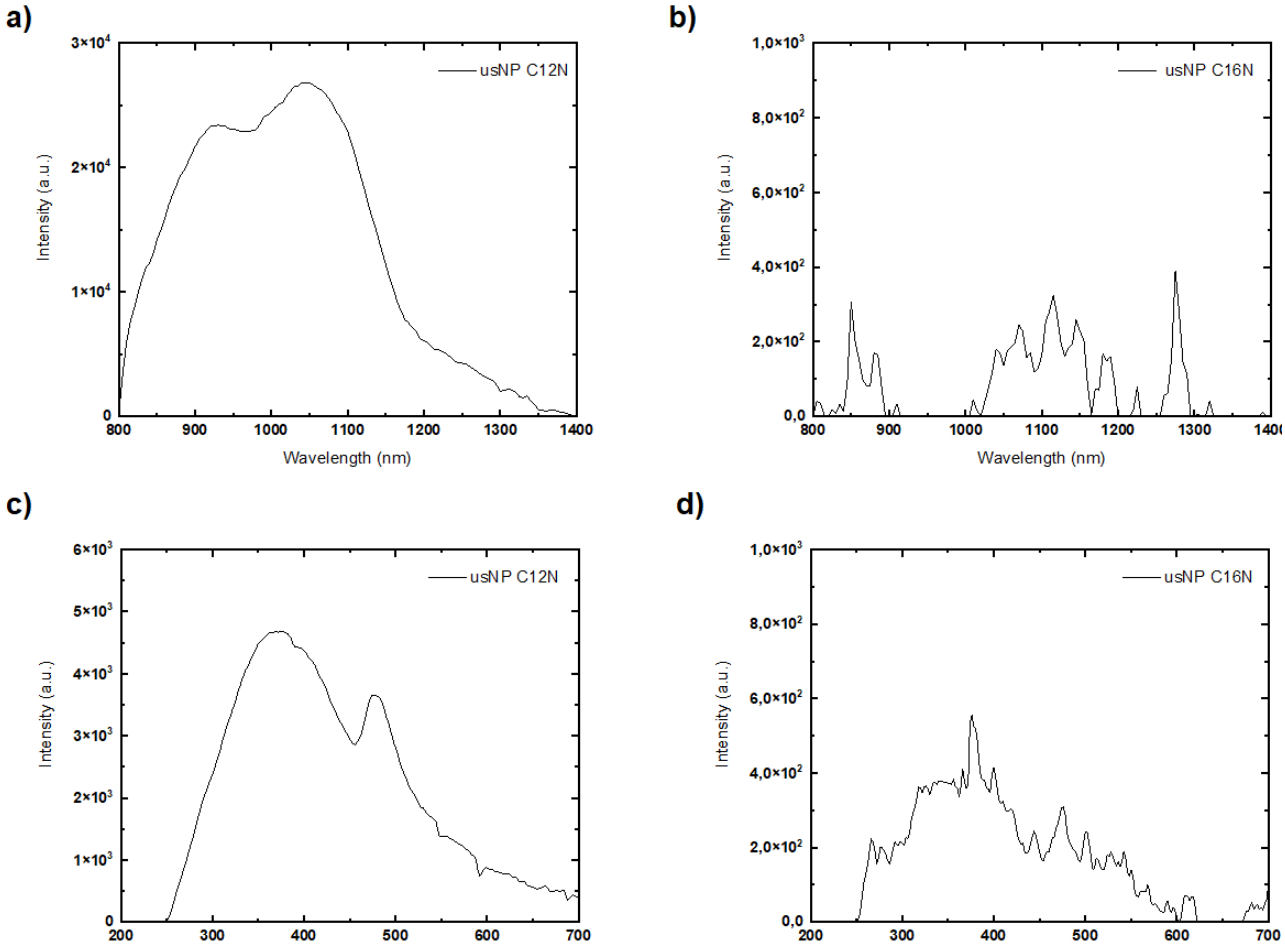

Figure 3.19. Emission (**a**, **b**) and excitation (**c**, **d**) spectra of both ultrasmall homoligand AuNPs (λ_{ex} 520 nm; λ_{em} 1100 nm). The analyses have carried out in PBS at [AuNPs] of 0.025 mg/mL.

As showed, usNP C12N have a much higher emission intensity compared to the usNP C16N. This behaviour could be due to the argument mentioned in Chapter 1, i.e., the proximity of positive charges to the gold core can enhance the AuNPs fluorescence, due to the charge transfer from the Au core to the cations that increase the energy gap between the binding levels of the Au atoms. Moreover, usNP C12N result to be more stable in PBS solution than usNP C16N. Despite the intensity difference of the emission spectra, the quantum yields for both systems were calculated, recording the respective absorption spectra. By combining the data obtained from the emission and excitation spectra (Figure 3.19c, Figure 3.19d), the quantum yield was calculated using the following formula:

$$\phi = \phi_r \frac{I}{I_r}\frac{A_r}{A}\frac{n^2}{n_r^2} \quad (3)$$

where ϕ is the quantum yield, I the integrated area of emission spectrum, A the absorbance at the excitation wavelength, and n is the refractive index of the solvent. The subscript r indicates the values taken from the reference standard used to calculate the quantum yield (Figure 3.20).[21]

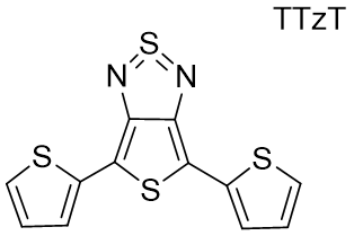

Figure 3.20. Standard (r) used is 4,6-di(thiophen-2-yl)thieno [3.4-c][1.2.5]thiadiazole (TTzT) with QY (DMSO) 2%.

The quantum yields of usNP C12N and usNP C16N have been calculated both in aqueous and in PBS medium. The corresponding results are reported in Table 3.4.

Table 3.4. Quantum yields calculated for both usNP C12N and usNP C16N in aqueous and PBS solution.

	ϕ
usNP C12N in aqueous solution	0.07%
usNP C12N in PBS solution	0.02%
usNP C16N in aqueous solution	0.0008%
usNP C16N in PBS solution	0.0004%

As expected, usNP C12N have the highest quantum yield. However, in both cases, the presence of PBS leads to a decrease in quantum yield, this is not unexpected because the luminescence properties of gold nanoparticles and thiolate protected gold clusters are known to be sensitive to the medium. Nevertheless, the quantum yield of these species is extremely low even considering that typically NIR-emitting thiolate-protected gold clusters, show low QY (<1%) in conventional solvents and ambient environments.[22]

3.1.5 NP C12N and NP C16N: synthesis and NMR and UV-vis analysis

The synthesis of cationic homoligand nanoparticles of diameter smaller than about 6 nm was performed using a protocol based on the Brust-Schiffrin method with some modifications.[23] Briefly, two separated phases are prepared; the organic phase containing TOAB dissolved in chloroform, and the aqueous phase where hydrogen tetrachloroaurate (III) is dissolved in MilliQ water. The two phases were mixed and stirred vigorously to transfer the gold (III) into the organic phase by TOAB. this process is evidenced by the color change of the organic phase from colorless to red-orange, indicating the formation of tetraoctylammonium-gold pairs. After discarding the aqueous solution, at the organic phase a solution of $NaBH_4$ freshly prepared is added in a few seconds. Upon vigorous stirring, the color changed from red-orange to red-violet, indicating the nucleation of gold clusters. Next, the aqueous phase is discarded and a solution of charged thiol in methanol was added to the organic phase. A vigorous stirring is maintained for a couple of hours to allow the complete passivation of the nanoparticles. Once the synthesis was completed, the reaction mixture is dried under reduced pressure to proceed with the purification of the charged AuNPs. The developed procedure consists of five cycles of precipitation and centrifugation. The AuNPs are first dissolved in a few ml of methanol and then precipitated by the addition of diethyl ether. This procedure drastically reduces the synthesis time compared to that used for ultrasmall AuNPs, but in the absence of stabilizers such as dioctylamine, aggregates are formed during the reduction step. However, the amount of thiol used to passivate AuNPs in this procedure is less than that required in the dioctylamine-based protocol, and its addition is carried out after $NaBH_4$ treatment.

Therefore, this procedure is very useful if the thiol is not compatible with the reduction conditions, or/and is very onerous both in terms of cost and time dedicated to its synthesis.

At the end, the AuNPs were collected and the absence of unbound ligands and other reagents was assessed by ^{1}H-NMR analysis. Once the purity of the AuNPs solution was confirmed, I proceeded with the characterization of both nanoparticles systems. Figure 3.21 and Figure 3.22 display the ^{1}H-NMR and UV-vis spectra of NP C12N. Contrary to the previous AuNPs, these nanoparticles show a pronounced LSPR band centered at about 530 nm. Regarding NP C16N, the relative ^{1}H-NMR and UV-vis spectra are shown in Figure 3.23 and Figure 3.24.

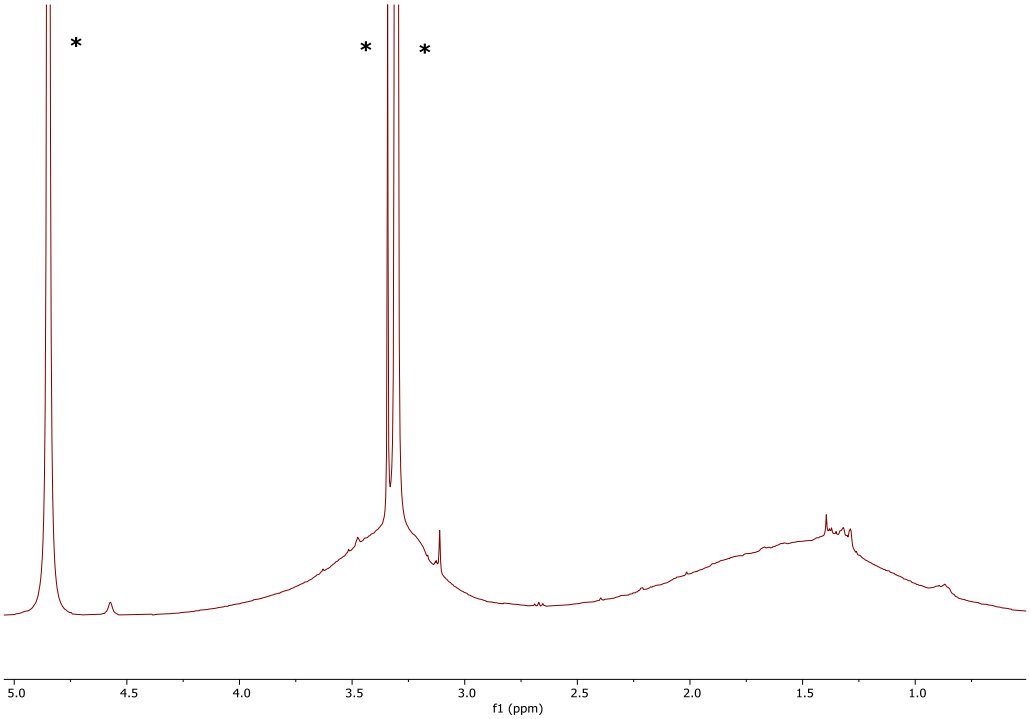

Figure 3.21. ^{1}H NMR (400 MHz, CD_3OD) of NP C12N. The solvent peaks are indicated by an asterisk (methanol, water).

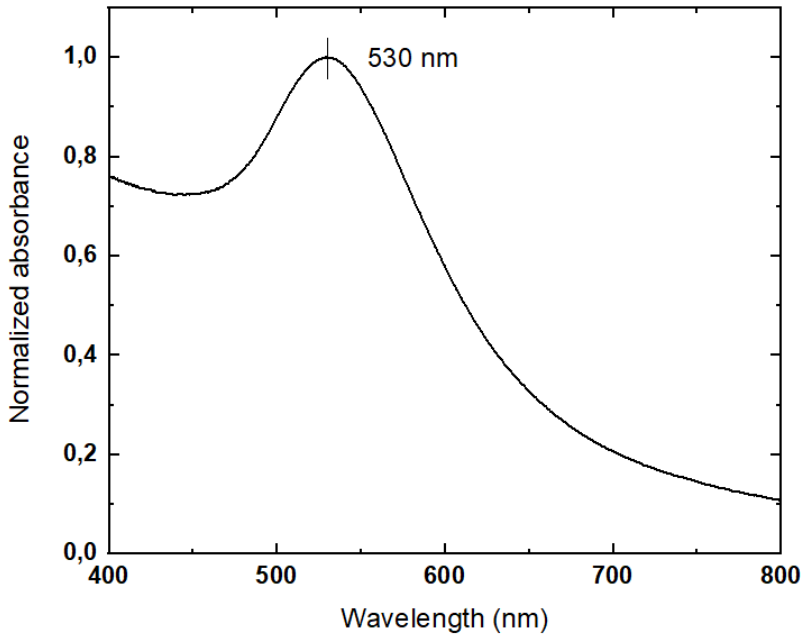

Figure 3.22. UV-vis spectrum of NP C12N in milliQ water ([AuNPs] 0.1 mg/mL).

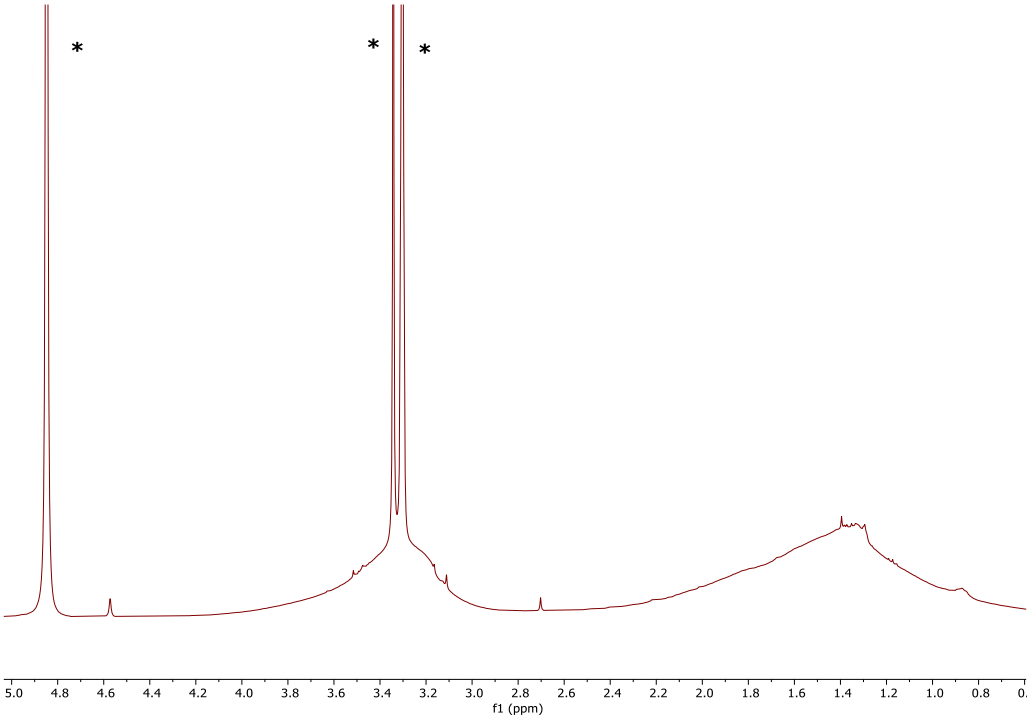

Figure 3.23. ^{1}H NMR (400 MHz, CD_3OD) of NP C16N. The solvent peaks are indicated by an asterisk (methanol, water).

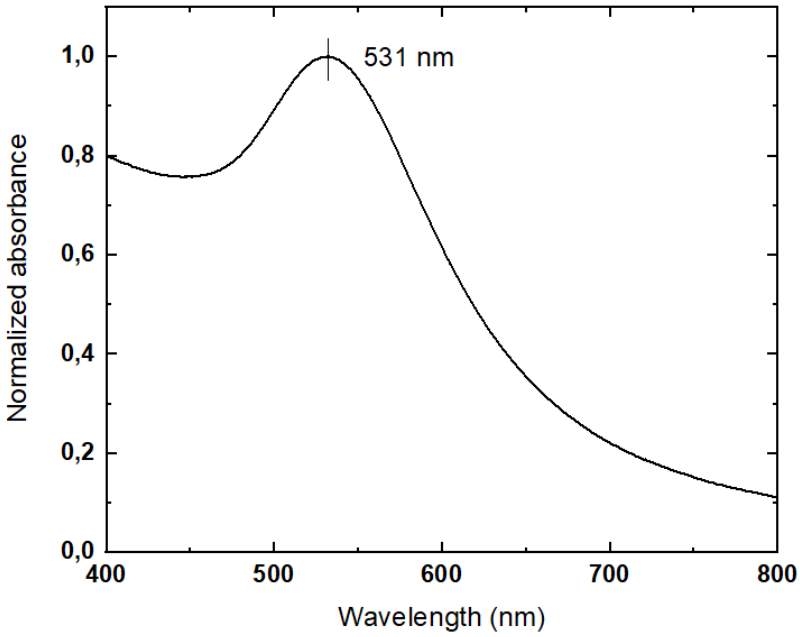

Figure 3.24. UV-vis spectrum of NP C16N in milliQ water ([AuNPs] 0.1 mg/mL).

3.1.6 NP C12N and NP C16N: characterization

The analysis of the small homoligand AuNPs size was performed by TEM analyses. In Figure 3.25 the size distribution and a representative TEM image of NP C12N are reported, and the related diameter was found to be 4.7 ± 1.3 nm considering a set of 1487 AuNPs. The same analysis was applied to NP C16N, and the pertinent TEM image and size distribution are shown in Figure 3.26. In this case, the core diameter could be calculated as 5.6 ± 1.6 nm considering a set of 960 nanoparticles.

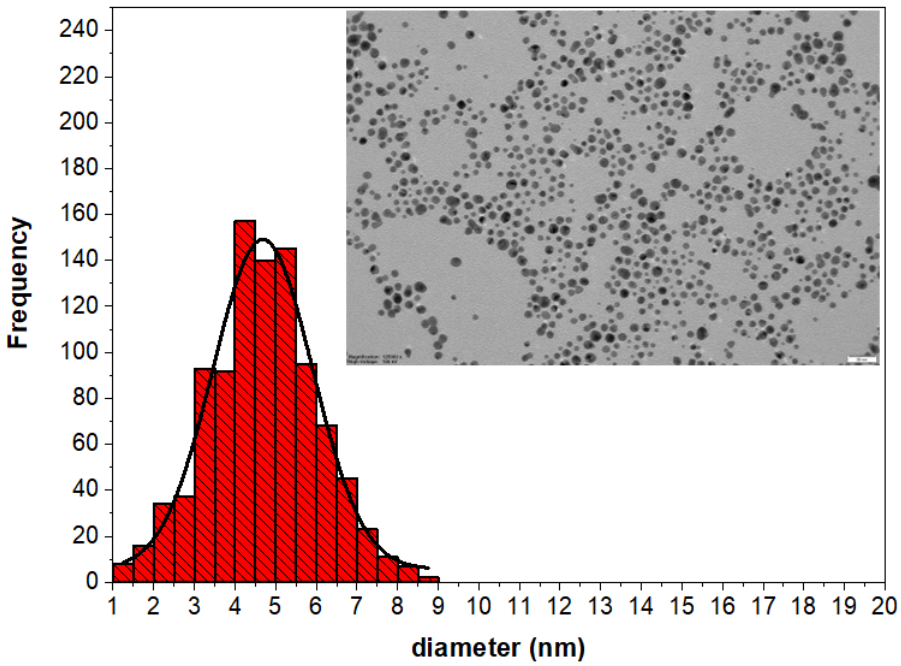

Figure 3.25. TEM and size distribution of NP C12N. Scale bar 50 nm.

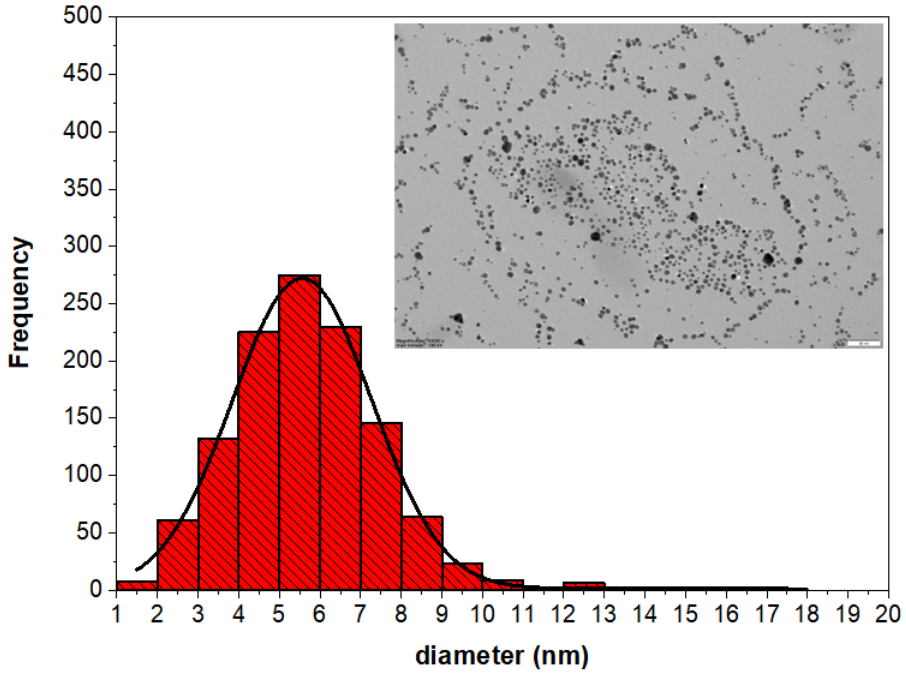

Figure 3.26. TEM and size distribution of NP C16N. Scale bar 50 nm.

After determination of the average size of the nanoparticles core, the systems were characterised by thermogravimetric analyses to assess the percentage of organic material in each nanoparticle preparation. In Figure 3.27 and Figure 3.28 are reported the TGA curve and its derivative for NP C12N and NP C16N respectively.

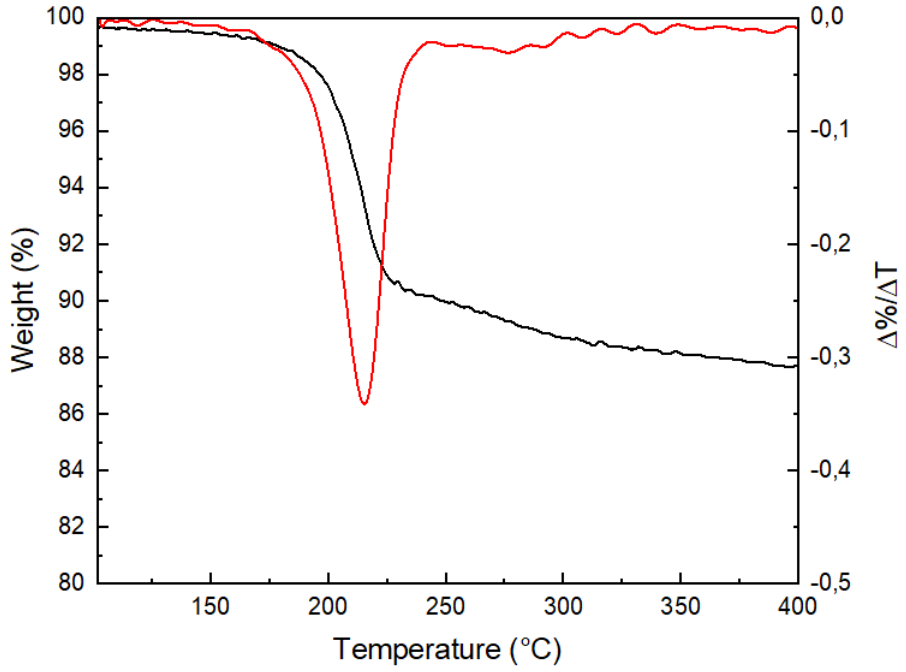

Figure 3.27. TGA curves of NP C12N.

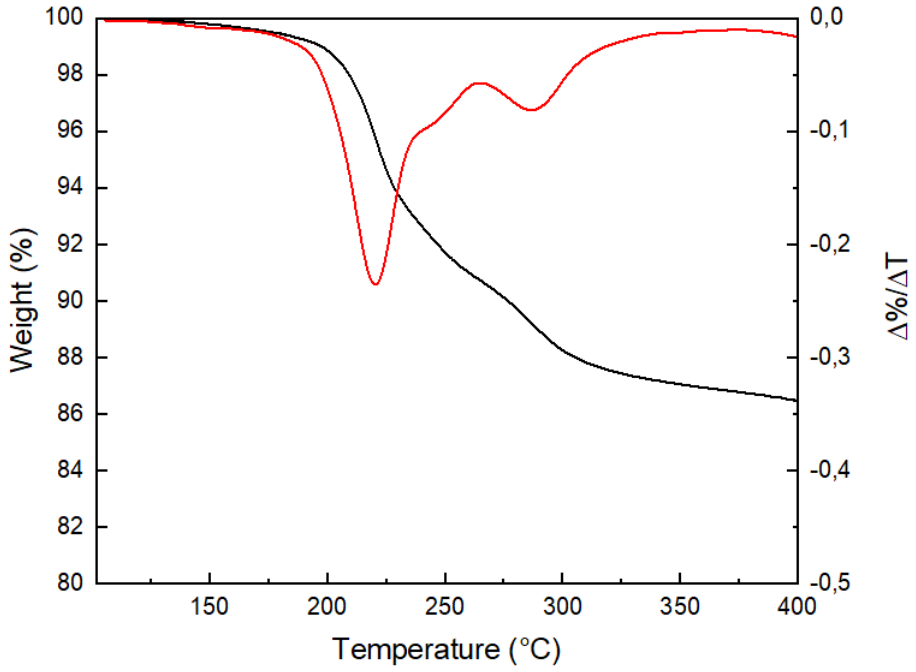

Figure 3.28. TGA curves of NP C16N.

As for the ultrasmall AuNPs, the composition of the inorganic core of NP C12N and NP C16N have been calculated by using the D coefficient calculated from eq. 2. By combining these data and the mass loss determined by TGA the composition of the nanoparticles could be determined, Table 3.5.

Table 3.5. Composition of NP C12N and NP C16N.

	Diameter (nm)	TGA (% organic)	Composition
NP C12N	4.7 ± 1.3	14	$Au_{3680}L_{346}$
NP C16N	5.6 ± 1.7	14.5	$Au_{6180}L_{558}$

Once the dimension and the monolayer composition have been analysed in detail, I have evaluated the stability of these nanosystems in aqueous solutions by ζ-potential measurements and DLS analysis to calculate the hydrodynamic diameter. The corresponding results are shown in the Table 3.6.

Table 3.6. ζ-potential observed for the small homoligand cationic AuNPs in aqueous medium.

	[AuNPs] in mg/mL	ζ-potential in mV	Hydrodynamic diameter (nm)
NP C12N	0.025	+ 45.5	8.8 ± 2.1
NP C16N	0.025	+ 33.2	9.4 ± 2.5

3.2 Synthesis and characterization of cationic heteroligand AuNPs

As mentioned before, **HF6** is chosen as fluorinated component for the preparation of *H*-/*F*-mixed monolayer AuNPs. Regarding the formation of well-separated domains on the AuNP monolayer, fluorinated ligands are known for their lipophobic nature, and so in combination with hydrogenated ligands this feature can be exploited to induce phase separation in 3D SAMs. In this contest, the studies carried out by the Prof. Pasquato group and collaborators have confirmed regardless of the nature and length of the hydrogenated ligand, ligand **HF6** separates in small domains.[24–26] In the last work of Posocco and Pasquato groups, the hydration of different AuNPs coated by mixtures of ligands bearing different hydrophobicities (Figure 3.29) has been investigated in depth.[27]

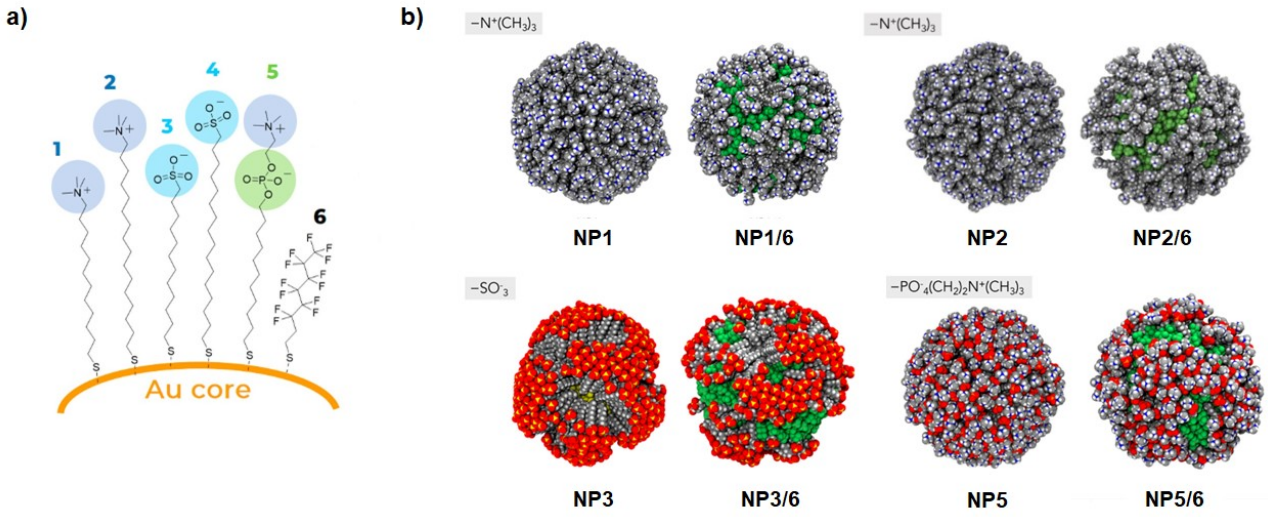

Figure 3.29. Ligand structures (**a**) chosen to coat the AuNPs, in which **HF6** (6) is used for the preparation of mixed monolayers. The differences in the hydrogenated ligand structures consist of the nature and charge of the end group, and length of the alkyl chain. The corresponding molecular structures of homoligand (NP1, NP3, NP5) and heteroligand (NP1/6, NP3/6, NP5/6) AuNPs are obtained by molecular dynamics simulations (**b**). Adapted from Gabellini, C. et al. *ACS Nano* **2022**, *16* (12), 20902–20914.

In particular, they have reported the water molecules distribution at increasing distances from the inorganic core by AA-MD simulations (atomistic all-atom molecular dynamics), underlining a substantial difference between homoligand and heteroligand AuNPs. Indeed, the former show a uniform diffusion of the water molecules within the organic monolayer, which corresponds to a gradual decrease in the content of water molecules as the distance from the core decreases. On the contrary, the heteroligand AuNPs show a high hydration already at short distances from the inorganic

core. In Figure 3.30 the water density of AuNP monolayers contained C12N and C16N as hydrogenated ligands is reported.

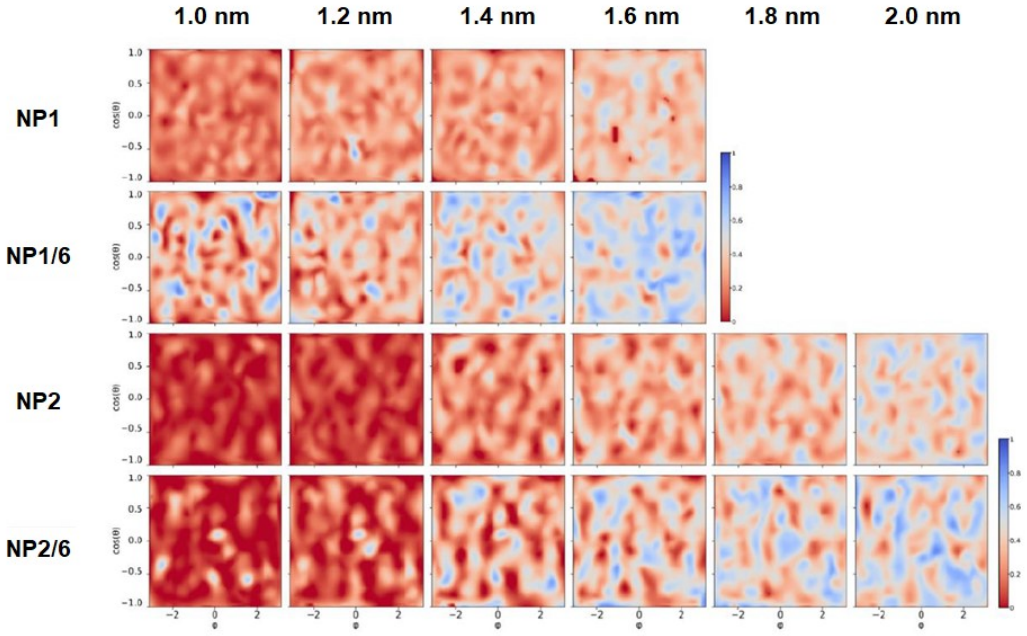

Figure 3.30. Normalized water distribution at increasing distance from the gold surface for homoligand (**NP1** and **NP2**) and the corresponding heteroligand (**NPI/6** and **NP2/6**). The adopted colour code indicated in red to salmon the poorly hydrated areas, and in blue the highly hydrated areas (at a certain distance from the gold surface). Adapted from Gabellini, C. et al. *ACS Nano* **2022**, *16* (12), 20902–20914.

This difference is explained by the fact that the alkyl chain of **HF6** is considerably shorter than that of the related hydrogenated ligands. Thus, the corresponding domains permit the diffusion of water molecules at closer distances to the core, with respect to homoligand AuNPs at the same distance from the gold surface. Other important observations derived from the hydration analyses are first that both homoligand and heteroligand AuNPs with zwitterionic thiolates as hydrogenated components (NP5 and NP5/6) showed a very low water distribution within the monolayer. An explanation of these results is the formation of an expanded ligand/water hydrogen-bond network on the nanoparticle surface. Contrary, as mentioned before the presence of a small and charged end-group provides an anisotropic monolayer organization due to the alkyl chain-bundle formation. So, the AuNPs in which the ligands 3 and 4 are used as hydrogenated components (NP3, NP3/6, NP4, NP4/6) showed different-hydrated areas already close to the core, in which regions with hydration comparable to that of bulk solvent (areas between the chain-bundles) are alternated to dehydrated areas (Figure 3.31).

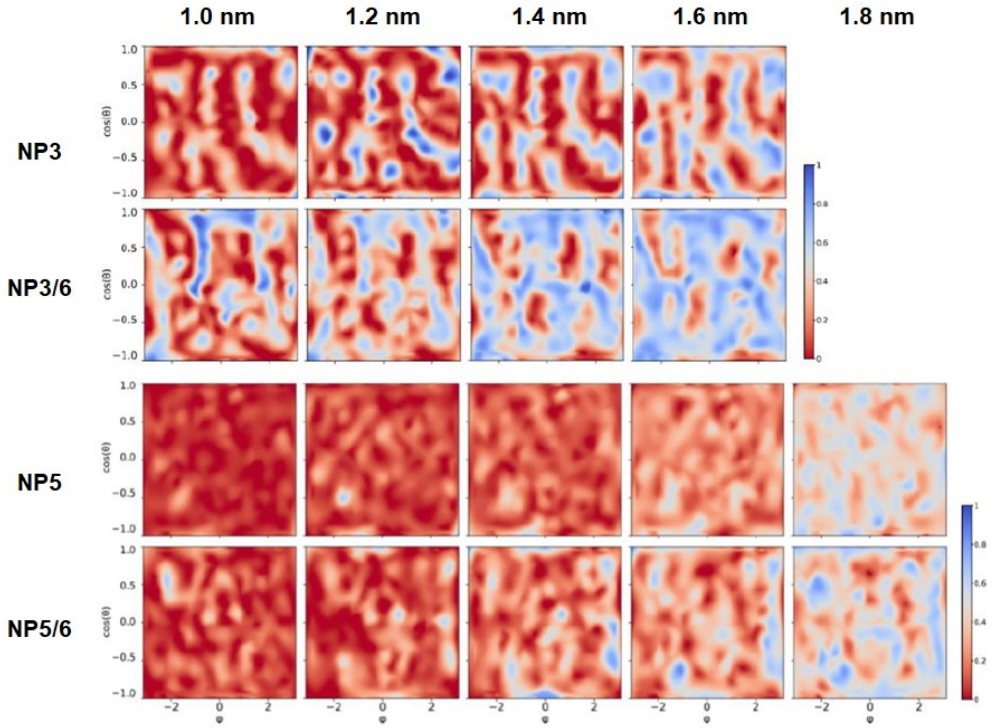

Figure 3.31. Normalized water distribution at increasing distance from the gold surface for homoligand (**NP3** and **NP5**) and heteroligand (**NP3/6** and **NP5/6**). Adapted from Gabellini, C. et al. *ACS Nano* **2022**, *16* (12), 20902–20914.

From these results, it can be deduced that the choice of using mixtures composed of C12N/F6 and C16N/F6 allows to obtain mixed monolayers with a good solvent-accessible surface area, in addition to a radial organization of the ligands as previously described. On the other hand, these mixtures avoid excessive exposure of the inorganic core to the external environment, as occurs in the case of mixtures in which the charged hydrogenated ligand has a small terminal group.

3.2.1 Small heteroligand AuNPs: synthesis and NMR and UV-vis analysis

The synthetic procedure for the preparation of the *H-/F*-mixed nanoparticles of ~ 5 nm is the same used for the corresponding homoligand AuNPs. The crucial difference lies in the passivation step of the nanoparticles. For heteroligand AuNPs, a solution containing both the hydrogenated and the fluorinated thiol in a specific ratio was added to the weakly passivated nanoparticles. Different mixtures for each pair of ligands (**HC12N/HF6** and **HC16N/HF6,** Table 3.7), were considered changing the *H/F* ratio to find which of them provided water-soluble nanoparticles.

Table 3.7. Mixture of H/F ligands used for the NP C12NF6 and NP C16NF6

NP C12NF6		
	***H/F*- synthesis ratio**	**Water solubility**
Run 1	5 : 1	yes
Run 2	3 : 1	yes
NP C16NF6		
	***H/F*- synthesis ratio**	**Water solubility**
Run 3	3 : 1	yes
Run 4	2 : 1	yes
Run 5	1.5 : 1	slightly
Run 6	1 : 1	slightly

Not unexpectedly, only in the cases in which an excess of the hydrogenated ligand was used respect to the fluorinated component, mixed monolayer nanoparticles with good solubility in water could be obtained. The ^{1}H-NMR, ^{19}F-NMR and UV-vis spectra of the nanoparticles coated by respectively C12N/F6 (NP C12NF6, *runs 1-2*), and C16N/F6 (NP C16NF6, *runs 3-4*) are showed below in Figures 3.32-3.43.

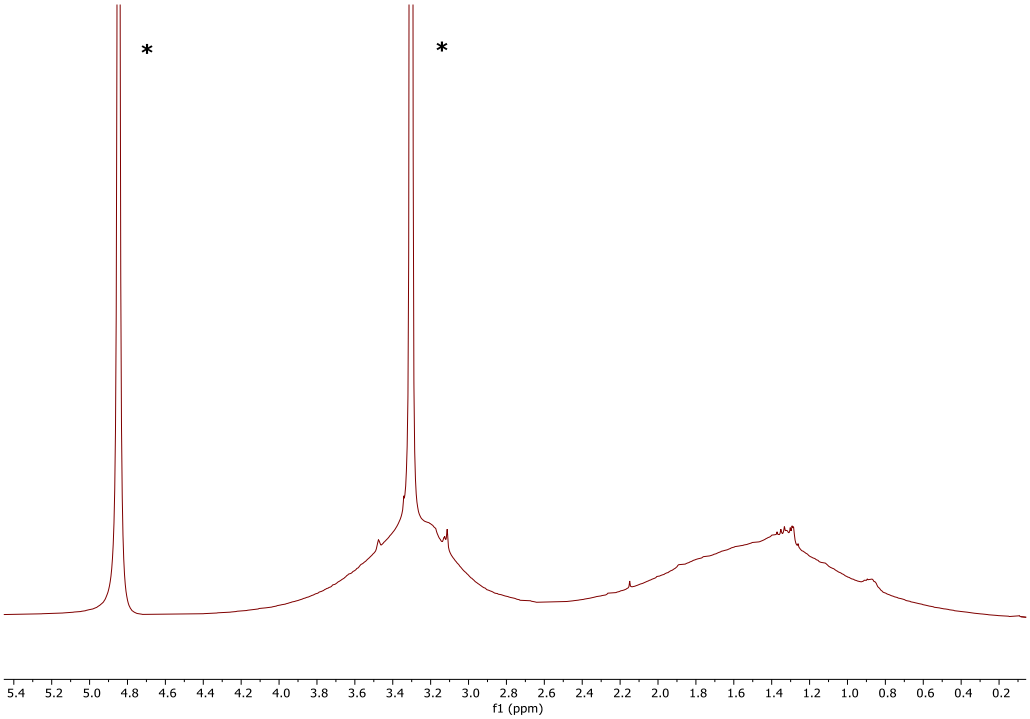

Figure 3.32. ^{1}H-NMR (400 MHz, CD_3OD) of NP C12NF6 (run 1). The solvent peaks are indicated by an asterisk (methanol, water).

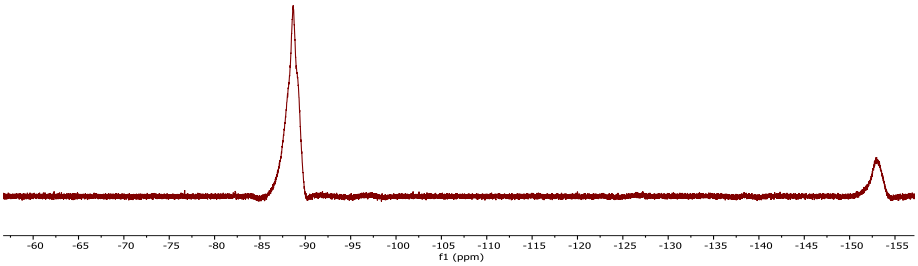

Figure 3.33. ^{19}F-NMR (376 MHz, CD_3OD) of NP C12NF6 (run 1).

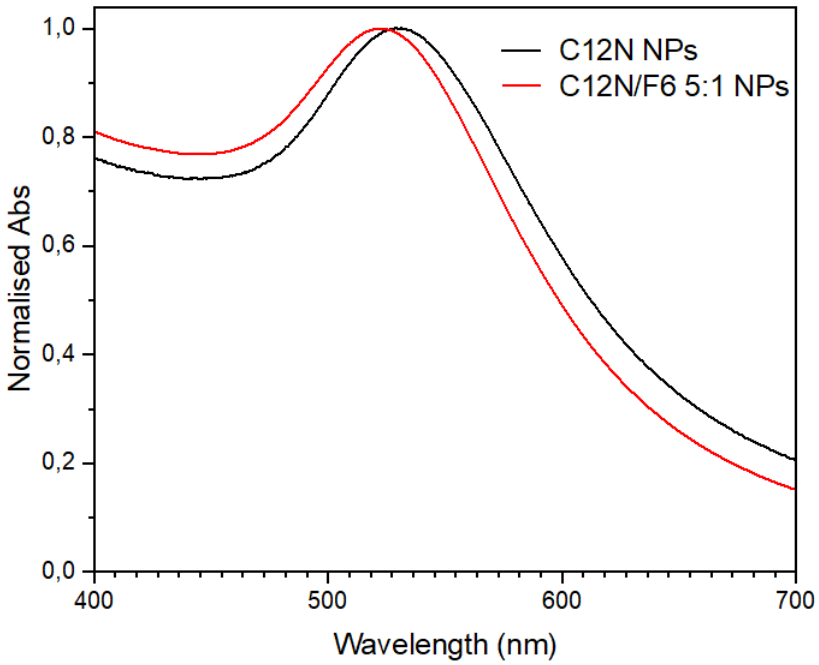

Figure 3.34. Comparison between NP C12N and NP C12NF6 (run 1) in milliQ water ([AuNPs] 0.1 mg/mL).

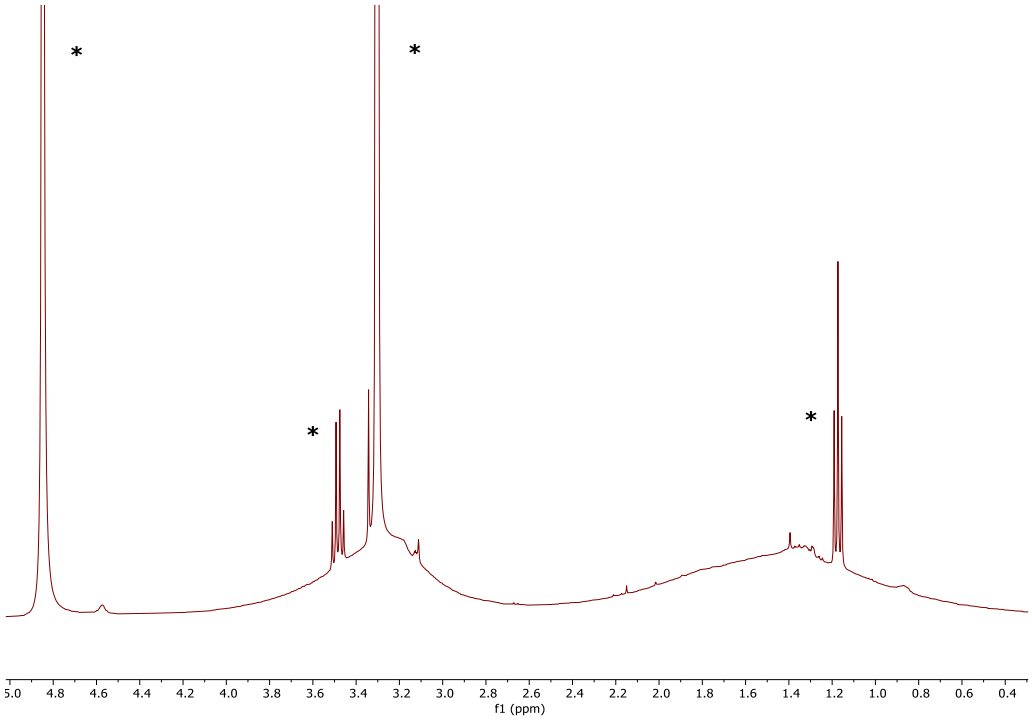

Figure 3.35. ^{1}H NMR (400 MHz, CD_3OD) of NP C12NF6 (run 2). The solvent peaks are indicated by an asterisk (diethyl ether, methanol, water).

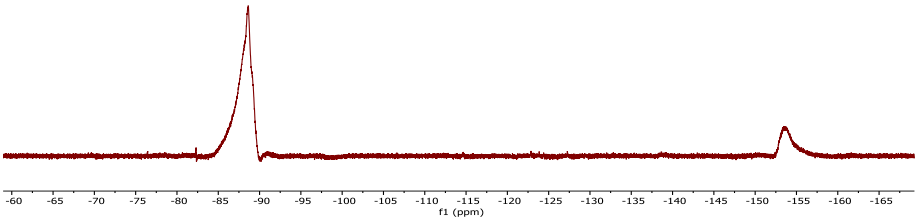

Figure 3.36. ^{19}F-NMR (376 MHz, CD_3OD) of NP C12NF6 (run 2).

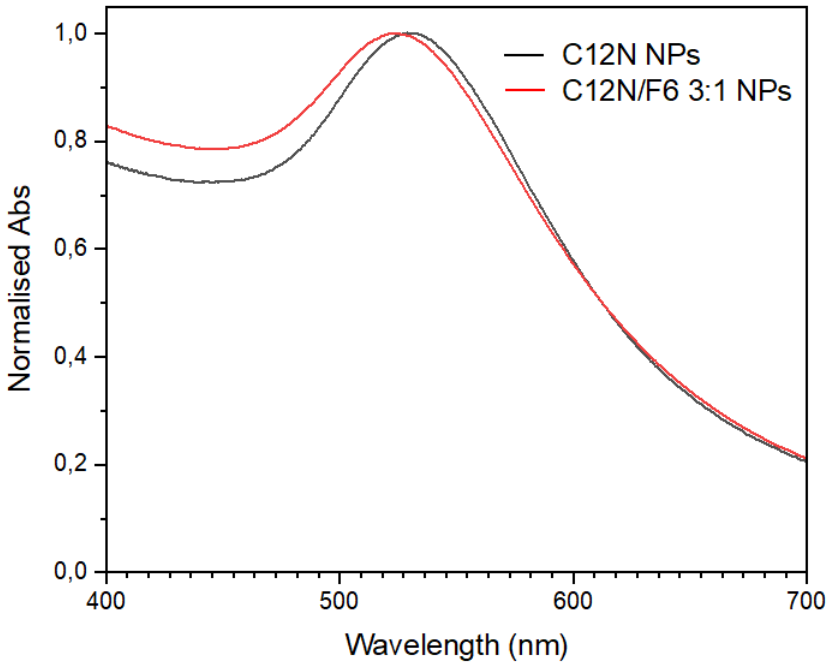

Figure 3.37. Comparison between NPC12N and NP C12NF6 (run 2) in milliQ water ([AuNPs] 0.1 mg/mL).

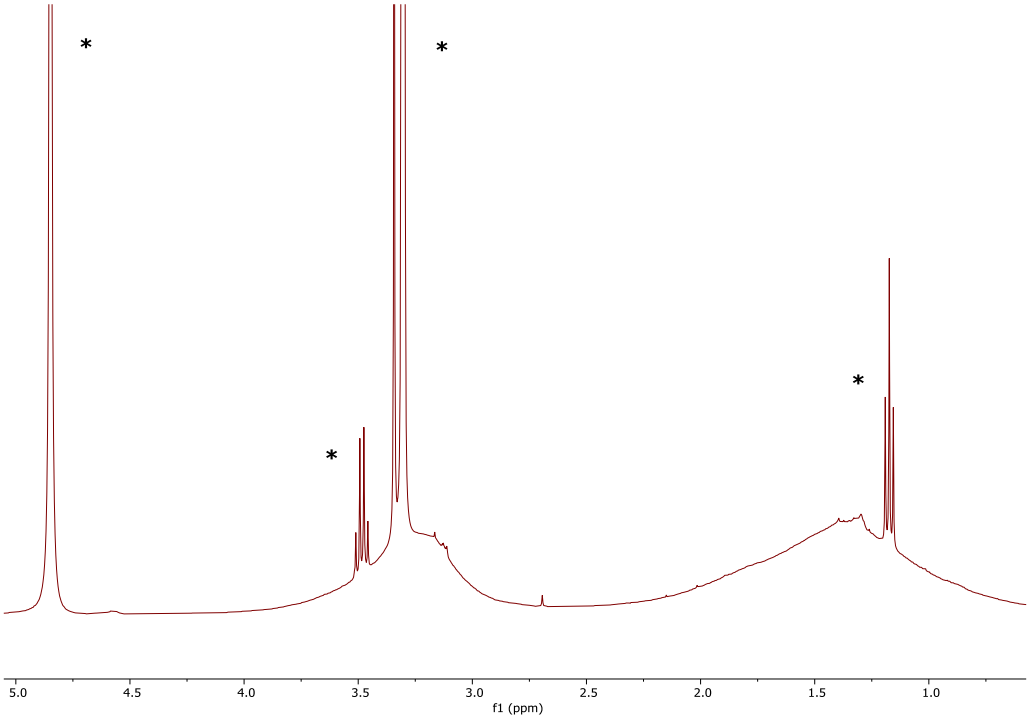

Figure 3.38. ^{1}H NMR (400 MHz, CD_3OD) of NP C16NF6 (run 3). The solvent peaks are indicated by an asterisk (diethyl ether, methanol, water).

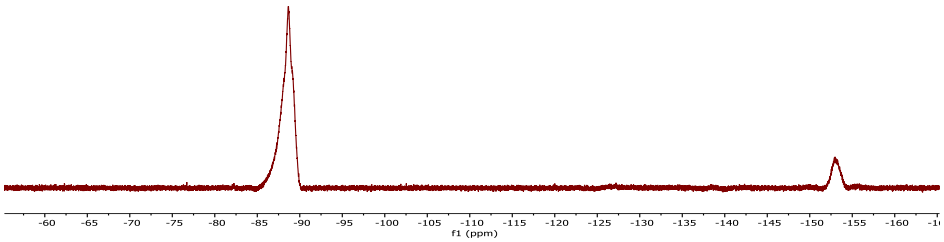

Figure 3.39. ^{19}F-NMR (376 MHz, CD_3OD) of NP C16NF6 (run 3).

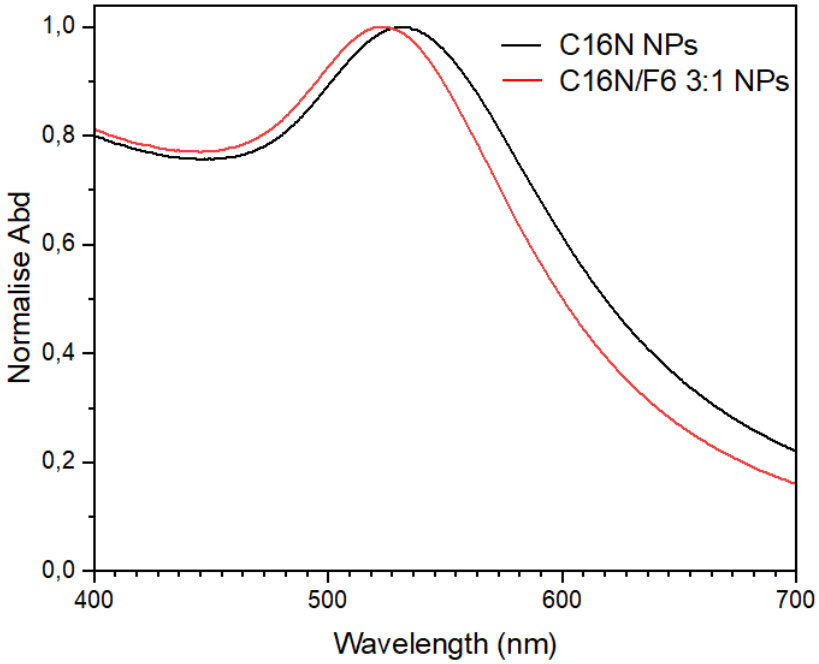

Figure 3.40. Comparison between NP C16N and NP C16NF6 (run 3) in milliQ water ([AuNPs] 0.1 mg/mL).

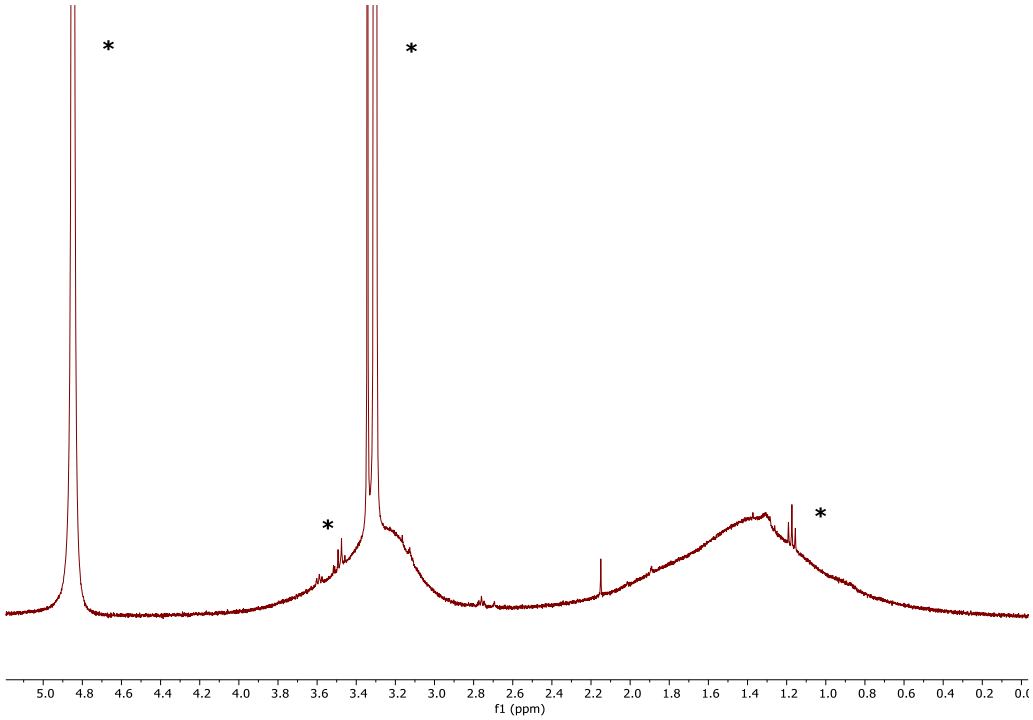

Figure 3.41. ^{1}H NMR (400 MHz, CD_3OD) of NP C16NF6 (run 4). The residual solvent peaks are indicated by an asterisk (diethyl ether, methanol, water).

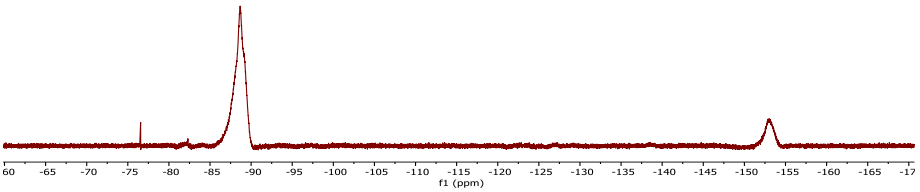

Figure 3.42. ^{19}F-NMR (376 MHz, CD_3OD) of NP C16NF6 (run 4).

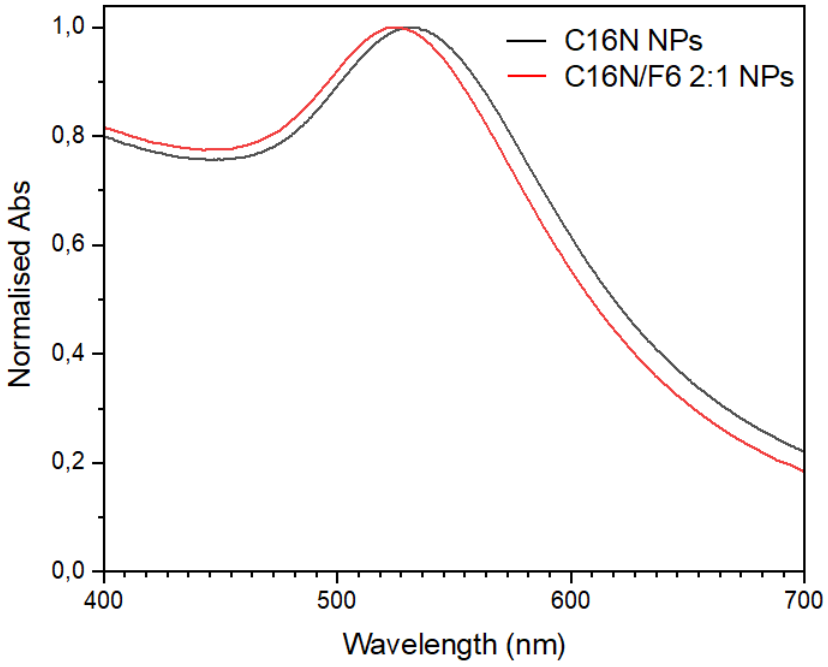

Figure 3.43. Comparison between NP C16N and NP C16NF6 (run 4) in milliQ water ([AuNPs] 0.1 mg/mL).

3.2.2 NP C12NF6 and NP C16NF6: characterization

The detailed size analysis of the small heteroligand AuNPs was performed by TEM. Representative TEM images of the mixed monolayer nanoparticles and the corresponding size distribution histogram for each sample are reported below. The average core size for NP C12NF6 (runs 1-2) is respectively 4.1 ± 0.9 (Figure 3.44) and 5.2 ± 1.2 (Figure 3.45) considering a set of 581 and 1000 AuNPs. While

for NP C16NF6 (runs 3 and 4), the calculated average core size is respectively 4.3 ± 1.1 (Figure 3.46) and 4.0 ± 1.3 (Figure 3.47) considering a set of 1701 and 971 AuNPs.

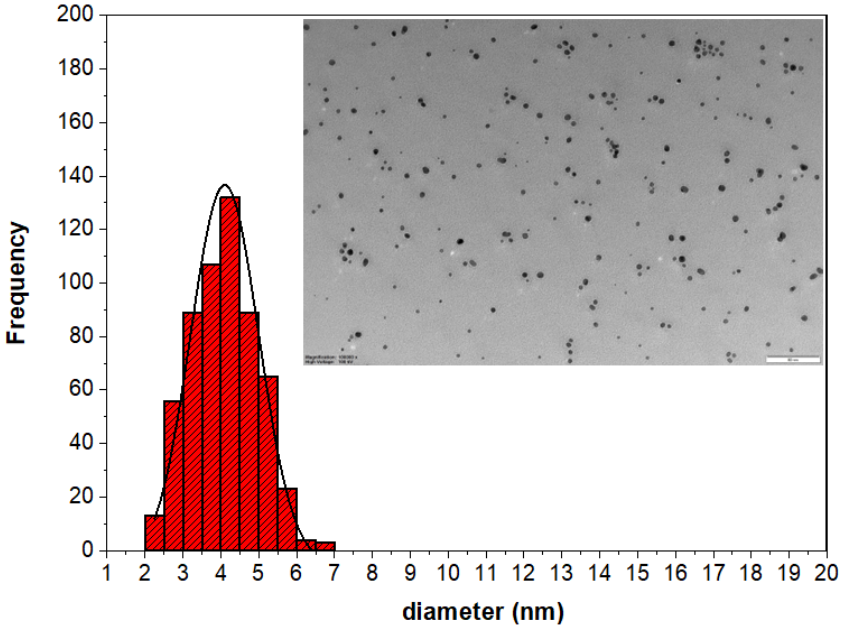

Figure 3.44. TEM and size distribution of NP C12NF6 (run 1). Scale bar 50 nm.

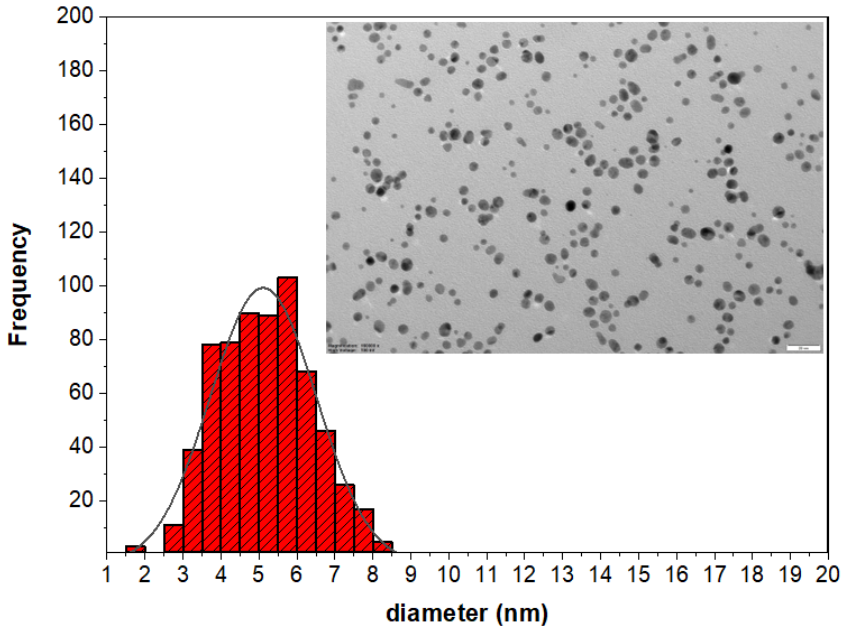

Figure 3.45. TEM and size distribution of NP C12NF6 (run 2). Scale bar 20 nm.

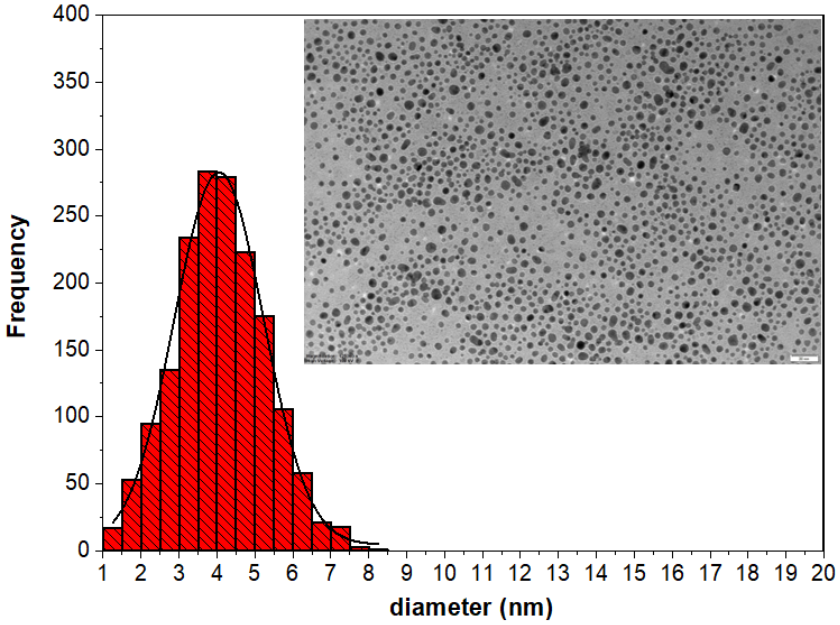

Figure 3.46. TEM and size distribution of NP C16NF6 (run 3). Scale bar 20 nm.

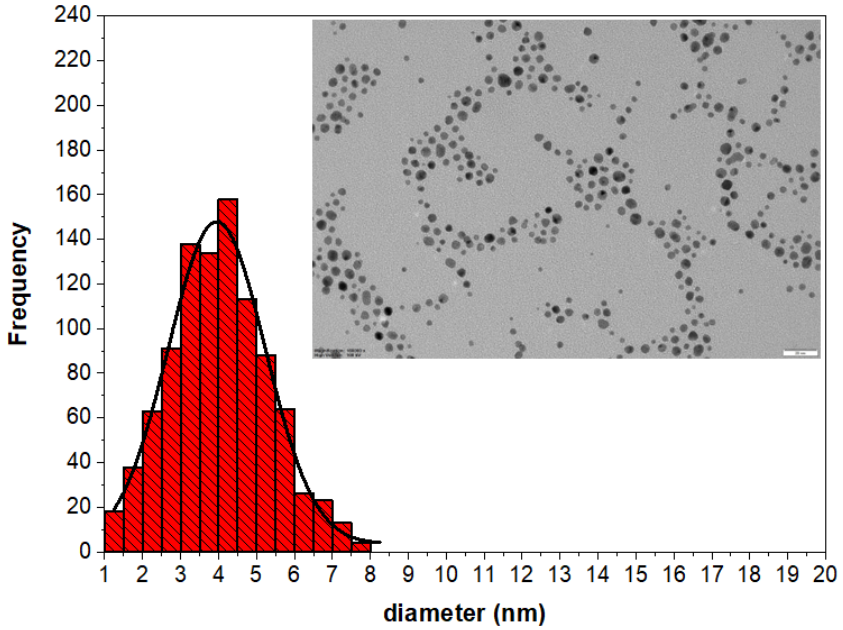

Figure 3.47. TEM and size distribution of NP C16NF6 (run 4). Scale bar 20 nm

Once the size of the inorganic core was determined, I continued the AuNP characterization by analysing the composition of both the monolayer and the inorganic core by TGA analysis. Unlike the homoligand AuNPs, the characterization of mixed monolayer nanoparticles requires the assessment of the ligand ratio within the monolayer. This is necessary because, in general, when a mixture of thiols is used for the nanoparticle passivation, the composition of the monolayer may be different from the one used for the synthesis. To gain this information it is necessary to combine the results of

TGA analyses with those obtained from the decomposition of the nanoparticles monolayer by iodine treatment. By the addition of an excess of iodine to a small amount of the heteroligand AuNPs, the thiolates are smoothly and efficiently oxidized to disulphides, resulting in the decomposing of the organic coating and formation of a disulfides mixture that can be analysed by NMR spectroscopy. This approach requires first to calculate the *H/F*- ratio from the ^{1}H-NMR spectrum of the disulfide solution, this information combined with the weight loss determined by TGA slows to calculate the number of chains of each ligand present in the nanoparticle monolayer. Prior to these analyses, it was necessary to ascertain what ^{1}H-NMR signals could be used for determining the ligand ratio in the disulfide mixture. To this end, a series of standard solution of the fluorinated and hydrogenated thiols used for the nanoparticle preparations were oxidised by addition of I_2 and the resulting mixture of disulfides was analysed by ^{1}H-NMR (Figure 3.48); the combination of 1D and 2D experiments allowed the assignment of the resonance for the homogenous and mixed disulfides formed. The chemical shifts of the peaks related to the obtainable disulfide species are reported below (Table 3.8).

Table 3.8. Chemical shifts of the signals pertaining to the protons in alpha position to the sulfur atoms of each disulfide species.

***F*- ligand**		
		Chemical shift (δ)
Disulfide	F-CH_2-CH_2-S-S-CH_2-CH_2-F	3.0 – 2.98 ppm
Mixed disulfide	H-CH_2-CH_2-S-**S-CH_2-CH_2-F**	2.92 – 2.86 ppm
H- ligand		
		Chemical shift (δ)
Mixed disulfide	F-CH_2-CH_2-S-**S-CH_2-CH_2-H**	2.76 – 2.72 ppm
Disulfide	H-CH_2-CH_2-S-S-CH_2-CH_2-H	2.70 – 2.64 ppm

With this information, the integration of the signals obtained for the I_2 induced decomposition of the nanoparticles could be used to determine the ratio of the *H*- and *F*- species bound to the nanoparticle surface. The spectra of the monolayer decomposition of each batch of heteroligand AuNPs are reported below in Figures 3.49-3.52.

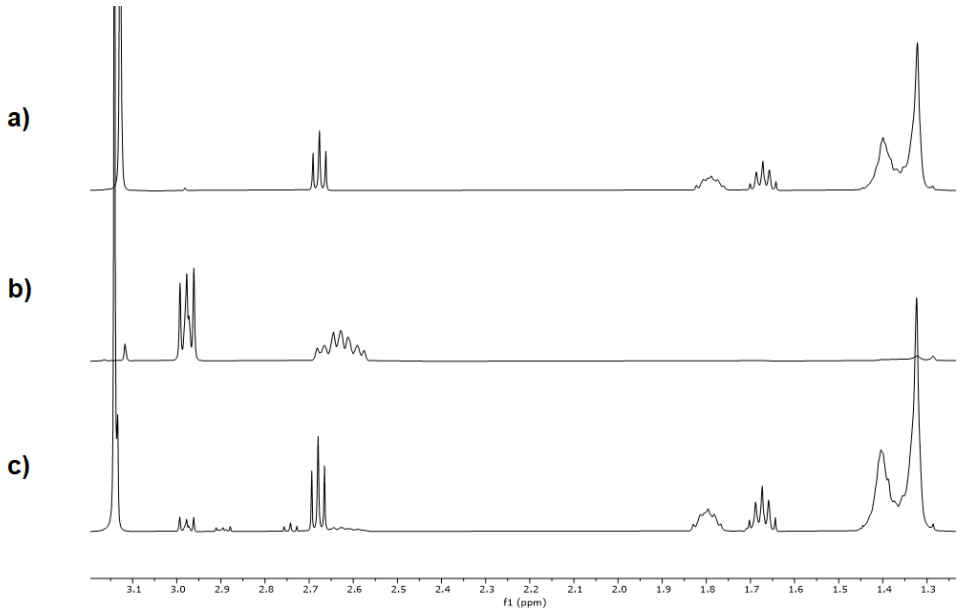

Figure 3.48. ^{1}H-NMR spectra (400 MHz, CD_3OD) of the oxidized H-ligand (**a**), the oxidated F-ligand (**b**) and the mixture of oxidated H/F- ligands.

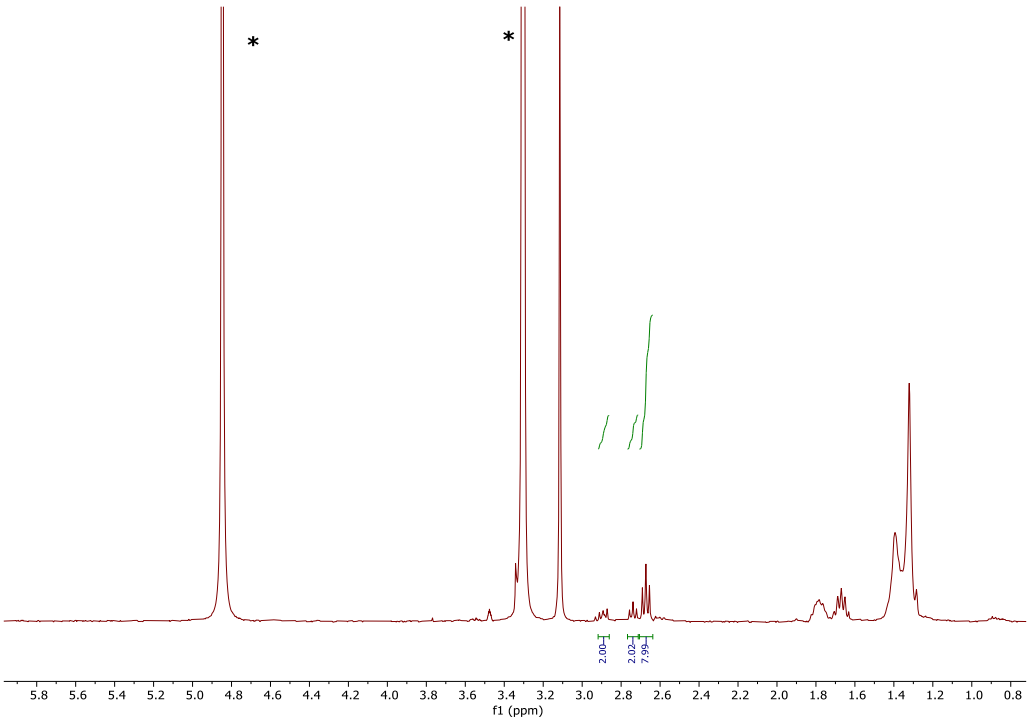

Figure 3.49. ^{1}H-NMR spectrum (400 MHz, CD_3OD) of the decomposition mixture of NP C12NF6 (run 1).

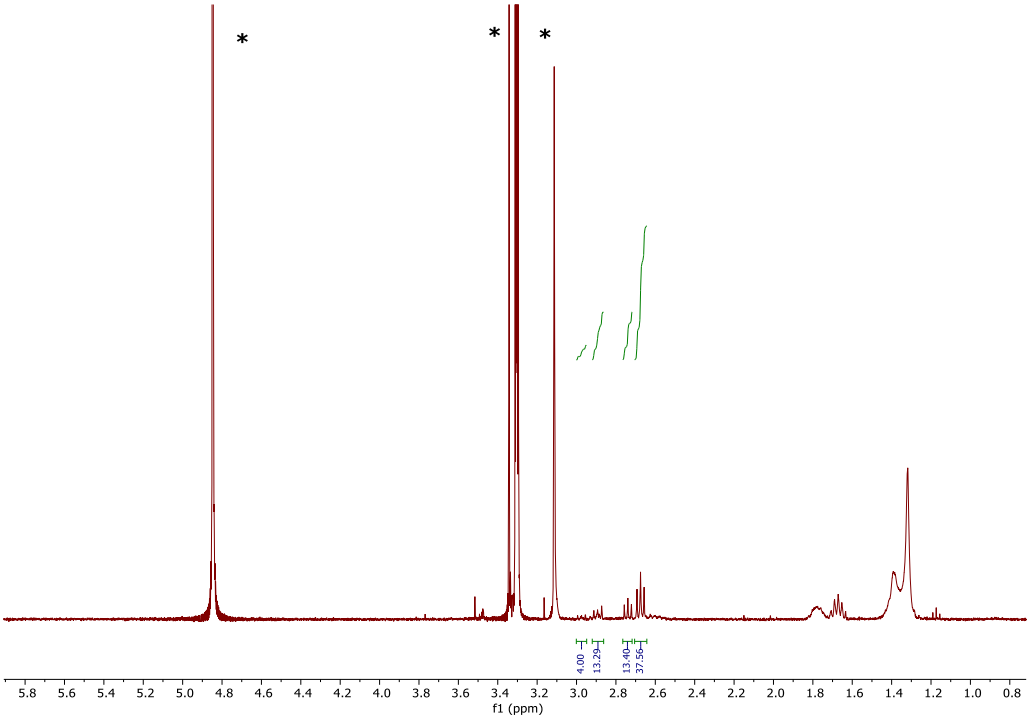

Figure 3.50. ^{1}H-NMR spectrum (400 MHz, CD_3OD) of the decomposition mixture of NP C12NF6 (run 2).

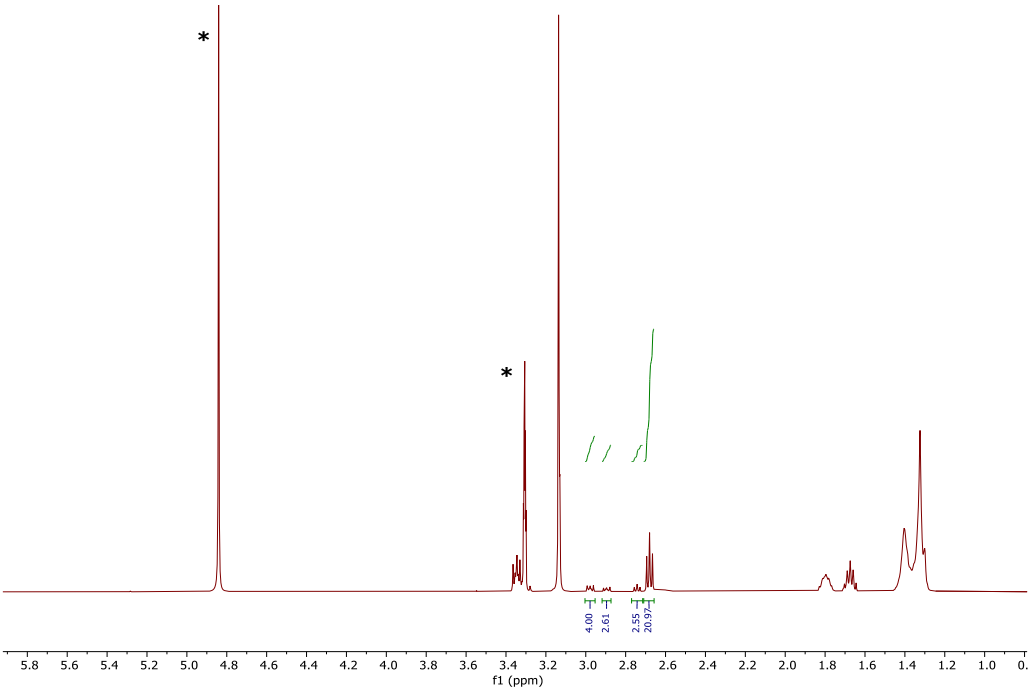

Figure 3.51. ^{1}H-NMR spectrum (400 MHz, CD_3OD) of the decomposition mixture of NP C16NF6 (run 3).

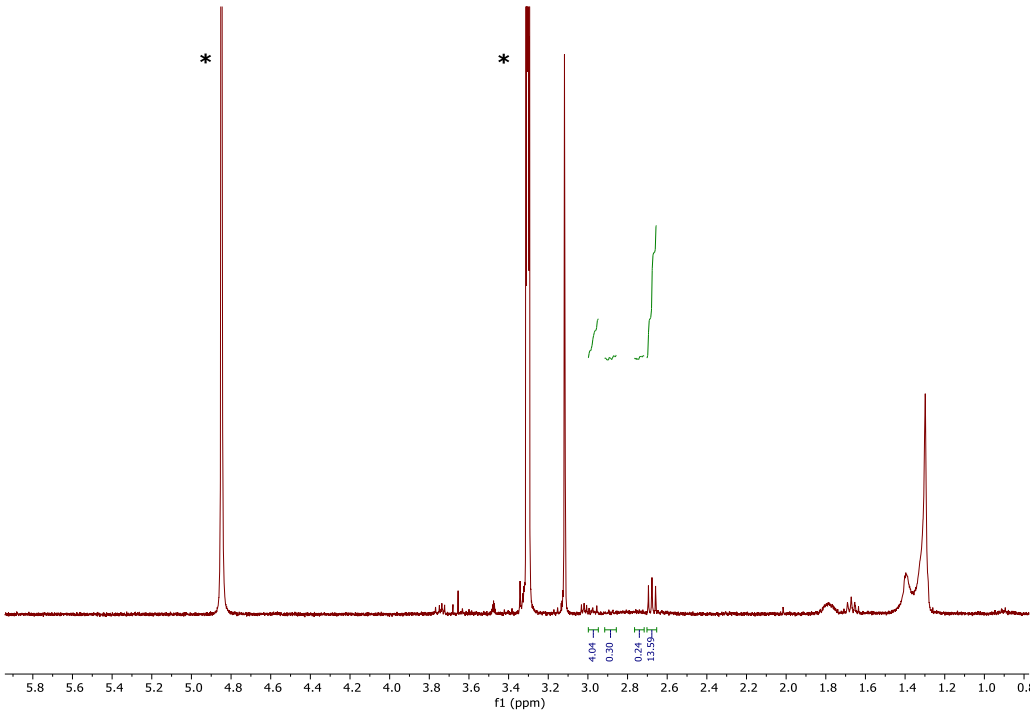

Figure 3.52. ^{1}H-NMR spectrum (400 MHz, CD_3OD) of the decomposition mixture of NP C16NF6 (run 4).

In Table 3.9 the values of monolayer *H/F*- ratio obtained from NMR analysis are reported.

Table 3.9. Comparison between the H/F- ratio used during the AuNPs synthesis and that obtained from monolayer decomposition.

NP C12NF6		
	***H/F*- synthesis ratio**	***H/F*- monolayer ratio**
Run 1	5 : 1	5 : 1
Run 2	3 : 1	2.9 : 1
NP C16NF6		
	***H/F*- synthesis ratio**	***H/F*- monolayer ratio**
Run 3	3 :1	3.6 : 1
Run 4	2 : 1	3.1 : 1

After determining the monolayer *H/F*- ligand ratio by NMR spectroscopy, the composition of heteroligand AuNP were analysed by TGA (Figures 3.53-3.56). For each thermogravimetric analysis, I reported both the TGA curve and the corresponding derivative, labelled in black and red respectively.

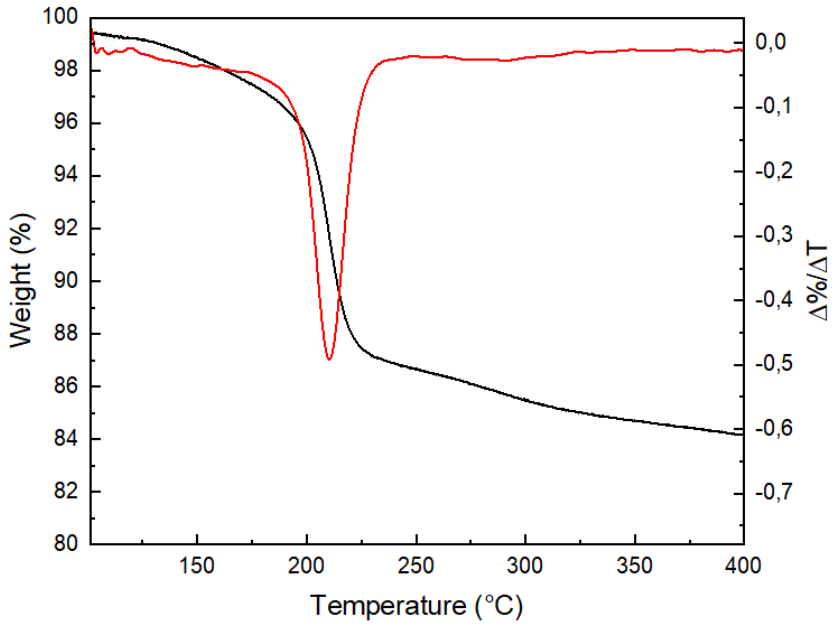

Figure 3.53. TGA curves of NP C12NF6 (5:1).

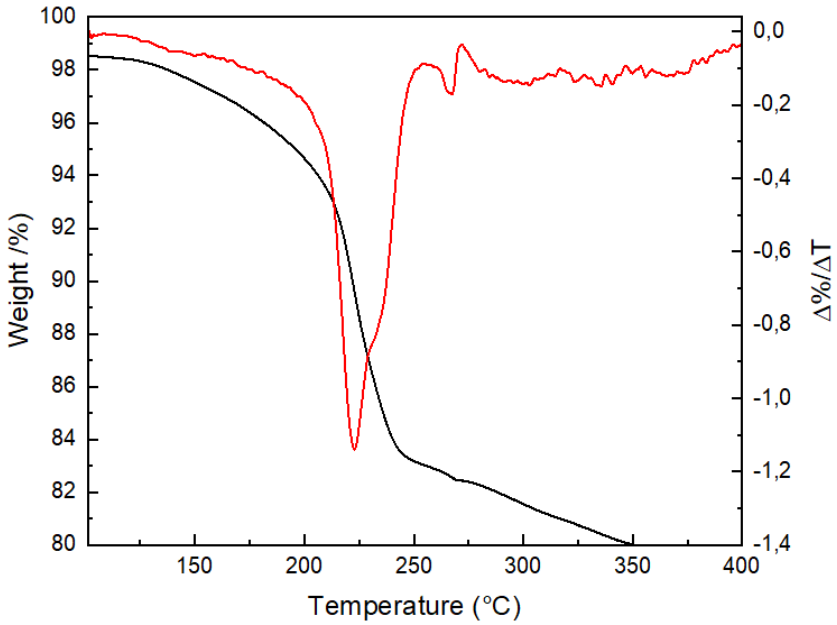

Figure 3.54. TGA curves of NP C12NF6 (2.9:1).

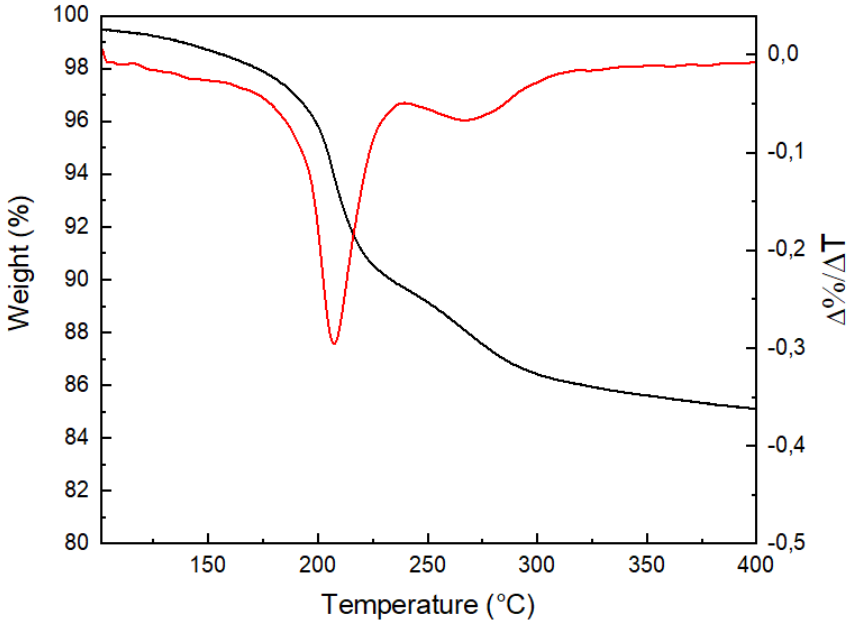

Figure 3.55. TGA curves of NP C16NF6 (3.6:1).

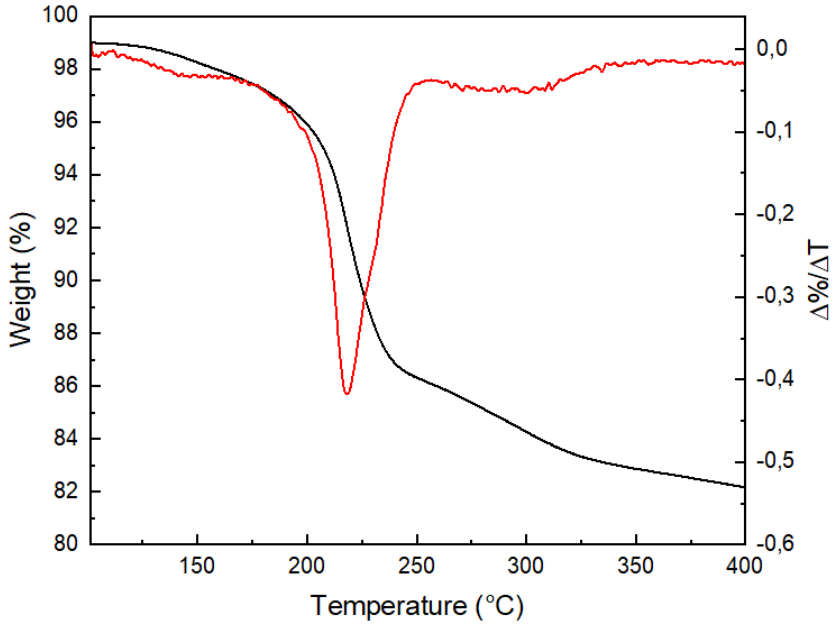

Figure 3.56. TGA curves of NP C16NF6 (3.1:1).

The probable compositions of the whole set of heteroligand nanoparticles are reported in Table 3.10.

Table 3.10. Composition of heteroligand AuNPs.

	L/F6 Synthesis ratio	L/F6 (NMR analysis)	Diameter (nm)	TGA (% organic)	Composition
NP C12NF6 (5:1)	5:1	5:1	4.1 ± 0.9	15	$Au_{2425}L_{250}(F6)_{50}$

NP C12NF6 (2.9:1)	3:1	2.9:1	5.2 ± 1.2	15.7	$Au_{4842}L_{400}(F6)_{138}$
NP C16NF6 (3.6:1)	3:1	3.6:1	4.3 ± 1.1	13.9	$Au_{2779}L_{211}(F6)_{58}$
NP C16NF6 (3.1:1)	2:1	3.1:1	4.0 ± 1.3	15.6	$Au_{2320}L_{196}(F6)_{63}$

Once the dimension and the monolayer composition have been analysed in detail, the colloidal stability of these nanosystems was studied in aqueous solutions by ζ-potential measurements and DLS analysis to calculate the hydrodynamic diameter. The corresponding results are shown in the Table 3.11, in which a higher ζ-potential is observed for the heteroligand AuNPs with the greater *H/F*- ratio due to the higher number of cationic charges on their surface.

Table 3.11. ζ-potential observed for the heteroligand AuNPs in aqueous medium.

	[AuNPs] in mg/mL	**ζ-potential in mV**	**Hydrodynamic diameter (nm)**
NP C12NF6 (5:1)	0.025	+ 43.5	8.7 ± 2.4
NP C12NF6 (2.9:1)	0.025	+ 18.4	10 ± 2.7
NP C16NF6 (3.6:1)	0.025	+ 40.2	10 ± 2.5
NP C16NF6 (3.1:1)	0.025	+ 15.7	9.3 ± 2.9

3.3 Preliminary Fluorescence studies of AuNPs: titration with PPP-$OPSO_3$

The homoligand and mixed monolayer nanoparticles were tested for their quenching properties towards a series of fluorophores and for their ability to enter in the formation of stable fluorophore-nanoparticle constructs in which the fluorescent moiety is quenched because of the binding to the nanoparticle surface via electrostatic and possibly hydrophobic interactions. Indeed, the approach of the fluorophore to the gold core via electrostatic interactions should result in a certain fluorescence quenching that will depend on the affinity and number of interactions established between the fluorophore and the AuNPs surface. To select the most promising fluorophore for the preparation of the construct, the fluorescence intensity of different types of anionic donors was analysed in the presence of increasing amounts of AuNPs. NP16 were used as quencher in preliminary experiments. The fluorophores analysed were two low molecular weight organic dyes, namely pyranine and carboxyfluorescein, and a fluorescent conjugated polymer, PPP-$OPSO_3$ (poly(2,5-bis(3-

sulfonatopropoxy)-1,4-phenylene, disodium salt-alt-1,4-phenylene). The structure and the characteristic wavelengths of each fluorophore are reported in Figure 3.57.

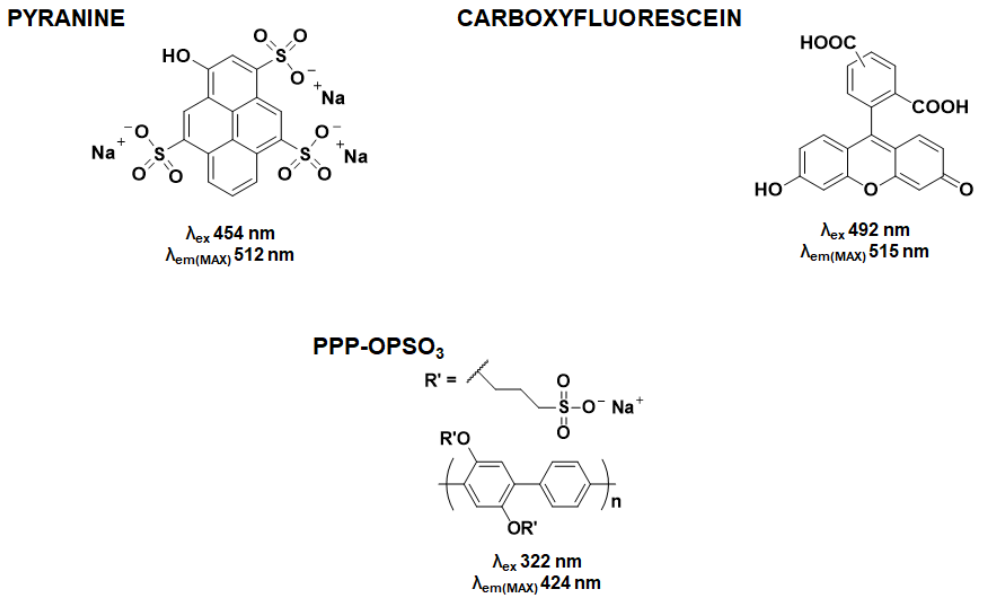

Figure 3.57. The fluorophore candidates for AuNP fluorescence studies.

The experiment consisted in a titration of a fluorophore solution of known concentration with a standard solution of AuNPs (as titrant). The fluorescence intensity was recorded prior to any addition of nanoparticles solution and after each nanoparticle addition. In these experiments the low molecular weight fluorophores displayed a limited fluorescence quenching while the quenching efficiency of the nanoparticles is much higher for PPP-$OPSO_3$ (Figure 3.58).

Unfortunately, the precise molecular weight (MW) of the commercially available PPP-$OPSO_3$ used in this thesis is not disclosed. However, the MW of the very same polymer obtained from the same commercial source, was determined by Yao and Fukui to be 1-2 10^4 Da that is consistent with 40 to 80 repeating phenylene rings per unit.[28,29] Most importantly, these authors could also pinpoint that this polymer is aggregated in aqueous solution. Indeed, we could also confirm this aggregation behaviour by DLS analyses that allowed us to estimate a hydrodynamic diameter of 217 nm for the PPP-$OPSO_3$ aggregates. The apparent MW of these aggregates has been estimated by considering the relationship between the hydrodynamic diameter of the polymer (or its aggregates) and the number of repeating units in each polymer chain, according to the following equation:

$$D_H = a\sqrt{N} \qquad (4)$$

Where D_H is the hydrodynamic diameter, "*a*" is the length of the repeating unit, and N is the number of the repeating units. We used the D_H of 217 nm determined by DLS, while the term "a" was set equal to 1.2 nm as reported in the literature.[28] Considering the molecular weight of one repeating unit is 472 g/mol, the apparent MW of the polymer has been estimated to be about 1500 kDa. The ill-defined MW of PPP-OPSO$_3$ and the presence of polymer aggregates is a severe limitation that hinders the calculation of the nanoparticles-polymer binding constants, *vide infra*.

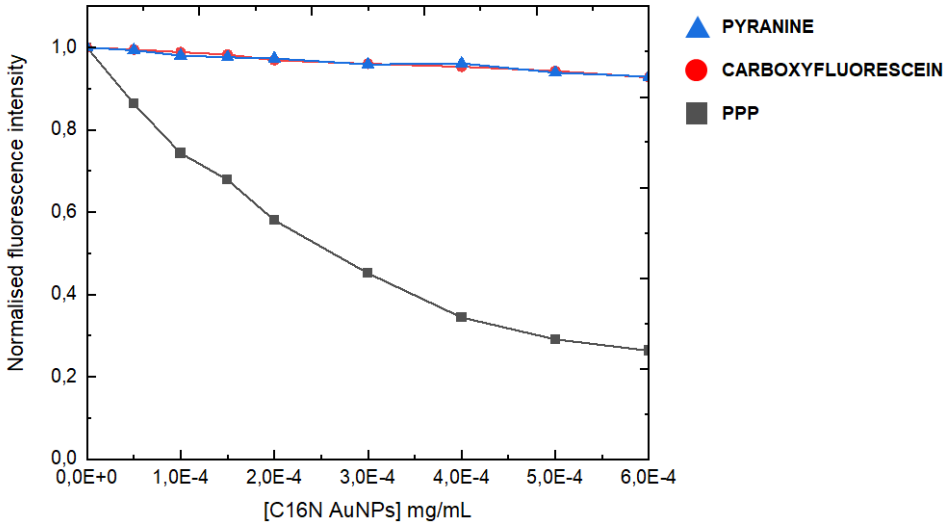

Figure 3.58. The fluorescence quenching efficiency of NP C16N towards anionic monomeric (pyranine and carboxyfluorescein) and polymeric (PPP-OPSO$_3$) fluorescent species. The experiments were carried out in PBS (50 mM, 150 mM NaCl, pH 7.3).

The high quenching efficiency of the nanoparticles towards PPP-OPSO$_3$ respect to those towards pyranine and carboxyfluorescein is consistent with the possibility of multivalent interaction in the case of the polymer-AuNP construct.

Afterwards, the quenching efficiency of the entire set of cationic nanoparticles toward PPP-OPSO$_3$ was also analysed in PBS through titrations of standard AuNP solutions with PPP-OPSO$_3$ as titrant. The results of the fluorescence titration are reported synoptically in Figure 3.59. The fluorescence of the free PPP-OPSO$_3$ in the absence of AuNPs was recorded up to the second addition, to establish an upper limit of the fluorescence intensity expected in the experiments with the nanoparticles; further additions could not be performed because the fluorescence intensity saturated the detector.

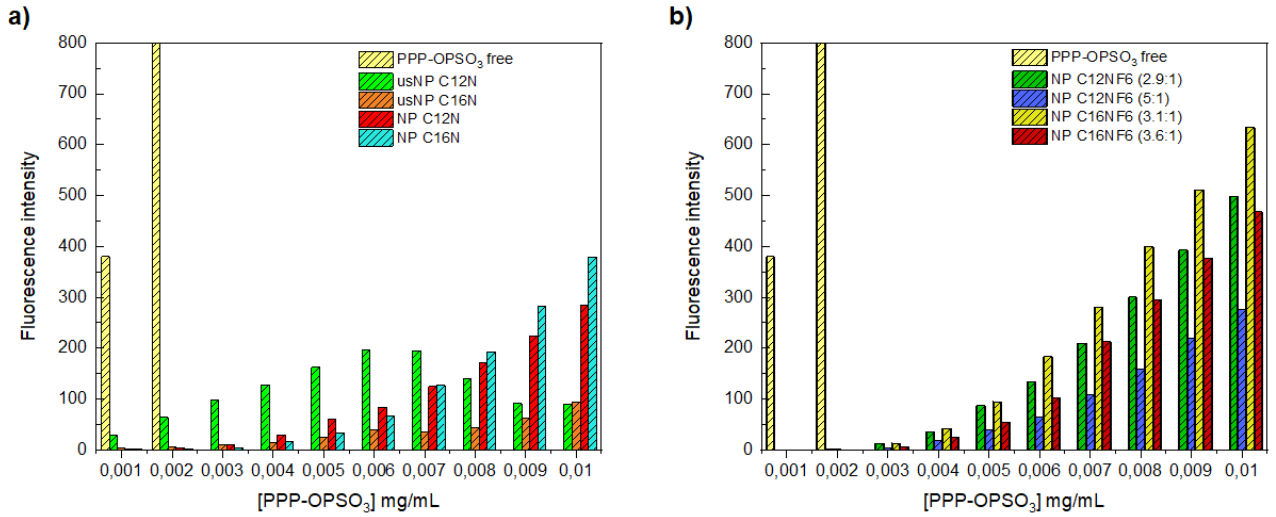

Figure 3.59. Fluorescence titration curves for the complexation of PPP-OPSO$_3$ with cationic homoligand (**a**) and heteroligand **(b)** gold nanoparticles in PBS. The concentration of the nanoparticle solution [AuNPs] is 0.05 mg/mL.

All the nanoparticles in the set have shown excellent quenching activity towards PPP-OPSO$_3$, however, the homoligand AuNPs proved to be more effective respect to the heteroligand ones (Figure 3.59a). This observation is consistent with the higher positive charge density on homoligand nanoparticles surface and suggests that the presence of hydrophobic areas due to the fluorinated ligands does not play a major role in the interaction with the fluorophores. In addition, based on the fluorescence signals recorded for each type of AuNP, other considerations can be pinpointed: (i) the quenching efficiency is influenced by the distance between the inorganic core and the fluorophore (AuNPs bearing C16N show lower quenching than those featuring the C12N ligands), and (ii) the AuNP size affects the quenching efficiency allowing to obtain diverse fluorescence signals for the homoligand AuNPs of varying sizes. All nanoparticles show a monotonic trend, except the usNP12 which display a bell-shaped behaviour. From these data it appears that a relatively high concentration of PPP-OPSO$_3$ is necessary to trigger the fluorescence quenching in the case of usNP12. This may be the result of a reduced affinity of usNP12 towards PPP-OPSO$_3$, *vide infra*.

Regardless of this different behaviour exhibited by AuNPs, the results of the fluorescence experiments have highlighted the quenching property of the AuNP set and the diverse affinity towards the conjugated polymer based on the monolayer composition. These data have provided the foundations for the design of more complex fluorescence studies, in which systems able to act as biological membrane models have been exploited to analyse the changes in AuNPs/PPP-OPSO$_3$ interactions and evaluate the resulting fluorescence profiles.

3.4. AuNPs-PPP-$OPSO_3$ constructs: determination of the association constants

In collaboration with the group of Prof. Marco Montalti, it has been possible to determine the quenching mechanism between the AuNPs and PPP-$OPSO_3$. In detail, they tested four types of nanoparticles, namely NP C12N, NP C16N, NP C12NF6 (5:1), and NP C16NF6 (3.6:1) and prepared the corresponding diluted aqueous solutions. Then, PPP-$OPSO_3$ was added to the nanoparticle solution and both emission spectrum and excited state lifetime have been registered after each PPP-$OPSO_3$ addition. In all cases, the lifetime does not change with the PPP-$OPSO_3$ concentration, and this behavior is typical of a static rather than a dynamic quenching, which means that nanoparticles and PPP-$OPSO_3$ could be associated at the ground state, forming an NP/PPP-$OPSO_3$ complex. Considering a general host-guest (HG) complex formation:

$$mH + nG \leftrightarrows H_mG_n \quad (3)$$

where K_{ass} is the overall association constant, whose value could be determined by various techniques (UV-vis and fluorescence spectroscopy, NMR), allowing the evaluation of the H-G affinity.[30] For this purpose, preliminary fluorescence experiments apt to determine the AuNPs/PPP-$OPSO_3$ association constant of both homoligand and heteroligand nanoparticles have been performed by Dr. Arianna Menichetti of the group of Prof. Marco Montalti at Università di Bologna. The experiments consist of a titration of PPP-$OPSO_3$ solution (0.001 mg/mL) using an AuNPs solution (2 mg/mL) as titrant in an aqueous environment. After each AuNP addition, the fluorescence intensity of PPP-$OPSO_3$ has been recorded. Then, the resulting emission spectra have been analysed by the software HyperQuad (HyperSpec), which provides a system for simulating titration curves. In these experiments, the molecular weight of each analysed nanoparticles system has been calculated by using the compositions of cores and organic coatings evaluated by the AuNP characterization. This analysis pinpointed that the best fit of the experimental data was achieved by using a 1:3 host-guest model, considering PPP-$OPSO_3$ and the nanoparticles as host and guest respectively. The graphs reported in Figure 3.60 and Figure 3.61 show the data fitting of each titration and the related overall K_{ass} calculated by the software.

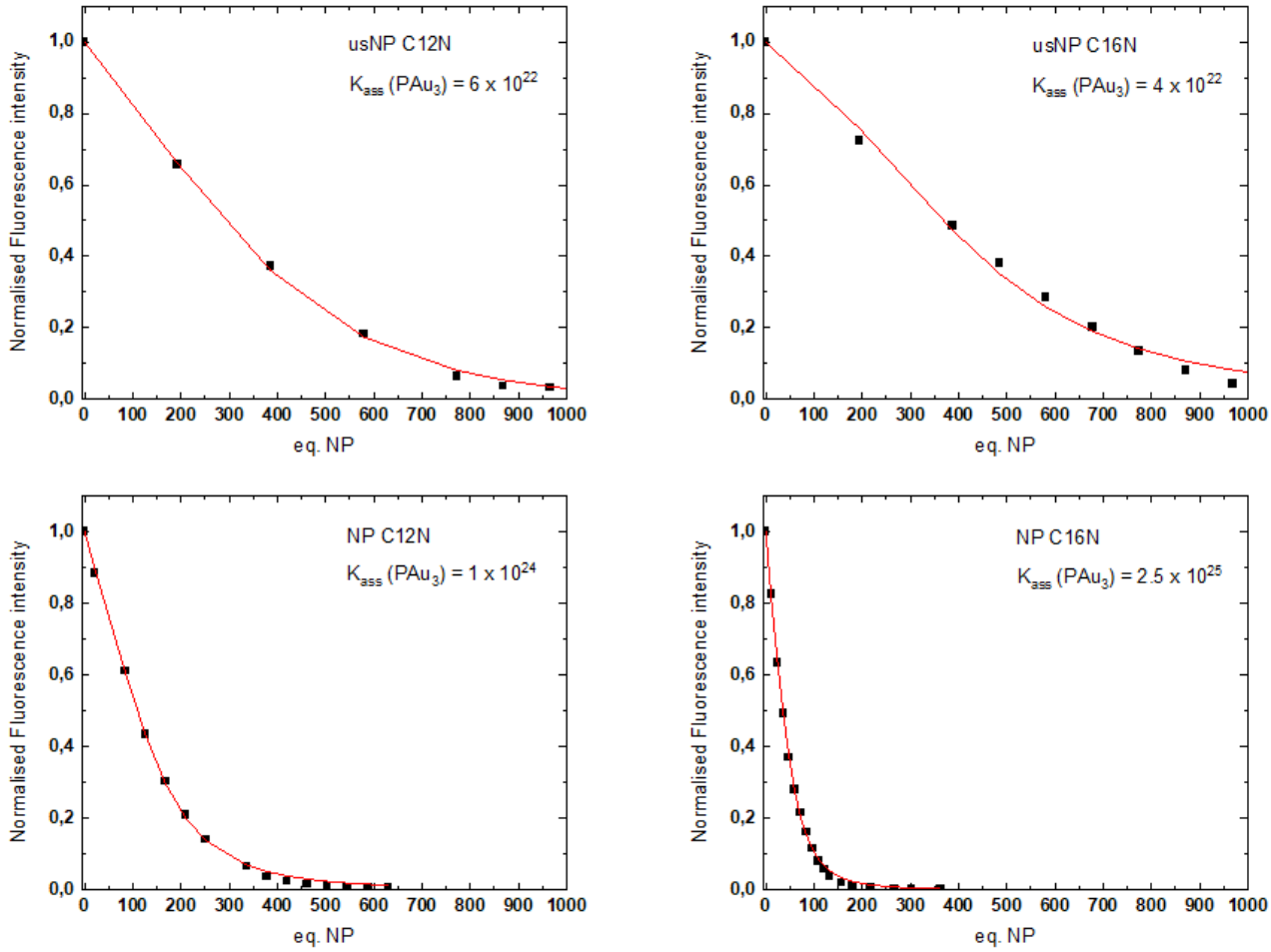

Figure 3.60. Experimental data obtained by the titration of 0.001 mg/mL PPP-$OPSO_3$ solution with a 2 mg/mL homoligand AuNP solution. The values reported on the x axis is related to the nanoparticle equivalent present in the PPP solution after the nanoparticle addition. In the legend, "P" indicated PPP-$OPSO_3$, "Au" the nanoparticles.

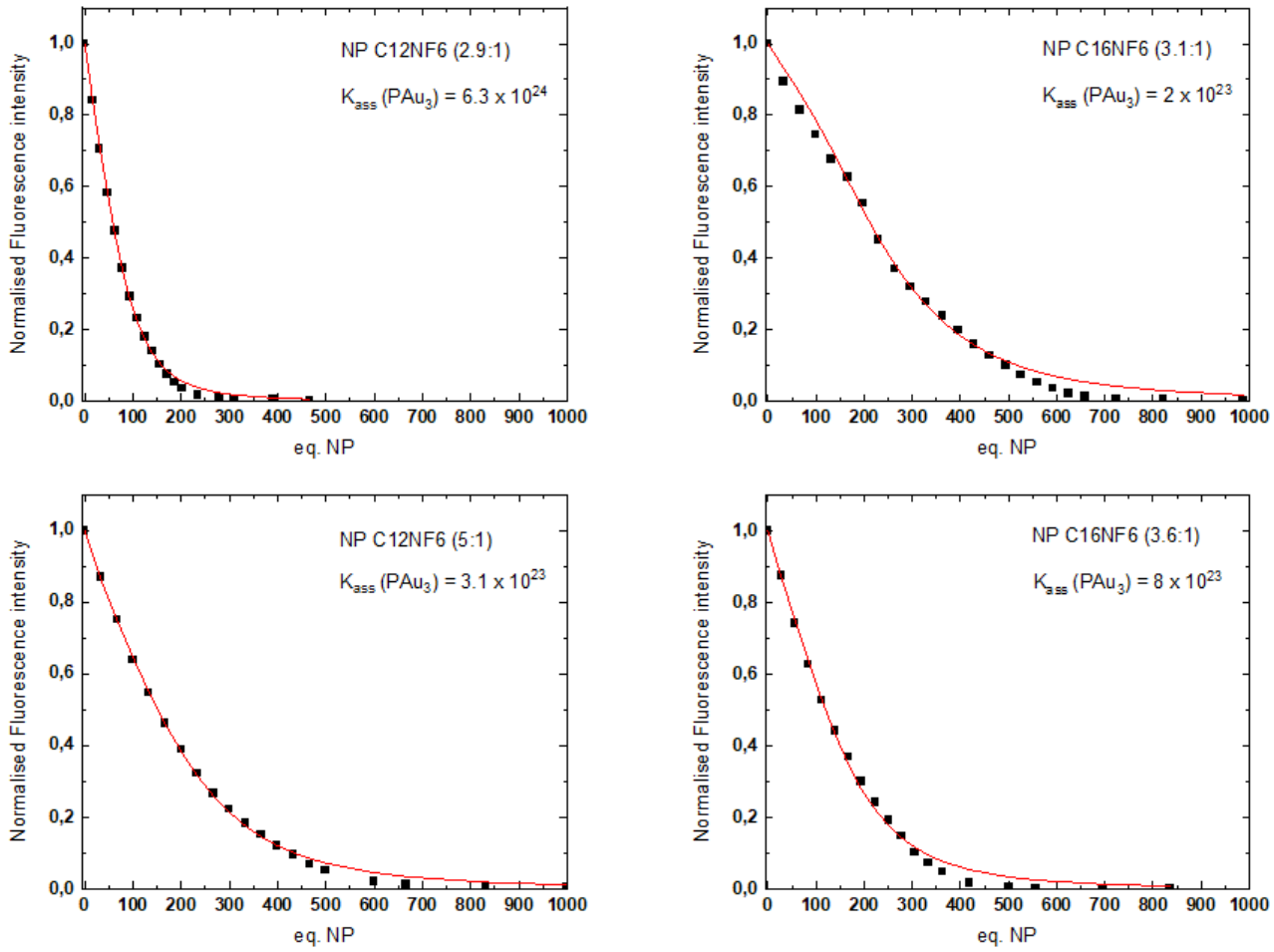

Figure 3.61. Experimental data obtained by the titration of 0.001 mg/mL PPP-$OPSO_3$ solution with a 2 mg/mL heteroligand AuNP solution. The values reported on the x axis is related to the nanoparticle equivalent present in the PPP solution after each addition. In the legend, "P" indicated PPP-$OPSO_3$, "Au" the nanoparticles.

Referring to the Figure 3.60 and Figure 3.61, as expected the ultrasmall homoligand AuNPs (usNP C12N and usNP C16N) have a lower K_{ass} compared to that of larger NP C12N and NP C16N, most likely due to the higher density of cationic charges on the outer surface of the latter. Therefore, it appears that larger nanoparticles are better binder towards PPP-$OPSO_3$. On the other hand, considering the value of K_{ass} of NP C16N and those of the corresponding heteroligand nanoparticles (NP C16NF6 (3.1:1); NP C16NF6 (3.6:1)), the latter ones show a lower affinity towards PPP-$OPSO_3$, suggesting that the major contribution to the AuNP- PPP-$OPSO_3$ binding is electrostatic, it has to be noted, however, that in this case the gold core size of the mixed monolayer nanoparticles is significantly smaller than the homoligand ones. Comparing the K_{ass} values of NP C12N and NP C12NF6 (2.9:1), that have gold cores of similar size, it may be inferred that the fluorinated ligands also contribute to the binding of the polymer through further hydrophobic interactions.

3.5 Liposomes as biological membrane models

Regarding the biomedical and biological applications of the AuNPs, it is often hard to determine the factors influencing and triggering the interactions between the nanoparticles and biological systems because of the inherent complexity of these systems. Therefore, we decided to use, for preliminary experiments, simplified models of biological models capable of mimicking the most relevant features of bio-interfaces. In this context the use of liposomes proved to be extremely important for understanding both the physicochemical properties driving nano-bio interactions, and the reciprocal effects resulting from the interaction in terms of structural alterations.[31–33]Furthermore, the use of a simplified membrane model allows a much more straightforward comparison of the experimental results with the outcomes of computational analyses used to study the interaction between nanoparticles and lipid bilayers. This is indeed a widely used and fundamental approach for understanding and predicting the effects of AuNPs on biological membranes. Several studies have addressed the key elements that affect the interaction between the AuNPs and lipid bilayers-based mimics, revealing that both Van der Waals, electrostatic forces and the ligand arrangement in the nanoparticles monolayer are the major triggers.[34,35] On the other hand, it is equally important to understand what happens once the interaction between nanoparticles and these membrane models has been established because the events following nanoparticle adhesion are those leading to nanoparticle internalization. A recent work has provides crucial information about the consequences due to the AuNPs adhesion on lipid bilayers by combining MD simulations and experimental techniques, such as laser scanning confocal microscopy (LSCM), and fluorescence correlation spectroscopy (FCS).[36] In detail, the authors have chosen cationic AuNPs (~ 4 nm) as model of charged nanomaterials to interact with mixed anionic (POPG; 1-palmitoyl-2-oleoyl-*sn*-glycero-3-phosphoglycerol) and zwitterionic (POPC; 1-palmitoyl-2-oleoyl-*sn*-glycero-3-phosphocholine) mixed lipid bilayers, characterizing the structural and dynamics effect of AuNPs adhesion. In addition to electrostatic forces, their results reported that an entropy contribution due to counter anion contributes to the strong adhesion of cationic AuNPs coated by *N,N,N*-trimethyl-11-mercaptoundecylammonium on lipid layers. Analysing the distribution of counterions on both the AuNPs and lipids surface before and after AuNPs adhesion, these authors have observed that a certain amount of both Cl^- and Na^+ are released after the AuNPs-lipid layer interaction has occurred, favouring the adhesion process. Regarding the effect on the AuNPs-lipid interaction, they have observed a perturbation of the membrane composition, in which in correspondence of the adhesion points POPG enriched patches

are formed. In addition, the AuNPs adhesion reduce the lateral mobility due the capture of a certain amount of anionic lipids by the AuNPs.

These results along with those of other studies provide precious information on the interaction of AuNPs with biomimetic systems, providing fundamental concepts on the nano-bio interfaces and the mechanisms involved.

Following this approach, in this thesis work liposomes were used for preliminary studies as simplified models of bacterial cell walls. The bacterial cell envelopes are extremely complex multi-layered structures that are very different in the Gram-positive and Gram-negative bacteria. Gram-positive bacteria are characterised by a two-layer envelope in which a thick peptidoglycan layer surrounds the inner plasma membrane. In Gram-positive bacteria the peptidoglycan layer is spanned by long anionic polymers: teichoic acids. These anionic polymers are composed by repeated units of glycerol phosphate, glucosyl phosphate, or ribitol phosphate and collectively represent more than 60% by mass of bacterial cell wall. Instead, Gram-negative bacteria are characterised by a three-layer envelope in which the inner plasma membrane is surrounded by a thin peptidoglycan layer that is surrounded by an outer membrane. The external leaflet of the outer membrane is composed of glycolipids and among them the main components are lipopolysaccharides. These molecules, besides being extremely variable in composition from strain to strain, are characterised by the presence of sugar-bound phosphate groups in the form of phosphate monoesters or pyrophosphate or 2-aminoethylphosphate. Because of the above considerations, the choice of phospholipid bilayers to model the bacterial cell wall is justified by the analogy of the groups providing the negative charges to the surface although remaining an oversimplification. The approach followed in this thesis work consists in studying the liposome interactions with the homoligand and heteroligand AuNPs and evaluate the corresponding fluorescence profile in presence of PPP-$OPSO_3$. to this end two anionic liposomes composed respectively of a mixture of POPG/POPC (Figure 3.62a, L_1) and of pure POPG (Figure 3.62b, L_2) were prepared.

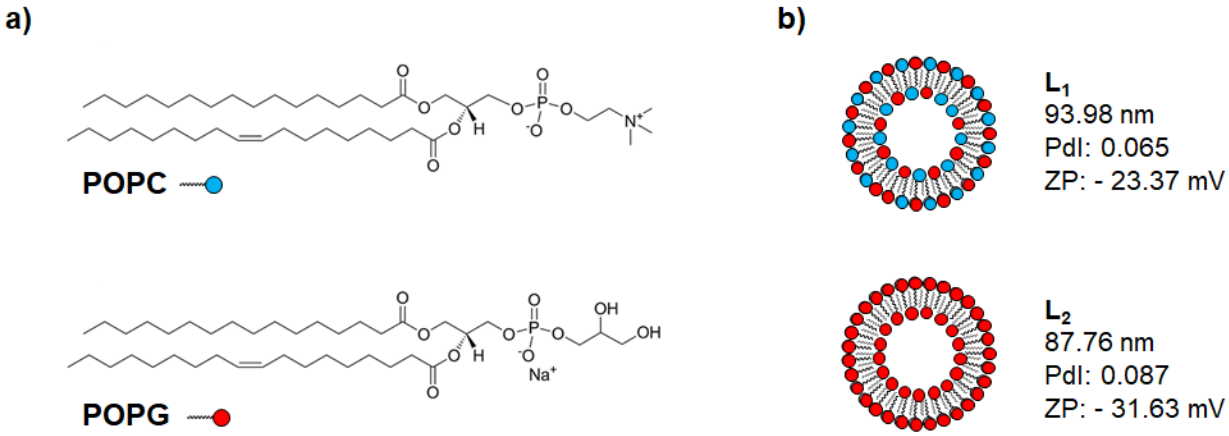

Figure 3.62. Structures of POPC and POPG (**a**) and anionic liposomes derived (**b**). Each liposome has been characterised by DLS and ζ-potential analyses carried out in PBS solution, with a [lipid] concentration as 0.1 mg/mL.

The preparation and characterization of L_1 and L_2 are discussed in detail in the following paragraph.

3.6 Preparation and characterization of anionic liposomes

For the preparation of both anionic liposomes, I employed a procedure similar to the protocols reported in the references [34], [35], and [36] (Scheme 3).[37–39]

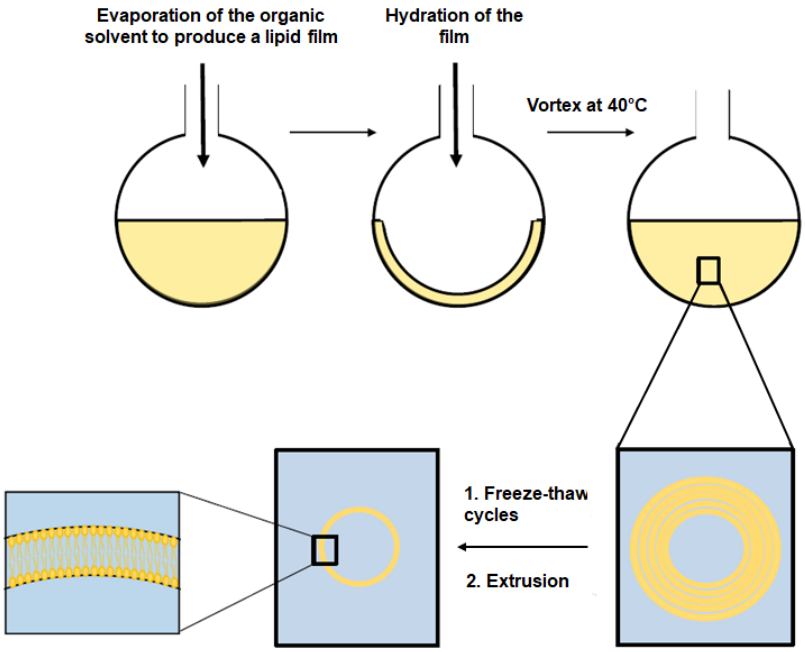

Scheme 3. Representation of the procedure used for the liposome preparation.

Liposome L_1 with a diameter of ~ 100 nm, a precise amount of POPC and POPG were dissolved in dichloromethane to obtain a 1:1 POPC/POPG ratio with a [lipid] of 3 mg/mL. The gentle evaporation

of the solvent by a stream of nitrogen provided a dry lipid film that was hydrated with a PBS solution at 40°C. The resulting liposome dispersion was subjected to five freeze-thaw cycles act as a "mild" homogenization step. The final step consisted in several cycles of extrusion through a 100 nm membrane filter to produce a dispersion of liposomes of the desired size and a narrow size dispersion. The liposome L_2 was prepared by using the same procedure, in which only POPG was used as lipid component. The hydrodynamic diameter of the liposomes was determined by DLS analysis, and the results obtained are reported in Figure 3.63 and Figure 3.64. Moreover, for each liposome preparation the corresponding ζ-potential was evaluated using the same condition used for the DLS analyses (Table 3.12). As expected, L_2 shows a more negative ζ-potential than L_1 since only the anionic lipid POPG was used in its synthesis, whereas the L_1 has been synthetised used a mixture of POPG and the zwitterionic POPC bearing a choline at the end of its structure. Anyway, both liposomes exhibit a moderately negative ζ-potential in PBS, such as to obtain stable systems under buffer conditions.

Table 3.12. ζ-potential determination of both anionic liposomes. The analysis is carried out in PBS at a [lipid] of 0.1 mg/mL.

Liposome	**ζ-potential (mV)**
L_1	- 23.37
L_2	- 31.63

.

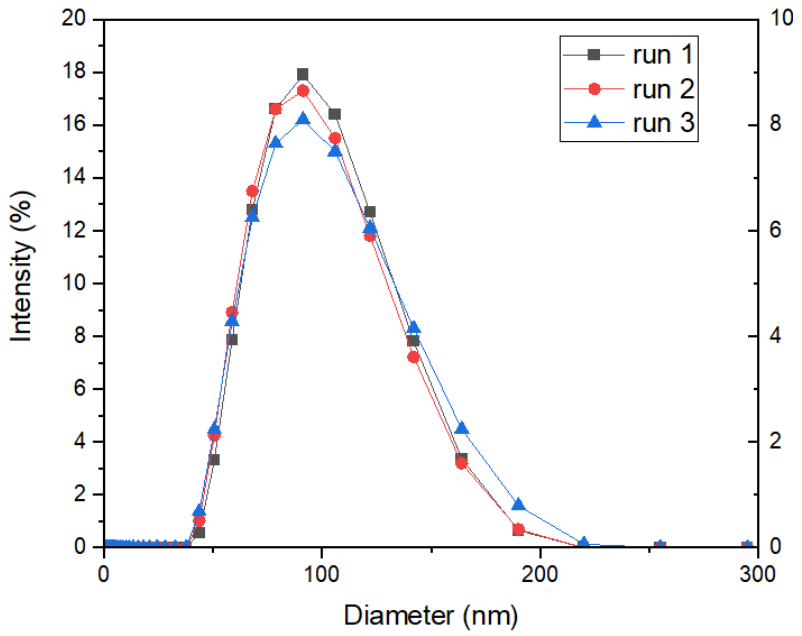

Figure 3.63. DLS analysis of L_1 solution in PBS at a [lipid] of 0.1 mg/mL.

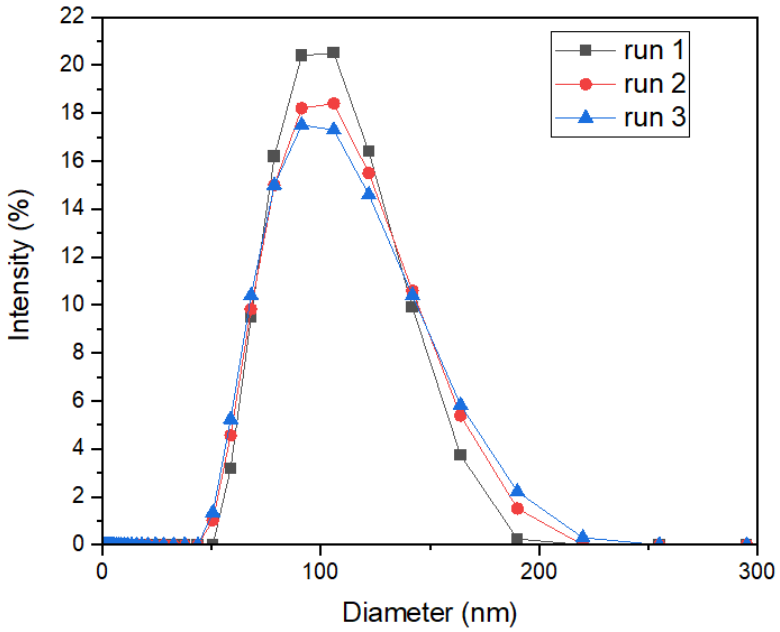

Figure 3.64. DLS analysis of L_2 solution in PBS at a [lipid] of 0.1 mg/mL.

3.7 Fluorescence studies of AuNPs-PPP-OPSO$_3$ in presence of anionic liposomes

The liposomes L_1 and L_2 were used to study the influence of negatively charged surfaces on the interaction between PPP-OPSO$_3$ and nanoparticles and therefore on their quenching efficiency towards the fluorescent polymer. In a preliminary experiment, a PBS solution containing the AuNPs and PPP-OPSO$_3$ quenched construct was titred with a solution of liposomes with a nominal concentration of lipid of 5 mg/mL. However, under these conditions the AuNPs-polymer construct displayed a limited stability, and some precipitation could be observed in a relatively short time, probably triggered by the ionic strength of the medium, that prevented the acquisition of reliable results. Previous DLS analyses had indeed shown the lower solution stability of AuNPs in PBS compared to that in aqueous solution likely because of the screening of repulsive interactions between nanoparticles in the presence of salts; this effect was more pronounced in the case of the AuNPs-polymer construct where part of the surface charges of the nanoparticles are already screened by the polymer. To overcome this issue, a different approach was attempted changing the initial conditions: namely a solution containing AuNPs was pre-incubated with the liposome solution to obtain 0.05 mg/mL and 0.1 mg/mL as final concentrations of nanoparticles and lipids respectively in the cuvette. No precipitate formation was found in this case, even after several minutes of liposome incubation

with both homoligand and heteroligand AuNPs, indicating a stabilization of AuNPs in PBS from the likely interaction of AuNPs with the lipid membranes of liposomes. To this solution small aliquots of a concentrated polymer solution [1 mg/mL] were added performing a titration and recording the fluorescence intensity upon each addition. The results of these titration experiments are shown in Figure 3.65 and Figure 3.66 for liposomes L_1 and L_2 respectively.

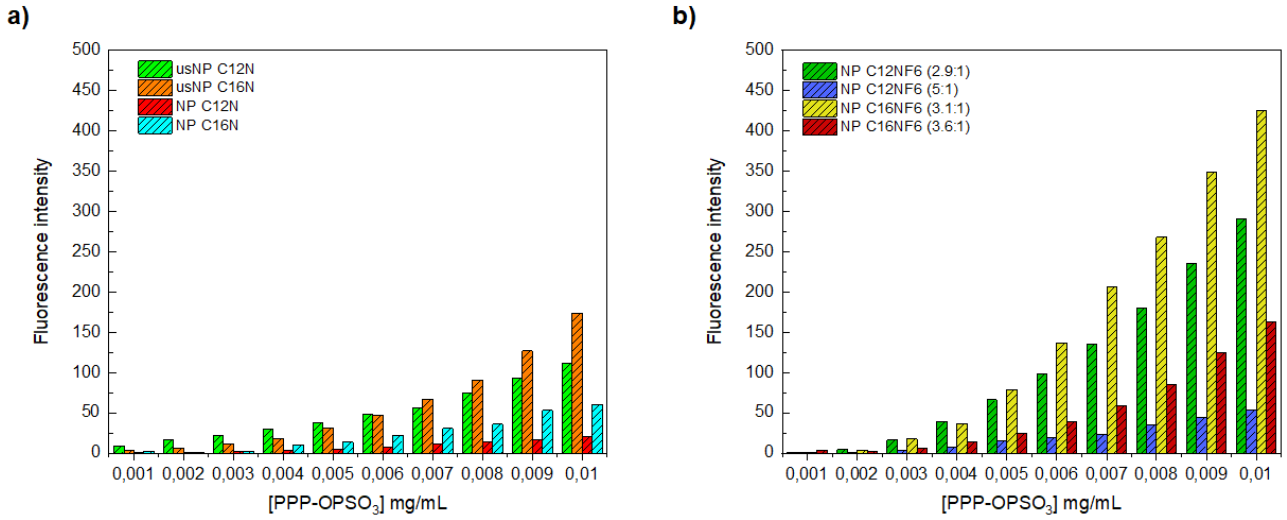

Figure 3.65. Fluorescence titration curves for the complexation of PPP-$OPSO_3$ with cationic homoligand (**a**) and heteroligand **(b)** gold nanoparticles preincubated with liposome L_1 in PBS. The concentration of the nanoparticle solution [AuNPs] is 0.05 mg/mL, while the [lipid] is 0.1 mg/mL.

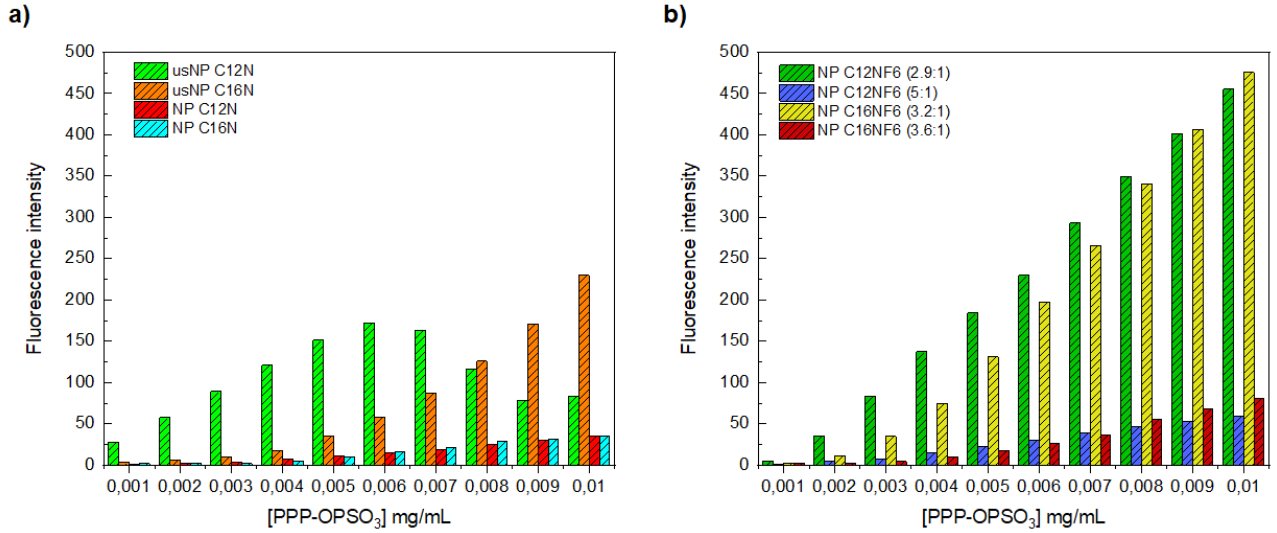

Figure 3.66. Fluorescence titration curves for the complexation of PPP-$OPSO_3$ with cationic homoligand (**a**) and heteroligand **(b)** gold nanoparticles preincubated with liposome L_2 in PBS. The concentration of the nanoparticle solution [AuNPs] is 0.05 mg/mL, while the [lipid] is 0.1 mg/mL.

In this experimental setup, the nanoparticles that more efficiently interact with the liposome membrane should display the smaller quenching towards the polymeric fluorophore. This because

the interaction with the external leaflet of the lipid bilayer screens the positive charges on the nanoparticles surface hampering the primary recognition event at the basis of the fluorescence quenching: the binding to the nanoparticle surface by charge pairing. From inspection of Figure 3.65 and Figure 3.66, it can be inferred that each element in the set of nanoparticles used behave differently with some selectively in the liposome recognition that depends on the nanoparticle size and monolayer composition. In particular, the heteroligand AuNPs display a more efficient interaction with the liposomial membrane respect to homoligand nanoparticles and among homoligand nanoparticles the ultrasmall perform better than the larger ones. In the set of mixed monolayer nanoparticles, the ones with the lowest *H/F*- ratio shown the stronger interaction with liposomes, also in the case of NP16/6 whose batches have a less marked difference in *H*- and *F*- ligand numbers than those of NP12/6. These results are consistent with those reported by Posocco and co-workers, in which the adhesion to a model membrane of both homoligand and heteroligand AuNPs bearing polyethylene glycol–modified *H/F* amphiphilic thiols (Figure 3.67) was investigated by *in-silico* methods and experimentally by SPR on immobilised liposomal membranes.[40]

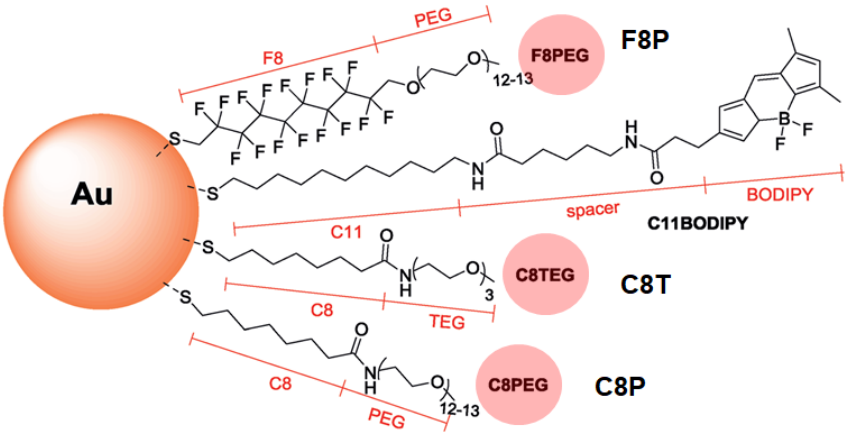

Figure 3.67. Representation of thiol structures used to cover the AuNPs. Adapted from Marson, D. et al. Small 2019, 15 (17).

The authors demonstrated that for mixed monolayer nanoparticles the contacts of the monolayer with the membrane almost all involve the fluorinated chains. On the other hand, among the homoligand AuNPs, the one featuring fluorinated ligands in the monolayer display the more favourable adhesion free energy (i.e., gives the strongest interaction). This effect was ascribed to the increased hydrophobic effect of the fluorinated moiety.

Combining these results with those obtained from the fluorescence titrations of AuNPs-liposome solutions, it can be inferred that the presence of fluorinated ligands improves the binding to the lipid

bilayer, also in the case of NP C16NF6 where the *H/F* ratio of the two batches (3.6:1 and 3.1:1) is less marked than for NP C12NF6 (5:1 and 3:1). These observations underline the crucial role of these moieties in promoting interactions with biological systems. Another explanation could be that the less interaction of the homoligand nanoparticles interacting toward the liposomal membrane induces the AuNPs precipitations due to the lower stability of AuNPs in buffer solution. So, the different quenching efficiency of the homoligand AuNPs could be due to their lower concentration in the buffer solution.

Referring to Figure 3.65 and Figure 3.66, another important aspect to stress is that although the simplified structure of the biomimetic membranes, when the entire set of nanoparticles is considered, the two liposomes show a different fluorescence profile which could, in principle, be used to distinguish the two different liposomes. This aspect can be better emphasized by selecting an arbitrary PPP-$OPSO_3$ concentration value and convert the measured fluorescence intensity into a red-intensity scale (Figure 3.68).

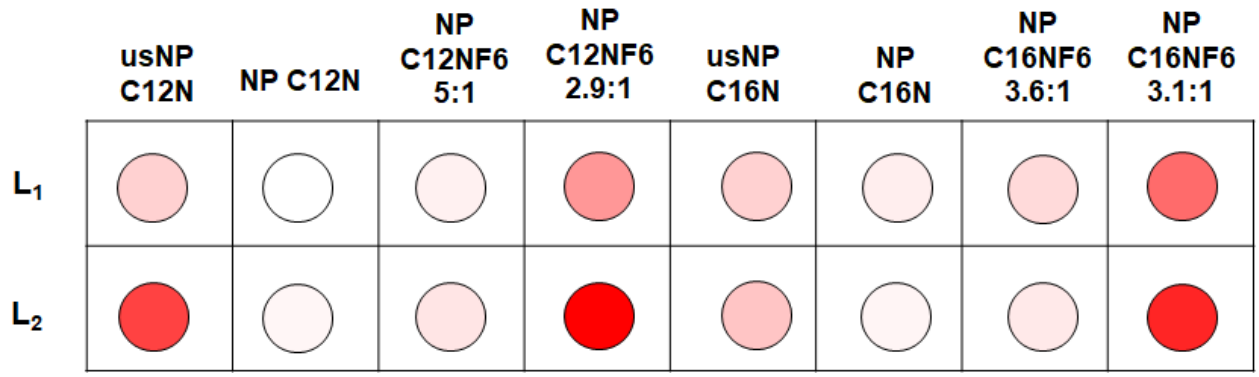

Figure 3.68. Conversion of fluorescence intensity of AuNPs-liposome solution into a red-intensity scale at a [PPP-$OPSO_3$] of 0.006 mg/mL.

As it can be seen from Figure 3.68 the intensity pattern is significantly different for the two liposomes allowing a naked-eye differentiation. Mancin and co-workers recently displayed that the interaction of small cationic nanoparticles, featuring guanidinium or tetralkylamonium ions on their outer surface (core size 1.5-2.4 nm), with the liposomal membranes is essentially nondisruptive.[41] To confirm also in our case the membrane integrity of liposome in presence of AuNPs at the concentrations adopting for the fluorescence studies, DLS analyses were performed to evaluate the shift of the hydrodynamic diameter of liposome/AuNPs systems, and the possible disappearance of liposome peaks. The relative results have showed in Figure 3.70 and Figure 3.71, in which the liposome L_1 has been used. The size distribution by number of the liposome L_1 is reported in Figure 3.69. Approximately 1.7 minutes are used for each run.

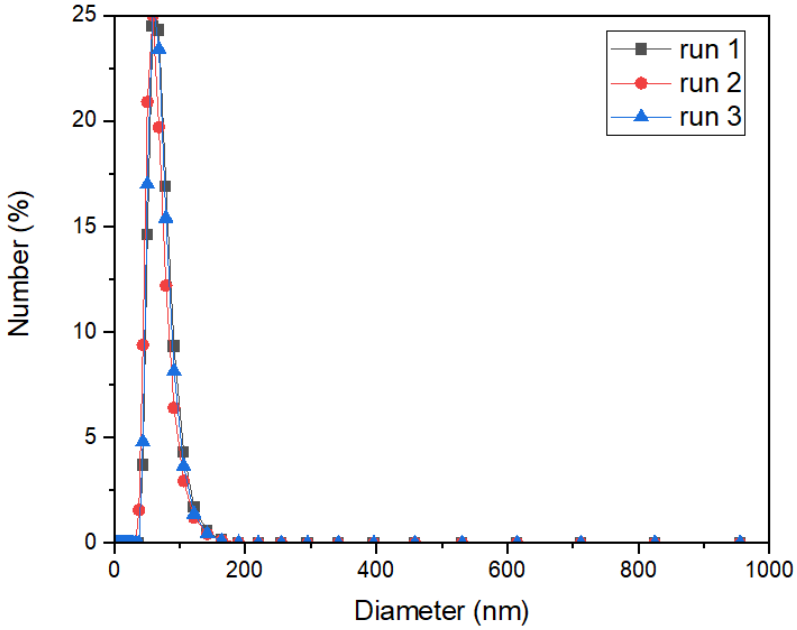

Figure 3.69. Size distribution of L_1 in PBS at [lipid] of 0.1 mg/mL by DLS analysis.

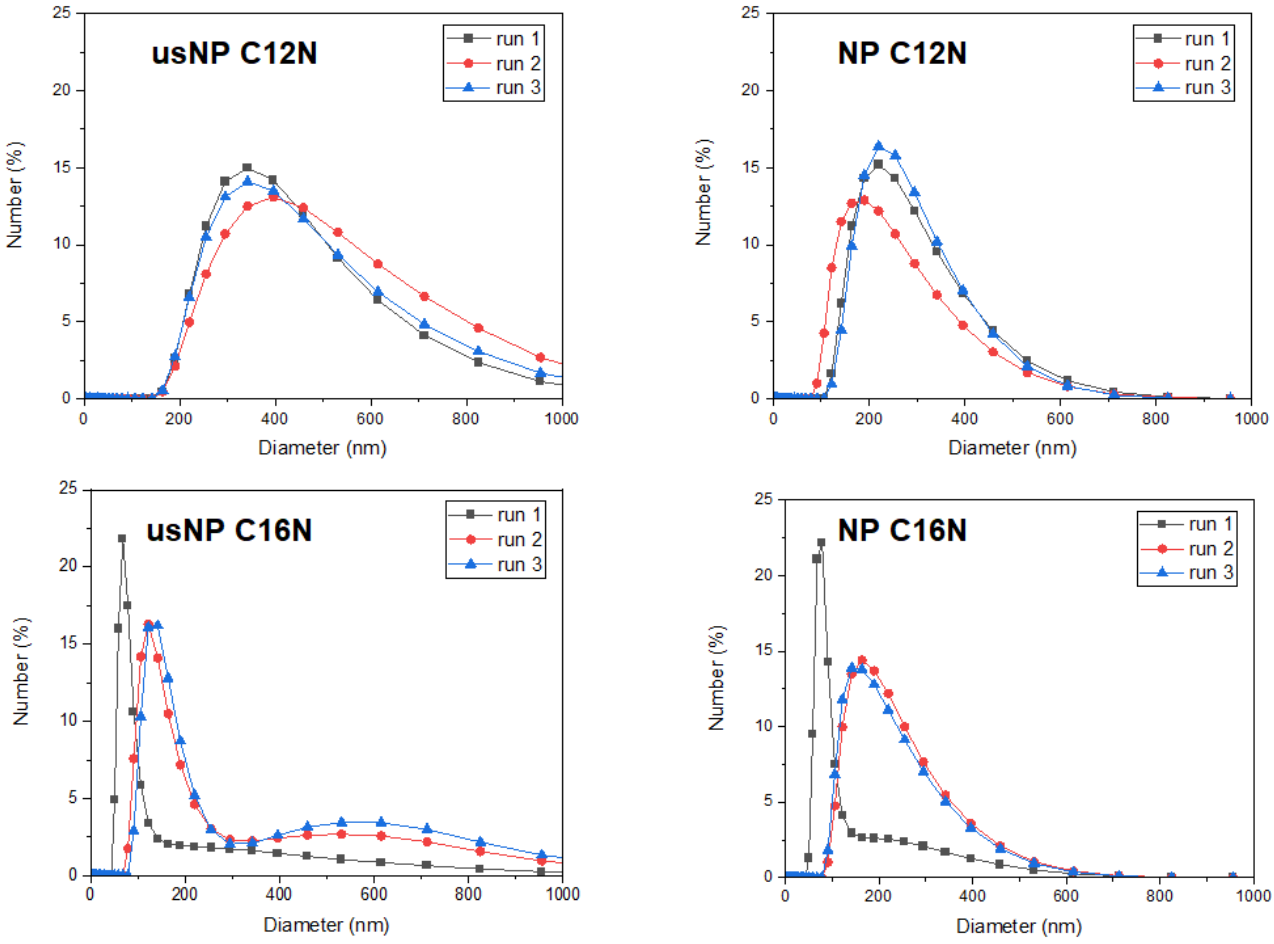

Figure 3.70. DLS analysis of solutions containing L_1 ([lipid] 0.1 mg/mL) and ultrasmall and small homoligand AuNPs ([AuNPs] 0.05 mg/mL) in PBS.

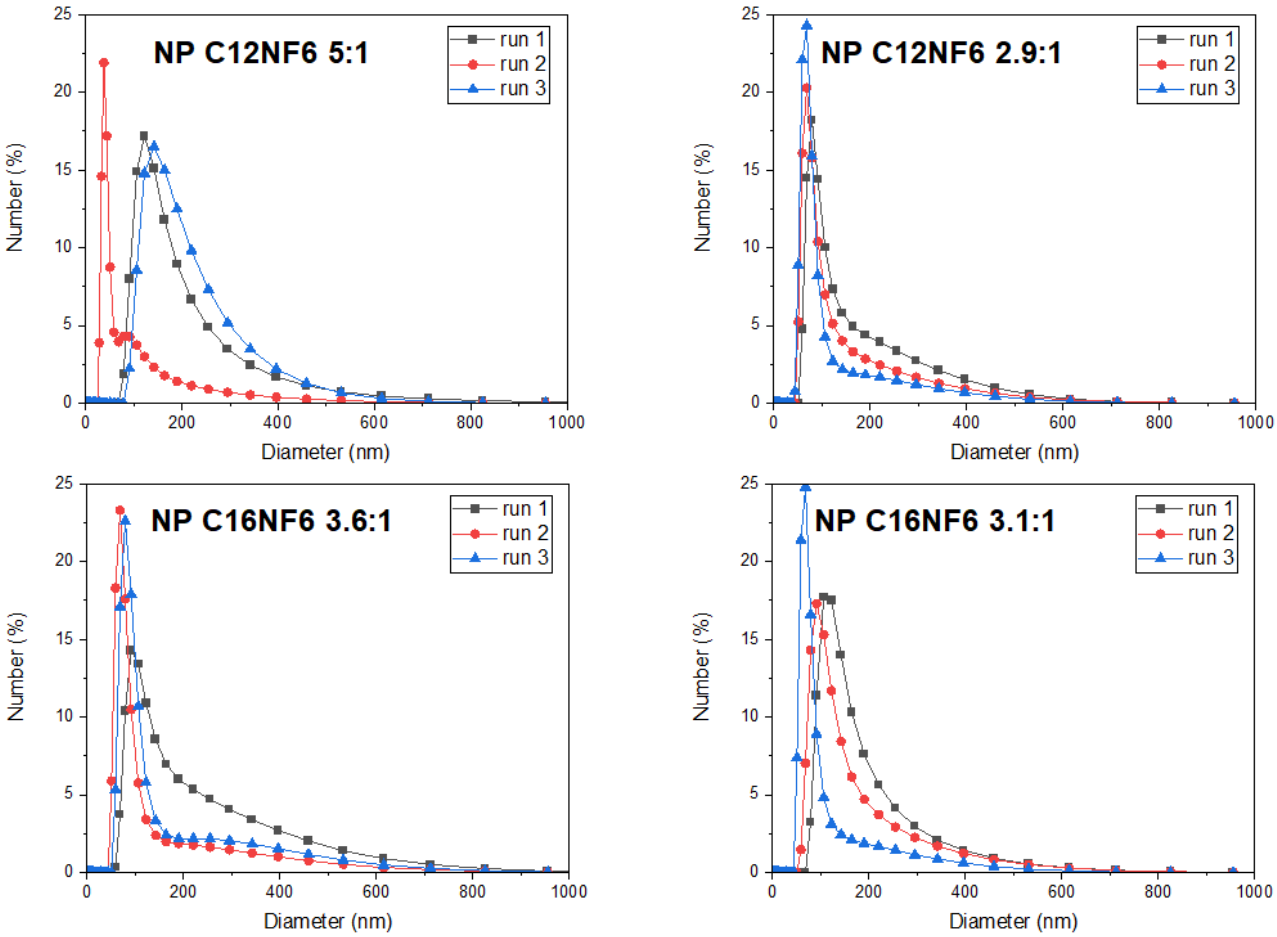

Figure 3.71. DLS analysis of solutions containing L_1 ([lipid] 0.1 mg/mL) and heteroligand AuNPs ([AuNPs] 0.05 mg/mL) in PBS.

As shown in Figure 3.70, in the presence of the homoligand AuNPs, the distribution curve shifts to higher diameters and broaden, especially in the case of usNP C12. However, for heteroligand AuNPs, this shift is definitely reduced (Figure 3.71). These data may suggest some degree of disruption of the liposomal membrane, but there are also studies in which TEM analyses of zwitterionic liposomes interacting with anionic nanoparticles result in. cooperative aggregation to form inhomogeneous decorations on the lipid surface, that in some cases allow the approach of multiple liposome structures (Figure 3.72b). [42] On the other hand, some TEM images have shown linear and cooperative wrappings where the AuNPs appear to be enclosed in tubular structures within the lipid bilayers (Figure 3.72a).

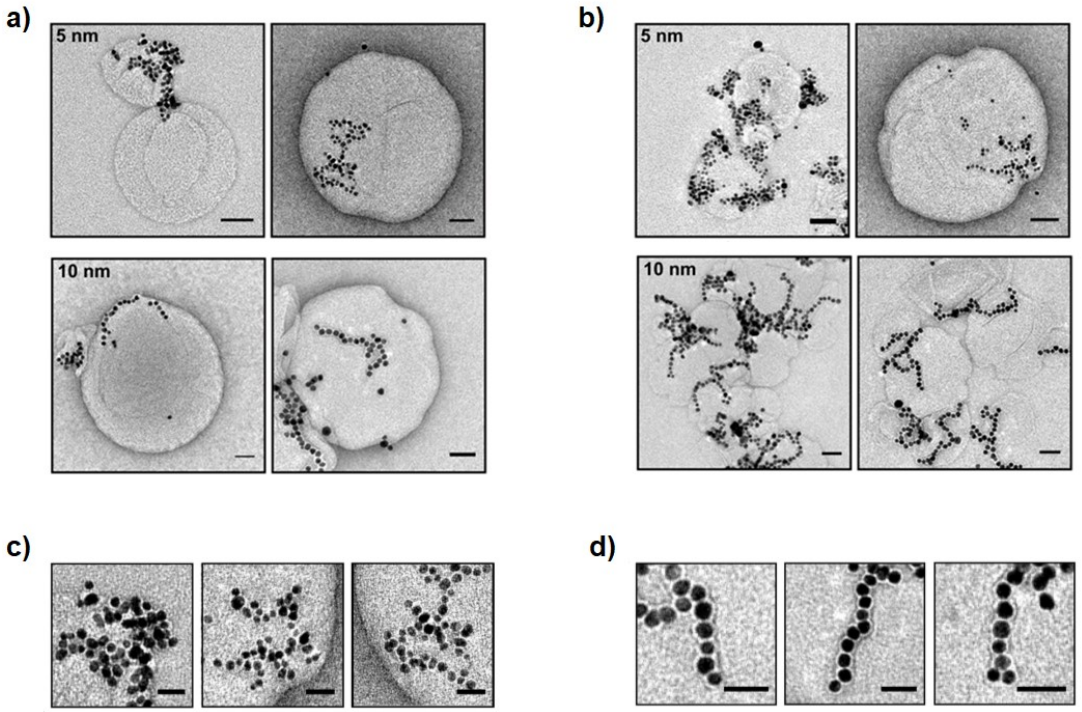

Figure 3.72. The TEM images reported for AuNP-liposome mixtures analysed. In detail, liposomes composed by DOPC (**a**) and POPC (**b**) are injected in a citrate-AuNPs solution. The images showed the AuNPs aggregation on the liposome surface, particularly evident for 5 nm AuNPs, and the formation of an inhomogeneous decoration of the lipid vesicles. Figures **d** and **c** reported the presence of a linear cooperative aggregation longitudinal and perpendicular to the bilayer and absorption plane (tubulation) of small 10 nm AuNPs. Scale bar 50 nm. Adapted from Contini, C. et al. *Commun. Chem*. **2020**, 3 (1), 130.

Using these results as a reference, it could be inferred that the homoligand AuNPs tend to aggregate on the lipid surface, promoting the approach of several liposomes. On the other hand, heteroligand AuNPs could interact more closely with the lipid membrane due to the presence of fluorinated ligands thus preventing the bridging of different liposomes. Further studies will be needed to assess whether, for these nanoparticles systems, the transition to a lower size regime affects the size distribution of the liposomes L_1 and L_2.

3.8 Fluorescence studies of AuNPs-PPP-OPSO$_3$ in the presence of bacteria: preliminary *in vitro* analysis

In collaboration with the group of Prof.ssa Cristina Airoldi and prof. Alessandro Palmioli at Università of Milano-Bicocca, the quenching efficiency toward PPP-OSO$_3$ of four batches of nanoparticles, namely NP C12N, NP C16N, NP C12NF6 (2.9:1), and NP C16NF6 (3.1:1), have been analysed in the presence of four bacterial strains (*E. coli, P. putida, S. epidermidis, and M smegmatis*),

using similar conditions described for the fluorescence studies with the anionic liposomes. In detail, 0.05 mg/mL of AuNPs have been incubated with the analysed bacterial strain (OD_{600} 0.1) for 5 minutes at room temperature in a phosphate saline buffer (10 mM). Afterward, PPP-OSO_3 was added to the solution obtaining a polymer concentration of 0.006 mg/mL, and the resulting system was left to incubate for two minutes. Then, the fluorescence intensity of PPP-OSO_3 was recorded. The chosen bacterial strains are composed of two Gram-negative bacteria (*E. coli, P. putida*), a Gram-positive bacterium (*S. epidermidis*), and a mycobacterium (*M. smegmatis*). To clarify, the fluorescence signal of free PPP-OSO_3 at the same concentration in PBS (without the bacteria and nanoparticles) exceeds the maximum intensity detectable by the fluorometer used for these biological analyses. The corresponding fluorescence results are reported in Figure 3.73.

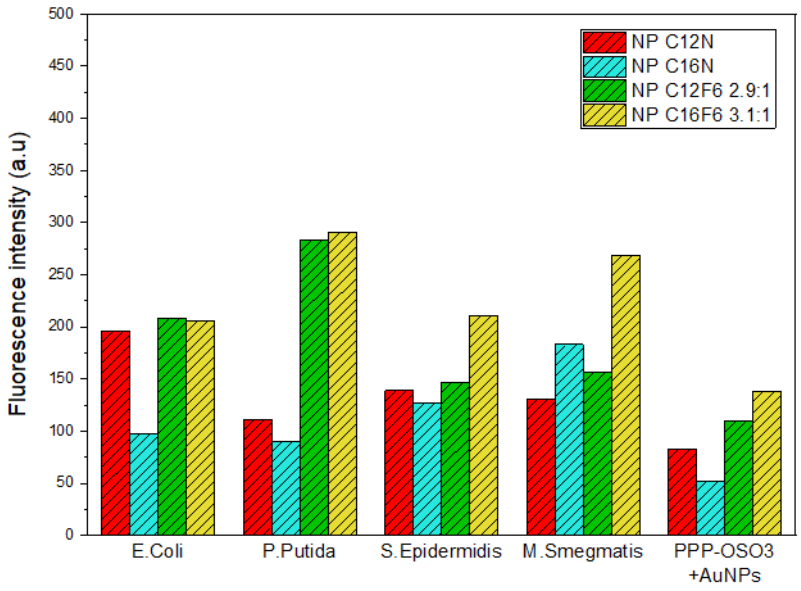

Figure 3.73. Fluorescence intensity at 425 nm of 0.006 mg/mL PPP-OSO_3 in PBS (10 mM) in the presence of a bacterial strain (OD 0.1) incubated with each batch of AuNPs (0.05 mg/mL). The latter column is referred to the fluorescence signals of solutions containing 0.006 mg/mL PPP-OSO_3 and nanoparticles (0.05 mg/mL).

As control experiments, they evaluated the fluorescence intensity of PPP-OSO_3 in a 10mM phosphate saline buffer in the presence of each bacterial strain, observing the same saturated fluorescence signal obtained by the free PPP-OSO_3 solution. These results suggest that the interactions between the PPP-OSO_3 and the elements present on the outer membranes of the chosen bacterial strains, if any, do not affect the fluorescence of the polymer. The fluorescence signals measured at 425 nm of each bacteria strain/AuNPs solution are converted into a color-intensity scale, with the aim of underlining the different fluorescence patterns (Figure 3.74).

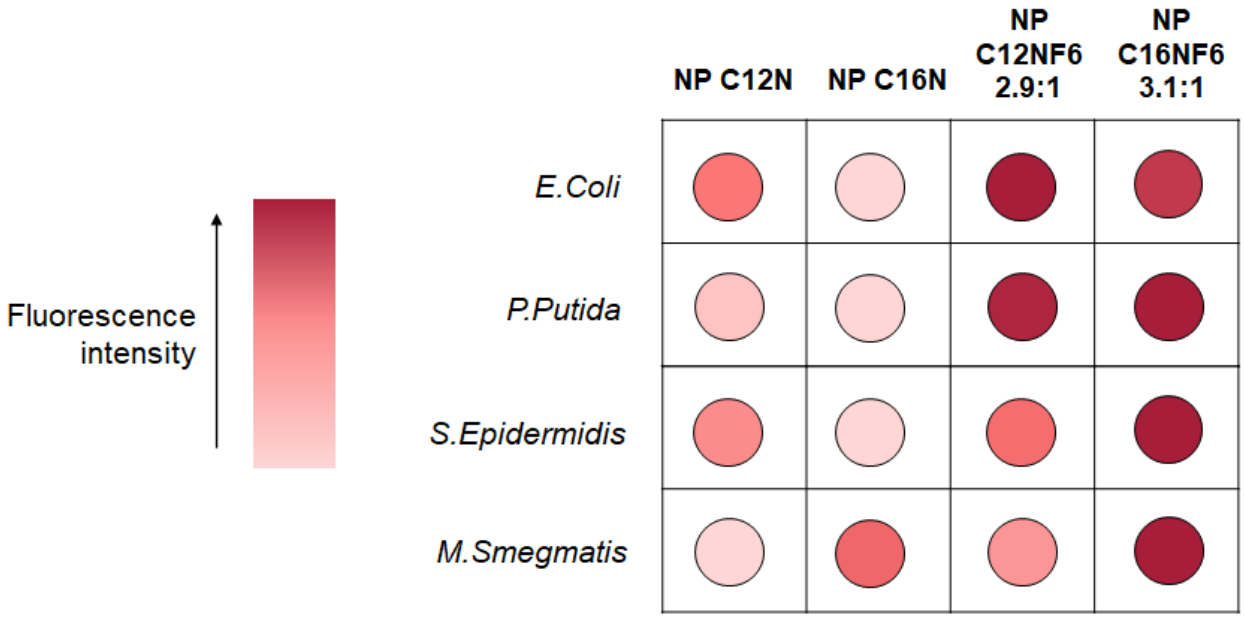

Figure 3.74. Conversion of fluorescence intensity at 425 nm of AuNPs-bacteria solution into a color-intensity scale at an [PPP-OPSO$_3$] of 0.006 mg/mL.

Referring to Figure 3.74, it is interesting to note that the heteroligand AuNPs are the ones that seem to interact most efficiently with the bacterial membrane in almost all the experiments. This is in good agreement with what observed in the case of anionic liposomes, supporting the hypothesis that the fluorinated moiety allows the targeting of different pathogen-associated molecular patterns exposed on the outer bacterial wall via hydrophobic interactions. Even considering a restricted library composed only of the NP C12N, NP C16N, NP C12F6 (2.9:1) and NP C16NF6 (3.1:1) the discrimination of the Gram-negative *E. coli* and *P. putida* respect to the Gram-positive *E. epidermidis* and the mycobacterium *M. smegmatis* was very promising. Moreover, even between the two Gram-negative bacteria (*E. coli* and *P. putida*), where the difference in the fluorescence pattern is less pronounced this still remains noticeable. Despite preliminary, these results constitute a first clue that our approach is able to provide a rapid differentiation of bacteria stains.

References

(1) Bidoggia, S.; Milocco, F.; Polizzi, S.; Canton, P.; Saccani, A.; Sanavio, B.; Krol, S.; Stellacci, F.; Pengo, P.; Pasquato, L. Fluorinated and Charged Hydrogenated Alkanethiolates Grafted on Gold: Expanding the Diversity of Mixed-Monolayer Nanoparticles for Biological Applications. *Bioconjugate Chem.* **2017**, *28* (1), 43–52. https://doi.org/10.1021/acs.bioconjchem.6b00585.

(2) Miranda, O. R.; Chen, H.-T.; You, C.-C.; Mortenson, D. E.; Yang, X.-C.; Bunz, U. H. F.; Rotello, V. M. Enzyme-Amplified Array Sensing of Proteins in Solution and in Biofluids. *J. Am. Chem. Soc.* **2010**, *132* (14), 5285–5289. https://doi.org/10.1021/ja1006756.

(3) Paulini, R.; Frankamp, B. L.; Rotello, V. M. Effects of Branched Ligands on the Structure and Stability of Monolayers on Gold Nanoparticles. *Langmuir* **2002**, *18* (6), 2368–2373. https://doi.org/10.1021/la0155395.

(4) Pellizzoni, E.; Şologan, M.; Daka, M.; Pengo, P.; Marson, D.; Posel, Z.; Franchi, S.; Bignardi, L.; Franchi, P.; Lucarini, M.; Posocco, P.; Pasquato, L. Thiolate End-Group Regulates Ligand Arrangement, Hydration and Affinity for Small Compounds in Monolayer-Protected Gold Nanoparticles. *Journal of Colloid and Interface Science* **2022**, *607*, 1373–1381. https://doi.org/10.1016/j.jcis.2021.09.083.

(5) Hassinen, J.; Liljeström, V.; Kostiainen, M. A.; Ras, R. H. A. Rapid Cationization of Gold Nanoparticles by Two-Step Phase Transfer. *Angewandte Chemie* **2015**, *127* (27), 8101–8104. https://doi.org/10.1002/ange.201503655.

(6) Joseph, Y.; Besnard, I.; Rosenberger, M.; Guse, B.; Nothofer, H.-G.; Wessels, J. M.; Wild, U.; Knop-Gericke, A.; Su, D.; Schlögl, R.; Yasuda, A.; Vossmeyer, T. Self-Assembled Gold Nanoparticle/Alkanedithiol Films: Preparation, Electron Microscopy, XPS-Analysis, Charge Transport, and Vapor-Sensing Properties. *J. Phys. Chem. B* **2003**, *107* (30), 7406–7413. https://doi.org/10.1021/jp030439o.

(7) Weare, W. W.; Reed, S. M.; Warner, M. G.; Hutchison, J. E. Improved Synthesis of Small (DCORE ≈ 1.5 Nm) Phosphine-Stabilized Gold Nanoparticles. *J. Am. Chem. Soc.* **2000**, *122* (51), 12890–12891. https://doi.org/10.1021/ja002673n.

(8) Woehrle, G. H.; Brown, L. O.; Hutchison, J. E. Thiol-Functionalized, 1.5-Nm Gold Nanoparticles through Ligand Exchange Reactions: Scope and Mechanism of Ligand Exchange. *J. Am. Chem. Soc.* **2005**, *127* (7), 2172–2183. https://doi.org/10.1021/ja0457718.

(9) Manea, F.; Bindoli, C.; Polizzi, S.; Lay, L.; Scrimin, P. Expeditious Synthesis of Water-Soluble, Monolayer-Protected Gold Nanoparticles of Controlled Size and Monolayer Composition. *Langmuir* **2008**, *24* (8), 4120–4124. https://doi.org/10.1021/la703558y.

(10) Jana, N. R.; Peng, X. Single-Phase and Gram-Scale Routes toward Nearly Monodisperse Au and Other Noble Metal Nanocrystals. *J. Am. Chem. Soc.* **2003**, *125* (47), 14280–14281. https://doi.org/10.1021/ja038219b.

(11) Hühn, J.; Carrillo-Carrion, C.; Soliman, M. G.; Pfeiffer, C.; Valdeperez, D.; Masood, A.; Chakraborty, I.; Zhu, L.; Gallego, M.; Yue, Z.; Carril, M.; Feliu, N.; Escudero, A.; Alkilany, A. M.; Pelaz, B.; del Pino, P.; Parak, W. J. Selected Standard Protocols for the Synthesis, Phase Transfer, and Characterization of Inorganic Colloidal Nanoparticles. *Chem. Mater.* **2017**, *29* (1), 399–461. https://doi.org/10.1021/acs.chemmater.6b04738.

(12) Hostetler, M. J.; Wingate, J. E.; Zhong, C.-J.; Harris, J. E.; Vachet, R. W.; Clark, M. R.; Londono, J. D.; Green, S. J.; Stokes, J. J.; Wignall, G. D.; Glish, G. L.; Porter, M. D.; Evans, N. D.; Murray, R. W. Alkanethiolate Gold Cluster Molecules with Core Diameters from 1.5 to 5.2 Nm: Core and Monolayer Properties as a Function of Core Size. *Langmuir* **1998**, *14* (1), 17–30. https://doi.org/10.1021/la970588w.

(13) Wu, M.; Vartanian, A. M.; Chong, G.; Pandiakumar, A. K.; Hamers, R. J.; Hernandez, R.; Murphy, C. J. Solution NMR Analysis of Ligand Environment in Quaternary Ammonium-Terminated Self-Assembled Monolayers on Gold Nanoparticles: The Effect of Surface Curvature and Ligand Structure. *J. Am. Chem. Soc.* **2019**, *141* (10), 4316–4327. https://doi.org/10.1021/jacs.8b11445.

(14) Lata, K.; Jaiswal, A.; Naik, L.; Sharma, R. Gold Nanoparticles: Preparation, Characterization and Its Stability in Buffer. *Nano Trends: A Journal of Nanotechnology and Its Applications* **2015**, *17*, 1–10.

(15) White, B.; Banerjee, S.; O'Brien, S.; Turro, N. J.; Herman, I. P. Zeta-Potential Measurements of Surfactant-Wrapped Individual Single-Walled Carbon Nanotubes. *J. Phys. Chem. C* **2007**, *111* (37), 13684–13690. https://doi.org/10.1021/jp070853e.

(16) Hu, G.; Jin, R.; Jiang, D. Beyond the Staple Motif: A New Order at the Thiolate–Gold Interface. *Nanoscale* **2016**, *8* (48), 20103–20110. https://doi.org/10.1039/C6NR07709A.

(17) Zeng, C. Precision at the Nanoscale: On the Structure and Property Evolution of Gold Nanoclusters. *Pure and Applied Chemistry* **2018**, *90* (9), 1409–1427. https://doi.org/10.1515/pac-2018-0511.

(18) Pyo, K.; Thanthirige, V. D.; Kwak, K.; Pandurangan, P.; Ramakrishna, G.; Lee, D. Ultrabright Luminescence from Gold Nanoclusters: Rigidifying the Au(I)–Thiolate Shell. *J. Am. Chem. Soc.* **2015**, *137* (25), 8244–8250. https://doi.org/10.1021/jacs.5b04210.

(19) Wu, Z.; Du, Y.; Liu, J.; Yao, Q.; Chen, T.; Cao, Y.; Zhang, H.; Xie, J. Aurophilic Interactions in the Self-Assembly of Gold Nanoclusters into Nanoribbons with Enhanced Luminescence. *Angewandte Chemie International Edition* **2019**, *58* (24), 8139–8144. https://doi.org/10.1002/anie.201903584.

(20) Zhu, C.; Xin, J.; Li, J.; Li, H.; Kang, X.; Pei, Y.; Zhu, M. Fluorescence or Phosphorescence? The Metallic Composition of the Nanocluster Kernel Does Matter. *Angewandte Chemie International Edition* **2022**, *61* (31), e202205947. https://doi.org/10.1002/anie.202205947.

(21) Canola, S.; Mardegan, L.; Bergamini, G.; Villa, M.; Acocella, A.; Zangoli, M.; Ravotto, L.; Vinogradov, S. A.; Di Maria, F.; Ceroni, P.; Negri, F. One- and Two-Photon Absorption Properties of Quadrupolar Thiophene-Based Dyes with Acceptors of Varying Strengths. *Photochem Photobiol Sci* **2019**, *18* (9), 2180–2190. https://doi.org/10.1039/c9pp00006b.

(22) Li, Q.; Zeman, C. J. I.; Schatz, G. C.; Gu, X. W. Source of Bright Near-Infrared Luminescence in Gold Nanoclusters. *ACS Nano* **2021**, *15* (10), 16095–16105. https://doi.org/10.1021/acsnano.1c04759.

(23) Lin, C.-A. J.; Sperling, R. A.; Li, J. K.; Yang, T.-Y.; Li, P.-Y.; Zanella, M.; Chang, W. H.; Parak, W. J. Design of an Amphiphilic Polymer for Nanoparticle Coating and Functionalization. *Small* **2008**, *4* (3), 334–341. https://doi.org/10.1002/smll.200700654.

(24) Şologan, M.; Gentilini, C.; Bidoggia, S.; Boccalon, M.; Pace, A.; Pengo, P.; Pasquato, L. Gold Nanoparticles Protected by Mixed Hydrogenated/Fluorinated Monolayers: Controlling and Exploring the Surface Features. *J Nanopart Res* **2018**, *20* (6), 152. https://doi.org/10.1007/s11051-018-4231-5.

(25) Marson, D.; Guida, F.; Şologan, M.; Boccardo, S.; Pengo, P.; Perissinotto, F.; Iacuzzi, V.; Pellizzoni, E.; Polizzi, S.; Casalis, L.; Pasquato, L.; Pacor, S.; Tossi, A.; Posocco, P. Mixed Fluorinated/Hydrogenated Self-Assembled Monolayer-Protected Gold Nanoparticles: In Silico and In Vitro Behavior. *Small* **2019**, *15* (17), 1900323. https://doi.org/10.1002/smll.201900323.

(26) Şologan, M.; Marson, D.; Polizzi, S.; Pengo, P.; Boccardo, S.; Pricl, S.; Posocco, P.; Pasquato, L. Patchy and Janus Nanoparticles by Self-Organization of Mixtures of Fluorinated and Hydrogenated Alkanethiolates on the Surface of a Gold Core. *ACS Nano* **2016**, *10* (10), 9316–9325. https://doi.org/10.1021/acsnano.6b03931.

(27) Gabellini, C.; Şologan, M.; Pellizzoni, E.; Marson, D.; Daka, M.; Franchi, P.; Bignardi, L.; Franchi, S.; Posel, Z.; Baraldi, A.; Pengo, P.; Lucarini, M.; Pasquato, L.; Posocco, P. Spotting Local Environments in Self-Assembled Monolayer-Protected Gold Nanoparticles. *ACS Nano* **2022**, *16* (12), 20902–20914. https://doi.org/10.1021/acsnano.2c08467.

(28) Yao, H.; Fukui, C. Size and Morphology Effects on the Fluorescence Properties of π-Conjugated Poly(p-Phenylene) Polyelectrolyte Nanoparticles Synthesized via Polyion Association. *J. Mater. Chem. C* **2016**, *4* (14), 2945–2953. https://doi.org/10.1039/C5TC03337C.

(29) Wang, J.; Wang, D.; Miller, E. K.; Moses, D.; Bazan, G. C.; Heeger, A. J. Photoluminescence of Water-Soluble Conjugated Polymers: Origin of Enhanced Quenching by Charge Transfer. *Macromolecules* **2000**, *33* (14), 5153–5158. https://doi.org/10.1021/ma000081j.

(30) Thordarson, P. Determining Association Constants from Titration Experiments in Supramolecular Chemistry. *Chem. Soc. Rev.* **2011**, *40* (3), 1305–1323. https://doi.org/10.1039/C0CS00062K.

(31) Canepa, E.; Salassi, S.; Marco, A. L. de; Lambruschini, C.; Odino, D.; Bochicchio, D.; Canepa, F.; Canale, C.; Dante, S.; Brescia, R.; Stellacci, F.; Rossi, G.; Relini, A. Amphiphilic Gold Nanoparticles Perturb Phase Separation in Multidomain Lipid Membranes. *Nanoscale* **2020**, *12* (38), 19746–19759. https://doi.org/10.1039/D0NR05366J.

(32) Hou, W.-C.; Moghadam, B. Y.; Corredor, C.; Westerhoff, P.; Posner, J. D. Distribution of Functionalized Gold Nanoparticles between Water and Lipid Bilayers as Model Cell Membranes. *Environ. Sci. Technol.* **2012**, *46* (3), 1869–1876. https://doi.org/10.1021/es203661k.

(33) William, N.; Bamidoro, F.; Beales, P. A.; Drummond-Brydson, R.; Hondow, N.; Key, S.; Kulak, A.; Walsh, A. C.; Winter, S.; Nelson, L. A. Tuning Stable Noble Metal Nanoparticles Dispersions to Moderate Their Interaction with Model Membranes. *Journal of Colloid and Interface Science* **2021**, *594*, 101–112. https://doi.org/10.1016/j.jcis.2021.03.009.

(34) Montis, C.; Generini, V.; Boccalini, G.; Bergese, P.; Bani, D.; Berti, D. Model Lipid Bilayers Mimic Non-Specific Interactions of Gold Nanoparticles with Macrophage Plasma Membranes. *Journal of Colloid and Interface Science* **2018**, *516*, 284–294. https://doi.org/10.1016/j.jcis.2018.01.064.

(35) Michel, R.; Gradzielski, M. Experimental Aspects of Colloidal Interactions in Mixed Systems of Liposome and Inorganic Nanoparticle and Their Applications. *International Journal of Molecular Sciences* **2012**, *13* (9), 11610–11642. https://doi.org/10.3390/ijms130911610.

(36) Pfeiffer, T.; De Nicola, A.; Montis, C.; Carlà, F.; van der Vegt, N. F. A.; Berti, D.; Milano, G. Nanoparticles at Biomimetic Interfaces: Combined Experimental and Simulation Study on Charged Gold Nanoparticles/Lipid Bilayer Interfaces. *J. Phys. Chem. Lett.* **2019**, *10* (2), 129–137. https://doi.org/10.1021/acs.jpclett.8b03399.

(37) Routledge, S. J.; Linney, J. A.; Goddard, A. D. Liposomes as Models for Membrane Integrity. *Biochemical Society Transactions* **2019**, *47* (3), 919–932. https://doi.org/10.1042/BST20190123.

(38) Kopec, W.; Żak, A.; Jamróz, D.; Nakahata, R.; Yusa, S.; Gapsys, V.; Kepczynski, M. Polycation–Anionic Lipid Membrane Interactions. *Langmuir* **2020**, *36* (42), 12435–12450. https://doi.org/10.1021/acs.langmuir.0c01062.

(39) Rasmussen, M. K.; Pedersen, J. N.; Marie, R. Size and Surface Charge Characterization of Nanoparticles with a Salt Gradient. *Nat Commun* **2020**, *11* (1), 2337. https://doi.org/10.1038/s41467-020-15889-3.

(40) Marson, D.; Guida, F.; Şologan, M.; Boccardo, S.; Pengo, P.; Perissinotto, F.; Iacuzzi, V.; Pellizzoni, E.; Polizzi, S.; Casalis, L.; Pasquato, L.; Pacor, S.; Tossi, A.; Posocco, P. Mixed Fluorinated/Hydrogenated Self-Assembled Monolayer-Protected Gold Nanoparticles: In Silico and In Vitro Behavior. *Small* **2019**, *15* (17), 1900323. https://doi.org/10.1002/smll.201900323.

(41) Morillas-Becerril, L.; Franco-Ulloa, S.; Fortunati, I.; Marotta, R.; Sun, X.; Zanoni, G.; De Vivo, M.; Mancin, F. Specific and Nondisruptive Interaction of Guanidium-Functionalized Gold

Nanoparticles with Neutral Phospholipid Bilayers. *Commun Chem* **2021**, *4* (1), 1–12. https://doi.org/10.1038/s42004-021-00526-x.

(42) Contini, C.; Hindley, J. W.; Macdonald, T. J.; Barritt, J. D.; Ces, O.; Quirke, N. Size Dependency of Gold Nanoparticles Interacting with Model Membranes. *Commun Chem* **2020**, *3* (1), 1–12. https://doi.org/10.1038/s42004-020-00377-y.

(43) Boisselier, E.; Salmon, L.; Ruiz, J.; Astruc, D. How to Very Efficiently Functionalize Gold Nanoparticles by "Click" Chemistry. *Chem. Commun.* **2008**, No. 44, 5788–5790. https://doi.org/10.1039/B812249K.

(44) Li, N.; Binder, W. H. Click-Chemistry for Nanoparticle-Modification. *J. Mater. Chem.* **2011**, *21* (42), 16717–16734. https://doi.org/10.1039/C1JM11558H.

(45) van der Meer, S. B.; Loza, K.; Wey, K.; Heggen, M.; Beuck, C.; Bayer, P.; Epple, M. Click Chemistry on the Surface of Ultrasmall Gold Nanoparticles (2 Nm) for Covalent Ligand Attachment Followed by NMR Spectroscopy. *Langmuir* **2019**, *35* (22), 7191–7204. https://doi.org/10.1021/acs.langmuir.9b00295.

(46) Kolb, H. C.; Finn, M. G.; Sharpless, K. B. Click Chemistry: Diverse Chemical Function from a Few Good Reactions. *Angewandte Chemie International Edition* **2001**, *40* (11), 2004–2021. https://doi.org/10.1002/1521-3773(20010601)40:11<2004::AID-ANIE2004>3.0.CO;2-5.

(47) Huisgen, R. 1,3-Dipolar Cycloadditions. Past and Future. *Angewandte Chemie International Edition in English* **1963**, *2* (10), 565–598. https://doi.org/10.1002/anie.196305651.

(48) Huisgen, R. Kinetics and Mechanism of 1,3-Dipolar Cycloadditions. *Angewandte Chemie International Edition in English* **1963**, *2* (11), 633–645. https://doi.org/10.1002/anie.196306331.

(49) Agard, N. J.; Prescher, J. A.; Bertozzi, C. R. A Strain-Promoted [3 + 2] Azide−Alkyne Cycloaddition for Covalent Modification of Biomolecules in Living Systems. *J. Am. Chem. Soc.* **2004**, *126* (46), 15046–15047. https://doi.org/10.1021/ja044996f.

(50) Li, Z.; Seo, T. S.; Ju, J. 1,3-Dipolar Cycloaddition of Azides with Electron-Deficient Alkynes under Mild Condition in Water. *Tetrahedron Letters* **2004**, *45* (15), 3143–3146. https://doi.org/10.1016/j.tetlet.2004.02.089.

(51) McKay, C. S.; Moran, J.; Pezacki, J. P. Nitrones as Dipoles for Rapid Strain-Promoted 1,3-Dipolar Cycloadditions with Cyclooctynes. *Chem. Commun.* **2010**, *46* (6), 931–933. https://doi.org/10.1039/B921630H.

(52) McKay, C. S.; Blake, J. A.; Cheng, J.; Danielson, D. C.; Pezacki, J. P. Strain-Promoted Cycloadditions of Cyclic Nitrones with Cyclooctynes for Labeling Human Cancer Cells. *Chem. Commun.* **2011**, *47* (36), 10040–10042. https://doi.org/10.1039/C1CC13808A.

(53) Ning, X.; Temming, R. P.; Dommerholt, J.; Guo, J.; Ania, D. B.; Debets, M. F.; Wolfert, M. A.; Boons, G.-J.; van Delft, F. L. Protein Modification by Strain-Promoted Alkyne–Nitrone Cycloaddition. *Angewandte Chemie* **2010**, *122* (17), 3129–3132. https://doi.org/10.1002/ange.201000408.

(54) Staudinger, H.; Meyer, J. Über Neue Organische Phosphorverbindungen III. Phosphinmethylenderivate Und Phosphinimine. *Helvetica Chimica Acta* **1919**, *2* (1), 635–646. https://doi.org/10.1002/hlca.19190020164.

(55) Saxon, E.; Bertozzi, C. R. Cell Surface Engineering by a Modified Staudinger Reaction. *Science* **2000**, *287* (5460), 2007–2010. https://doi.org/10.1126/science.287.5460.2007.

(56) Lin, F. L.; Hoyt, H. M.; van Halbeek, H.; Bergman, R. G.; Bertozzi, C. R. Mechanistic Investigation of the Staudinger Ligation. *J. Am. Chem. Soc.* **2005**, *127* (8), 2686–2695. https://doi.org/10.1021/ja044461m.

(57) Dorn, R. S.; Prescher, J. A. Bioorthogonal Phosphines: Then and Now. *Israel Journal of Chemistry* **2023**, *63* (1–2), e202200070. https://doi.org/10.1002/ijch.202200070.

(58) Schilling, C. I.; Jung, N.; Biskup, M.; Schepers, U.; Bräse, S. Bioconjugation Viaazide–Staudinger Ligation: An Overview. *Chem. Soc. Rev.* **2011**, *40* (9), 4840–4871. https://doi.org/10.1039/C0CS00123F.

(59) Köhn, M.; Breinbauer, R. The Staudinger Ligation—A Gift to Chemical Biology. *Angewandte Chemie International Edition* **2004**, *43* (24), 3106–3116. https://doi.org/10.1002/anie.200401744.

(60) van Berkel, S. S.; van Eldijk, M. B.; van Hest, J. C. M. Staudinger Ligation as a Method for Bioconjugation. *Angewandte Chemie International Edition* **2011**, *50* (38), 8806–8827. https://doi.org/10.1002/anie.201008102.

(61) Gobbo, P.; Luo, W.; Cho, S. J.; Wang, X.; Biesinger, M. C.; Hudson, R. H. E.; Workentin, M. S. Small Gold Nanoparticles for Interfacial Staudinger–Bertozzi Ligation. *Org. Biomol. Chem.* **2015**, *13* (15), 4605–4612. https://doi.org/10.1039/C5OB00372E.

(62) Kovalyshyn, S. Sintesi e Caratterizzazione Di Un Legante per Click Chemistry Su Nanoparticelle d'oro. tesi magistrale, Università di Trieste, 2022.

(63) Sharma, R.; Holland, G. P.; Solomon, V. C.; Zimmermann, H.; Schiffenhaus, S.; Amin, S. A.; Buttry, D. A.; Yarger, J. L. NMR Characterization of Ligand Binding and Exchange Dynamics in Triphenylphosphine-Capped Gold Nanoparticles. *J. Phys. Chem. C* **2009**, *113* (37), 16387–16393. https://doi.org/10.1021/jp905141h.

(64) Zhang, S.-S.; Feng, L.; Senanayake, R. D.; Aikens, C. M.; Wang, X.-P.; Zhao, Q.-Q.; Tung, C.-H.; Sun, D. Diphosphine-Protected Ultrasmall Gold Nanoclusters: Opened Icosahedral Au13 and Heart-Shaped Au8 Clusters. *Chem. Sci.* **2018**, *9* (5), 1251–1258. https://doi.org/10.1039/C7SC03566G.

(65) Marbella, L. E.; Crawford, S. E.; Hartmann, M. J.; Millstone, J. E. Observation of Uniform Ligand Environments and 31P–197Au Coupling in Phosphine-Terminated Au Nanoparticles. *Chem. Commun.* **2016**, *52* (58), 9020–9023. https://doi.org/10.1039/C6CC00464D.

(66) Polgar, A. M.; Weigend, F.; Zhang, A.; Stillman, M. J.; Corrigan, J. F. A N-Heterocyclic Carbene-Stabilized Coinage Metal-Chalcogenide Framework with Tunable Optical Properties. *J. Am. Chem. Soc.* **2017**, *139* (40), 14045–14048. https://doi.org/10.1021/jacs.7b09025.

(67) Manea, F.; Bindoli, C.; Polizzi, S.; Lay, L.; Scrimin, P. Expeditious Synthesis of Water-Soluble, Monolayer-Protected Gold Nanoparticles of Controlled Size and Monolayer Composition. *Langmuir* **2008**, *24* (8), 4120–4124. https://doi.org/10.1021/la703558y.

(68) Luo, W.; Gobbo, P.; Gunawardene, P. N.; Workentin, M. S. Fluorogenic Gold Nanoparticle (AuNP) Substrate: A Model for the Controlled Release of Molecules from AuNP Nanocarriers via Interfacial Staudinger–Bertozzi Ligation. *Langmuir* **2017**, *33* (8), 1908–1913. https://doi.org/10.1021/acs.langmuir.6b03647.

Chapter 4

4. Peptide-decorated AuNPs

To improve the specific-site interactions with the bacterial membrane components and increase the diversity in the gold nanoparticle library, an array of different positively charged peptide ligands have been designed to generate a second set of SAM-AuNPs. The choice of using amino acids as building blocks of the AuNP ligands should allow further interactions with the different moieties present on the bacterial walls, compared to the no-specific electrostatic interactions due to the sole use of cationic ligands. In this thesis, a preliminary assessment of the viability of peptides conjugation to gold nanoparticles with a click chemistry approach was performed. In particular, we focused on nanoparticle functionalization via the Bertozzi-Staudinger ligation reaction.

4.1 Bioconjugation of AuNPs: click chemistry strategy

The functionalization of AuNPs with biomolecules to achieve the corresponding bioconjugates is a key element for the applications of these nanomaterials in many fields, especially in biology and medicine. Several strategies have been investigated to prepare AuNP bioconjugates for different aims, and generally, they are based on (i) electrostatic interactions between the AuNP monolayer and some moieties on the biomolecule side chains, and (ii) on a direct thiol-to-thiol exchange exploiting thiol-containing biomolecules. These methods generally result in uncontrolled bioconjugation, whereas many applications require precise control over the number of biomolecules introduced on the AuNP monolayer. For this purpose, the formation of covalent bonds between the biomolecules and properly functionalised AuNPs seems to be the most effective strategy. In this contest, a promising method consists in the design of AuNPs that exhibits an interfacial chemoselective reactive moiety that acts as an anchoring group to incorporate the desired biomolecule, exploiting the concept of click chemistry.[1–3]

The term "click chemistry" describes a type of reactions having specific characteristics, such as high yields, high reaction rates, simple purification methods, and producing inoffensive or no by-products.[4] Moreover, click reactions have to be stereospecific and proceed selectively with a particular functional group. Usually, the click reactions are based on a high thermodynamic driving force, usually greater than 20 kcal mol^{-1} to achieve all these requirements. The severe criteria of click chemistry concern also the use of available reagents and materials, non-toxic and easily removable solvents, and mild reaction conditions. These characteristics are also shared by another important concept, namely bioorthogonal chemistry in which a unique motif (chemical reporter) that does not biologically exist in nature is incorporated into a target biomolecule and must react selectively with a functional group present on a probe (Scheme 4.1).

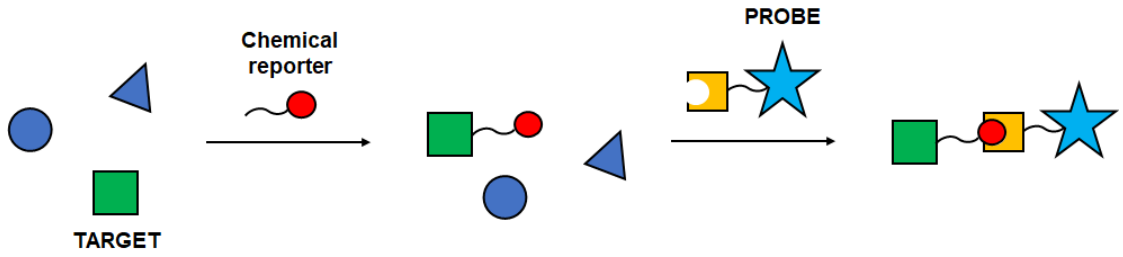

Scheme 4.1. The bioorthogonal chemistry strategy.

The azide group ($R–N_3$) perfectly meets the bioorthogonal criteria, underscored by its small size, its inert nature to many chemical and biological functionalities, and its stability in physiological conditions. Moreover, it is relatively simple to incorporate this functional group even in complex systems. The most common click reactions are indeed those in which an azide and an alkyne react to form a triazole click adduct in the presence of a Cu(I) catalyst: copper catalysed azide alkyne cycloadditions (CuAAC, Scheme 4.2a) and the strain-promoted alkyne-azide cycloaddition (SPAAC, Scheme 4.2b).[5–7]

Scheme 4.2. Schematic illustration of CuAAC (**a**) and SPAAC (**b**).

However, both reactions showed some issues due to respectively the Cu(I) cytotoxicity and the susceptibly of the strained alkynes towards several nucleophiles. To overcome the first, other mechanisms to avoid the addition of Cu(I) have been investigated, but even in these cases, the selected reagents showed a high reactivity towards other nucleophiles besides the azide group.[8] Alternatively, the use of nitrones has been exploited in the reactions known as the strain-promoted alkyne-nitrone

cycloaddition (SPANC),[9–11] however, this strategy exhibits synthetic challenges for nitrones preparation.

In 1919, Staudinger discovered the reaction between azides and phosphines[12], in which the first step involves the nucleophilic attack by the phosphorus atom on the electrophilic nitrogen of the azide to form a phosphazide intermediate. This intermediate undergoes spontaneous rearrangement to produce an iminophosphorane (or azaylide) through the elimination of N_2. In anhydrous conditions, the reaction is stopped at the iminophosphorane. However, in the presence of water, the iminophosphorane is hydrolyzed producing the corresponding primary amine and phosphine oxide (Scheme 4.3). For this reason, the Staudinger reaction has been used often to reduce azides to amines.

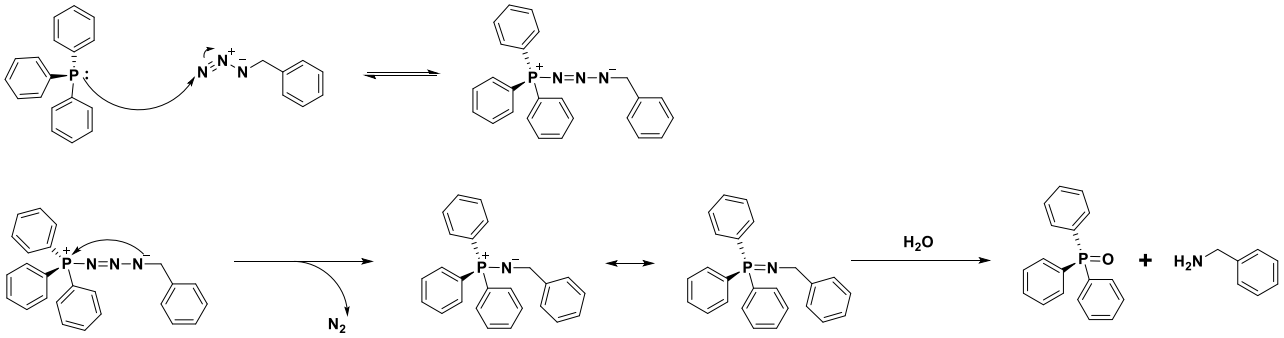

Scheme 4.3. Staudinger mechanism.

The reaction is chemoselective with high yields and requires mild conditions, and both reactive functionalities are abiotic and non-reactive towards biomolecules in agreement with the requirements of bioorthogonal chemistry. However, the hydrolytic instability of the iminophosphorane prevents the use of the Staudinger reaction as a method to robustly tag chemical reporters in living systems. Moreover, the absence of a ligation, i.e., a generation of a new bond between the scaffolds, does not permit to define the Staudinger reaction as a click reaction.

4.2 Staudinger-Bertozzi ligation

Recognizing the potentiality of the Staudinger reaction, Bertozzi and co-workers[13] modified the phosphine structure to enable the rearrangement of the unstable intermediate iminophosphorane to a stable covalent adduct. As they have demonstrated, the addition of a properly positioned "electrophilic trap", such as a methyl ester, within the phosphine structure allows the capture of iminophosphorane via intramolecular cyclization, leading the formation of a stable amide bond (Scheme 4.4).

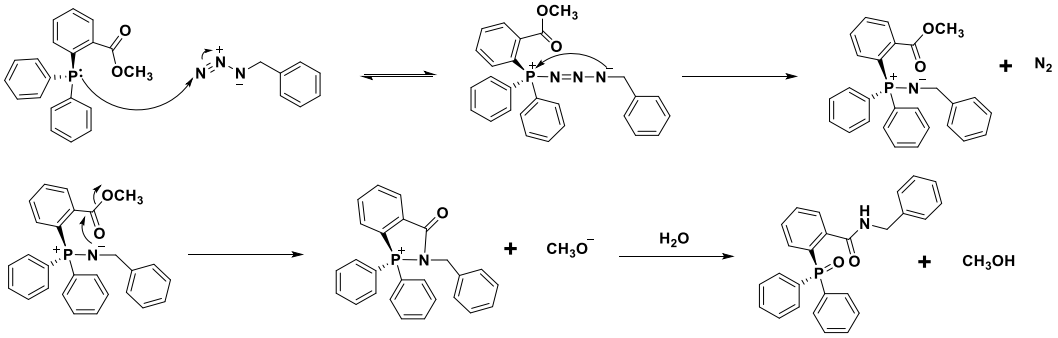

Scheme 4.4. Mechanism of the Staudinger-Bertozzi ligation.

Regarding the kinetics parameters of this reaction, some studies have demonstrated that the rate-determining step of the Staudinger-Bertozzi ligation (SBL) depends on the substitution of the phenyl group bound to the phosphorus atom and on the azide structure (Scheme 4.5).

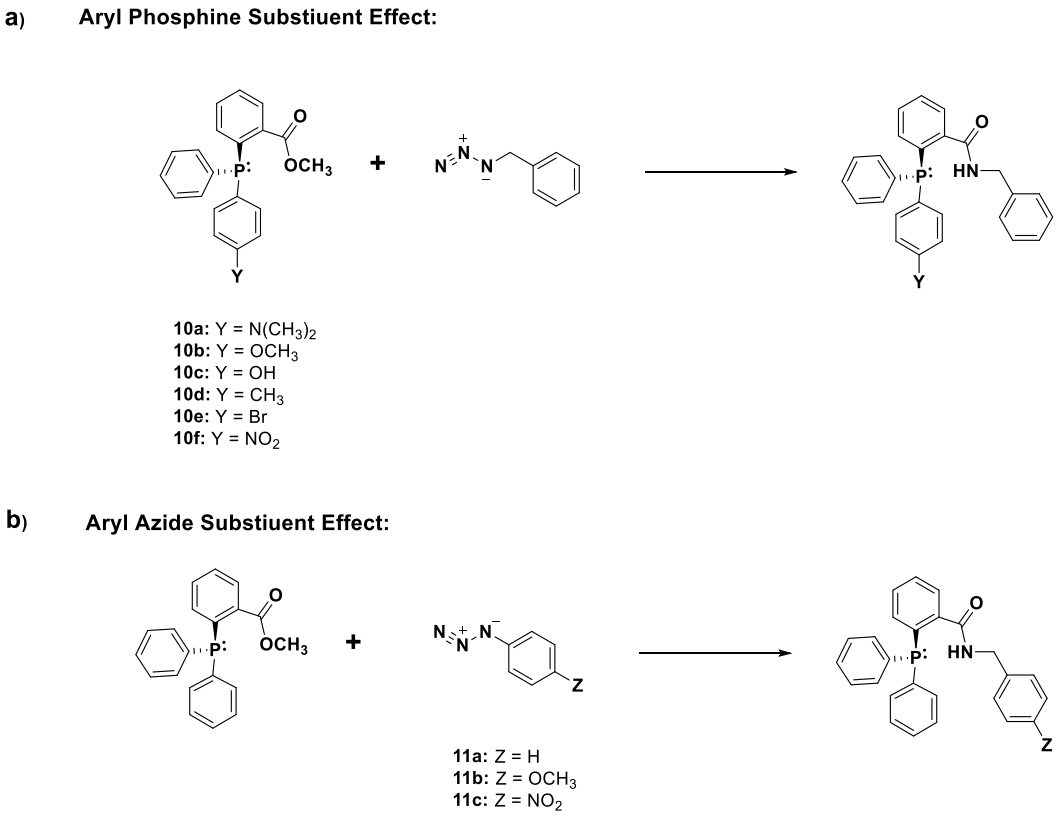

Scheme 4.5. Substituent effects on the rate of the SBL.

By reactions between diversely substituted phosphines and the benzyl azide (Scheme 4.5a), it was found that electron-donating substituents on the aromatic rings greatly accelerate the SBL rate, demonstrating that the rate-determining step is the phosphazide formation (Scheme 4.4, first step). On the other hand, using aryl azides with varying substituents (Scheme 4.5b) it was observed the decrease of the SBL rate with electron withdrawing substituents. In detail, the reaction between the

phosphine and the azide **11a** required about 24 hours, but the reactions with the azide **11b** and **11c** required 8 and 48 hours respectively. These results have suggested that in SBL reactions with aryl azides the rate-determining step is the intramolecular amide bond-forming step, due to the enhanced azaylide stability by resonance stabilization effects. On the other hand, the size of the leaving groups has no influence on the overall rate, but interestingly it affects the ligation/hydrolysis product ratio. Indeed, higher ligation yields have been observed using relatively small ester leaving groups.[14]

Apart from the mechanistic investigations, the considerable potential of the SBL has been confirmed by its applications in numerous fields, from organic synthesis to peptide or protein synthesis, cell surface engineering, dye-labeling of various biomolecules, drug delivery, and coating of microarrays.[15–18]

4.3 Synthesis of AuNP bioconjugates via Staudinger-Bertozzi ligation

As mentioned, characteristics of a click reaction include high chemoselectivity, high yields, and mild conditions. All these aspects are highly attractive both for bioorthogonal chemistry and for the design and functionalization of well-defined AuNP surfaces. In this context, Gobbo *et al.*[19] have reported the effective potential of the Staudinger Bertozzi ligation as a tool to conjugate biomolecules onto the AuNP surface. In particular, they have designed and synthetised a specific thiol-containing the methyl-2-(diphenylphosphino)benzoate group to prepare novel reactive AuNPs defined as Staudinger-AuNPs (Scheme 4.6). The introduction of this ligand on the surface of the nanoparticles has occurred through a thiol-to-thiol exchange obtaining the corresponding water-soluble Staudinger-AuNPs. To test the high chemoselectivity of these nanoparticles, the authors have chosen an azide-modified peptide (CRGDK) and followed the reaction with the Staudinger-AuNPs by ^{31}P-NMR spectroscopy. The resulting ^{31}P-NMR-spectrum of the SBL product showed that the reaction stopped at ~30% because of the large size of the peptide.

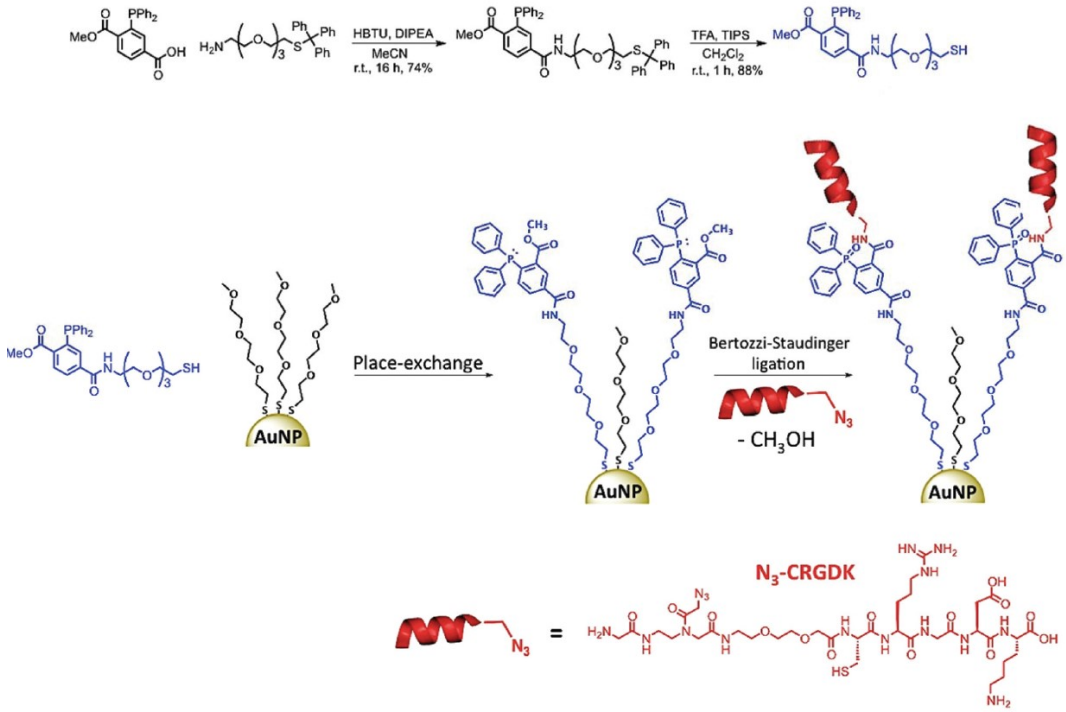

Scheme 4.6. Synthetic strategy for obtaining the Staudinger-AuNPs. From Gobbo, P. et al. Org. Biomol. Chem. 2015, 13 (15), 4605–4612.

Inspired by this work, this strategy has been adapted to explore the possibility of generating "activated" nanoparticles for conjugation with (bio)molecules through a click-chemistry approach, aiming to increase the diversity of the AuNPs library to be used for bacteria recognition. In this chapter the results obtained in the synthesis of AuNPs of various sizes activated with a methyl-2-(diphenylphosphino)benzoate motif on their outer surface will be illustrated and discussed.

Part of the activities of this project involved a MSc student carrying out her experimental thesis work. [20] These activities included the synthesis and characterization of ligand **12** (Figure 4.1) for the preparation of both homoligand and heteroligand "activated" AuNPs.

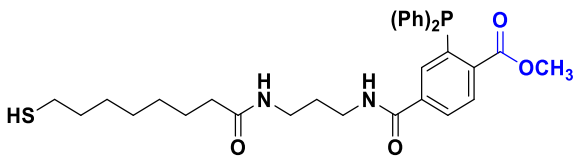

Figure 4.1. Structure of ligand **12** contains the methyl-2-(diphenylphosphino)benzoate motif.

For this preliminary study the synthesis of heteroligand activated AuNPs has been performed using blends of **12** in combination with the commercially available (11-Mercaptoundecyl)-*N,N,N*-trimethylammonium bromide (**HC11N**) instead of the ligands **HC12N** and **HC16N**, which ensures

the obtainment of water-soluble nanoparticles and electrostatic interactions with the bacterial wall elements.

The ligand **12** has been used for the preparation of heteroligand nanoparticles of 2 and 4 nm in a mixture of **HC11N**. Mixtures of **12** with **HC11N** were prepared to coat nanoparticles of ~ 2 and ~ 4 nm, but only in some cases it was possible to obtain mixed monolayer nanoparticles comprising a discrete amount of **12** in their monolayer and a good stability. For the preparation of these heteroligand AuNPs, direct synthesis and thiol-to-thiol exchange have been used for the AuNPs preparation.

However, the introduction of **12** into the nanoparticle monolayer was not easy, obtaining AuNPs with a small fraction of **12** on their monolayer both via direct synthesis and thiol-to-thiol exchange. These observations are in line with the high bulkiness of **12**. Overall, the preparations of activated AuNPs, turned out, in our hand, to be cumbersome and the materials obtained not very stable likely because of the considerable steric hindrance of the ligand end-group, which does not allow to obtain well-packed and therefore stable monolayers. Furthermore, secondary effects due to the establishment of bonds between the gold surface and the phosphorus atom of **12** cannot be excluded. This observation is based on the remarkable increase in the chemical shift of this atom shown ^{31}P-NMR after the AuNP passivation (from -4.52 ppm to 30.5 ppm).[21–25].

Once an azide-modified amino acid and the activated AuNPs were prepared, an experiment of Staudinger-Bertozzi ligation was carried out to test the validity of this approach on nanoparticles bearing **HC11N** and **12**.

4.4 Synthesis of 12

The ligand **12** was obtained through five synthetic steps with an overall yield of 68%, starting from commercial reagents (Scheme 4.7).

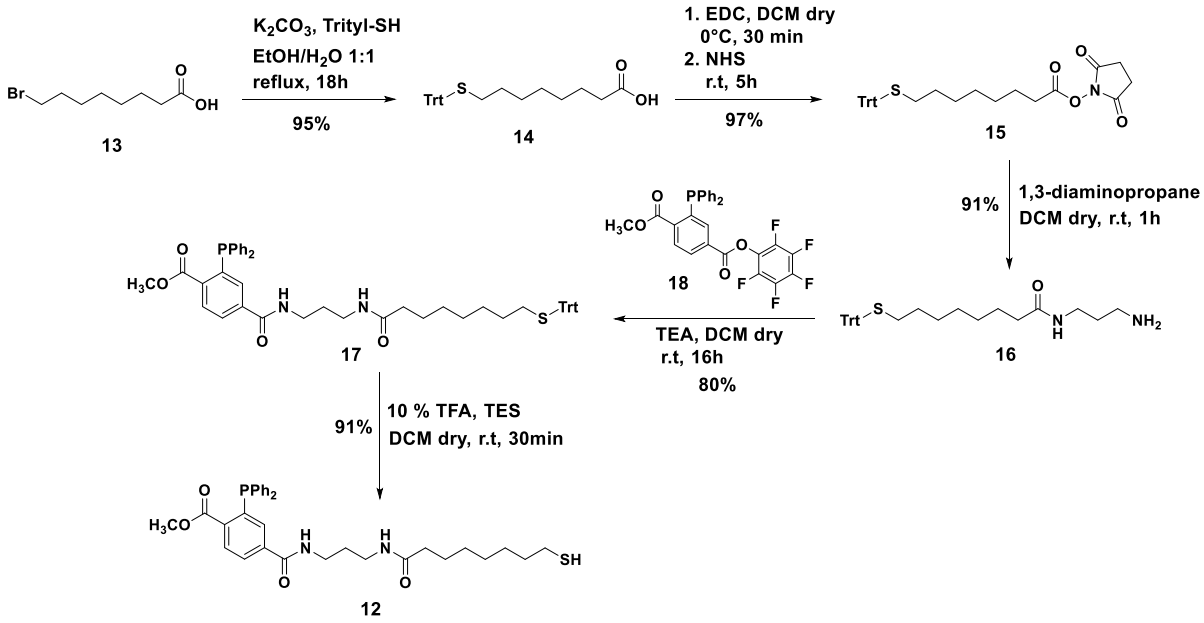

Scheme 4.7. Synthesis scheme of **12**.

The synthetic approach required the preparation of the aminothiol **16**, in which the amino function was used to insert the functional motif requested for the SBL. Regarding the synthesis of compound **16**, the procedure has required the insertion of the thiol function protected by the triphenylmethyl group (Trt) on the commercial 8-bromooctanoic acid (**13**), obtaining the product **14**. The product was obtained with a yield of 95% and the corresponding ^{1}H-NMR spectrum is showed in Figure 4.2.

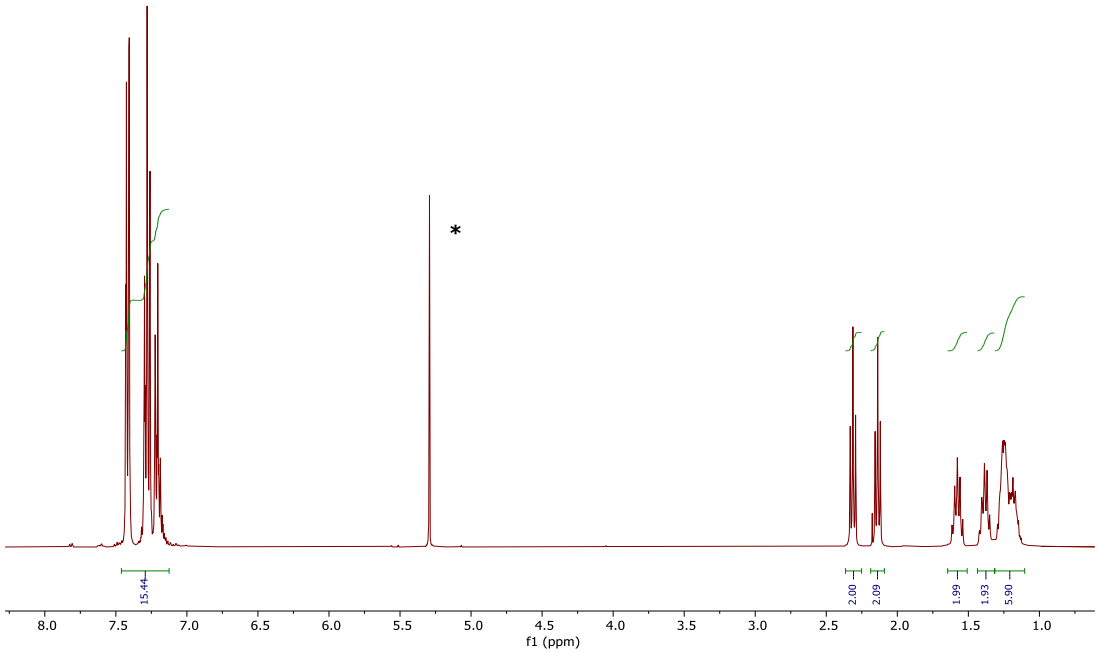

Figure 4.2. ^{1}H-NMR (400 MHz, $CDCl_3$) of product **14**. The solvent peaks are indicated by an asterisk (dichloromethane).

The peak at 2.14 ppm corresponds to the methylene protons in the α to the sulfur atoms, while the multiple peaks in the range of 7.12-7.46 ppm are due to the aromatic protons of the trityl group. The presence of these peaks confirms the success of the reaction.

The carboxyl group of the compound **14** was subsequently converted into an active ester by reaction with *N*-hydroxysuccinimide in the presence of the coupling agent EDC, obtaining the compound **15**. The product was obtained with a yield of 97% and the corresponding ^{1}H-NMR spectrum is showed in Figure 4.3, in which a shift from 2.32 to 2.56 ppm of the peaks due to the methylene protons in α to the carboxyl group is observed.

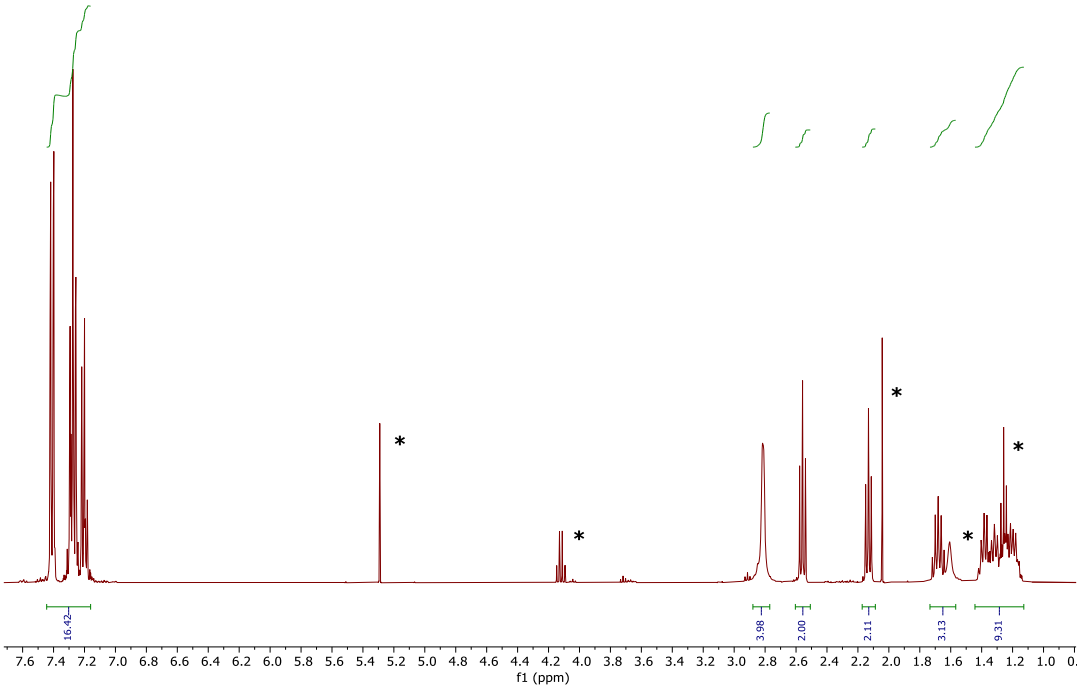

Figure 4.3. ^{1}H-NMR (400 MHz, $CDCl_3$) of product **15**. The solvent peaks are indicated by an asterisk (acetone, ethyl ether, dichloromethane).

The active ester **15** was subsequently converted to compound **16** by reaction with 1,3-diaminopropane. The optimization of the reaction conditions involved the use of an excess of 1,3-diaminopropane to avoid the formation of the di-substitution product. The use of an excess of the diamine did not cause problems for the product isolation since its excess was easily removed by evaporation under reduced pressure. Product **16** was obtained with a yield of 90% and the corresponding ^{1}H-NMR spectrum is shown in Figure 4.4, whose showed peaks are consistent with the product structure. Once the conversion of the ester **15** into the amide **16** is completed, the peaks of the protons in α to the carboxyl group of the former shift to high fields overlapping those of the methylene protons in α to sulfur, generating a multiplet centered at 2.11 ppm.

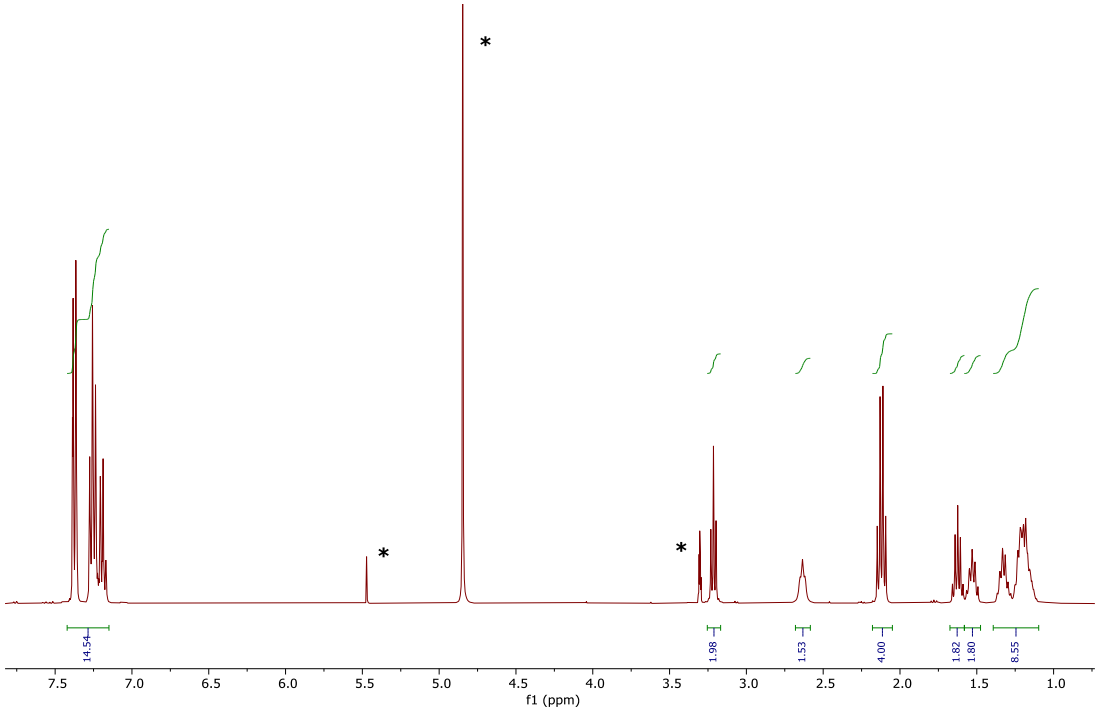

Figure 4.4. ^{1}H-NMR (400 MHz, CD_3OD) of product **16**. The solvent peaks are indicated by an asterisk (methanol, dichloromethane).

Next, a coupling reaction between the product **16** and the 2-(Diphenylphosphino)terephthalic acid 1-methyl 4-pentafluorophenyl diester (**18**) was performed. The reaction was carried out under an argon atmosphere to avoid possible oxidation of the phosphine. Furthermore, all the solvents used in the work-up operations were previously deoxygenated. The coupling product **17** was characterized by ^{1}H-, ^{31}P-NMR spectroscopy to evaluate the presence of reagents and by ^{19}F-NMR to evaluate the residual presence of pentafluorophenol. The corresponding ^{1}H-NMR and ^{31}P-NMR spectra are showed in Figure 4.5 and Figure 4.6, in which only a peak at -4.52 ppm in ^{31}P-NMR spectrum is observed, confirming the presence of the phosphine without unwanted oxidations neither during the reaction nor during the purification procedure.

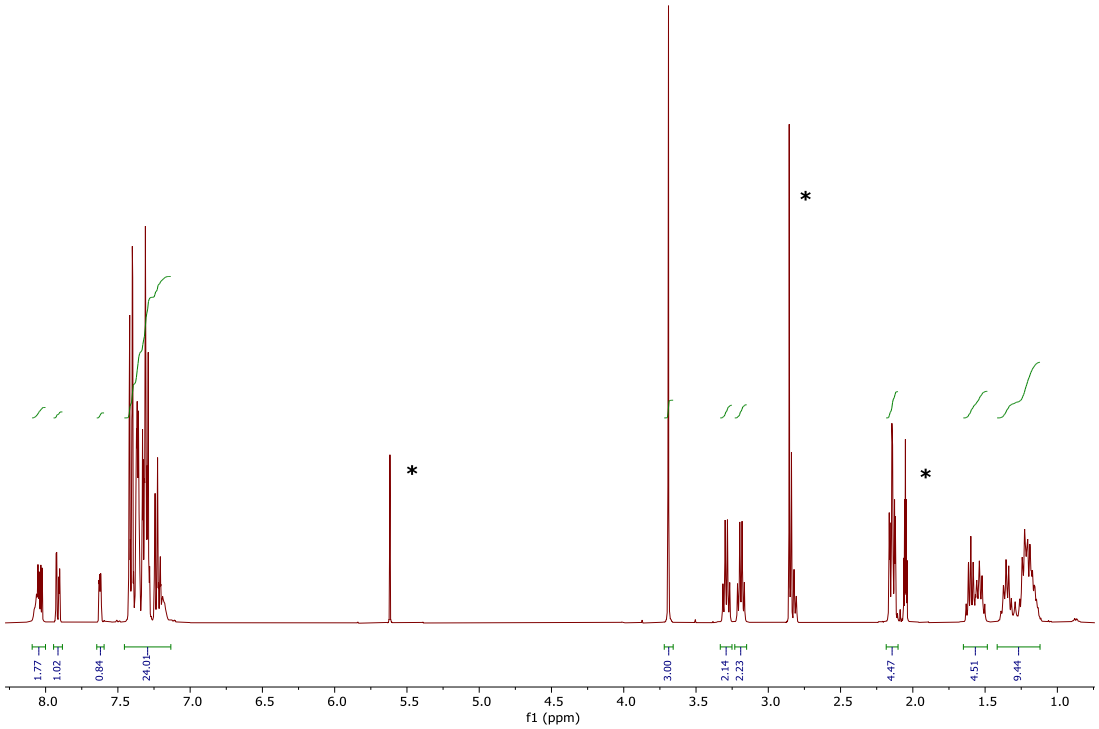

Figure 4.5. ^{1}H-NMR (400 MHz, $(CD_3)_2CO$) of the product **17**. The solvent peaks are indicated by an asterisk (acetone, water, dichloromethane).

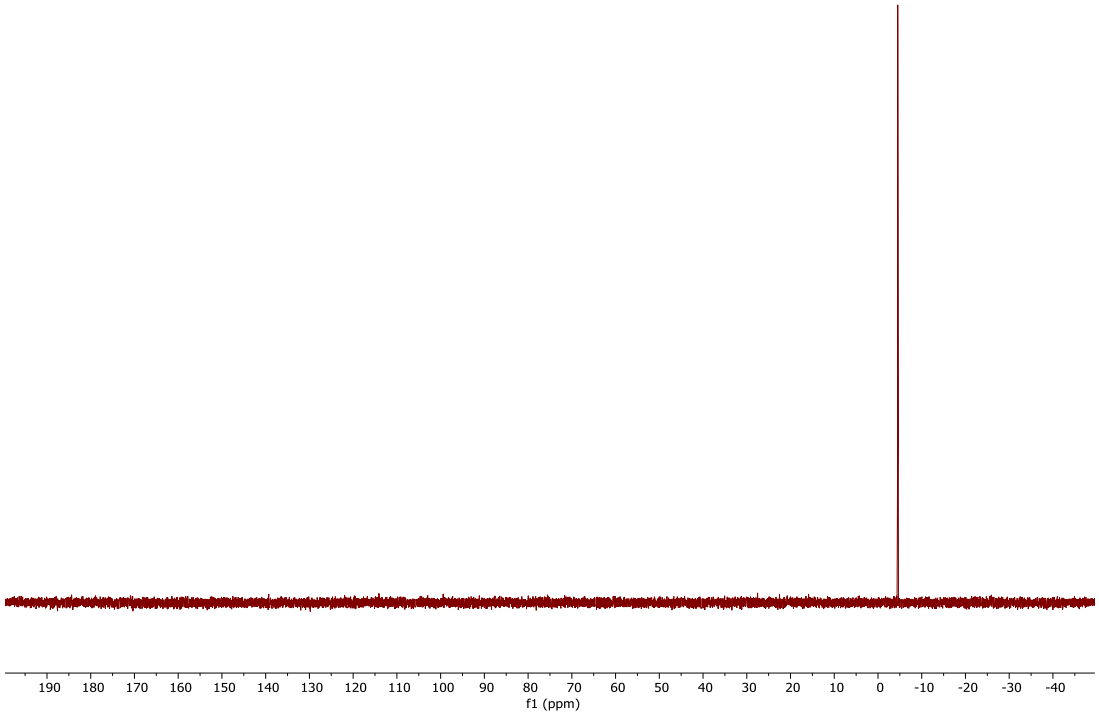

Figure 4.6. ^{31}P-NMR (400 MHz, $(CD_3)_2CO$) of the product **17**.

The last step of the synthesis is represented by the deprotection of the thiol group to obtain the desired ligand **12**. The deprotection reaction was carried out under an argon atmosphere, to avoid possible oxidation of the phosphine and the thiol produced, using a solution of 10% TFA in dichloromethane and an excess of triethylsilane as carbocation scavenger. The comparison between the ^{1}H-NMR spectra of **12** (Figure 4.7) and the coupling precursor (Figure 4.5) allows to confirm the removal of the protecting group, and the appearance of the characteristic peak of the protons in α to the free thiol at 2.5 ppm. However, the formation of about 5.5% of disulfide can also be pinpointed as confirmed by the triplet at 2.58 ppm. In the ^{31}P-NMR spectrum (Figure 4.8) only the phosphine peak at – 4.2 ppm could be observed, without any peaks related to the oxidation of the phosphine.

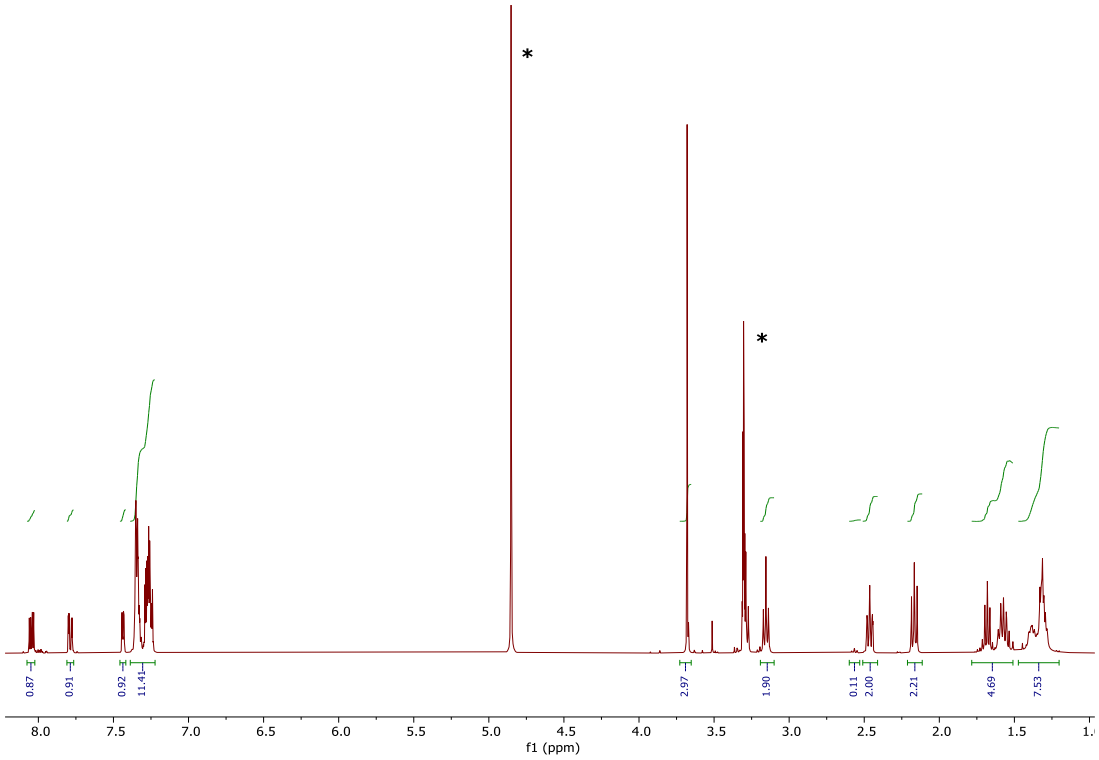

Figure 4.7. ^{1}H-NMR (400 MHz, CD_3OD) of **12**. The solvent peaks are indicated by an asterisk (methanol, dichloromethane).

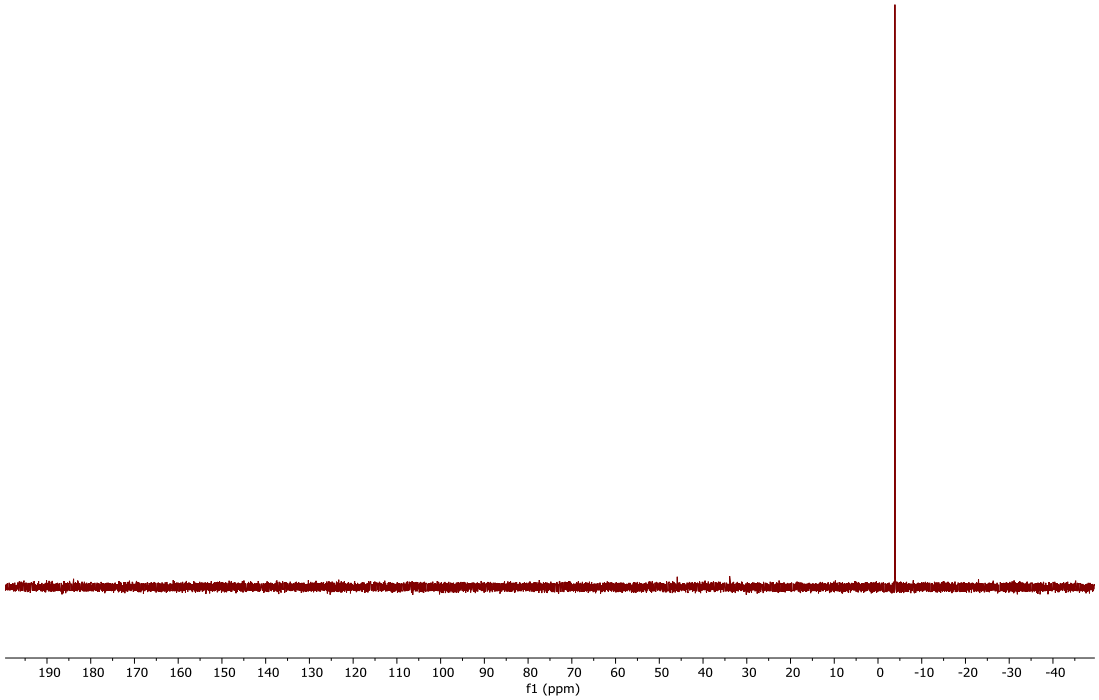

Figure 4.8. ^{31}P-NMR (400 MHz, CD_3OD) of **12.**

4.5 Activated NP C11N/12: synthesis and NMR and UV-vis analysis

Preliminary experiments were performed to evaluate the possibility of obtaining homoligand AuNPs using only the **12** ligand. Not unexpectedly, on the basis of the steric hindrance of the ligand, only highly unstable systems were obtained. The further activities focused on the development of mixed monolayer nanoparticles using blends of the **HC11N** and **12** (Scheme 4.8).

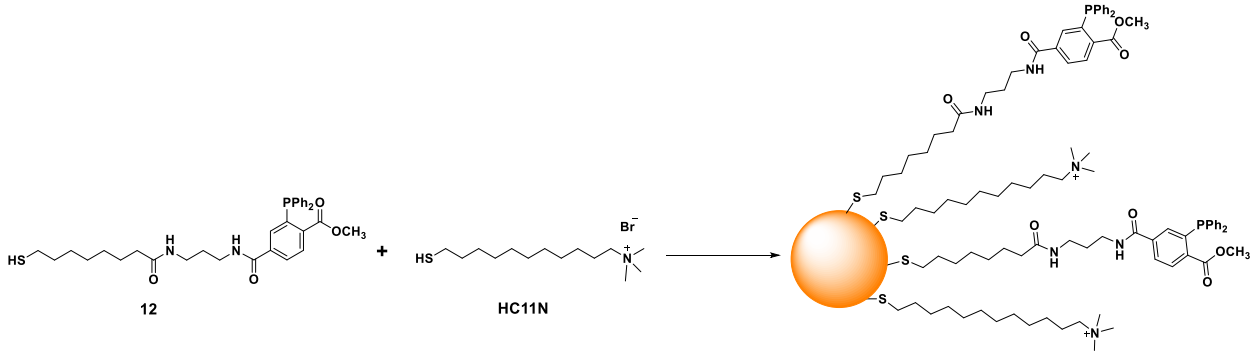

Scheme 4.8. Schematic representation of heteroligand **12**/**HC11N** AuNPs preparation.

To this aim, different **HC11N/12** have been tested for the synthesis of ~ 2 and ~ 4 nm AuNPs. The commercially available **HC11N** has been chosen as an affordable alternative to thiols **HC12N** and **HC16N** because of the similar chain length to **12** to ensure exposure of both end-groups and favour enough intrachain interactions such as to form a stable monolayer. The synthetic procedures for NP C11N/12 of ~ 4 nm is the same described in Chapter 3. After the formation of the nanoparticles by addition of $NaBH_4$, a few drops of triethylamine were added and followed by the addition of a **HC11N/12** solution, to neutralise the residual TFA present in the ligand **12**. In Table 4.1 are reported the different **HC11N/12** ratios tested in these AuNP synthesis.

Table 4.1. **HC11N/12** ratio used for the preparation of heteroligand AuNPs of ~ 4 nm.

Run	HC11N/12	Annotation
1	1:1	NP C11N/12 I
2	3:1	NP C11N/12 II

The purification procedure used was the same applied to the first set of AuNPs, consisting of five cycles of precipitation and centrifugation. After this process, the AuNPs have been collected and the residual presence of free ligands and other reagents was assessed by ^{1}H-NMR analysis. Detailed characterization of the AuNPs was performed by TEM, TGA, and analysing the monolayer composition by NMR spectroscopy. In Figure 4.9 and Figure 4.11, the ^{1}H-NMR of NP C11N/12 I and NP C11N/12 II are shown and in both spectra a broad peak is observed at around 7.6 ppm related to the aromatic protons of **12**. The relative UV-vis spectra are reported in Figure 4.10 and Figure 4.12.

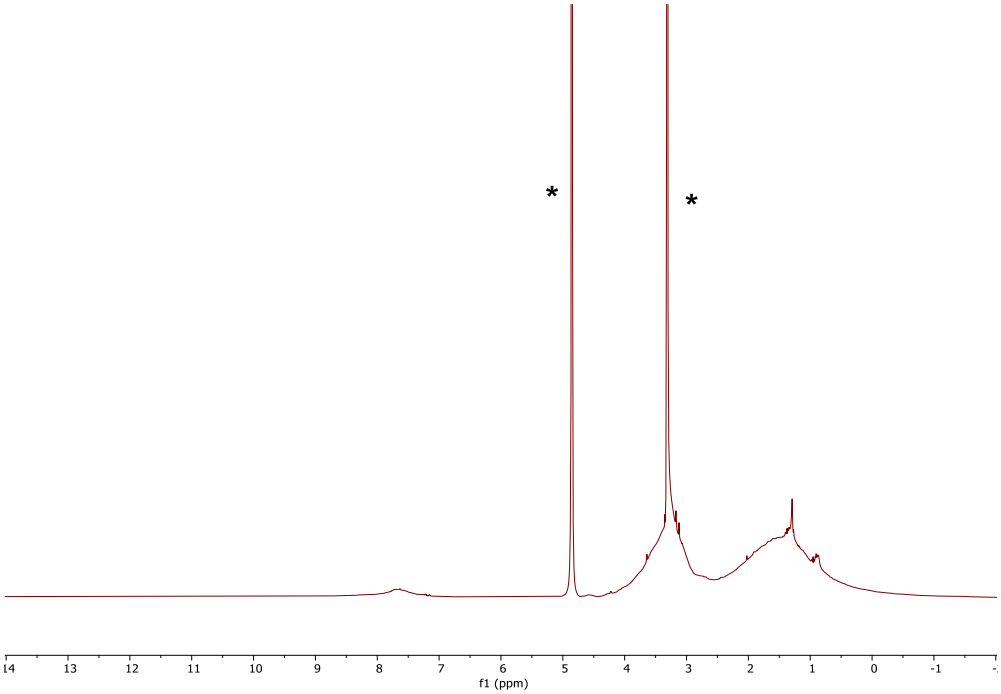

Figure 4.9. ^{1}H NMR (400 MHz, CD_3OD) of NP C11N/12 I. The solvent peaks are indicated by an asterisk (methanol, water).

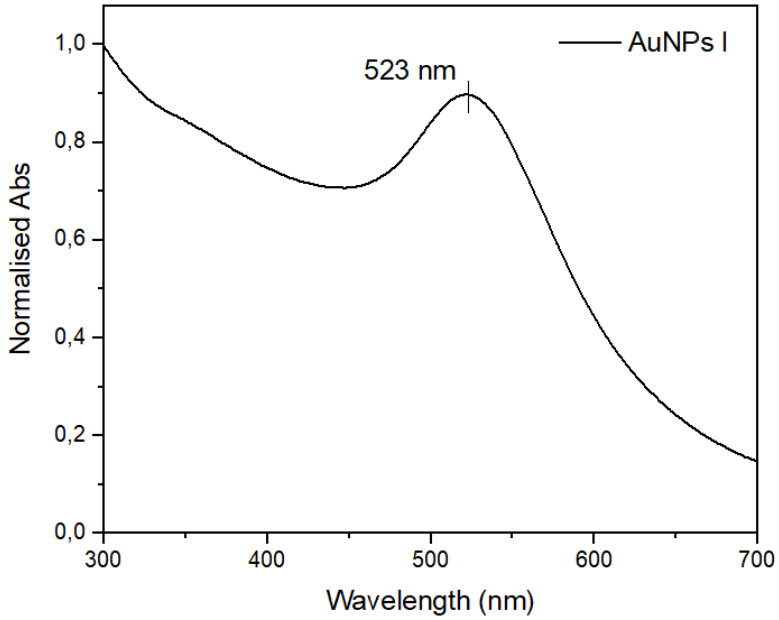

Figure 4.10. UV-vis spectrum of NP C11N/12 I in milliQ water ([AuNPs] 0.05 mg/mL).

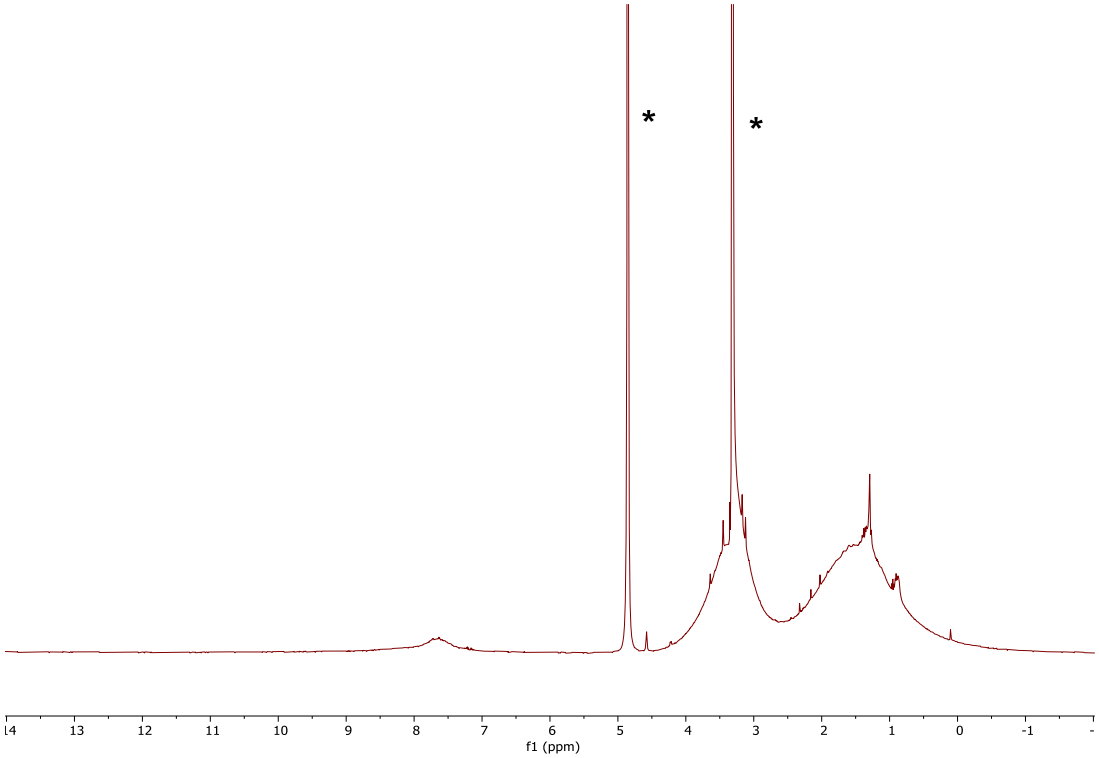

Figure 4.11. ^{1}H NMR (400 MHz, CD_3OD) of NP C11N/12 II. The solvent peaks are indicated by an asterisk (methanol, water).

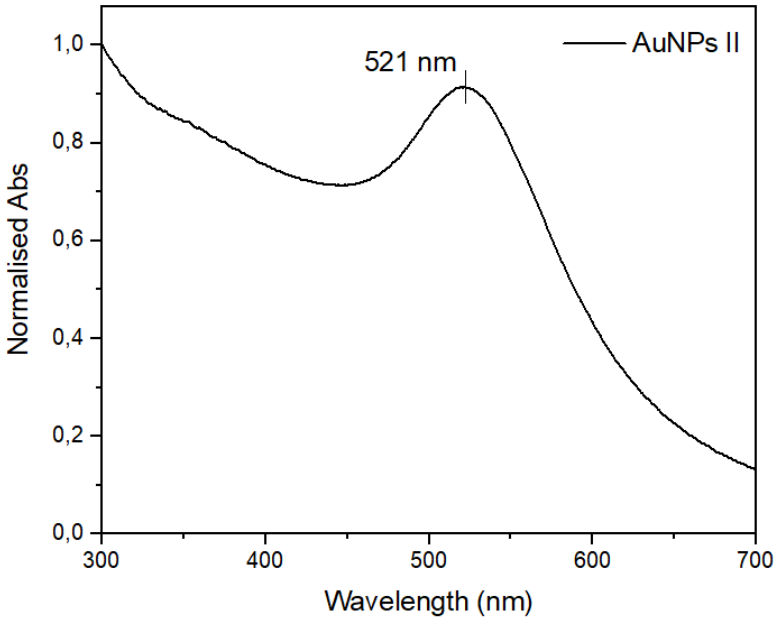

Figure 4.12. UV-vis spectrum of NP C11N/12 II in milliQ water ([AuNPs] 0.05 mg/mL).

4.6 Activated NP C11N/12: characterization

Detailed size analysis of NP C11N/12 was performed by TEM; Figure 4.13 shows a representative TEM image of NP C11N/12 I and the corresponding size distribution, by which it was possible to calculate an average core size of 4.3 ± 1.3 nm considering a set of 664 AuNPs. Regarding the NP C11N/12 II, the relative TEM image and size distribution are shown in Figure 4.14. In this case, the core diameter is calculated as 4.2 ± 1.3 nm considering a set of 724 AuNPs.

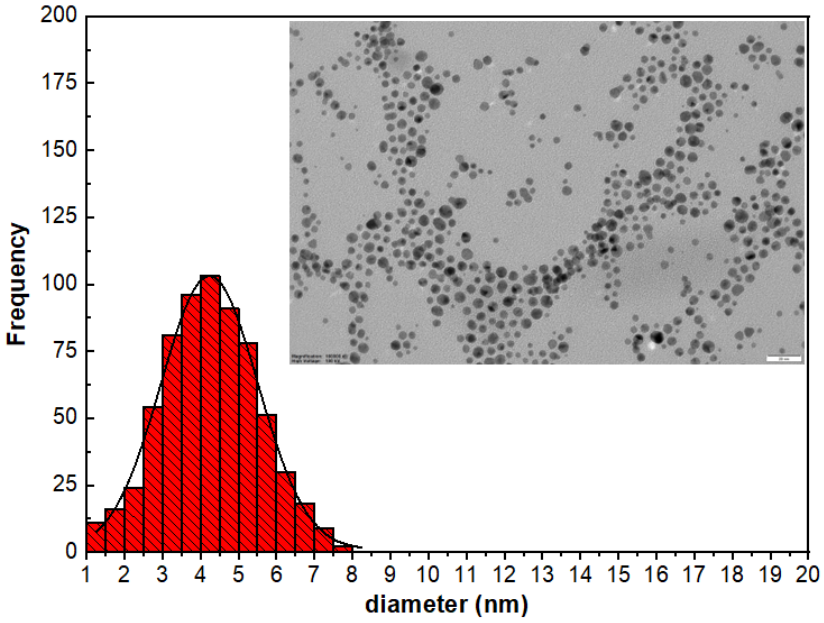

Figure 4.13. TEM and size distribution of NP C11N/12 I. Scale bar 20 nm.

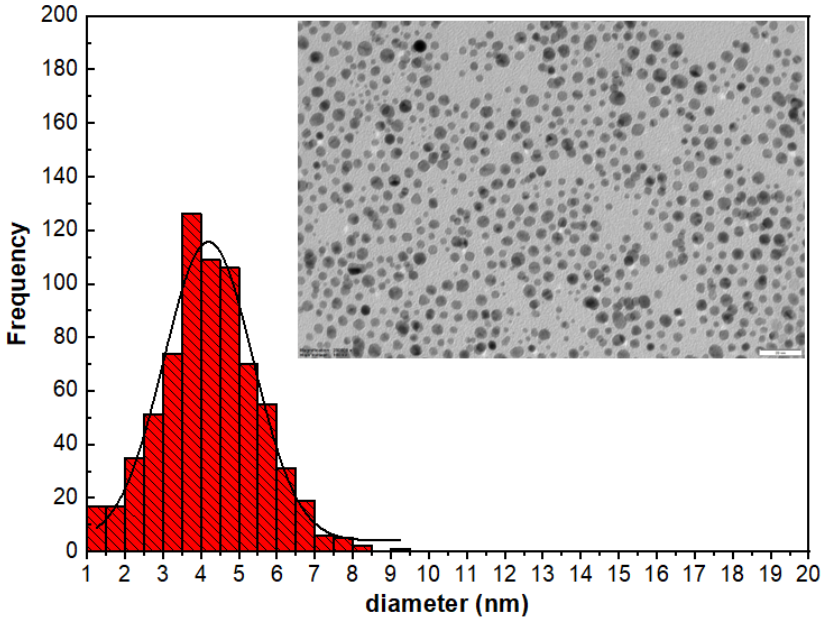

Figure 4.14. TEM and size distribution of NP C11N/12 II. Scale bar 20 nm.

After characterization of the inorganic core size the AuNP were further characterized by analysing of the composition of both monolayer and inorganic core by TGA analysis for each batch of activated AuNPs. As mentioned in chapter 3, for the evaluation of mixed monolayer composition the results coming from the TGA analyses were combined with those obtained from the decomposition of the monolayer by iodine treatment. The mixture of disulfides obtained by the decomposition of the organic coating has been analysed by NMR spectroscopy. In the ^{1}H-NMR spectrum of the disulfide mixture solutions several superimpositions of signals complicated complete assignment. For this reason, the peaks of the aromatic protons of **12** and the methylene protons in α to the disulfide bond of the **HC11N** chain were chosen as characteristic peaks to evaluate the final **HC11N/12** ratio. The diverse chemical shift of the methylene protons in α to the disulfide bond of the **HC11N** (2.68 ppm, Figure 4.15a) and **12** (2.56 ppm, Figure 4.15b) has permitted to use the former as characteristics signal for the monolayer composition. The related chemical shifts are reported below.

Table 4.2. Chemical shifts calculated in CD_3OD of the characteristic peaks of **12** and **HC11N**.

	Chemical shift (δ)
$(C_6H_5)_2(C_6H_3)P$ of 12	8.18 – 7.30 ppm
'R-CH_2-S-S-CH_2-R' of HC11N	2.70 – 2.63 ppm

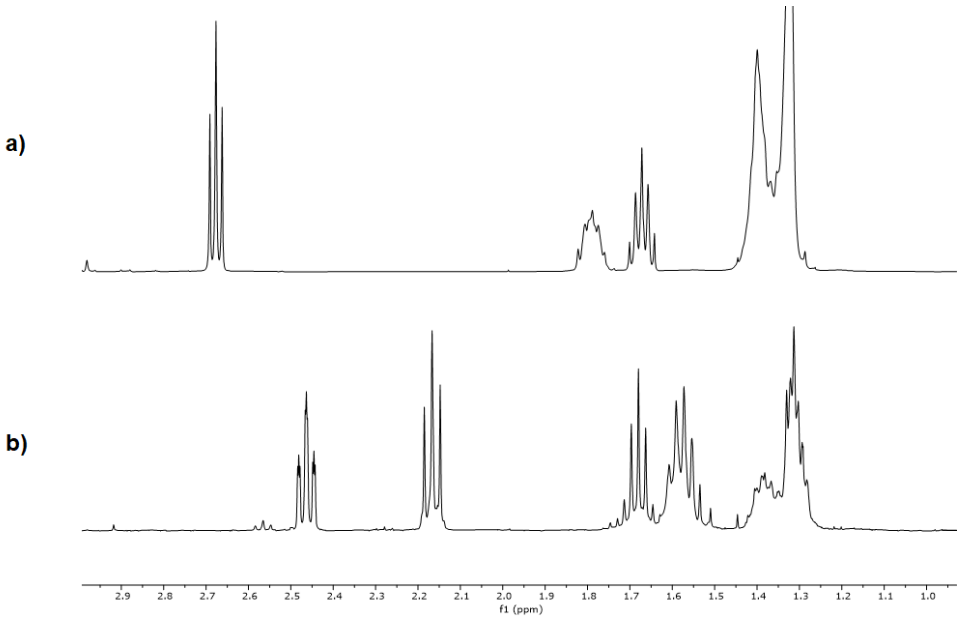

Figure 4.15. ^{1}H-NMR spectra (400 MHz, CD_3OD) of the oxidized **HC11N** (**a**), and the partially oxidated **12** (**b**). The peak of the methylene protons in α to disulfide of C11N show different chemical shift compared to that of the α protons of **12**.

The ^{1}H-NMR spectra of the disulfide mixtures resulting from decomposition of NP C11N/12 I and NP C11N/12 II are reported in Figure 4.16 and Figure 4.17, respectively.

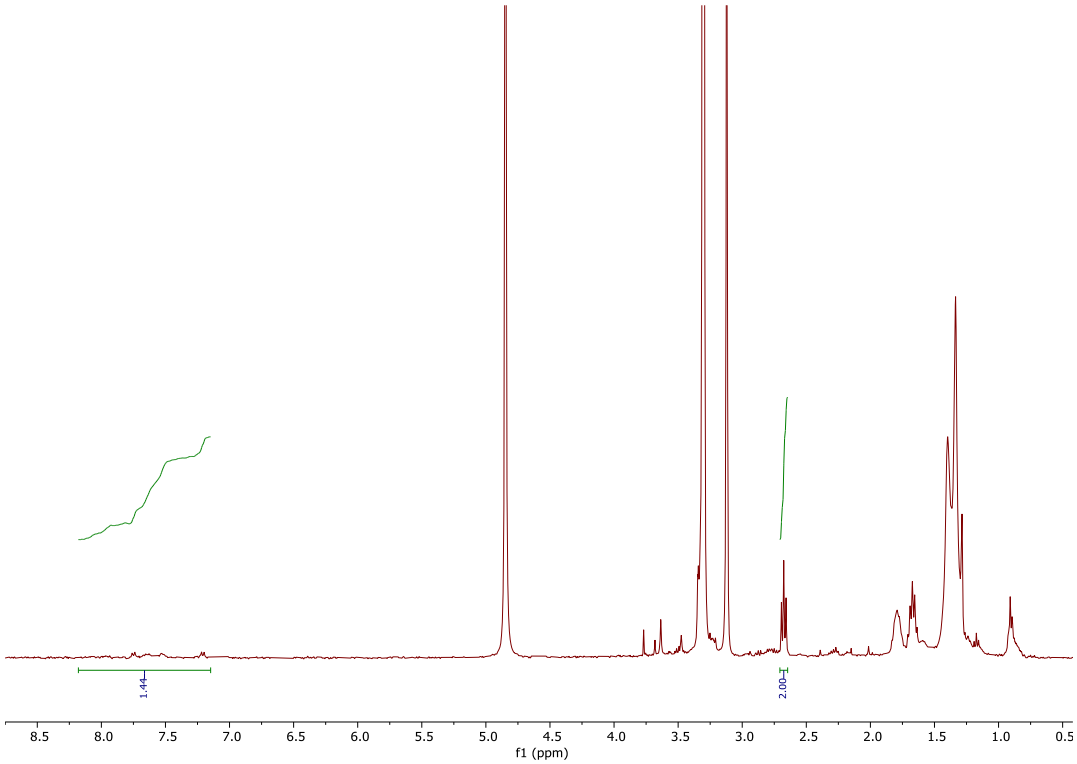

Figure 4.16. ^{1}H-NMR spectrum (400 MHz, CD_3OD) of the decomposition mixture of NP C11N/12 I.

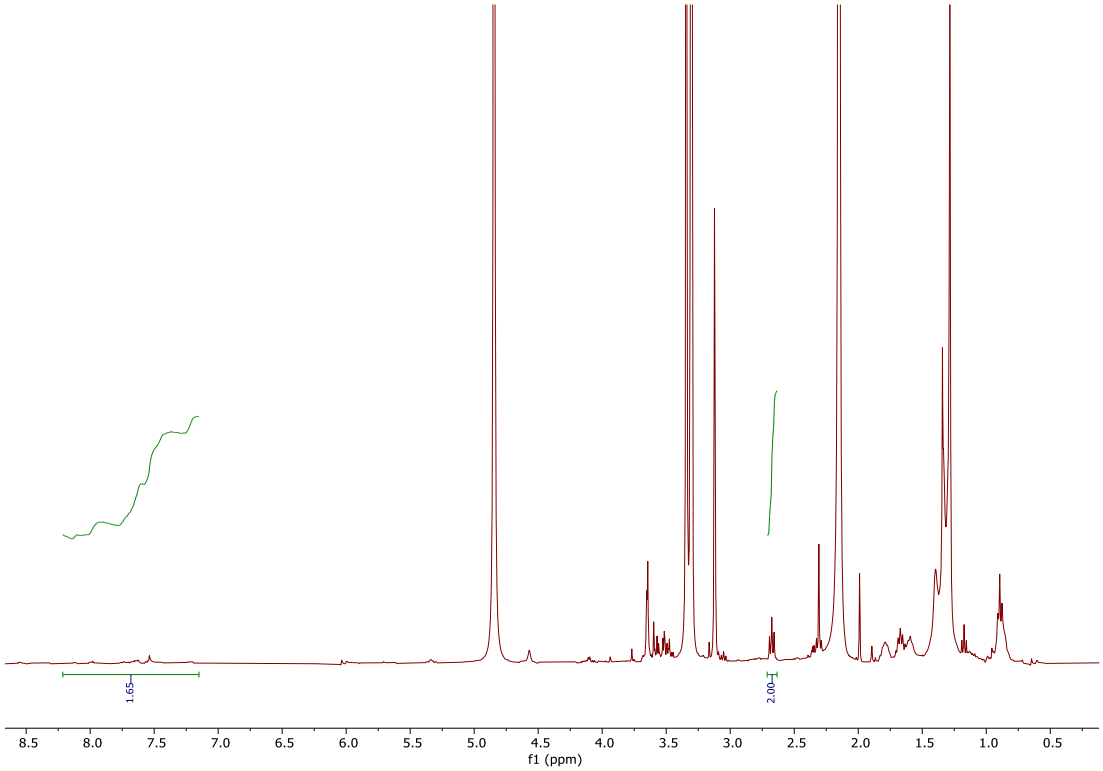

Figure 4.17. ^{1}H-NMR spectrum (400 MHz, CD_3OD) of the decomposition mixture of NP C11N/12 II.

In Table 4.3 the **HC11N/12** ratio obtained from NMR analysis are reported along with the organic percentage calculated by TGA analysis. The composition of each batch of nanoparticle has been estimated using the TGA and decomposition results.

Table 4.3. Comparison between the **HC11N/12** ratio used during the AuNPs synthesis and that obtained from monolayer decomposition.

	HC11N/12 synthesis ratio	**HC11NN/12 (NMR analysis)**	**Diameter (nm)**	**TGA (% organic)**	**Composition**
NP C11N/12 I	1 : 1	10 : 1	4.3 ± 1.3	15.7%	$Au_{2740}(C11N)_{263}(12)_{26}$
NP C11N/12 II	3 : 1	8 : 1	4.2 ± 1.3	14.5%	$Au_{2664}(C11N)_{225}(12)_{28}$

As it can be seen in Table 4.3, only a reduced loading of **12** could be obtained despite the high amount of this ligand used in the synthesis. For each thermogravimetric analysis, both the TGA curve and the corresponding derivative are reported, labelled in black and red respectively (Figure 4.18 and Figure 4.19).

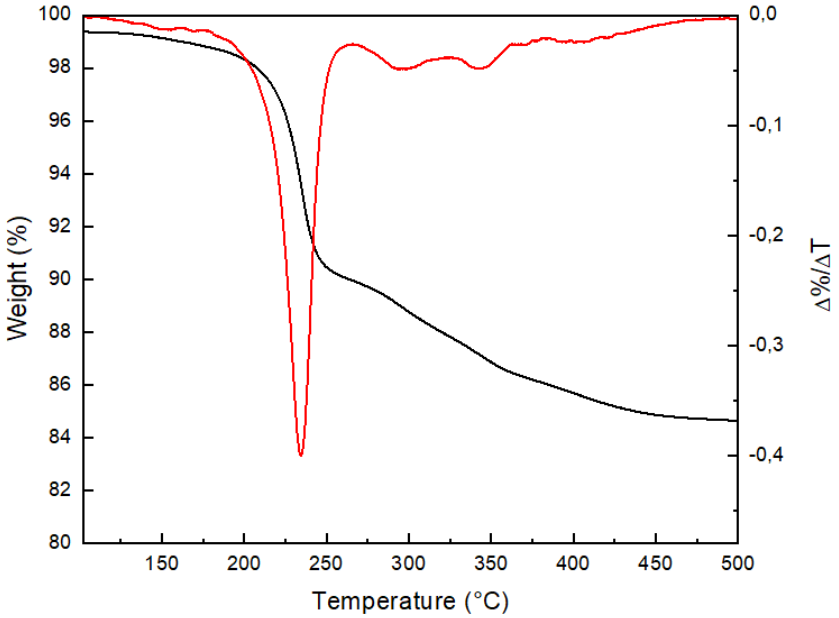

Figure 4.18. TGA curves of NP C11N/12 I.

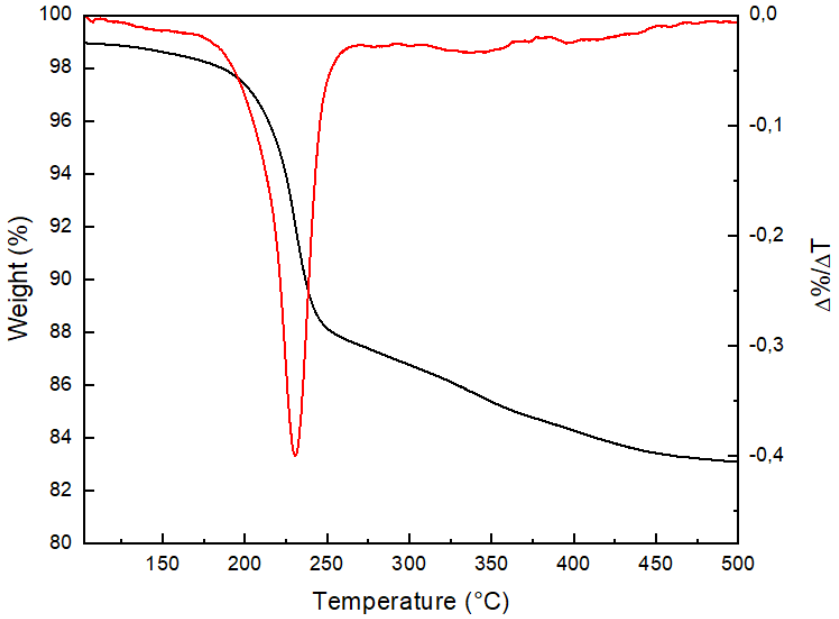

Figure 4.19. TGA curves of NP C11N/12 II.

4.7 Activated ultrasmall NP C11N/12: synthesis and NMR and UV-vis analysis

After preparation of the activated nanoparticles with core size of 4 nm, the activities focused on the possibility of preparing analogous activated ultrasmall AuNPs by using **HC11N/12** mixtures. Two

different synthetic procedures were tested for obtaining these nanoparticles: (i) the same direct synthesis adopted for the ultrasmall charged AuNPs described in the Chapter 3, and (ii) a thiol-to-thiol exchange in which AuNPs coated by **HC11N** were reacted with the ligand **12**. For clarity, the nanoparticles obtained by direct synthesis are reported as usNP C11N/12, while the ones prepared by the exchange reaction are reported as usNP C11N/12 III. In both procedures, a 3:1 **HC11N**/**12** ligand ratio was used.

4.7.1 Ultrasmall AuNPs by direct synthesis: usNP C11N/12

The nanoparticles were obtained following the procedure developed by Scrimin and co-workers, using a mixture of **HC11N**/**12** in a 3:1 ratio which was added to a solution of weakly passivated nanoparticle solution. After the preparation, the obtained AuNPs were purified and then analysed by NMR spectroscopy to evaluate the absence of free ligands and other reagents. In addition, a preliminary UV-vis analysis has been performed to evaluate the AuNP core size. Figure 4.20 and Figure 4.21 showed the ^{1}H-NMR and UV-vis spectra of usNP C11N/12 respectively.

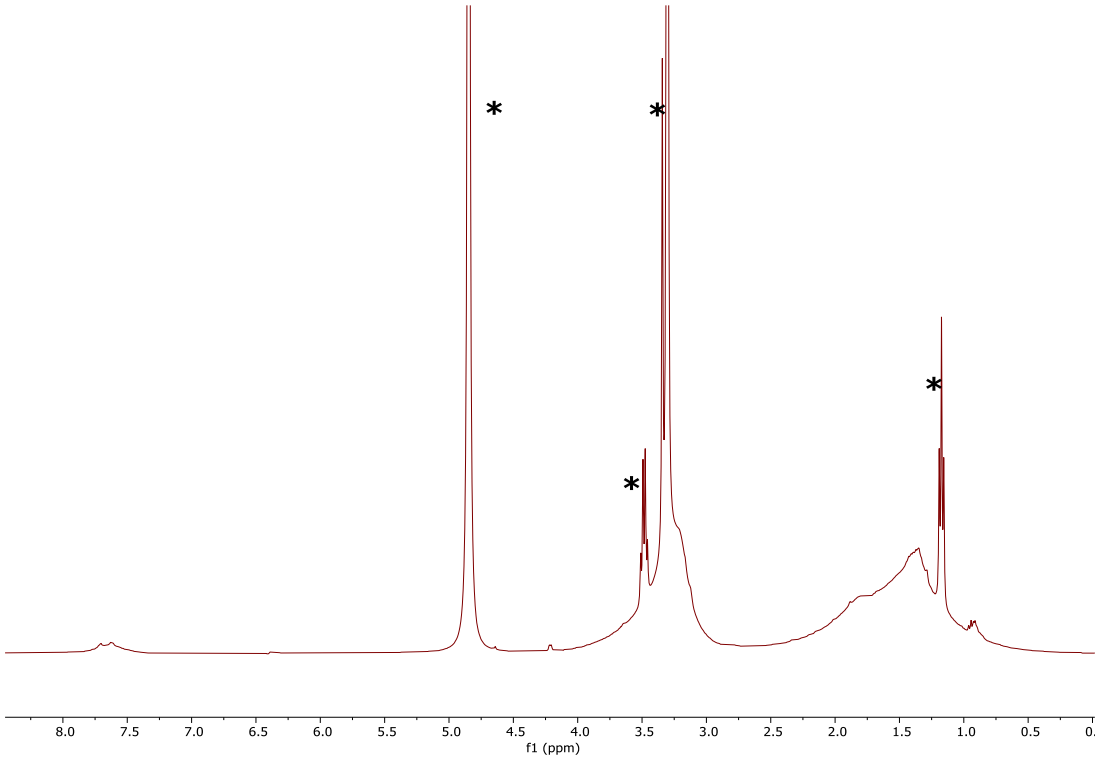

Figure 4.20. ^{1}H NMR (400 MHz, CD_3OD) of usNP C11N/12. The solvent peaks are indicated by an asterisk (diethyl ether, methanol, water)

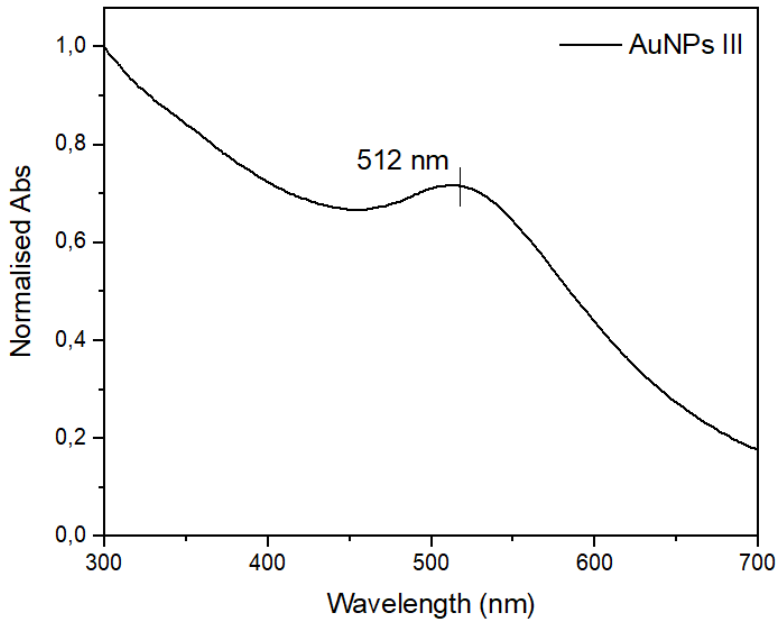

Figure 4.21. UV-vis spectrum of usNP C11N/12 in milliQ water ([AuNPs] 0.05 mg/mL).

The UV-Vis analysis has revealed the presence of a low SPR at 512 nm probably due to a subpopulation of nanoparticles with a diameter greater than 3 nm. A detailed size analysis of these nanoparticles was performed by TEM, whose results are showed in Figure 4.22. For usNP C11N/12 the average core size results to be 2.8 ± 0.8 nm considering a set of 842 AuNPs.

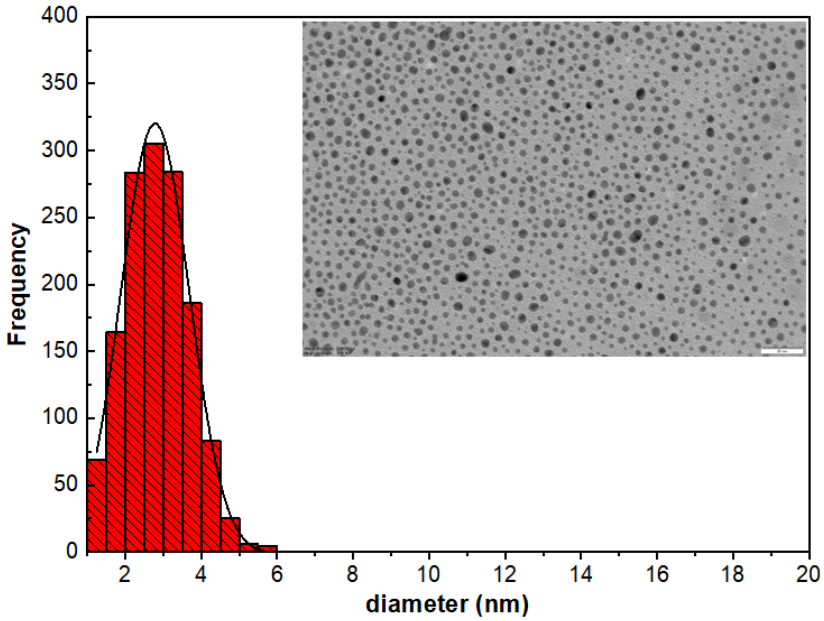

Figure 4.22. TEM and size distribution of usNP C11N/12. Scale bar 20 nm.

Afterwards, 4-5 milligrams of usNP C11N/12 have been treated with an iodine solution to provide the monolayer decomposition. The resulted disulfide mixture has analysed by NMR spectroscopy, and Figure 4.23 reports the corresponding ^{1}H-NMR spectrum.

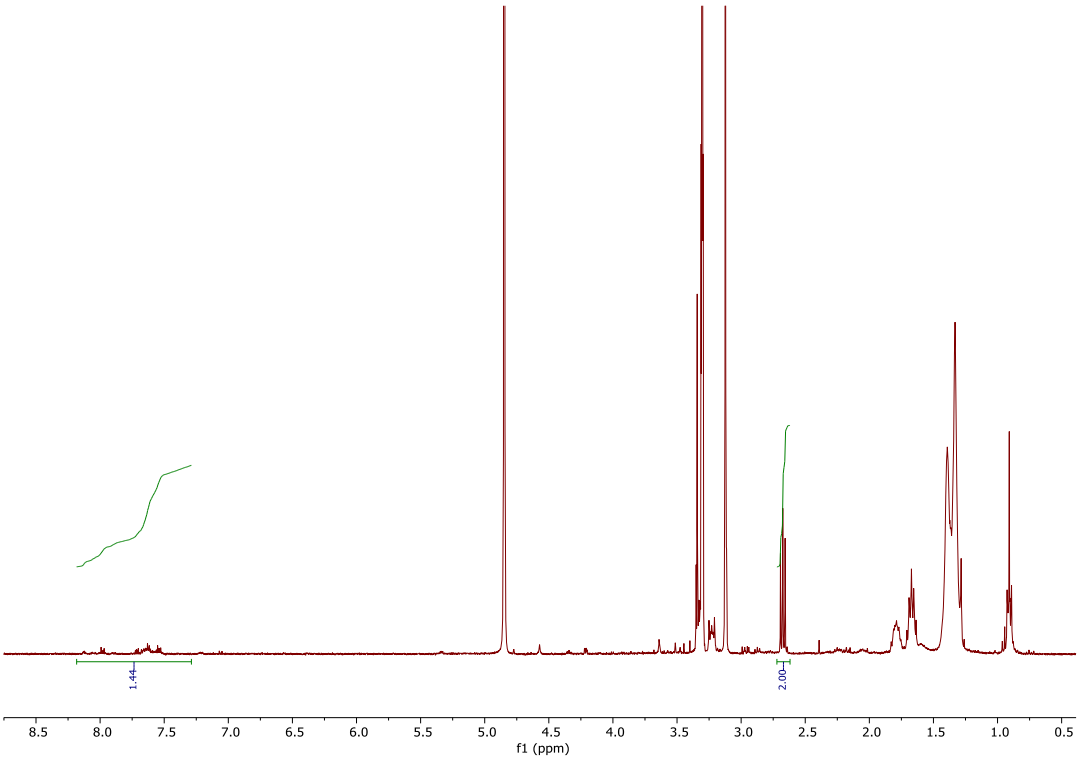

Figure 4.23. ^{1}H-NMR spectrum (400 MHz, CD_3OD) of the decomposition mixture of usNP C11N/12.

The C11N/12 ratio obtained by this analysis was 9:1. Then, these nanoparticles were further characterised by TGA analysis in order to assess the percentage of organic material respect to gold. The TGA curve and corresponding derivative are reported in Figure 4.24, labelled in black and red respectively.

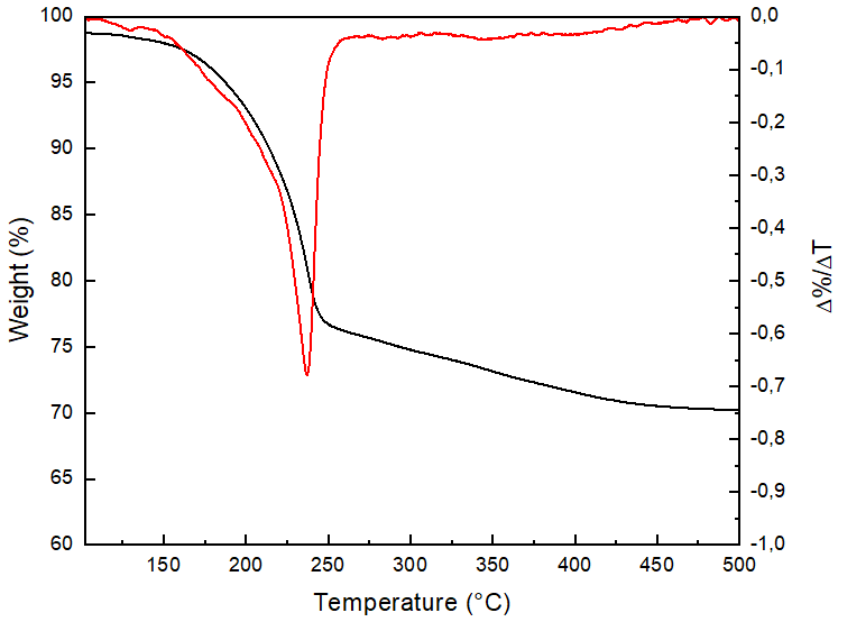

Figure 4.24. TGA curves of usNP C11N/12.

By combining the data obtained by TEM, TGA and decomposition of the nanoparticles to assess by NMR the ligand ratio, it was possible to define the composition of the nanoparticles, Table 4.4. Even in this case, the amount of ligand **12** is lower than that expected on the basis of the synthesis ratio.

Table 4.4. Core composition for usNP C11N/12.

	HC11N/12 Synthesis ratio	**HC11N/12 (NMR analysis)**	**Diameter (nm)**	**TGA (%organic)**	**Composition**
usNP C11N/12	3:1	9:1	2.8 ± 0.8	28.8	$Au_{803}(C11NN)_{161}(12)_{18}$

4.7.2 Ultrasmall AuNPs by exchange reaction: usNP C11N/12 III

Since in all previous synthesis the amount of **12** effectively bound to the gold core remained lower than that expected, a further AuNP synthesis was performed by the exchange reaction starting from the usNP C11N of 2 nm. These homoligand AuNPs have been prepared according to the Scrimin procedure as described in Chapter 3, and after the purification the obtained homoligand AuNPs were analysed by NMR and UV-vis spectroscopy Figure 4.25 and Figure 4.26.

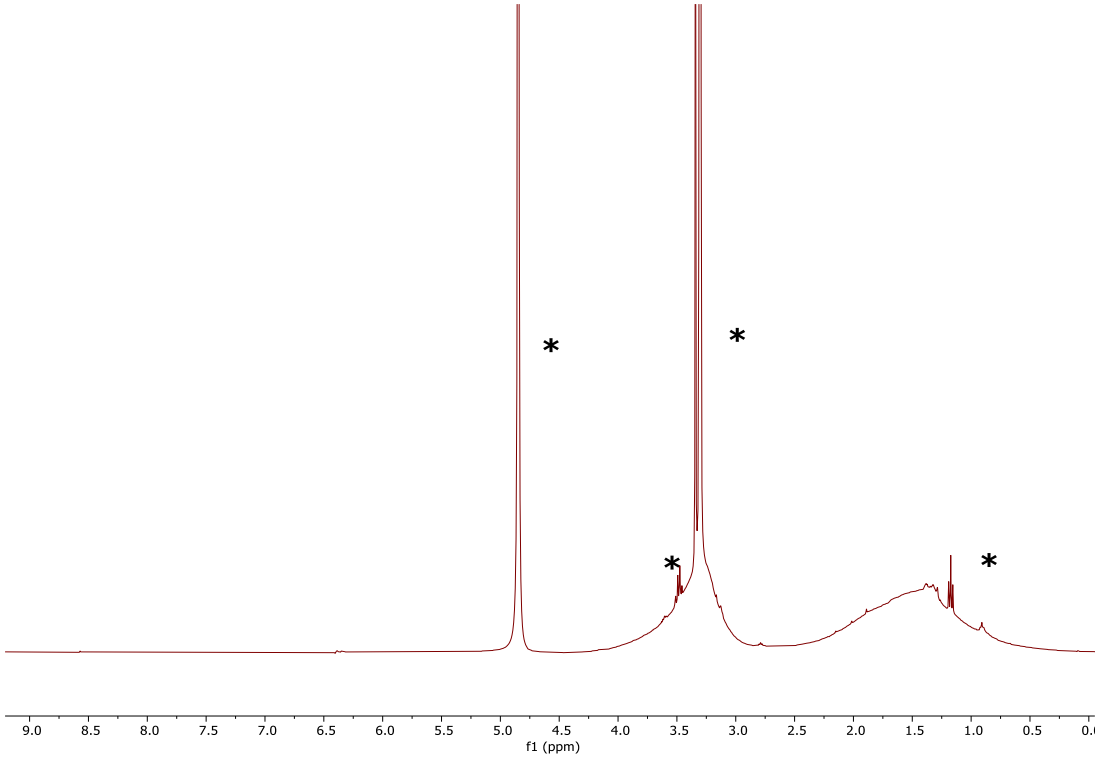

Figure 4.25. ^{1}H NMR (400 MHz, CD_3OD) of usNP C11N. The solvent peaks are indicated by an asterisk (diethyl ether, methanol, water)

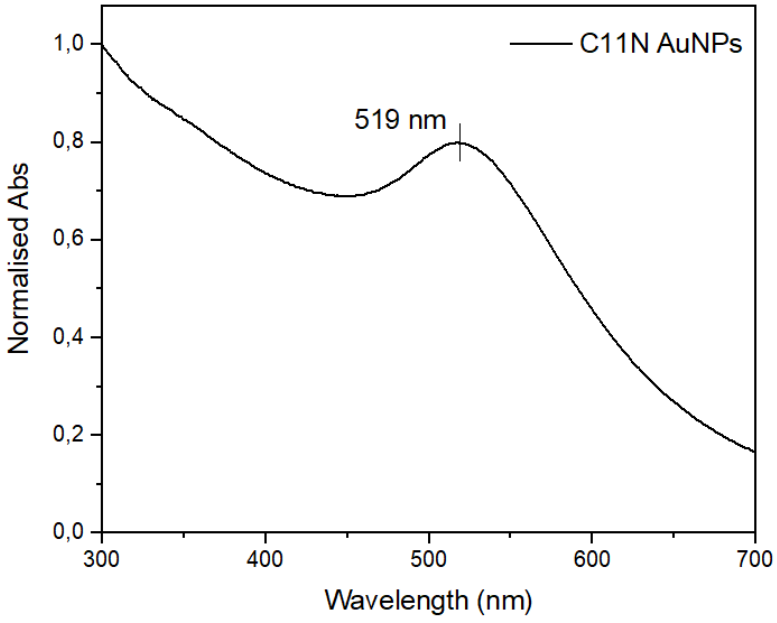

Figure 4.26. UV-vis spectrum of usNP C11N in milliQ water ([AuNPs] 0.05 mg/mL).

Even in this case, the UV-Vis analysis has revealed the presence of a SPR at around 519 nm probably due to a subpopulation of nanoparticles with a diameter greater than 3 nm. A detailed size analysis of these nanoparticles was performed by TEM. A representative micrograph alongside with the

statistical analysis of the nanoparticle diameters is showed in Figure 4.27. For usNP C11N, the average core size results to be 3.0 ± 0.9 nm considering a set of 1631 AuNPs.

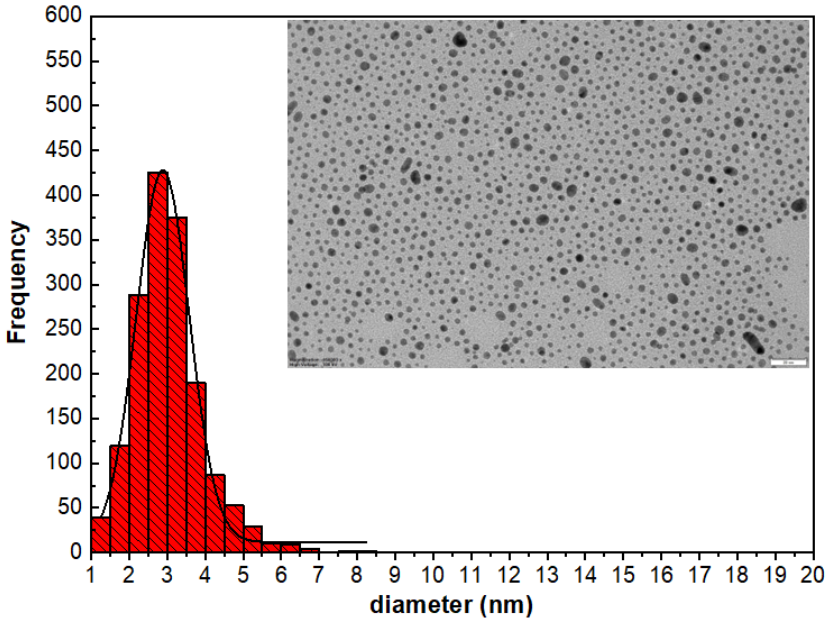

Figure 4.27. TEM and size distribution of usNP C11N. Scale bar 20 nm.

Starting from the homoligand usNP C11N, the corresponding heteroligand AuNPs were synthetised by performing a ligand exchange reaction with **12**. In detail, usNP C11N were dissolved in deoxygenated methanol and were reacted with an amount of **12** to achieve a **HC11N/12** molar ratio of 3:1. Before the thiol addition, a small amount triethylamine was added to neutralize the TFA associated with **12**. The exchange reaction was carried out at room temperature for three days, and no color change of the solution or precipitation of the nanoparticles was observed. After purification, the nanoparticles were characterized by NMR and UV-vis spectroscopy. Figure 4.28 and Figure 4.29 display the ^{1}H-NMR and UV-vis spectra of the obtained usNP C11N/12 III.

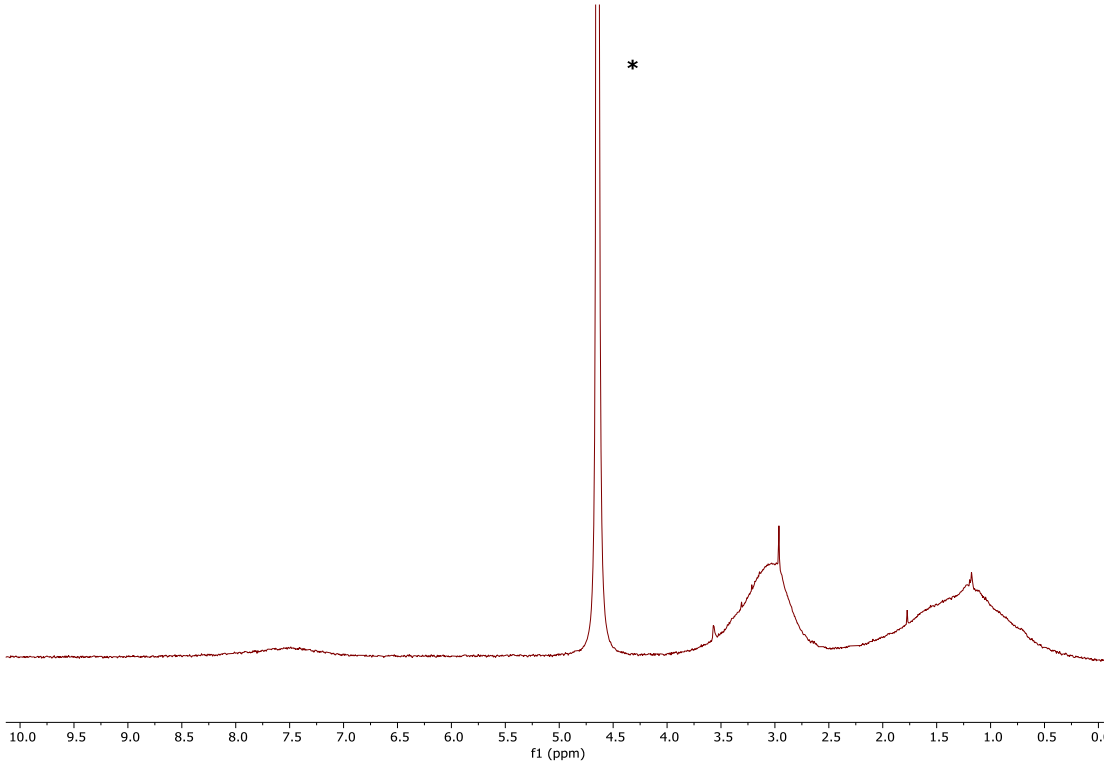

Figure 4.28. ^{1}H NMR (400 MHz, CD_3OD) of usNP C11N/12 III The solvent peaks are indicated by an asterisk (water).

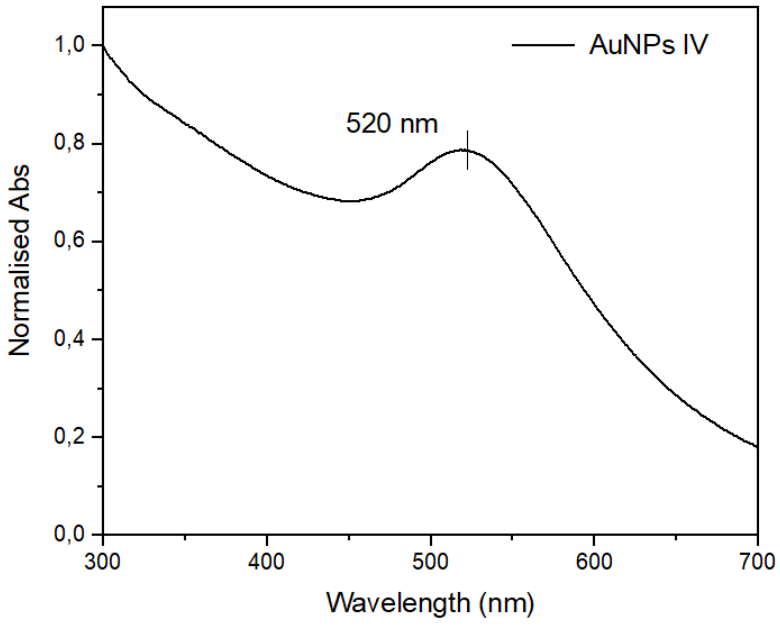

Figure 4.29. UV-vis spectrum of usNP C11N/12 III in milliQ water ([AuNPs] 0.05 mg/mL).

Compared the ^{1}H-NMR spectra of usNP C11N (Figure 4.25) and usNP11/12 III, a broad peak in the aromatic region appeared in the latter, confirming the introduction of the new ligand on the AuNP surface. The determination of the monolayer composition was carried out as previously described. In

detail, 4-5 milligrams of usNP11/12 III were treated by iodine to produce the disulfide mixture. The ^{1}H-NMR of the disulfide mixture obtained by monolayer decomposition is reported in Figure 4.30.

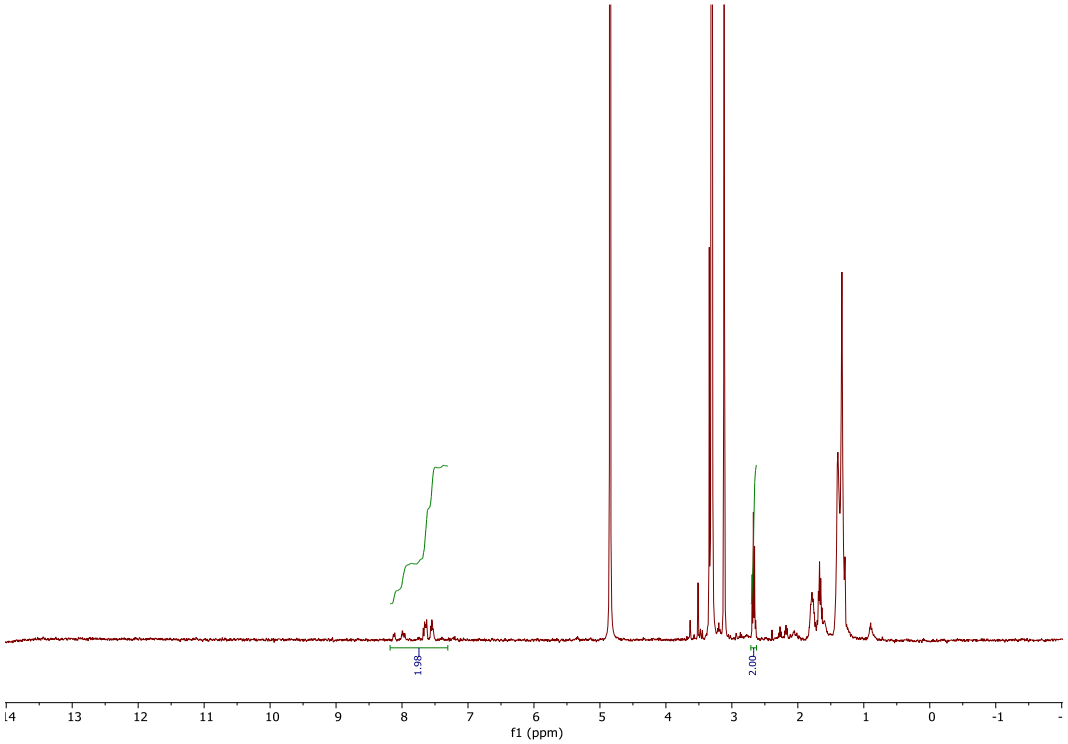

Figure 4.30. ^{1}H-NMR spectrum (400 MHz, CD_3OD) of the decomposition mixture of usNP C11N/12 III.

In this case, the C11N/12 was found to be 6.7:1, so the exchange procedure seemed to allow the insertion of a larger amount of phosphine without leading to an irreversible AuNP aggregation. However, after the exchange reaction, the size of the inorganic core was analysed again to check for any changes. Indeed, a larger size associated with a broader size distribution, 3.7 ± 1.3 nm, could be highlighted compared with the value of 3.0 ± 0.9 nm for the nanoparticles before the reaction. The TEM analysis of usNP C11N/12 III is reported in Figure 4.31, considering a set of 560 AuNPs.

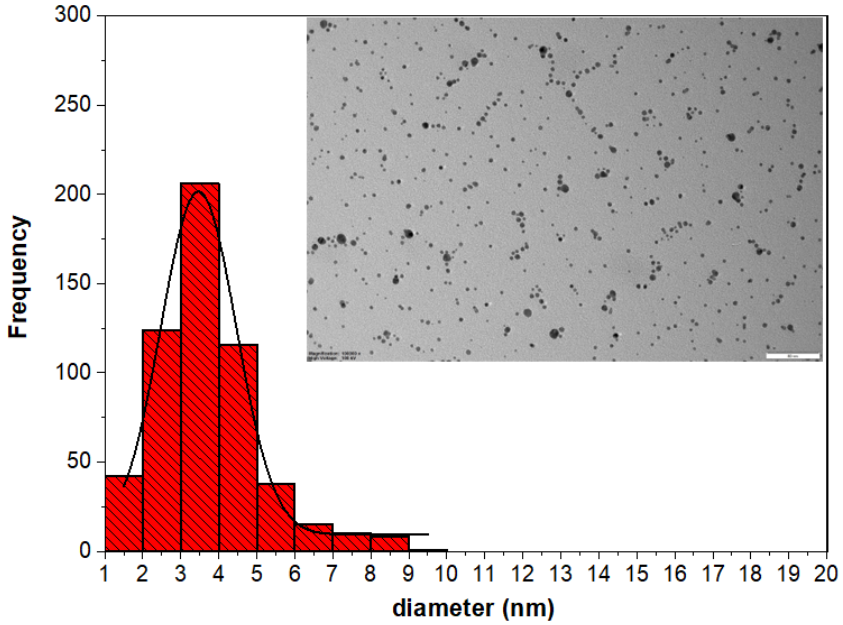

Figure 4.31. TEM and size distribution of usNP C11N/12 III. Scale bar 50 nm

Regarding the assessment of the composition of the AuNP, a TGA analysis was also performed, and Figure 4.32 reports the TGA curve and the corresponding derivative of usNP C11N/12 III, labelled in black and red respectively.

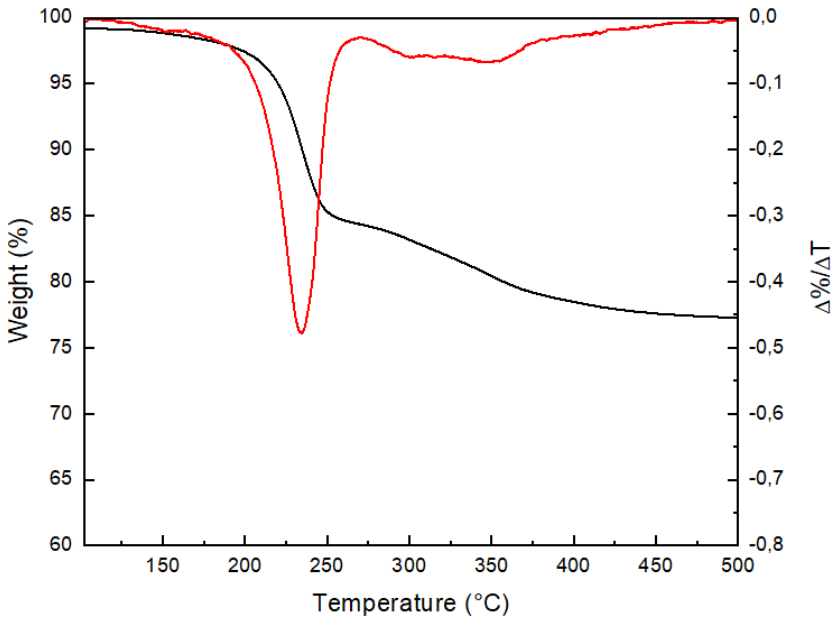

Figure 4.32. TGA curves of usNP C11N/12 III.

By combining the data obtained by TEM, NMR and TGA analysis, it was possible to determine the composition of the nanoparticles, whose data are collectively reported in Table 4.5.

Table 4.5. Composition of usNP C11N/12 III.

	HC11N/12 Synthesis ratio[a]	HC11N/12 (NMR analysis)	Diameter (nm)	TGA (%organic)	Composition
usNP C11N/12 III	3:1	6.7:1	3.7 ± 1.3	22.1%	$Au_{1781}(C11N)_{242}(12)_{36}$

[a] ratio of ligands used in the place exchange reaction.

4.8 Conjugation of an azide-modified amino acid to usNP C11N/12 III by Staudinger-Bertozzi ligation

Once the set of activate AuNPs was prepared and characterised, usNP C11N/12 III have been chosen as test system for the Staudinger-Bertozzi ligation with an azide-modified lysine (Figure 4.33), as it has been established that these nanoparticles display the highest loading of **12** on their monolayer.

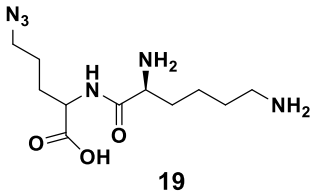

19

Figure 4.33. Structure of the azide-modified lysine as reagent for the SBL with usNP11/12 III.

In details, the compound **19** necessary for the Bertozzi-Staudinger reaction was obtained by a coupling reaction between the $N_{\alpha},N_{\varepsilon}$-di-Boc-L-lysine hydroxysuccinimide ester and the (*S*)-5-Azido-2-(Fmoc-amino)pentanoic acid. The coupling was carried out by solid phase peptide synthesis (SPPS) using the 2-chlorotrityl chloride (CTC) resin. The selected building blocks display a combination of protecting groups that allow achieving the product **19** completely deprotected upon cleavage from the resin (Scheme 4.9).

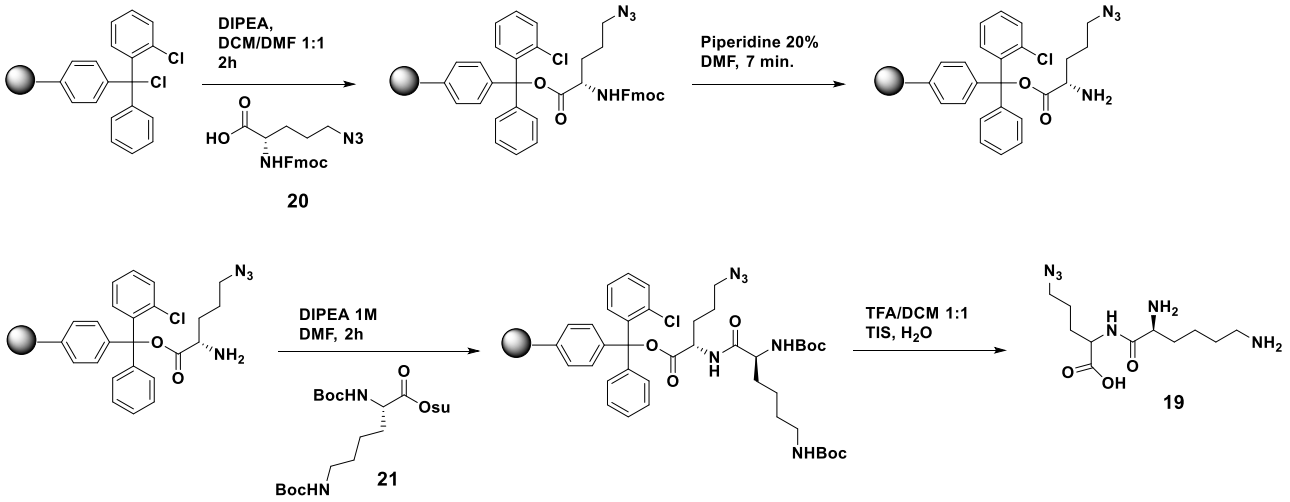

Scheme 4.9. Synthesis of the compound **19** by SPPS.

The compound **19** was characterised by NMR spectroscopy, whose ^{1}H-NMR spectrum is showed in Figure 4.34.

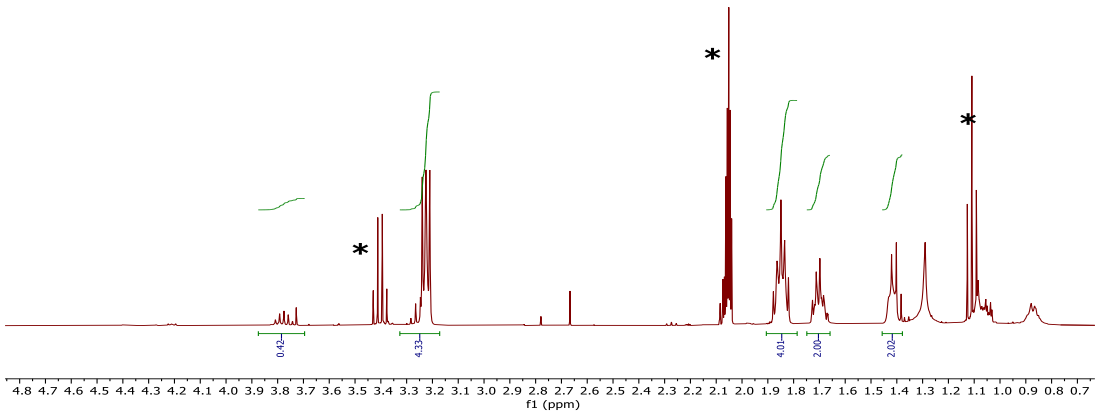

Figure 4.34. ^{1}H NMR (400 MHz, $(CD_3)_2CO$) of compound **19**. The solvent peaks are indicated by an asterisk (acetone, diethyl ether).

For the SBL, reaction conditions similar to those proposed by Gobbo *et al*. were used. In details, an excess of compound **19** equal to 3.5 equivalents with respect to the bound **12** on the AuNPs surface was used. Then, usNP C11N/12 III were solubilized in DMSO-d_6 in the presence of compound **19** and water such as to obtain a final AuNPs concentration of 10 mg/mL. The system was left at 37°C in a thermostatic bath for one week, and no color changes of the reaction mixture were observed during this period. For the reaction monitoring, several ^{31}P-NMR spectra in DMSO-d_6 were

periodically recorded. However, these analyses did not show any evidence (no signals) of reaction progression due to probably the low amount of **12** on the nanoparticle monolayer. Furthermore, once the reaction was stopped and the AuNPs has been purified, the ^{1}H-NMR spectrum of usNP C11N/12 III did not show any peaks due to the amino acid residue, decomposition of the nanoparticles with release of the ligands as disulfides did not highlight the presence of amino acid signals. Similarly, the ESI mass analysis of the disulfide mixture could not confirm the ligation.

Overall, in our hands, the preparation of mixed monolayer nanoparticles featuring **12** and the positively charged C11N ligands proved to be very cumbersome and often resulted in nanoparticles systems with low stability. Certainly, the interaction of the phosphorous atom with the gold core to give nanoparticles assemblies could be a possible explanation for the observed behaviour. The functionalised nanoparticles system used to test the Bertozzi Staudinger ligation did not allow to achieve the desired conjugation, most likely because of the low loading of ligand **12** on the nanoparticles monolayer. Further studies using more flexible cationic ligands resembling those used by Gobbo *et al.*[19,26] will be necessary to develop cationic nanoparticles to be used for the Bertozzi-Staudinger ligation reaction with short peptides.

4.9 Synthesis HP1

With the aim of functionalising cationic nanoparticles with peptide moieties, a more conventional strategy based on the place exchange reaction was considered, to this end, the cationic peptide-containing thiol HP1, Figure 4.35, was designed and synthesised. The structure of HP1 is characterised by a tripeptide moiety, a short spacer and an alkyl chain bearing the thiol moiety necessary for grafting on the gold nanoparticle surface.

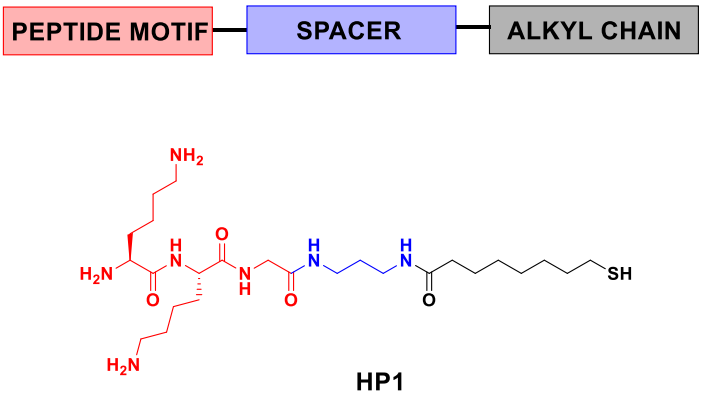

Figure 4.35. Structures of the designed peptide-containing ligand for the preparation of a second set of charged AuNPs.

In detail, the peptide motif is composed of two lysine bearing positive charges at physiological pH, and a glycine at the C-terminal whose carboxylic group is essential for the insertion of the peptide portion on the functionalised protected thiol **16**. The peptide motif was prepared by solid phase peptide synthesis (SPPS) using the 2-chlorotrityl chloride (CTC) resin (Scheme 4.10). The selected amino acids display a combination of protecting groups that should allow achieving the desired peptides with protected side chains and N_{α}-terminal amino group. Instead, the terminal carboxylic group of the glycine has to be available for the subsequent coupling reaction.

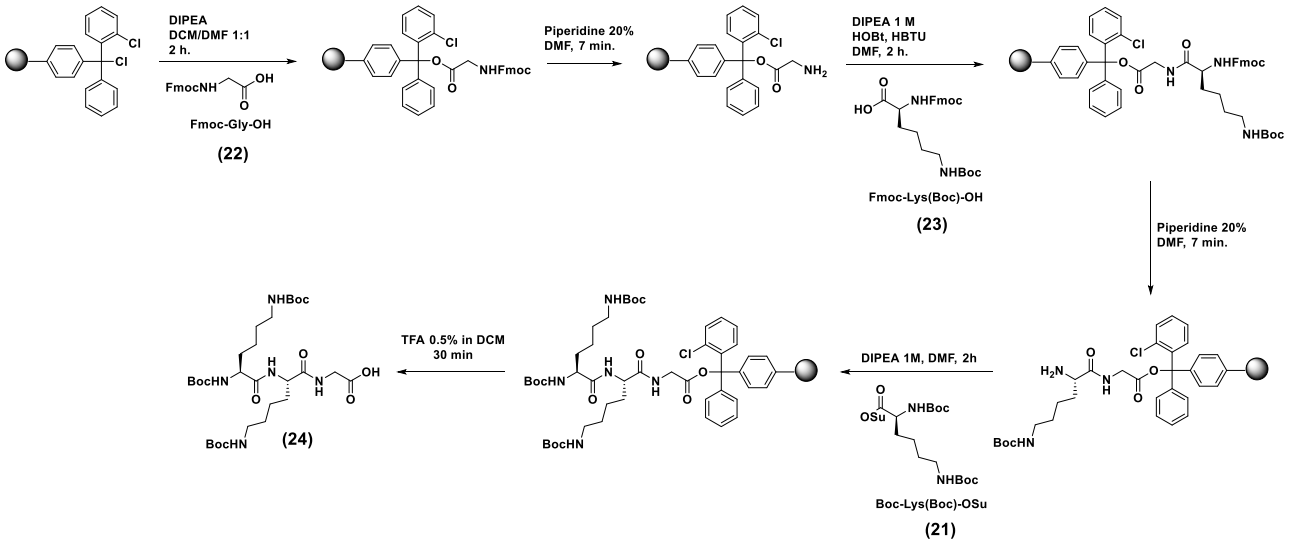

Scheme 4.10. Synthesis of the peptide Lys-Lys-Gly (**24**) by SPPS.

The protected peptide **24** was characterised by ^{1}H-NMR (Figure 4.36) and ESI-MS. Regarding the ^{1}H-NMR spectrum, the characteristic peaks are those of the methylene protons in α to the Boc-protected amino group of the lysine side chains 3.08-3.01 ppm, the multiplet at 3.80-4.0 ppm relative to the α protons of glycine and the internal lysine, and the signal of the α proton of the N-terminal lysine at 4.38 ppm.

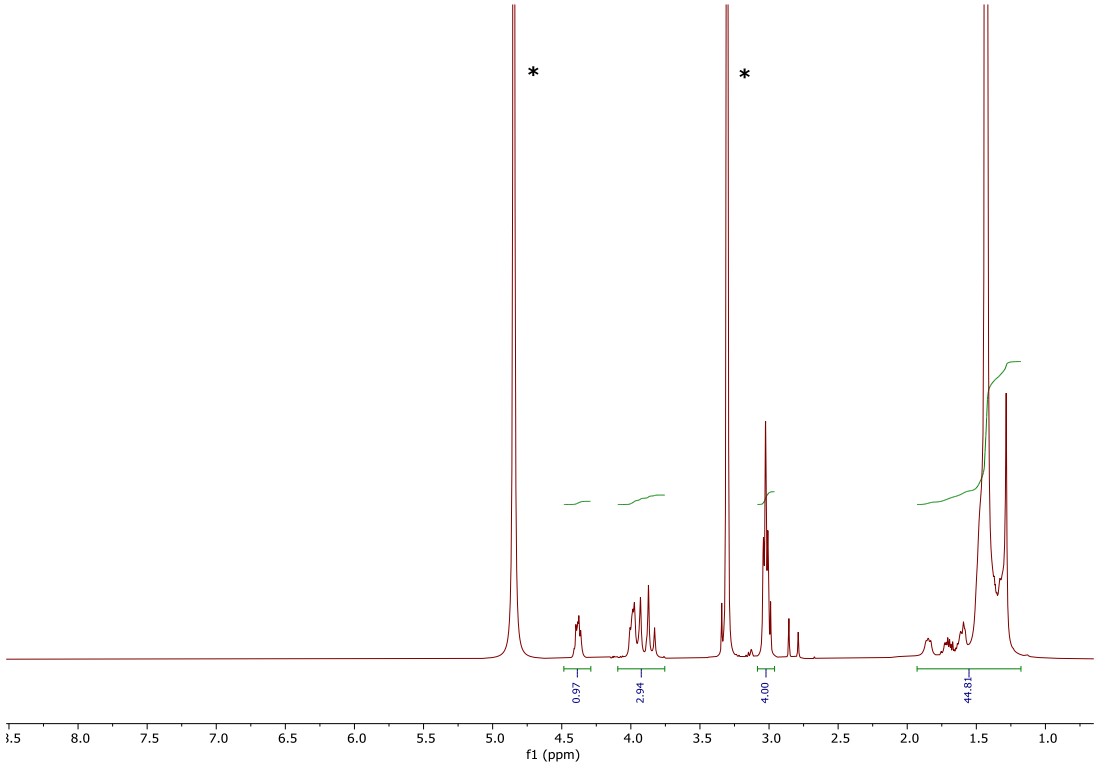

Figure 4.36. ^{1}H NMR (400 MHz, CD_3OD) of compound **24**. The solvent peaks are indicated by an asterisk (methanol, water).

The synthetic strategy for the preparation of **HP1** consists of a coupling reaction between the protected peptide **24** and compound **16**, followed by the simultaneous deprotection of the thiol group and the amino groups of the amino acid-side chains (Scheme 4.11).

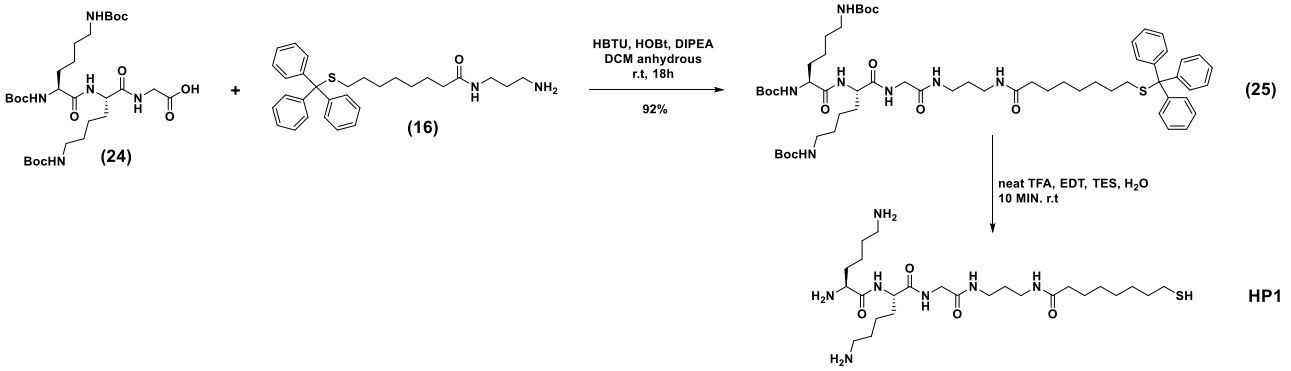

Scheme 4.11. Synthesis of **HP1** starting from corresponding building blocks.

The coupling reaction was performed using the common activating agents used in the SPPS, namely HBTU and HOBt, obtaining the compound **25** whose ^{1}H-NMR spectrum are shown in Figure 4.37.

The absence of the signal of the methylene protons in α to the amino group of **16** at 2.63 ppm confirms the coupling.

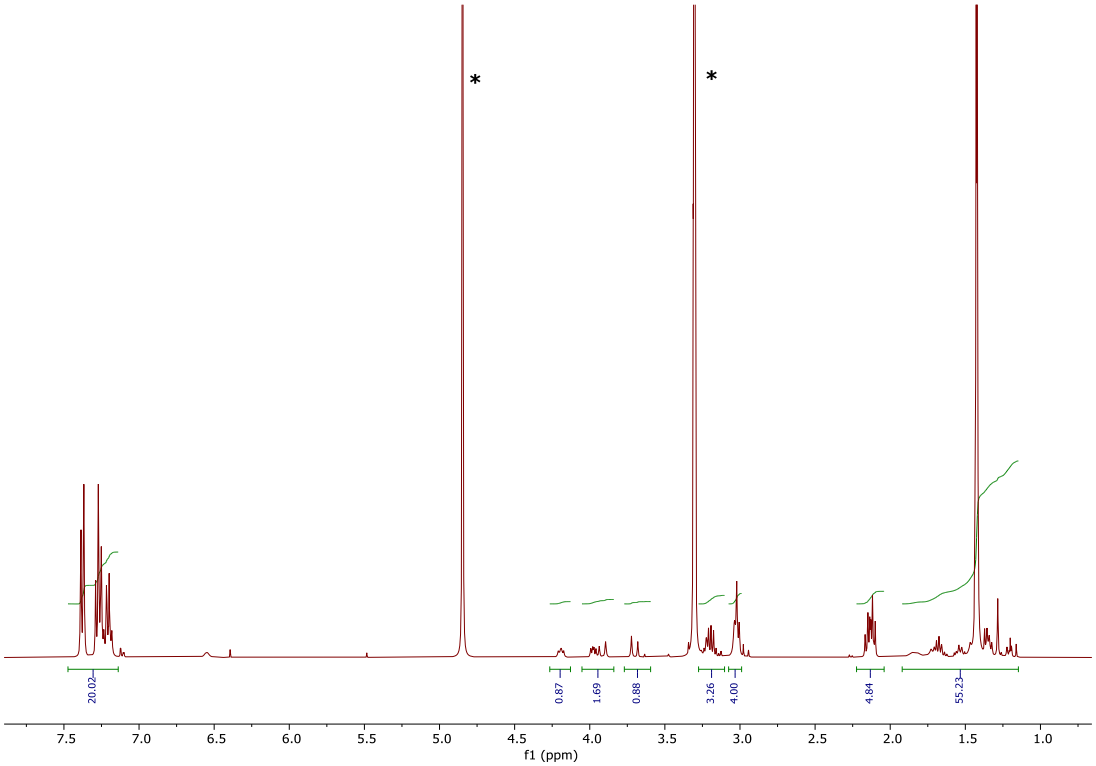

Figure 4.37. ^{1}H-NMR (400 MHz, CD_3OD) of product **25**. The solvent peaks are indicated by an asterisk (methanol, water).

The subsequent step involved several problems regarding the optimization of the deprotection cocktail, since in most cases the alkylation of the sulfur atom by the *tert*-butyl group occurred. However, the addition of 1,2-ethanedithiol (EDT) in the cleavage mixture (neat TFA /H_2O/EDT/TES; 94:2.5:2.5:1) prevented this side reaction, allowing the preparation of **HP1**. The corresponding ^{1}H-NMR spectrum is reported in Figure 4.38 and shows the characteristic peak of the protons in α to the free thiol function, and the absence of the signal related to the Boc-protons.

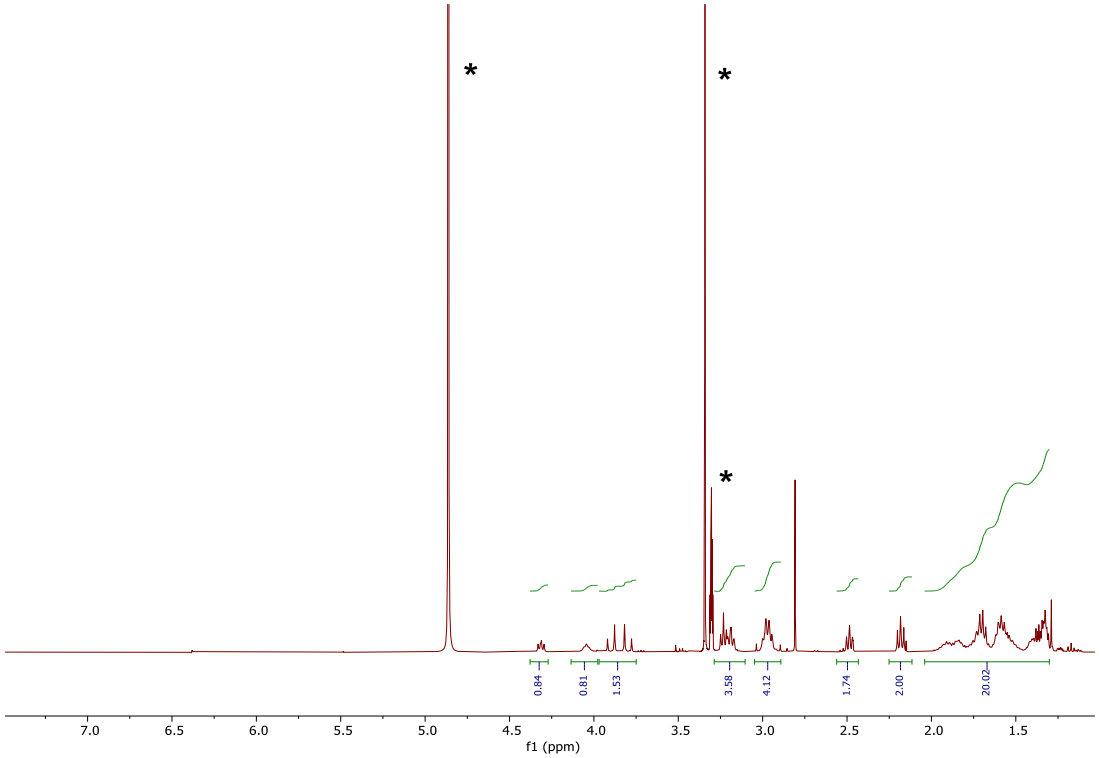

Figure 4.38. ^{1}H-NMR (400 MHz, CD_3OD) of **HP1**. The solvent peaks are indicated by an asterisk (methanol, water).

Unfortunately, within the time span of this PhD thesis it was not possible to use ligand **HP1** for the preparation of gold nanoparticles, this activity will be part of the future development of this project. In particular, we aim at preparing a series of mixed monolayer gold nanoparticles of varying size using **HP1** and the ligands **HC12N** and **HC16N**. The assessment of the bacteria nanoparticles interaction in this case will help in understanding whether the peptide moieties can increase the selectivity of the library towards different Gram-negative strains and/or improve the discriminating properties towards Gram positive/negative and mycobacteria. In addition, the possibility to prepare gold nanoparticles using blends of **HP1** and a fluorinated ligand will also be explored.

References

(1) Boisselier, E.; Salmon, L.; Ruiz, J.; Astruc, D. How to Very Efficiently Functionalize Gold Nanoparticles by "Click" Chemistry. *Chem. Commun.* **2008**, No. 44, 5788–5790. https://doi.org/10.1039/B812249K.

(2) Li, N.; Binder, W. H. Click-Chemistry for Nanoparticle-Modification. *J. Mater. Chem.* **2011**, *21* (42), 16717–16734. https://doi.org/10.1039/C1JM11558H.

(3) van der Meer, S. B.; Loza, K.; Wey, K.; Heggen, M.; Beuck, C.; Bayer, P.; Epple, M. Click Chemistry on the Surface of Ultrasmall Gold Nanoparticles (2 Nm) for Covalent Ligand Attachment Followed by NMR Spectroscopy. *Langmuir* **2019**, *35* (22), 7191–7204. https://doi.org/10.1021/acs.langmuir.9b00295.

(4) Kolb, H. C.; Finn, M. G.; Sharpless, K. B. Click Chemistry: Diverse Chemical Function from a Few Good Reactions. *Angew. Chem. Int. Ed.* **2001**, *40* (11), 2004–2021. https://doi.org/10.1002/1521-3773.

(5) Huisgen, R. 1,3-Dipolar Cycloadditions. Past and Future. *Angew. Chem. Int. Ed. Engl.* **1963**, *2* (10), 565–598. https://doi.org/10.1002/anie.196305651.

(6) Huisgen, R. Kinetics and Mechanism of 1,3-Dipolar Cycloadditions. *Angew. Chem. Int. Ed. Engl.* **1963**, *2* (11), 633–645. https://doi.org/10.1002/anie.196306331.

(7) Agard, N. J.; Prescher, J. A.; Bertozzi, C. R. A Strain-Promoted [3 + 2] Azide−Alkyne Cycloaddition for Covalent Modification of Biomolecules in Living Systems. *J. Am. Chem. Soc.* **2004**, *126* (46), 15046–15047. https://doi.org/10.1021/ja044996f.

(8) Li, Z.; Seo, T. S.; Ju, J. 1,3-Dipolar Cycloaddition of Azides with Electron-Deficient Alkynes under Mild Condition in Water. *Tetrahedron Lett.* **2004**, *45* (15), 3143–3146. https://doi.org/10.1016/j.tetlet.2004.02.089.

(9) McKay, C. S.; Moran, J.; Pezacki, J. P. Nitrones as Dipoles for Rapid Strain-Promoted 1,3-Dipolar Cycloadditions with Cyclooctynes. *Chem. Commun.* **2010**, *46* (6), 931–933. https://doi.org/10.1039/B921630H.

(10) McKay, C. S.; Blake, J. A.; Cheng, J.; Danielson, D. C.; Pezacki, J. P. Strain-Promoted Cycloadditions of Cyclic Nitrones with Cyclooctynes for Labeling Human Cancer Cells. *Chem. Commun.* **2011**, *47* (36), 10040–10042. https://doi.org/10.1039/C1CC13808A.

(11) Ning, X.; Temming, R. P.; Dommerholt, J.; Guo, J.; Ania, D. B.; Debets, M. F.; Wolfert, M. A.; Boons, G.-J.; van Delft, F. L. Protein Modification by Strain-Promoted Alkyne–Nitrone Cycloaddition. *Angew. Chem.* **2010**, *122* (17), 3129–3132. https://doi.org/10.1002/ange.201000408.

(12) Staudinger, H.; Meyer, J. Über Neue Organische Phosphorverbindungen III. Phosphinmethylenderivate Und Phosphinimine. *Helv. Chim. Acta* **1919**, *2* (1), 635–646. https://doi.org/10.1002/hlca.19190020164.

(13) Saxon, E.; Bertozzi, C. R. Cell Surface Engineering by a Modified Staudinger Reaction. *Science* **2000**, *287* (5460), 2007–2010. https://doi.org/10.1126/science.287.5460.2007.

(14) Lin, F. L.; Hoyt, H. M.; van Halbeek, H.; Bergman, R. G.; Bertozzi, C. R. Mechanistic Investigation of the Staudinger Ligation. *J. Am. Chem. Soc.* **2005**, *127* (8), 2686–2695. https://doi.org/10.1021/ja044461m.

(15) Dorn, R. S.; Prescher, J. A. Bioorthogonal Phosphines: Then and Now. *Isr. J. Chem.* **2023**, *63* (1–2), e202200070. https://doi.org/10.1002/ijch.202200070.

(16) Schilling, C. I.; Jung, N.; Biskup, M.; Schepers, U.; Bräse, S. Bioconjugation Viaazide–Staudinger Ligation: An Overview. *Chem. Soc. Rev.* **2011**, *40* (9), 4840–4871. https://doi.org/10.1039/C0CS00123F.

(17) Köhn, M.; Breinbauer, R. The Staudinger Ligation—A Gift to Chemical Biology. *Angew. Chem. Int. Ed.* **2004**, *43* (24), 3106–3116. https://doi.org/10.1002/anie.200401744.

(18) van Berkel, S. S.; van Eldijk, M. B.; van Hest, J. C. M. Staudinger Ligation as a Method for Bioconjugation. *Angew. Chem. Int. Ed.* **2011**, *50* (38), 8806–8827. https://doi.org/10.1002/anie.201008102.

(19) Gobbo, P.; Luo, W.; Cho, S. J.; Wang, X.; Biesinger, M. C.; Hudson, R. H. E.; Workentin, M. S. Small Gold Nanoparticles for Interfacial Staudinger–Bertozzi Ligation. *Org. Biomol. Chem.* **2015**, *13* (15), 4605–4612. https://doi.org/10.1039/C5OB00372E.

(20) Kovalyshyn, S. Sintesi e Caratterizzazione Di Un Legante per Click Chemistry Su Nanoparticelle d'oro. tesi magistrale, Università di Trieste, 2022.

(21) Sharma, R.; Holland, G. P.; Solomon, V. C.; Zimmermann, H.; Schiffenhaus, S.; Amin, S. A.; Buttry, D. A.; Yarger, J. L. NMR Characterization of Ligand Binding and Exchange Dynamics in Triphenylphosphine-Capped Gold Nanoparticles. *J. Phys. Chem. C* **2009**, *113* (37), 16387–16393. https://doi.org/10.1021/jp905141h.

(22) Zhang, S.-S.; Feng, L.; Senanayake, R. D.; Aikens, C. M.; Wang, X.-P.; Zhao, Q.-Q.; Tung, C.-H.; Sun, D. Diphosphine-Protected Ultrasmall Gold Nanoclusters: Opened Icosahedral Au13 and Heart-Shaped Au8 Clusters. *Chem. Sci.* **2018**, *9* (5), 1251–1258. https://doi.org/10.1039/C7SC03566G.

(23) Marbella, L. E.; Crawford, S. E.; Hartmann, M. J.; Millstone, J. E. Observation of Uniform Ligand Environments and 31P–197Au Coupling in Phosphine-Terminated Au Nanoparticles. *Chem. Commun.* **2016**, *52* (58), 9020–9023. https://doi.org/10.1039/C6CC00464D.

(24) Polgar, A. M.; Weigend, F.; Zhang, A.; Stillman, M. J.; Corrigan, J. F. A N-Heterocyclic Carbene-Stabilized Coinage Metal-Chalcogenide Framework with Tunable Optical Properties. *J. Am. Chem. Soc.* **2017**, *139* (40), 14045–14048. https://doi.org/10.1021/jacs.7b09025.

(25) Manea, F.; Bindoli, C.; Polizzi, S.; Lay, L.; Scrimin, P. Expeditious Synthesis of Water-Soluble, Monolayer-Protected Gold Nanoparticles of Controlled Size and Monolayer Composition. *Langmuir* **2008**, *24* (8), 4120–4124. https://doi.org/10.1021/la703558y.

(26) Luo, W.; Gobbo, P.; Gunawardene, P. N.; Workentin, M. S. Fluorogenic Gold Nanoparticle (AuNP) Substrate: A Model for the Controlled Release of Molecules from AuNP Nanocarriers via Interfacial Staudinger–Bertozzi Ligation. *Langmuir* **2017**, *33* (8), 1908–1913. https://doi.org/10.1021/acs.langmuir.6b03647.

Conclusions and future perspectives

The research activities carried out in this thesis work have led to the preparation and characterization of a library of homoligand cationic AuNPs of different sizes displaying on their monolayer ligands of different lengths featuring tetraalkylammonium end-groups. These ligands were also used for the preparation of mixed monolayer nanoparticles in association with a fluorinated ligand. In addition, this thesis work also led to the set-up of a fluorescence-based transduction mechanism to report the binding event between the nanoparticles and the target. In detail, four types of homoligand cationic AuNPs of various sizes (usNP C12N, usNP C16N, NP C12N, and NP C16N) and four types of heteroligand AuNPs (NP C12N/F6 (5:1), NP C12N/F6 (2.9:1), NP C16N/F6 (3.6:1), and NP C16N/F6 (3.1:1)) have been prepared. For the mixed monolayer systems, blends of cationic hydrogenated ligands (**HC12N** or **HC16N**) and the fluorinated ligand HF6 were selected such to obtain nanoparticles with excellent solubility in water and different loading of the fluorinated ligand. Regarding the setup of the transduction mechanism, the anionic fluorescent polymer PPP-OSO_3 was selected to test and evaluate the quenching properties of each batch of nanoparticles in an aqueous environment. The titration of PPP-OSO_3 with the nanoparticles was accompanied by the quenching of the polymer fluorescence that was found to take place by a static quenching mechanism occurring on the polymer bound to the nanoparticle surface. Preliminary assessment of the binding affinity of PPP-OSO_3 for the gold nanoparticle surface was carried out in collaboration with the group of Prof. Marco Montalti of Università di Bologna. These studies pinpointed that the binding affinity depends on the positive charge density at the nanoparticle surface and that it is also influenced by the presence of hydrophobic fluorinated ligands. To deepen the study of AuNPs/PPP-OSO_3 interactions and evaluate the role of the fluorinated ligands in establishing the AuNPs-biointerface interactions, two liposomes of different negative charges density (L_1 and L_2) were prepared and used as simplified models of bacterial cell walls. These experiments allowed to pinpoint that the highest fluorescence signals, corresponding to a higher concentration of free polymer, were obtained when the heteroligand

AuNPs with the highest percentage of the fluorinated ligand (NP C12/F6 2.9 :1 and NP C16/F6 3.1:1) were used. This suggests that the hydrophobicity of the nanoparticle surface due to the introduction of fluorinated ligands plays a crucial role in promoting their interaction with the phospholipid membranes and thus preventing the nanoparticle interaction with the fluorescent polymer. These data are further evidence that tailoring the surface hydrophobicity of gold nanoparticles by using fluorinated ligands is a viable design strategy to optimise the nanoparticle-biointerface interactions. Furthermore, these data are in line with those reported in previous theoretical and experimental works, displaying that the adhesion free energy to a model membrane of AuNPs bearing fluorinated amphiphilic ligands is more favourable than that of analogous hydrogenated systems.

The library of gold nanoparticles as a whole was used in a proof of principle experiment to discriminate the two liposome L_1 and L_2. It has been possible to demonstrate that under the same experimental conditions, each member of the nanoparticle library displays a different fluorescence response and that, collectively, the use of a library allows one to obtain different fluorescence profiles for the two liposomes that can be primarily ascribed to their different surface charge.

With this result we endeavoured a preliminary assessment, to evaluate the validity of our approach for a rapid discrimination of different bacteria strains. The biological tests were carried out in collaboration with the group of Prof. Cristina Airoldi and Prof. Alessandro Palmioli of Università of Milano-Bicocca; in these experiments we considered two different Gram-negative bacteria: *E. coli* and *P. putida* a Gram-positive bacterium: *S. epidermidis* and a mycobacterium: *M. smegmatis*. By using a relatively small library of nanoparticles, it was possible to obtain fluorescence profiles that are significantly different and allow differentiating between the Gram positive, Gram negative and mycobacteria. Furthermore, also among the two Gram negative strains the fluorescence profiles proved to be noticeably different. These preliminary results will be complemented in future studies by considering the whole library of eight nanoparticle systems developed in this thesis work and the number of bacterial strains will be increased considering other Gram-positive bacteria and mycobacteria.

Regarding the activities aimed at the design and preparation of a second set of AuNPs bearing peptide-modified ligands, the initial approach based on the Staudinger-Bertozzi ligation reaction for the preparation of activated AuNPs brought to light a remarkable instability of these systems probably due both to a low packing of the monolayer due to the steric hindrance of the ligand **12**, and to a likely inter-nanoparticle interaction between the phosphorus atom present in the end-group of **12** and the

surface gold atoms of AuNPs. To overcome this issue, mixed monolayer AuNPs bearing ligand **12** and the commercially available (11-Mercaptoundecyl)-*N,N,N*-trimethylammonium bromide (**HC11N**) were prepared, so as to prevent the approach of the nanoparticles by electrostatic repulsions and increase the packing of the monolayer. In this way it was possible to obtain stable mixed systems (NP C11N/12 I, NP C11N/12 II, usNP C11N/12, and usNP C11N/12 III), but with a low percentage of ligand **12** in the corresponding monolayer. Despite the low **12**/**HC11N** ratio, a ligation test was attempted between the usNP C11N/12 III, which display the highest loading of **12** on their monolayer, and an azide-modified lysine prepared by the SPPS strategy. However, both the NMR and the ESI mass analyses did not highlight the successful ligation, suggesting the need of further studies on the optimization of the Staudinger-Bertozzi ligation conditions for the preparation of bioconjugate AuNPs with azide-modified amino acids/peptides. To explore other synthetic approaches aimed to obtain peptide-decorated cationic AuNPs, a more conventional strategy based on the place exchange reaction was considered, and to this end, the cationic peptide-containing thiol **HP1** was designed and successfully synthesized, whose cationic nature is given by the presence of two lysine in the peptide moiety. This ligand will be used in the future for the preparation of mixed-monolayer AuNPs of varying sizes in combination with an amphiphilic cationic ligand to increase the diversity of the nanoparticle library developed so far aiming at further differentiate its response to different bacteria strains.

Chapter 5

5. Materials and Methods: General information

All reagents employed were bought from Merk and used without purification. Solvents and deuterated solvents were purchased from Merk. Chlorinated solvents employed for dissolving Au NPs were treated with K_2CO_3 before use. Reactions were monitored by TLC on Merck silica gel plates (0.25 mm) and visualized by UV light, $KMnO_4$-H_2SO_4, or Pancaldi solution. Flash column chromatography was performed on Normasil silica gel 60® 40-63 mm purchased from Merk. Deionized water was purified by Millipore Milli-Q filtration system. All the glassware employed for the synthesis of AuNPs was cleaned with aqua regia and copiously rinsed with milliQ water before use. Only milli-Q water was used for the synthesis of the gold nanoparticles. In addition, both the gold precursor ($HAuCl_4$) and 2-(diphenylphosphino) terephthalic acid 1-methyl 4-pentafluorophenyl diester were weighted inside the "glove bag", under an argon atmosphere.

Nuclear Magnetic Resonance spectra were recorded on a Varian 400 MHz spectrometer. The NMR spectra have been processed by means of MestReNova software. ^{1}H-NMR spectra were referenced to the residual protons in the deuterated solvent. ^{13}C-NMR spectra were referenced to the solvent chemical shift. For the spectra analysed in deuterated chloroform, the solvent was always treated beforehand with basic alumina to remove the acidity. Chemical shifts (δ) are reported in ppm and the multiplicity of each signal is identified by the conventional abbreviations: s for singlet, d for doublet, t for triplet, q for quartet, m for multiplet, br for broad peak. Coupling constants (J) are reported in Hertz (Hz).

Mass spectrometry measurements on ligands were performed by the microTOF-Q spectrometer operating under direct infusion conditions, with electrospray ionization (ESI) and quadrupole mass

analyser and recorded by Dr. Fabio Hollan at the Department of Chemical and Pharmaceutical Sciences of the University of Trieste, Italy.

The FTIR-ATR spectra were recorded with the Shimadzu FTIR-ATR instrument and the data was processed with the appropriate LabSolutionIR software package.

UV-Visible spectroscopy analyses were carried out on a Perkin Elmer Lambda 32 spectrophotometer, using disposable cuvettes. All UV-vis data have been analysed using the OriginLab software.

Transmission Electron Microscopy images were collected with a Philips EM 208 Electron Microscope operating at 100 kV equipped with EMSIS QUEMESA camera. Samples for TEM analysis were prepared by depositing 20 µL of 0.1 mg/mL solutions of nanoparticles on 200 mesh copper grids covered with amorphous carbon film. All TEM images have been analysed through ImageJ and OriginLab software.

Thermogravimetric Analyses were performed on a TGA5500 instrument performing an equilibration of the sample at 100°C, followed by an isotherm at 100°C for 20 minutes, and a heating rate of 10°C·min^{-1} up to 600 °C, and finally a last isotherm for 5 minutes. The results obtained were analyzed with the TRIOS and OriginLab software.

5.1 Experimental section from Chapter 3

Synthesis of compound 2[1]

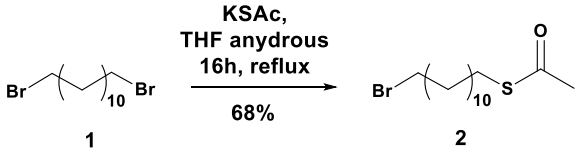

In a three-neck round bottom flask, 1 g (3.04 mmol, 2.2 eq.) of 1,12-dibromododecane (**1**) was dissolved in 7.2 mL of anhydrous THF. 0.158 g (1.38 mmol, 1 eq.) of KSAc were added to the solution and the mixture was carried out at reflux overnight under an argon atmosphere.

Purification: the mixture was dried under reduced pressure and the product was purified by gradient flash chromatography using petroleum ether:dichloromethane mixture from 9.5:0.5 to 7:3. The pure product was obtained as a white solid (0.305g, yield 68%).

^{1}H-NMR (400 MHz, $CDCl_3$) δ: 1.19÷1.47 (m, 16H, $\underline{CH_2}$- CH_2- CH_2-Br and -CH_2- $\underline{CH_2}$- CH_2- and $\underline{CH_2}$- CH_2- CH_2- $SCOCH_3$), 1.55 (m, 2H, -$\underline{CH_2}$- CH_2- $SCOCH_3$), 1.85 (m, 2H, -$\underline{CH_2}$- CH_2-Br), 2.32 (s, 3H, -SCO$\underline{CH_3}$), 2.86 (t, ^{3}J=7.4 Hz, 2H, -$\underline{CH_2}$- $SCOCH_3$), 3.40 (t, ^{3}J=7.0 Hz, 2H, -$\underline{CH_2}$- Br).

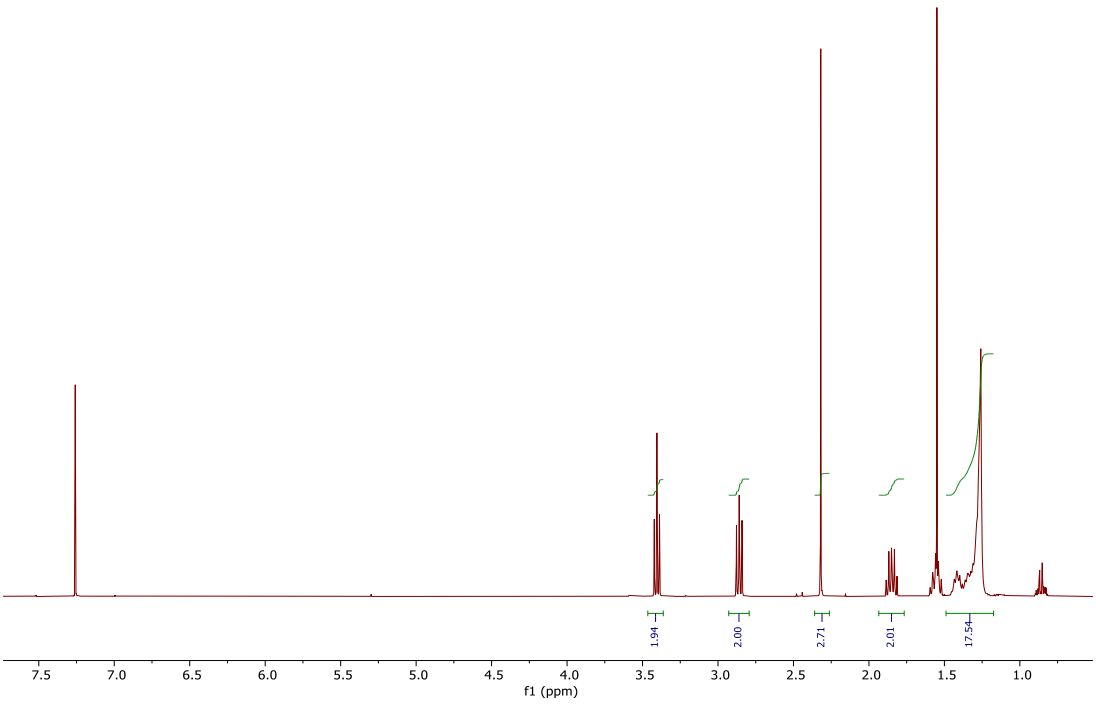

Synthesis of compound 3[1]

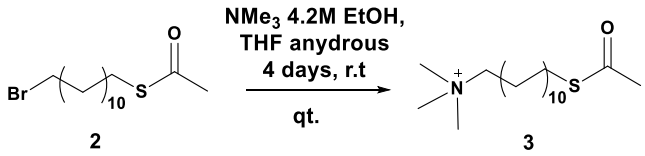

In a Pyrex tube, 0.292 g (0.905 mmol, 1 eq.) of **2** was dissolved in 10 mL of anhydrous THF. Then, 2.1 mL of trimethylamine 4.2 M solution in ethanol (9.05 mmol, 10 eq.) was added and the solution was stirred at room temperature for 4 days.

Purification: The resulting mixture was brought to dryness under reduced pressure to obtain the pure product as a white solid (0.89 g, quantitative yield).

^{1}H-NMR (400 MHz, $CDCl_3$) δ: 1.20÷1.46 (m,16H, -$\underline{CH_2}$- CH_2- CH_2- $N(CH_3)_3$ and -CH_2- $\underline{CH_2}$- CH_2- and -$\underline{CH_2}$- CH_2- CH_2- $SCOCH_3$), 1.57 (m, 2H, -$\underline{CH_2}$- CH_2- $SCOCH_3$), 1.76 (m, 2H, -$\underline{CH_2}$- CH_2- $N(CH_3)_3$), 2.33 (s, 3H, -SCO$\underline{CH_3}$), 2.86 (t, ^{3}J=7.4 Hz, 2H, -$\underline{CH_2}$- $SCOCH_3$), 3.46 (s, 9H, -N($\underline{CH_3}$)$_3$), 3.57 (m, 2H, -$\underline{CH_2}$- $N^{+}(CH_3)_3$).

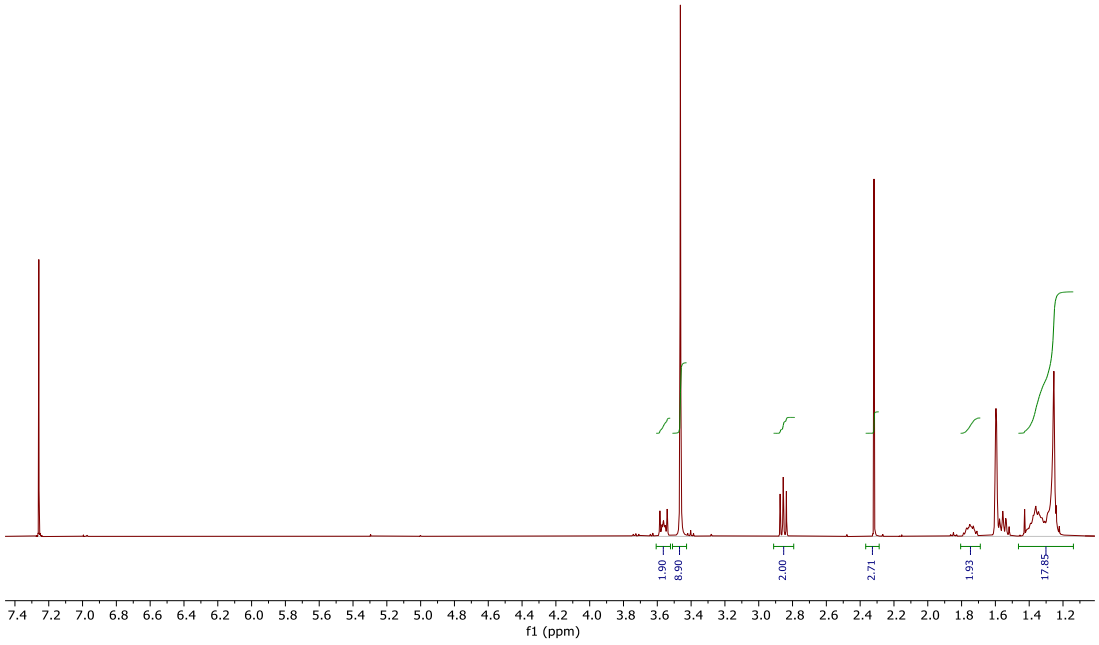

Synthesis of compound 4[1]

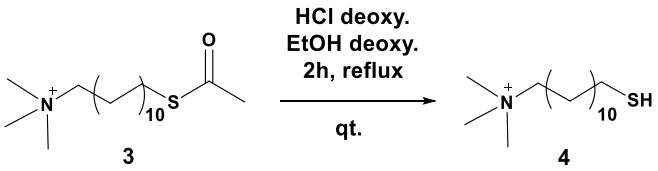

In a three-neck round bottom flask, 0.31 g (0.81 mmol, 1 eq.) of **3** were dissolved in 5 mL of deoxygenated ethanol. 5 mL of 6 M HCl deoxygenated solution was added. The resulting solution was heated at reflux temperature for 3 hours working under an argon atmosphere.

Purification: The resulting mixture was brought to dryness under reduced pressure in an argon atmosphere. A white solid was obtained (0.273 g, quantitative yield).

^{1}H-NMR (400 MHz, CD_3OD) δ: 1.20÷1.46 (m, 16H, -CH_2- $\underline{CH_2}$- CH_2 and -$\underline{CH_2}$- CH_2- CH_2- SH and $\underline{CH_2}$- CH_2- CH_2- $N(CH_3)_3$), 1.60 (m, 2H, -$\underline{CH_2}$-CH_2-SH), 1.76 (m, 2H, -$\underline{CH_2}$- CH_2-$N(CH_3)_3$), 2.5 (m, 2H, -$\underline{CH_2}$- SH), 3.17-3.61 (m, 11H, -$\underline{CH_2}$- $N(CH_3)_3$ and -$N(\underline{CH_3})_3$).

TOF (m/z): 260.2406 [M^+].

Synthesis of compound 6[1]

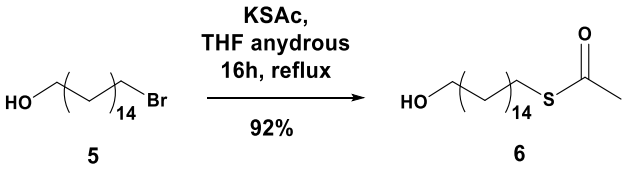

In a three-neck round bottom flask, 0.1 g (0.31 mmol, 1 eq.) of **5** were dissolved in 0.5 mL of anhydrous DMF, and 0.035 g of KSAc (0.31 mmol, 1 eq.) were added. The mixture was stirred at room temperature for 1 hour under an argon atmosphere.

Purification: diethyl ether was added to the reaction mixture to precipitate the KBr. The mixture was filtered under vacuum on a Büchner funnel. The organic phase was washed with water (3 x 10 mL) and dried over Na_2SO_4 And the solvent was removed under reduced pressure, obtaining the product as a white solid. (0.90 g, yield 92%).

^{1}H-NMR (400 MHz, $CDCl_3$) δ: 1.10÷1.32 (m, 24H, $\underline{CH_2}$- CH_2- CH_2- $SCOCH_3$ and CH_2- $\underline{CH_2}$- CH_2- and $\underline{CH_2}$- CH_2- CH_2- OH), 1.36 (m, 2H,-$\underline{CH_2}$- CH_2- $SCOCH_3$), 1.44 (m, 2H, $\underline{CH_2}$- CH_2- OH), 1.87 (s, 3H, $SCO\underline{CH_3}$), 2.77 (t, ^{3}J=7.4 Hz, 2H, $\underline{CH_2}$- $SCOCH_3$), 3.33 (t, ^{3}J=7.0 Hz, 2H, $\underline{CH_2}$- OH).

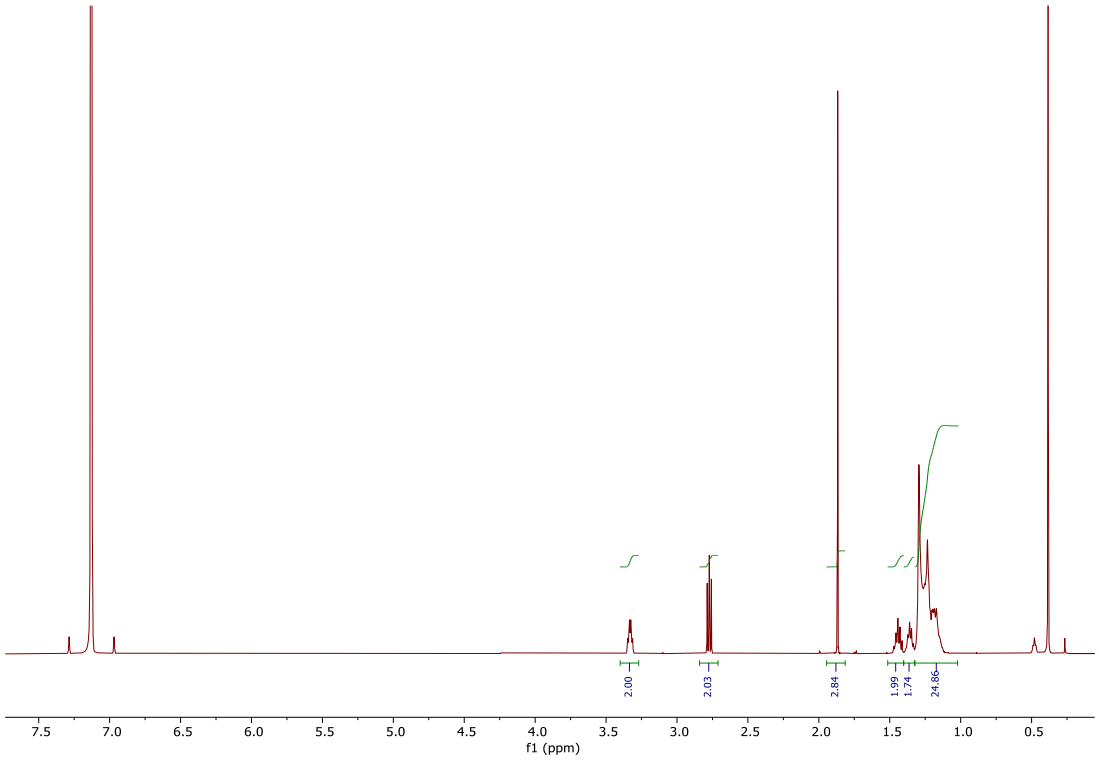

Synthesis of compound 7[2]

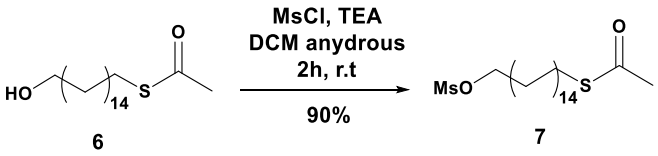

In a three-neck round bottom flask 0.148 g (0.47 mmol, 1 eq.) of **6** were dissolved in 1.6 mL of anhydrous DCM and 0.05 mL of MsCl (0.7 mmol, 1.5 eq.) were added at 0°C. The reaction mixture was stirred at 0°C for 5 minutes, then 0.13 mL of TEA (0.93 mmol, 2 eq.) were added dropwise. The mixture was stirred at room temperature for 2 hours working under an argon atmosphere.

Purification: The reaction mixture was washed with an aqueous solution of HCl 0.1M (1 x10 mL), water (2 x 10 mL), and brine (2 x 10 mL). The organic phase was dried over Na_2SO_4. After evaporation of the solvent under reduced pressure and drying in vacuum, the product was obtained as a white solid (0.165 g, yield 90%).

^{1}H-NMR (400 MHz, $CDCl_3$) δ: 1.10÷1.45 (m, 24H, $\underline{CH_2}$- CH_2- CH_2- OMs and CH_2- $\underline{CH_2}$- CH_2- and $\underline{CH_2}$- CH_2- CH_2- $SCOCH_3$), 1.56 (m, 2H, $\underline{CH_2}$-CH_2- S-$COCH_3$), 1.74 (m, 2H, $\underline{CH_2}$- CH_2- OMs), 2.30 (s, 3H, $SCO\underline{CH_3}$), 2.84 (t, ^{3}J=7.4 Hz, 2H, $\underline{CH_2}$- $SCOCH_3$), 3.00 (s, 3H, OMs-$\underline{CH_3}$), 4.23 (t, ^{3}J=6.7 Hz, 2H, $\underline{CH_2}$- OMs).

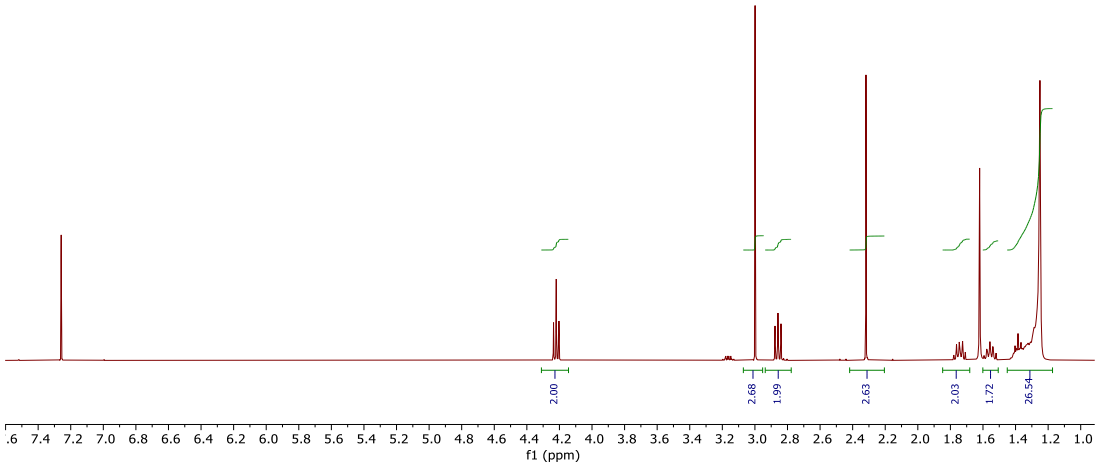

Synthesis of compound 8[2]

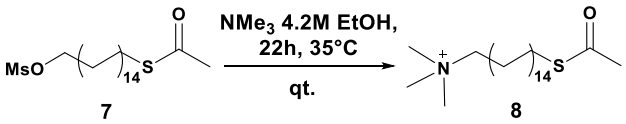

7 8

0.165 g (0.42 mmol, 1 eq.) of **7** were dissolved in 1 mL of anhydrous THF in a Pyrex tube. 4.0 mL of 4.2 M trimethylamine solution in ethanol were added (16.70 mmol, 40 eq.). The reaction mixture was stirred at 35°C for 22 hours.

Purification: The mixture was diluted with 1 mL of DCM and cooled at 0°C. Then diethyl ether was added until a white solid precipitated. The mixture was filtered under vacuum on a Büchner funnel, and the solid was washed with diethyl ether (5 x 10 mL). Then, the solid was recovered by dissolving it with dichloromethane (3 mL) and transferred in a round bottom flask. Then, the solvent was removed under reduced pressure obtaining a white solid (0.172 g, yield 90%).

^{1}H-NMR (400 MHz, $CDCl_3$) δ: 1.10÷1.45 (m, 24H, $\underline{CH_2}$- CH_2- CH_2- S-$COCH_3$ and CH_2- $\underline{CH_2}$- CH_2- and $\underline{CH_2}$- CH_2- CH_2- $N(CH_3)_3$), 1.56 (m, 2H, $\underline{CH_2}$- CH_2- $SCOCH_3$), 1.73 (m, 2H, -$\underline{CH_2}$- CH_2- $N(CH_3)_3$), 2.30 (s, 3H, SCO$\underline{CH_3}$), 2.77 (s, 3H, $^{-}$OMs- $\underline{CH_3}$), 2.84 (t, ^{3}J=7.4 Hz, 2H, -$\underline{CH_2}$- $SCOCH_3$), 3.33 (s, 9H, -N($\underline{CH_3}$)$_3$), 3.43 (m, 2H, $\underline{CH_2}$- $N(CH_3)_3$).

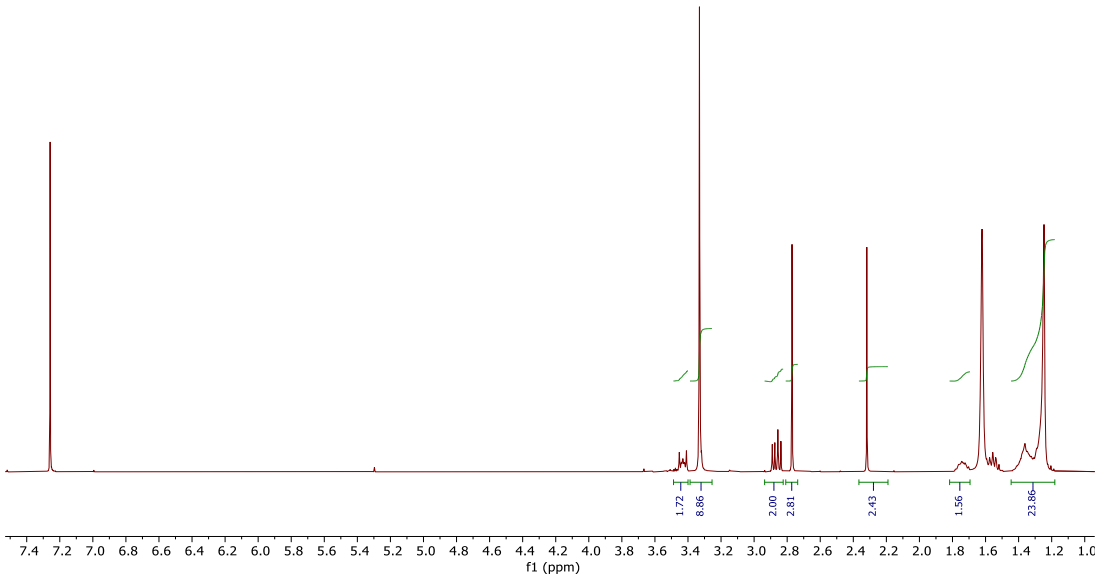

Synthesis of compound 9[1]

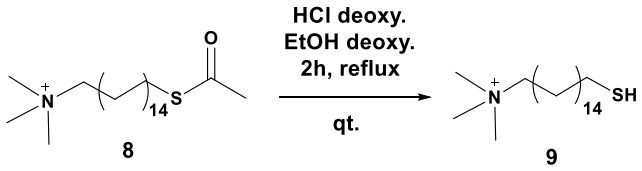

In a three-neck round bottom flask, 0.232 g (0.51 mmol) of **8** were dissolved in a mixture of 2 mL of deoxygenated EtOH and 2 mL of HCl 6M deoxygenated solution. The mixture was heated at reflux temperature under an argon atmosphere for 2 hours.

Purification: The reaction mixture was brought to dryness under reduced pressure in an argon atmosphere obtaining a white solid (0.21 g, quantitative yield).

^{1}H-NMR (400 MHz, CD_3OD) δ: 1.27÷1.46 (m, 24H, $\underline{CH_2}$- CH_2- CH_2-SH and CH_2- $\underline{CH_2}$- CH_2- and $\underline{CH_2}$- CH_2- CH_2- $N(CH_3)_3$), 1.58 (m, 2H, -$\underline{CH_2}$- CH_2- SH), 1.78 (m, 2H, -$\underline{CH_2}$- CH_2-$N(CH_3)_3$), 2.48 (m, 2H, -$\underline{CH_2}$- SH), 2.71 (s, 3H, $^-$OMs- $\underline{CH_3}$), 3.12 (s, 9H, -$N(\underline{CH_3})_3$), 3.31 (m, 2H, -$\underline{CH_2}$- $N(CH_3)_3$).

TOF (m/z): 316.3032 [M^+].

Synthesis of usNP C12N

A solution of $HAuCl_4 \cdot 3H_2O$ (0.05 g, 0.127 mmol, 1 eq.) in water (6 mL) was extracted with a solution of TOAB (3 g, 4.57 mmol, 36 eq.) in argon-purged toluene (125 mL). To the resulting reddish-orange organic solution, dioctylamine (3.36 g, 13.92 mmol, 55 eq.) was added. The mixture was vigorously stirred under argon for 40 min. During this period the color of the mixture faded. A solution of $NaBH_4$ (0.047 g, 1.23 mmol, 9.7 eq.) in H_2O (2 mL) was then rapidly added. The color of the solution turned rapidly to black due to nanoparticle formation. After 2 hours of stirring, the aqueous layer was removed. A solution of the thiol **HC12N** prepared by dissolving 0.022 g of **HC12N** (0.065 mmol) in 3 mL of deoxygenated methanol was rapidly added to the nanoparticle solution. The mixture was stirred overnight, and after this period 10 mL of water were added under vigorous stirring. The stirring was continued for 1 hour, and during this time the toluene solution become colourless, while the aqueous layer turned dark-brown.

Purification: the aqueous layer containing the nanoparticles was washed with toluene (2 x 30mL), ethyl ether (3 x 30 mL), and ethyl acetate (5 x 30 mL). Then, the aqueous solution was brought to dryness, and the solid residue was taken up with 2 mL of methanol and transferred to a centrifuge tube. Ethyl ether was slowly added to the solution until the precipitation of AuNPs occurred, then, the nanoparticles were collected by centrifugation (3800 x 8 min). The precipitation/centrifugation process was repeated 5 times. In the end, 0.04 g of AuNPs were obtained ($Au_{262}C12N_{80}$).

^{1}H-NMR (400 MHz, CD_3OD) δ: 1.21-1.67 (br.), 1.79-1.95 (br.), 3.13-3.90 (br.)

TEM: 1.95 ± 0.58 nm

λ_{ExMax}: 370 nm; λ_{EmMax}: 1050 nm (excitation and emission spectra were carried out in milliQ water)

Synthesis of usNP C16N

A solution of $HAuCl_4 \cdot 3H_2O$ (0.05 g, 0.127 mmol, 1 eq.) in water (6 mL) was extracted with a solution of TOAB (3 g, 4.57 mmol, 36 eq.) in argon-purged toluene (125 mL). To the resulting reddish-orange organic solution, dioctylamine (3.36 g, 13.92 mmol, 55 eq.) was added. The mixture was vigorously stirred under argon for 40 minutes. During this period the color of the mixture faded. A solution of $NaBH_4$ (0.047 g, 1.23 mmol, 9.7 eq.) in H_2O (2 mL) was then rapidly added. The color of the solution turns rapidly to black due to nanoparticle formation. After 2 hours of stirring, the aqueous layer was removed. A solution prepared by dissolving 0.026 g (0.063 mmol) of the thiol **HC16N** in 3 mL of deoxygenated methanol was rapidly added to the nanoparticle solution. The mixture was stirred overnight, and after this period 10 mL of water were then added under vigorous stirring. The stirring was continued for 1 hour, and during this time the toluene solution becomes colourless, while the aqueous turned bark-brown.

Purification: the aqueous layer containing the nanoparticles was washed with toluene (2 x 30mL), ethyl ether (3 x 30 mL), and ethyl acetate (5 x 30 mL). Then, the aqueous solution was brought to dryness, and the solid residue was taken up with 2 mL of methanol and transferred to a centrifuge tube. Ethyl ether was slowly added to the solution until the precipitation of AuNPs occurred, then, the nanoparticles were collected by centrifugation (3800 x 8 min). The precipitation/centrifugation process was repeated 5 times. In the end, 0.041 g of AuNPs were obtained ($Au_{323}C16N_{70}$).

^{1}H-NMR (400 MHz, CD_3OD) δ: 1.15-1.62 (br.), 1.72-1.95 (br.), 3.13-3.52 (br.)

TEM: 2.09 ± 0.74 nm

λ_{ExMax}: 370 nm; λ_{EmMax}: 1100 nm (excitation and emission spectra were carried out in milliQ water)

Synthesis of NP C12N

In a three-neck round bottom flask, 0.101 g of $HAuCl_4 \cdot 3H_2O$ (0.256 mmol, 1 eq.) were dissolved in 10 mL of deoxygenated milliQ water. Then, 0.757 g of TOAB (1.384 mmol, 5.4 eq.) were dissolved in 7.7 mL of deoxygenated chloroform and added to the $HAuCl_4$ solution. The reaction mixture was stirred at room temperature for 30 minutes. Afterward, the mixture was centrifuged to aid the separation of the aqueous and organic phases, and the aqueous phase was discarded. The red-orange coloured organic phase was washed 3 times with 8 mL of deoxygenated milliQ water. Then, a fresh

solution of 0.141 g of $NaBH_4$ (3.719 mmol, 14.5 eq.) in 6.8 mL of deoxygenated milliQ water was quickly added to the $AuCl_4^-TOA^+$ solution. The organic phase became dark violet due to AuNP formation. The reaction was stirred for 15 minutes at room temperature. After, the mixture was centrifuged to eliminate the aqueous phase, and the organic phase was washed 3 times with deoxygenated milliQ water (8 mL). Then, a solution of **HC12N** (0.013 g, 0.038 mmol) in 6 mL of deoxygenated methanol was added to the AuNPs solution. The mixture was stirred at room temperature for 2 hours.

Purification: The solvent was removed under reduced pressure and the resulting solid was dissolved in 2 mL of MeOH and transferred in a centrifuge tube. Ethyl ether was slowly added to the solution until the precipitation of AuNPs occurred, then, the nanoparticles were collected by centrifugation (3800 x 8 min). This process was repeated for six times. In the end, 0.03 g of AuNPs were obtained ($Au_{3680}C12N_{346}$).

^{1}H-NMR (400 MHz, CD_3OD) δ: 0.79-2.52 (br.), 2.86-4.13 (br).

TEM: 4.70 ± 1.33 nm

UV-vis: λ_{max} 530 nm (in MilliQ water)

Synthesis of NP C16N

In a three-neck round bottom flask, 0.094 g of $HAuCl_4 \cdot 3H_2O$ (0.237 mmol, 1 eq.) were dissolved in 9.3 mL of deoxygenated milliQ water. Then, 0.702 g of TOAB (1.283 mmol, 5.4 eq.) were dissolved in 7.1 mL of deoxygenated chloroform and added to the $HAuCl_4$ solution. The reaction mixture was stirred at room temperature for 30 minutes. After, the mixture was centrifuged to aid separation of the aqueous and organic phases and the aqueous layer was discarded. The red-orange coloured organic phase was washed 3 times with 8 mL of deoxygenated milliQ water. Then, a fresh solution of 0.130 g of $NaBH_4$ (3.44 mmol, 14.5 eq.) in 6.3 mL of deoxygenated milliQ water was quickly added to the $AuCl_4^-TOA^+$ solution. The organic phase became dark violet due to AuNP formation. The reaction mixture was stirred for 15 minutes at room temperature. After, the mixture was centrifuged and the aqueous phase discarded, and the organic phase was washed 3 times with deoxygenated milliQ water (8 mL). Then, a solution of **HC16N** (0.016 g, 0.035 mmol) in 6 mL of deoxygenated methanol was added to the AuNPs solution. The mixture was stirred at room temperature for 2 hours.

Purification: The solvent was removed under reduced pressure and the resulting solid was dissolved in 2 mL of MeOH and transferred in a centrifuge tube. Ethyl ether was slowly added to the solution until the precipitation of AuNPs occurred, then, the nanoparticles were collected by centrifugation (3800 x 8 min). This process was repeated for six times. In the end, 0.034 g of AuNPs were obtained ($Au_{6180}C16N_{558}$).

^{1}H-NMR (400 MHz, CD_3OD) δ: 0.72-2.41 (br.), 2.95-4.06 (br.)

TEM: 5.64 ± 1.61 nm

UV-vis: λ_{max} 531 nm (in MilliQ water)

Synthesis of NP C12NF6 (5:1)

In a three-neck round bottom flask, 0.1 g of $HAuCl_4 \cdot 3H_2O$ (0.254 mmol, 1 eq.) were dissolved in 10 mL of deoxygenated milliQ water. Then, 0.750 g of TOAB (1.37 mmol, 5.4 eq.) were dissolved in 7.6 mL of deoxygenated chloroform and added to the $HAuCl_4$ solution. The reaction mixture was stirred at room temperature for 30 minutes. After, the mixture was centrifuged to aid the separation of the aqueous and organic phases, and the aqueous layer was discarded. The red-orange coloured organic phase was washed 3 times with deoxygenated milliQ water (9 mL). Then, a fresh solution of 0.14 g of $NaBH_4$ (3.68 mmol, 14.5 eq.) in 6.7 mL of deoxygenated milliQ water was quickly added to the $AuCl_4^-TOA^+$ solution. The organic phase became dark violet due to AuNP formation. The reaction mixture was stirred for 15 minutes at room temperature. Afterward, the mixture was centrifuged to separate the phases, and the aqueous phase was discarded. The organic phase was washed 3 times with deoxygenated milliQ water (9 mL). Then, a solution of **HC12N/F6** (0.011 g, 0.032 mmol of **HC12N**; 0.0023 g, 0.006 mmol of **HF6**) in 6 mL of deoxygenated methanol was added to the AuNPs solution. The mixture was stirred at room temperature for 2 hours.

Purification: The solvent was removed under reduced pressure and the resulting solid was dissolved in 2 mL of MeOH and transferred in a centrifuge tube. Ethyl ether was slowly added to the solution until the precipitation of AuNPs occurred, then, the nanoparticles were collected by centrifugation (3800 x 8 min). This process was repeated for six times. In the end, 0.031 g of AuNPs were obtained ($Au_{2425}C12N_{250}F6_{50}$).

^{1}H-NMR (400 MHz, CD_3OD) δ: 0.6-2.57 (br.), 2.79-4.14 (br.)

^{19}F-NMR (400 MHz, CD_3OD) δ: -88, -153

TEM: 4.09 ± 0.87 nm

UV-vis: λ_{max} 523 nm (in MilliQ water)

Synthesis of NP C12NF6 (2.9:1)

In a three-neck round bottom flask, 0.064 g of $HAuCl_4 \cdot 3H_2O$ (0.162 mmol, 1 eq.) were dissolved in 6.5 mL of deoxygenated milliQ water. Then, 0.48 g of TOAB (0.877 mmol, 5.4 eq.) were dissolved in 5 mL of deoxygenated chloroform and added to the $HAuCl_4$ solution. The reaction mixture was stirred at room temperature for 30 minutes. Afterward, the mixture was centrifuged to aid separation of the aqueous and organic phases and the aqueous layer was discarded. The red-orange coloured organic phase was washed 3 times with deoxygenated milliQ water (6 mL). Then, a fresh solution of 0.09 g of $NaBH_4$ (2.35 mmol, 14.5 eq.) in 4.3 mL of deoxygenated milliQ water was quickly added to the $AuCl_4^-TOA^+$ solution. The organic phase became dark violet due to AuNP formation. The reaction was stirred for 15 minutes at room temperature. After, the mixture was centrifuged to separate the phases and the aqueous layer was discarded. The organic phase was washed 3 times with deoxygenated milliQ water (6 mL). Then, a solution of **HC12N**/**HF6** (0.0067 g, 0.020 mmol of **HC12N**; 0.0025 g, 0.007 mmol of **HF6**) in 6 mL of deoxygenated methanol was added to the AuNPs solution. The mixture was stirred at room temperature for 2 hours.

Purification: The solvent was removed under reduced pressure and the resulting solid was dissolved in 2 mL of MeOH and transferred in a centrifuge tube. Ethyl ether was slowly added to the solution until the precipitation of AuNPs occurred, then, the nanoparticles were collected by centrifugation (3800 x 8 min). This process was repeated for six times. In the end, 0.022 g of AuNPs were obtained ($Au_{4842}C12N_{400}F6_{138}$).

^{1}H-NMR (400 MHz, CD_3OD) δ: 0.64-2.37 (br.), 2.77-4.06 (br.)

^{19}F-NMR (400 MHz, CD_3OD) δ: -88, -153

TEM: 5.15 ± 1.25 nm

UV-vis: λ_{max} 524 nm (in MilliQ water)

Synthesis of NP C16NF6 (3.6:1)

In a three-neck round bottom flask, 0.1 g of $HAuCl_4 \cdot 3H_2O$ (0.254 mmol, 1 eq.) were dissolved in 10 mL of deoxygenated milliQ water. Then, 0.750 g of TOAB (1.37 mmol, 5.4 eq.) were dissolved in 7.6 mL of deoxygenated chloroform and added to the $HAuCl_4$ solution. The reaction mixture was stirred at room temperature for 30 minutes. After, the mixture was centrifuged to aid the separation between the aqueous and the organic phases and the aqueous phase was discarded. The red-orange coloured organic phase was washed 3 times with deoxygenated milliQ water (8 mL). Then, a fresh solution of 0.14 g of $NaBH_4$ (3.68 mmol, 14.5 eq.) in 6.7 mL of deoxygenated milliQ water was quickly added to the $AuCl_4^-TOA^+$ solution. The organic phase became dark violet due to AuNP formation. The reaction was stirred for 15 minutes at room temperature. After, the mixture was centrifuged to aid the separation of the aqueous and organic phases and the aqueous phase was discarded, and the organic phase was washed 3 times with deoxygenated milliQ water (8 mL). Then, a solution of **HC16N**/**HF6** (0.011 g, 0.027 mmol of **HC16N**; 0.003 g, 0.009 mmol of **HF6**) in 6 mL of deoxygenated methanol was added to the AuNPs solution. The mixture was stirred at room temperature for 2 hours.

Purification: The solvent was removed under reduced pressure and the resulting solid was dissolved in 2 mL of MeOH and transferred in a centrifuge tube. Ethyl ether was slowly added to the solution until the precipitation of AuNPs occurred, then, the nanoparticles were collected by centrifugation (3800 x 8 min). This process was repeated for six times. In the end, 0.027 g of AuNPs were obtained ($Au_{2779}C16N_{211}F6_{58}$).

^{1}H-NMR (400 MHz, CD_3OD) δ: 0.74-2.23 (br.), 2.88-3.34 (br.)

^{19}F-NMR (400 MHz, CD_3OD) δ: -88, -153

TEM: 4.28 ± 1.11 nm

UV-vis: λ_{max} 523 nm (in MilliQ water)

Synthesis of NP C16NF6 (3.1:1)

In a three-neck round bottom flask, 0.05 g of $HAuCl_4 \cdot 3H_2O$ (0.127 mmol, 1 eq.) were dissolved in 5 mL of deoxygenated milliQ water. Then, 0.375 g of TOAB (0.685 mmol, 5.4 eq.) were dissolved in 4 mL of deoxygenated chloroform and added to the $HauCl_4$ solution. The reaction mixture was stirred

at room temperature for 30 minutes. Afterward, the mixture was centrifuged to aid the separation of the aqueous and organic phases, and the aqueous layer was discarded. The red-orange coloured organic phase was washed 3 times with deoxygenated milliQ water (5 mL). Then, a fresh solution of 0.07 g of $NaBH_4$ (1.84 mmol, 14.5 eq.) in 3.4 mL of deoxygenated milliQ water was quickly added to the $AuCl_4^-TOA^+$ solution. The organic phase became dark violet due to AuNP formation. The reaction was stirred for 15 minutes at room temperature. Afterward, the mixture was centrifuged to aid the separation of the phases, and the aqueous phase was discarded. The organic phase was washed 3 times with deoxygenated milliQ water (5 mL). Then, a solution of **HC16N**/**HF6** (0.0057 g, 0.018 mmol of **HC16N**; 0.0026 g, 0.007 mmol of **HF6**) in 6 mL of deoxygenated methanol was added to the AuNPs solution and the reaction mixture was stirred at room temperature for 2 hours.

Purification: The solvent was removed under reduced pressure and the resulting solid was dissolved in 2 mL of MeOH and transferred in a centrifuge tube. Ethyl ether was slowly added to the solution until the precipitation of AuNPs occurred, then, the nanoparticles were collected by centrifugation (3800 x 8 min). This process was repeated for six times. In the end, 0.024 g of AuNPs were obtained ($Au_{2320}C16N_{196}F6_{63}$).

^{1}H-NMR (400 MHz, CD_3OD) δ: 0.61-2.33 (br.), 2.81-3.90 (br.)

^{19}F-NMR (400 MHz, CD_3OD) δ: -88, -153

TEM: 4.03 ± 1.29 nm

UV-vis: λ_{max} 524 nm (in MilliQ water)

Synthesis of liposome L_1

Both liposomes used in this thesis were prepared by extrusion protocol as described in Chapter 3. For the preparation of L_1, POPC (0.0075 g) and POPG (0.0075 g) were weighed into a glass flask and dissolved in dichloromethane (2 mL). The solvent was evaporated under a gentle stream of nitrogen to form a dry lipid film that was subsequently dried under reduced pressure for three hours. Then, 3 mL of a PBS solution (50mM, 150mM NaCl, pH 7.3) were added to obtain a lipid concentration of 5 mg/mL). The sample was gently stirred for 30 min at 40°C. The resulting dispersion was subjected to five freeze-thaw cycles from liquid nitrogen temperature to 40 °C and then extruded ten times through a 100 nm membrane filter using a gas-pressure extruder.

Synthesis of liposome L_2

Both liposomes used in this thesis were prepared by extrusion protocol as described in Chapter 3. For the preparation of L_2, POPG (0.015 g) was weighed into a glass flask and dissolved in dichloromethane (2 mL). The solvent was evaporated under a gentle stream of nitrogen to form a dry lipid film that was subsequently dried under reduced pressure for three hours. Then, 3 mL of a PBS solution (50mM, 150mM NaCl, pH 7.3) were added to obtain a lipid concentration of 5 mg/mL). The sample was gently stirred for 30 min at 40°C. The resulting dispersion was subjected to five freeze-thaw cycles from liquid nitrogen temperature to 40 °C and then extruded ten times through a 100 nm membrane filter using a gas-pressure extruder.

5.2 Experimental section from Chapter 4

Synthesis of compound 14

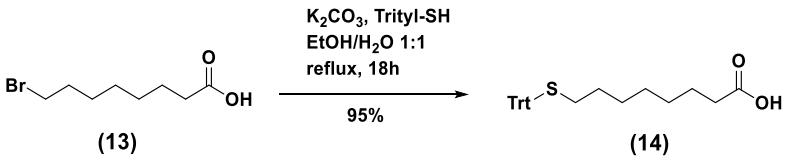

(13) (14)

In a 250 mL bottom flask, compound **13** (2 g, 8.96 mmol, 1 eq.), potassium carbonate (2.48 g, 0.0179 mmol, 2 eq.), and triphenylmethanethiol (2.48 g, 8.96 mmol, 1 eq.) were suspended in 90 mL of a 1:1 EtOH:H_2O mixture. The yellow suspension was left under stirring at reflux temperature for 18 hours. After this period, 18 mL of 1 M HCl are added, and once the mixture reached room temperature, three extractions are carried out with CH_2Cl_2 (3 x 40 mL). The organic phases were combined and washed three times with brine (3 x 40 mL). Then, the organic phase was treated with Na_2SO_4 and brought to dryness under reduced pressure, obtaining a yellow oil (3,57 g, yield 95%).

^{1}H NMR (400 MHz, $CDCl_3$) δ: 1.14 – 1.30 (m, 6H), 1.38 (q, J = 7.3, 6.7 Hz, 1H), 1.58 (p, J = 7.5 Hz, 1H), 2.14 (t, J = 7.3 Hz, 1H), 2.31 (t, J = 7.5 Hz, 1H), 7.18 – 7.43 (m, 15H).

^{13}C NMR (400 MHz, $CDCl_3$) δ: 24.91, 28.55, 28,85, 28.89, 28.99, 34.93, 66.51, 126.51, 127.79, 129.59, 145.05, 146.88, 180.52.

IR ν (cm^{-1}): 3055.24, 2926.01, 2852.72, 1703.14, 1556.55, 1487.12, 1442.74, 1265.30, 1182.07, 1031.92, 740.67, 765.30, 615.29, 507.28.

MS (ESI, CH_3CN): *m/z* = 441.1859 [M + Na^+], 457.1608 [M + H^+].

TLC [Rf; eluent solution]: [0.46; DCM/MeOH 9.5/0.5 (v/v)]; [0.37; DCM/AcOEt 8/2 (v/v)]; [0.31; AcOEt/EP 1/3 (v/v)].

Synthesis of compound 15

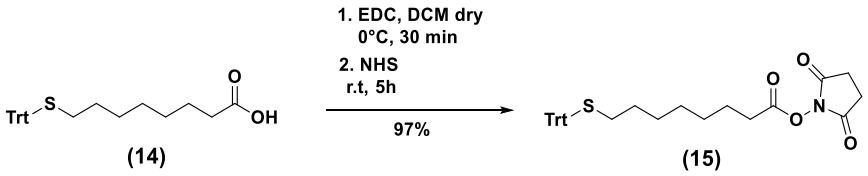

In a three-neck round bottom flask, compound **14** (1.356 g, 3.24 mmol, 1 eq.) was dissolved in 20 mL of anhydrous CH_2Cl_2 under an argon atmosphere. Then, the system was placed in an ice bath before the subsequent addition of EDC (0.756 g, 3.94 mmol, 1.2 eq.). The yellow mixture was left under stirring in the ice bath for 30 minutes. Then, *N*-hydroxysuccinimide (0.566 g, 4.92 mmol, 1.5 eq.) was added under stirring and the mixture was stirred at room temperature for 5 hours.

Purification: the reaction mixture was brought to dryness under reduced pressure obtaining a yellow oily solid. The residue was taken up with 60 mL of DCM and the resulting organic phase was extracted twice with water (2 x 20 mL), three times with a 5% $KHSO_4$ solution (3 x 25 mL), and with brine (1 x 20 mL). Then, the organic phase was treated with anhydrous Na_2SO_4, after the removal of the solvent under reduced pressure, a white solid was obtained (1,62 g, yield 97%.).

^{1}H NMR (400 MHz, $CDCl_3$) δ: 1.12 – 1.44 (m, 9H), 1.68 (p, J = 7.5 Hz, 2H), 2.13 (t, J = 7.3 Hz, 2H), 2.56 (t, J = 7.5 Hz, 2H), 7.46 – 7.16 (m, 15H).

^{13}C NMR (400 MHz, $CDCl_3$) δ: 24.44, 25.67, 28.45, 28.51, 28.57, 28.64, 30.87, 32.28, 66.39, 126.51, 127.92, 129.56, 145.05, 146.87, 168.62, 169.19.

IR *v* (cm^{-1}): 2927.94, 2854.65, 1784.15, 1732.08, 1593.20, 1487.12, 1440.83, 1363.67, 1205.51, 1062.78, 1045.42, 740.67.

MS (ESI, CH_3CN): m/z = 538.2026 [M + Na^+], 554.1790 [M + K^+].

TLC [Rf; eluent solution]: [0.86 ; DCM/MeOH 9.5/0.5 (v/v)]; [0.84 ; DCM/AcOEt 8/2 (v/v)]; [0.28 ; AcOEt/EP 1/3 (v/v)].

Synthesis of compound 16

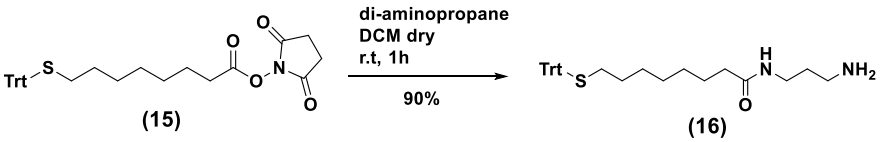

In a round bottom flask, 12.2 mL of 1,3-diamino propane (122 eq.) were dissolved in 62 mL of anhydrous CH_2Cl_2. 122 ml of a solution of ester **15** (0.619 g, 1.20 mmol, 1 eq.) in CH_2Cl_2 was added dropwise over one hour. During the addition, a white precipitate formed.

Purification: the reaction mixture was brought to dryness to remove the excess of 1,3-diaminopropane, and the residue was taken up in DCM and transferred to a separating funnel. Then, the organic phase was washed three times with 1% NaOH solution (3 x 100 mL), three times with water (3 x 100 mL), and with brine (1 x 50 mL). Afterward, the organic phase was treated with anhydrous Na_2SO_4, and the solvent was removed under reduced pressure obtaining a yellow oil (0.52 g, yield 91%).

^{1}H NMR (400 MHz, CD_3OD) δ: 1.11 – 1.37 (m, 8H), 1.53 (p, J = 7.5 Hz, 2H), 1.62 (p, J = 6.9 Hz, 2H), 2.12 (q, J = 7.3 Hz, 4H), 2.64 (t, J = 5.7 Hz, 2H), 3.21 (t, J = 6.8 Hz, 2H), 7.15 – 7.42 (m, 15H).

^{13}C NMR (400 MHz, CD_3OD) δ: 25.49, 26.27, 28.22, 28.30, 28.45, 28.60, 28.67, 29.20, 29.54, 31.48, 35.60, 35.74, 37.45, 69.16, 125.89, 127.38, 129.35, 176.12.

IR *v* (cm^{-1}): 3282.84, 2924.09, 2852.72, 1639.49, 1552.70, 1487.12, 1442.75, 740.67, 615.29.

MS (ESI, CH_3OH): m/z = 475.2777 [M + H^+].

TLC [Rf; eluent solution] [0; DCM/MeOH 9.5/0.5 (v/v)]; [0; DCM/AcOEt 8/2 (v/v)]; [0; AcOEt/EP 1/3 (v/v).

Synthesis of compound 17

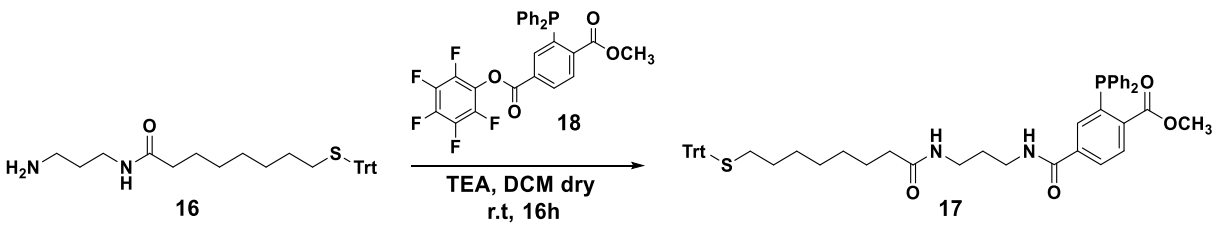

In a three-neck flask, 1-methyl-4-pentafluorophenyl-2-(diphenylphosphino)terephthalate **17** (0.115 g, 0.216 mmol, 1 eq.) was dissolved in 2.25 mL of anhydrous CH_2Cl_2 under argon atmosphere. Then, the amine **16** (0.202 g, 0.427 mmol, 2 eq.) was dissolved in 2.28 mL of anhydrous CH_2Cl_2 and added to the reaction mixture under stirring. A few drops of triethylamine (45.3 µL, 0.325 mmol, 1.5 eq.) were added and the reaction mixture was left under stirring for 4 hours at room temperature.

Purification: the mixture was transferred to a separating funnel and washed with 1M HCl (3 x 10 mL). The organic phase was recovered and then dried under reduced pressure. The obtained yellow oil was dissolved in deoxygenated ethyl ether and washed with 1% NaOH (4 x 10 mL) and brine (1 x 10 mL) into a separated funnel. Then, the organic phase was treated with anhydrous Na_2SO_4 and after removal of the solvent under reduced pressure, 0.142 g of a slightly yellow oil were obtained (yield 80%).

^{1}H NMR (400 MHz, $(CD_3)_2CO$) δ: 1.41 – 1.10 (m, 8H), 1.66 – 1.49 (m, 4H), 2.19 – 2.09 (m, 4H), 3.19 (q, J = 6.3 Hz, 2H), 3.29 (q, J = 6.3 Hz, 2H), 3.69 (s, 3H), 7.45 – 7.14 (m, 26H), 7.67 – 7.57 (m, 1H), 7.91 (dd, J = 8.0, 1.7 Hz, 1H), 8.04 (dd, J = 8.0, 3.5 Hz, 1H), 8.07 (s, 1H).

^{13}C NMR (400 MHz, $(CD_3)_2CO$) δ: 25.49, 28.35-29.55, 31.59, 35.77, 35.88, 36.09, 51.42, 65.38, 126.49-138.07, 140.61, 140.90, 145.16, 165.41, 166.43, 173.09.

^{31}P NMR (400 MHz, $(CD_3)_2CO$) δ: 2.40.

IR ν (cm^{-1}): 3298.28, 3055.24, 2924.09, 2852.72, 1712.79, 1643.35, 1531.48, 1433.11, 1359.82, 1271.09, 1114.86, 742.59. 696.30.

MS (ESI, CH_3OH): m/z = 579.2436 [M + H^+], 601.2264 [M + Na^+]

TLC [Rf; eluent solution]: [0.71; DCM/MeOH 9.5/0.5 (v/v)]; [0.24; DCM/AcOEt 8/2 (v/v)]; [0 AcOEt/EP 1/3 (v/v)].

Synthesis of compound 12

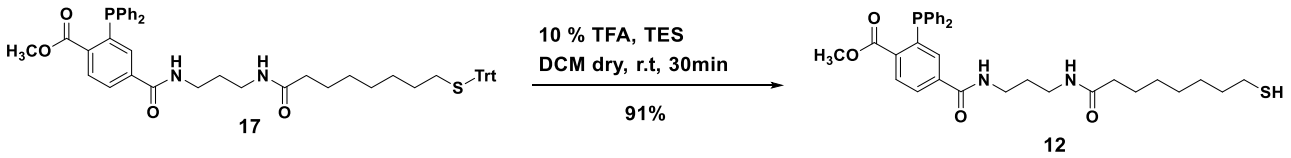

In a three-neck round bottom flask, the protected thiol **12** (0.033 g, 0.041 mmol, 1 eq.) was dissolved in 6 mL of anhydrous deoxygenated CH_2Cl_2 under argon atmosphere. The, TES (19.4 µL, 0.121

mmol, 3 eq.) and TFA (10% v/v) were added afterward. After the TFA addition, the reaction mixture turned intense yellow, the colour disappeared after a few seconds. The colorless solution was left under stirring for 30 minutes.

Purification: The reaction mixture was brought to dryness under reduced pressure and the resulting slightly yellow oil was washed five times with deoxygenated hexane (5 x 10 mL). Then, the residue was brought to dryness under reduced pressure, obtaining a colorless oil (0.021 g, yield 91%).

^{1}H NMR (400 MHz, CD_3OD) δ: 1.41 – 1.10 (m, 8H), 1.66 – 1.79 (m, 4H), 2.19 – 2.09 (m, 4H), 3.19 (q, J = 6.3 Hz, 2H), 3.29 (q, J = 6.3 Hz, 2H), 3.69 (s, 3H), 7.45 – 7.14 (m, 26H), 7.67 – 7.57 (m, 1H), 7.91 (dd, J = 8.0, 1.7 Hz, 1H), 8.04 (dd, J = 8.0, 3.5 Hz, 1H), 8.07 (s, 1H).

^{31}P NMR (400 MHz, (CD_3OD) δ: - 4.2.

^{13}C NMR (400 MHz, (CD_3OD) δ: 23.14, 25.47, 27.85, 28.41, 28.74, 29.09, 33.74, 35.85, 35.96, 36.29, 51.07,

MS (ESI, CH_3OH): m/z = 843.3372 [M + Na^+].

TLC [Rf, eluent solution]: [0.79; DCM/MeOH 9.5/0.5 (v/v)]; [0.33; DCM/AcOEt 8/2 (v/v)]; [0; AcOEt/EP 1/3 (v/v)].

Synthesis of compound 19

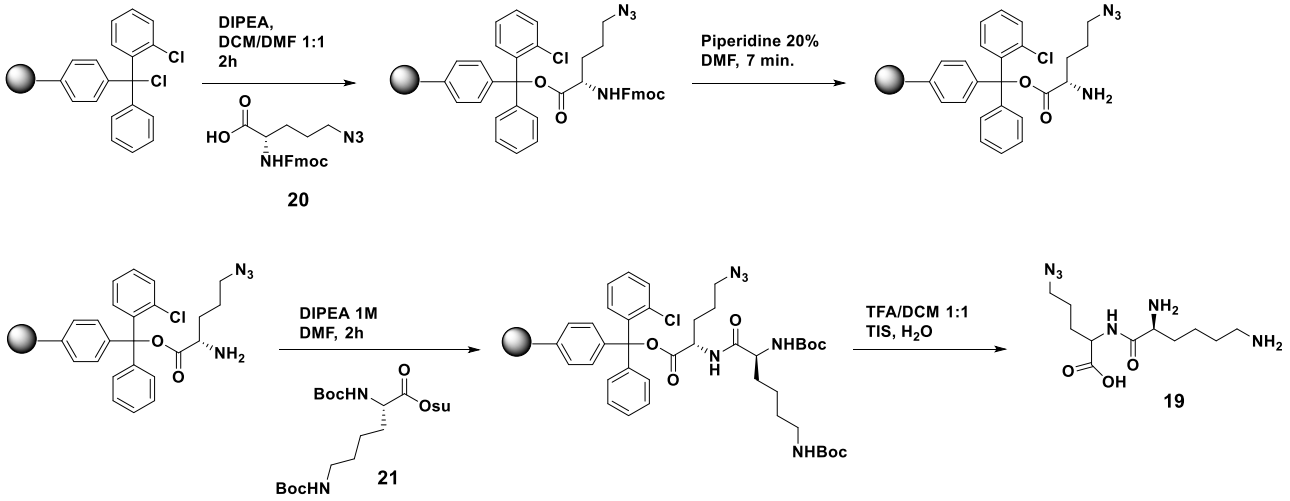

The azide-containing amino acid **19** was prepared via standard Fmoc SPPS procedures by using 2-chlorotrityl chloride resin as solid support. Firstly, the resin (0.8 g, 0.008 mmol) was swelled in 6 mL of DCM under mixing for 30 minutes. Then, by treatment with 80 µL of $SOCl_2$ in 6 mL of DCM, the

activation of the resin was performed at room temperature for 1 hour. Then, three washes with DCM (3 x 4 mL) and DMF (3 x 4 mL) were carried out. The loading of the (*S*)-5-Azido-2-(Fmoc-amino)pentanoic acid **20** (0.304 g, 0.8 mmol, 1 eq.) was performed using 0.72 mL of DIPEA and 5 mL of a solution of a DCM/DMF 1:1 mixture. The mixture was shaken for 2 hours at room temperature. After this period, the resin was washed three times with DCM (3 x 4 mL) and DMF (3 x 4 mL). Then, capping was performed by mixing the resin with a solution of dichloromethane (4 mL) and methanol (0.4 mL) for 10 minutes. Afterward, the resin was mixed with 5 mL of a 20% piperidine solution in DMF for 7 minutes, promoting the Fmoc deprotection. This treatment was performed two times. After this period, the resin was washed three times with DCM (3 x 4 mL) and DMF (3 x 4 mL). Then, the coupling with $N_{\alpha},N_{\varepsilon}$-di-Boc-L-lysine hydroxysuccinimide ester (**21**) was carried out using 3 eq. of **21**, and 1.6 mL of 1M DIPEA solution. The mixture was dissolved in 4 mL of DMF and stirred for 2 hours. After this period, the resin was washed three times with DCM (3 x 4 mL) and DMF (3 x 4 mL). Cleavage of **19** from the dried resin was performed by suspending the resin in a cleavage cocktail (10 mL) containing 1:1 TFA/DCM solution (99%), TIS (0.5%), and H_2O (0.5%) for 2 hours. Subsequently, the resin was washed 3 times with the cleavage solution, recovering the rinsing phases. The combined rinsing phases were brought to dryness under reduced pressure, obtaining the final product (0.03g).

^{1}H-NMR (400 MHz, CD_3OD) δ: 1.38 – 1.45 (m, 2H), 1.64 – 1.73 (m, 2H), 1.79 – 1.90 (m, 4H), 3.17–3.33 (m, 5H), 3.69–3.87 (m, 1H).

MS (ESI, CH_3OH): *m/z* = 287.12 [M + H^+]; 130.1 [M]$^+$ related to the lysine motif after amide bond cleavage.

Synthesis of NP C11N/12 I

In a three-neck round bottom flask, 0.03 g of $HauCl_4 \cdot 3H_2O$ (0.076 mmol, 1 eq.) were dissolved in 3 mL of deoxygenated milliQ water. Then, 0.225 g of TOAB (0.441 mmol, 5.4 eq.) were dissolved in 2.3 mL of deoxygenated chloroform and added to the $HauCl_4$ solution. The reaction mixture was stirred at room temperature for 30 minutes. After, the mixture was centrifuged to aid separation of the aqueous and organic phases and the aqueous phase was discarded. The red-orange coloured organic phase was washed 3 times with 10 mL of deoxygenated milliQ water. Then, a fresh solution of 0.045 g of $NaBH_4$ (1.19 mmol, 14.5 eq.) in 2 mL of deoxygenated milliQ water was quickly added to the $AuCl_4^-TOA^+$ solution. The organic phase became dark violet due to AuNP formation. The

reaction mixture was stirred for 15 minutes at room temperature. Afterward, the mixture was centrifuged to eliminate the aqueous phase, and the organic phase was washed 3 times with 10 mL of deoxygenated milliQ water. Then, 80 µL of triethylamine were added and subsequently, a 1:1 solution of **HC11N** (0.0022 g, 0.007 mmol) and **12** (0.0038 g, 0.006 mmol) in 6 mL of deoxygenated methanol were added to the AuNPs solution. The mixture was stirred at room temperature for 2 hours.

Purification: The reaction mixture was brought to dryness under reduced pressure. The residue was dissolved in 5 mL of deoxygenated MeOH and transferred in a centrifuge tube. Ethyl ether was slowly added to precipitate the nanoparticles (around 30 mL), and the resulting mixture was centrifuged to collect the AuNPs (2 cycles at 2500 rpm for 3 minutes, and 3 cycles at 4000 rpm for 15 minutes). This process was repeated six times. In the end, 0.01 g of AuNPs are obtained ($Au_{2740}C11N_{263}12_{26}$).

^{1}H-NMR (400 MHz, CD_3OD) δ: 0.44-2.60 (br.), 2.65-3.94 (br.), 7.42-8.45 (br.)

TEM: 4.26 ± 1.27 nm

UV-vis: λ_{max} 523 nm (in MilliQ water)

Synthesis of NP C11N/12 II

In a three-neck round bottom flask, 0.03 g of $HauCl_4 \cdot 3H_2O$ (0.076 mmol, 1 eq.) were dissolved in 3 mL of deoxygenated milliQ water. Then, 0.225 g of TOAB (0.441 mmol, 5.4 eq.) were dissolved in 2.3 mL of deoxygenated chloroform and added to the $HAuCl_4$ solution. The reaction mixture was stirred at room temperature for 30 minutes. After, the mixture was centrifuged to aid the separation of the phases, and the aqueous phase was discarded. The coloured red-orange organic phase was washed 3 times with 10 mL of deoxygenated milliQ water. Then, a fresh solution of 0.045 g of $NaBH_4$ (1.19 mmol, 14.5 eq.) in 2 mL of deoxygenated milliQ water was quickly added to the $AuCl_4^-TOA^+$ solution. The organic phase became dark violet due to AuNP formation. The reaction mixture was stirred for 15 minutes at room temperature. After, the mixture was centrifuged to aid the separation of the phases, and the aqueous phase was discarded. The organic phase was washed 3 times with 10 mL of deoxygenated milliQ water. Then, 80 µL of triethylamine were added and subsequently, a 3:1 solution of **HC11N** (0.0033 g, 0.010 mmol) and **12** (0.002 g, 0.0034 mmol) in 6 mL of deoxygenated methanol was added to the AuNPs solution. The mixture was stirred at room temperature for 2 hours.

Purification: The reaction mixture was brought to dryness under reduced pressure. The residue was dissolved in 5 mL of deoxygenated MeOH and transferred in a centrifuge tube. Ethyl ether was slowly added to precipitate the nanoparticles (around 30 mL), and the resulting mixture was centrifuged to collect the AuNPs (2 cycles at 2500 rpm for 3 minutes, and 3 cycles at 4000 rpm for 15 minutes). This process was repeated six times. In the end, 0.014 g of AuNPs are obtained ($Au_{2664}C11N_{225}12_{28}$).

^{1}H-NMR (400 MHz, CD_3OD) δ: 0.22-2.54 (br), 2.54-4.32 (br.), 7.42-8.45 (br.)

TEM: 4.22 ± 1.30 nm

UV-vis: λ_{max} 521 nm (in MilliQ water)

Synthesis of usNP C11N/12

A solution of $HAuCl_4 \cdot 3H_2O$ (0.06 g, 0.152 mmol, 1 eq.) in water (3.75 mL) was extracted with a solution of TOAB (3 g, 5.48 mmol, 36 eq.) in argon purged toluene (75 mL). To the resulting reddish-orange organic solution, dioctylamine (2.03 g, 8.4 mmol, 55 eq.) was added. The mixture was vigorously stirred under argon for 40 minutes. During this period the color of the mixture faded. A solution of $NaBH_4$ (0.056 g, 1.47 mmol, 9.7 eq.) in H_2O (1.2 mL) was then rapidly added. The color of the solution turned rapidly to black due to nanoparticle formation. After 2 hours of stirring, the aqueous layer was removed. To the above nanoparticle solution, a 3:1 solution of **HC11N** (0.002 g, 0.006 mmol) and **12** (0.001 g, 0.002 mmol) in 6 mL of deoxygenated methanol was added. The solution was stirred overnight, and after this period 10 mL of milliQ water were added under vigorous stirring. The stirring was continued for 1 hour, and during this time the toluene solution becomes colourless, while the aqueous layer turned brown-black.

Purification: the aqueous layer containing the nanoparticles was washed with toluene (2 x 30 mL), ethyl ether (3 x 30 mL), and ethyl acetate (5 x 30 mL). Then, the aqueous solution was brought to dryness, and the solid residue was taken up with 2 mL of methanol and transferred to a centrifuge tube. Ethyl ether (30 mL) was slowly added to the solution until the precipitation of AuNPs occurred, then, the nanoparticles were collected by centrifugation (2 cycles at 2500 rpm for 3 minutes, and 3 cycles at 4000 rpm for 15 minutes). The precipitation/centrifugation process was repeated five times. In the end, 0.028 g of AuNPs were obtained ($Au_{803}C11N_{161}12_{18}$).

^{1}H-NMR (400 MHz, CD_3OD) δ: 0.22-2.54 (br), 2.54-4.32 (br.), 7.42-8.45 (br.)

TEM: 2.83 ± 0.82 nm

UV-vis: λ_{abs} 512 nm (in MilliQ water).

Synthesis of usNP C11N

A solution of $HAuCl_4 \cdot 3H_2O$ (0.08 g, 0.203 mmol, 1 eq.) in water (5 ml) was extracted with a solution of TOAB (4 g, 7.31 mmol, 36 eq.) in argon purged toluene (100 ml). To the resulting reddish-orange organic solution, dioctylamine (2.71 g, 11.2 mmol, 55 eq.) is added. The mixture was vigorously stirred under argon for 40 minutes. During this period the color of the mixture faded. A solution of $NaBH_4$ (0.074 g, 1.97 mmol, 9.7 eq.) in H_2O (1.2 ml) was then rapidly added. The color of the solution turned rapidly to black due to nanoparticle formation. After 2 hours of stirring, the aqueous layer was removed. To the above nanoparticle solution, a solution of **HC11N** (0.033 g, 0.5 eq.) in 6 ml of deoxygenated methanol was added. The solution was stirred overnight, and after this period 10 ml of milliQ water were then added under vigorous stirring. The stirring was continued for 1 hour, and during this time the toluene solution becomes colourless, while the aqueous layer turned brown-black.

Purification: the aqueous layer containing the nanoparticles was washed with toluene (2 x 30 ml), ethyl ether (3 x 30 ml), and ethyl acetate (5 x 30 ml). Then, the aqueous solution was brought to dryness, and the solid residue was taken up with 2 ml of methanol and transferred to a centrifuge tube. Ethyl ether (20 ml) was slowly added to the solution until the precipitation of AuNPs occurred, then, the nanoparticles were collected by centrifugation (2 cycles at 2500 rpm for 3 minutes, and 3 cycles at 3800 rpm for 15 minutes). The precipitation/centrifugation process was repeated five times. In the end, 0.045 g of AuNPs were obtained.

^{1}H-NMR (400 MHz, CD_3OD) δ: 0.85-2.30 (br.), 2.70-3.90 (br.)

TEM: 3.03 ± 0.90 nm

UV-vis: λ_{abs} 519 nm (in MilliQ water).

Synthesis of usNP C11N/12 III

In a three-neck round bottom flask, 0.02 g of usNP11 was dissolved in 10 mL of deoxygenated methanol. Then, 20 µL of triethylamine were added to the AuNPs solution and subsequently, 2 mL

of **12** (0.002 g, 0.0034 mmol) solution in methanol was added. The reaction was stirred for three days at room temperature under an argon atmosphere.

Purification: the reaction mixture was concentrated under reduced pressure. The unbound **HC11N** and **12** were removed by adding ethyl ether to induce the AuNP precipitation, and then the resulting precipitate was collected by centrifugation (3800 rpm for 10 minutes). This process was performed five times. In the end, 0.02 g of AuNPs were obtained ($Au_{1781}C11N_{242}12_{36}$).

^{1}H-NMR (400 MHz, CD_3OD) δ: 0.22-2.54 (br), 2.54-4.32 (br.), 7.42-8.45 (br.)

TEM: 3.9 ± 1.20 nm

UV-vis: λ_{abs} 520 nm (in MilliQ water).

Staudinger-Bertozzi ligation on usNP C11N/12 III

In an NMR tube, 0.019 g of usNP C11/12 III were dissolved in 0.7 mL of DMSO-d_6 at room temperature. Afterward, 0.0016 g of compound **19** dissolved in 0.2 mL of DMSO-d_6 and 80 µL of milliQ water were added to the nanoparticle solution. The reaction mixture was sonicated at 37°C for 7 days.

Purification: the reaction was brought to dryness under reduced pressure. The excess of **19** was removed by dissolving the reaction mixture in methanol and adding ethyl ether to promote AuNP precipitation. Then, the AuNPs were collected by centrifugation (3500 rpm for 15 minutes). This process was performed seven times.

Synthesis of 24

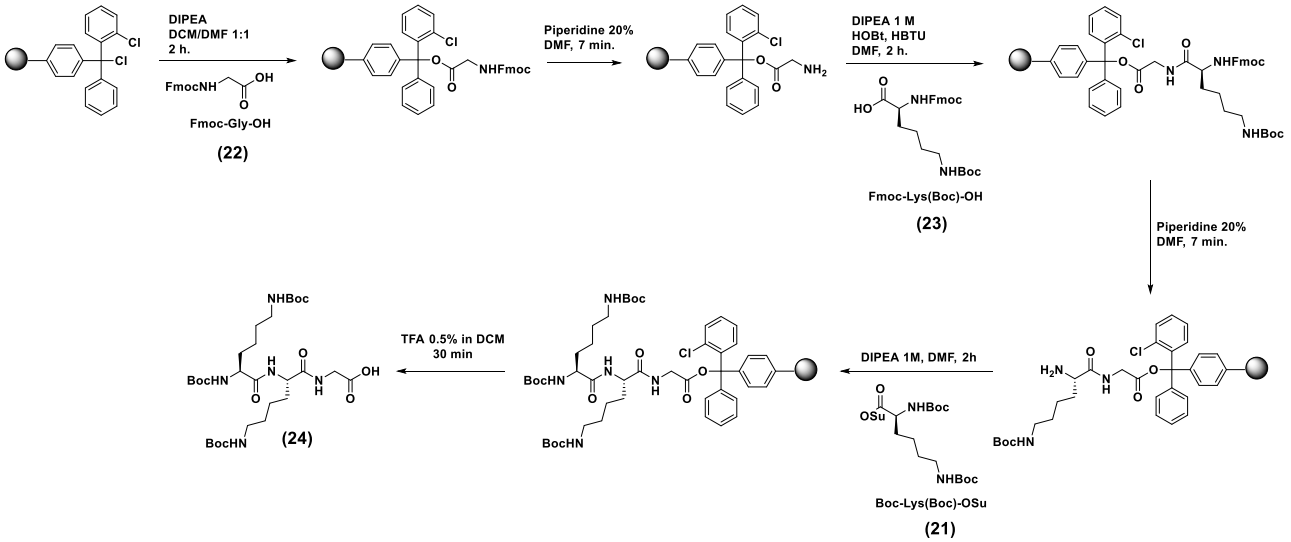

The protected peptide **24** was prepared via standard Fmoc SPPS procedures by using 2-chlorotrityl chloride resin as solid support. Firstly, the resin (0.3 g) was swelled in 2.5 mL of DCM under mixing for 30 minutes. Then, by treatment with 30 µL of $SOCl_2$ in 3 mL of DCM, the activation of the resin was performed at room temperature for 1 hour. Then, three washes with DCM (3 x 2 mL) and DMF (3 x 2 mL) were carried out. The loading of Fmoc-Gly-OH **22** (0.134 g, 0.45 mmol) was performed using 0.27 mL of DIPEA and 2 mL of a solution of a DCM/DMF 1:1 mixture. The mixture was shaken for 2 hours at room temperature. After this period, the resin was washed three times with DCM (3 x 2 mL) and DMF (3 x 2 mL). Then, capping was performed by mixing the resin with a solution of dichloromethane (2 mL) and methanol (0.15 mL) for 10 minutes. Afterward, the resin was mixed with 2 mL of a 20% piperidine solution in DMF for 7 minutes, promoting the Fmoc deprotection. This treatment was performed two times. Then, the coupling with Fmoc-Lys(Boc)-OH (**23**) was carried out using 3 eq. of **23** (0.632 g, 1.35 mmol), 4 e. of HOBt (0.243 g, 1.8 mmol), 4 eq. of HBTU (0.683 g, 1.8 mmol), and 0.6 mL of 1M DIPEA solution. The mixture was dissolved in 3 mL of DMF and stirred for 2 hours. After this period, the resin was washed three times with DCM (3 x 2 mL) and DMF (3 x 2 mL). Afterward, the resin was mixed with 2 mL of a 20% piperidine solution in DMF for 7 minutes, promoting the Fmoc deprotection. This process was repeated two times. After, the resin was washed three times with DCM (3 x 2 mL) and DMF (3 x 2 mL). Then, the coupling with N_α,N_ε-di-Boc-L-lysine hydroxysuccinimide ester (**21**) was carried out using 3 eq. of **21** (0.6 g, 1.35 mmol), and 0.6 mL of 1M DIPEA solution. The mixture was dissolved in 2 mL of DMF and stirred for 2 hours. After this period, the resin was washed three times with DCM (3 x 2 mL) and

DMF (3 x 2 mL). Cleavage of **24** from the dried resin was performed by suspending the resin in a cleavage cocktail (4 mL) containing TFA/DCM 0.5:99.5 solution for 30 minutes. Subsequently, the resin was washed 3 times with the cleavage solution, recovering the rinsing phases. The combined rinsing phases were brought to dryness under reduced pressure, obtaining the final product (0.105 g).

^{1}H-NMR (400 MHz, CD_3OD) δ: 1.28 – 1.89 (m, 44H), 2.94 – 3.07 (m, 4H), 3.73 – 4.06 (m, 3H), 4.28–4.46 (m, 1H).

MS (ESI, CH_3OH): *m/z* = 654.4 [M + Na^+]; *m/z* = 630.5 [M - H^+]$^-$;

Synthesis of 25

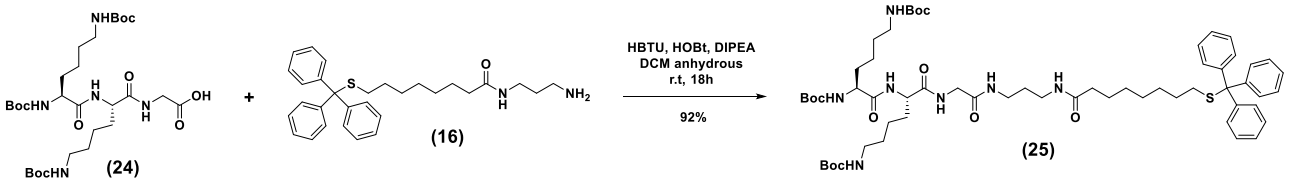

In a three-neck bottom round flask, compound **24** (0.05 g, 0.079 mmol) was dissolved in 2.5 mL of dry dichloromethane under an argon atmosphere. Then, HBTU (0.09 g, 0.24 mmol, 3 eq.), HOBt (0.032 g, 0.24 mmol, 3 eq.), and 80 µL of triethylamine were added and the reaction mixture was stirred for 30 minutes at room temperature. After this period, compound **16** (0.041 g, 0.0087 mmol, 1.1 eq.) was added to the mixture, and the reaction was left under stirring for 18 hours.

Purification: The reaction mixture was transferred to a separating funnel and washed with 1M HCl solution (10 mL x 2), and brine (10 mL x 3). Then, the organic phase was treated with anhydrous Na_2SO_4 and after removal of the solvent under reduced pressure, 0.079 g of a slightly yellow oil were obtained (yield 92%).

^{1}H-NMR (400 MHz, CD_3OD) δ: 1.15 – 1.89 (m, 56H), 2.01 – 2.20 (m, 4H), 2.97 – 3.06 (4H, m), 3.13 – 3.25 (4H, m), 3.60 – 3.75 (1H, m), 3.81 – 4.01 (m, 2H), 4.13 – 4.25 (m, 1H).

MS (ESI, CH_3OH): *m/z* = 1110.8 [M + Na^+];): *m/z* = 1126.7 [M + K^+];

Synthesis of HP1

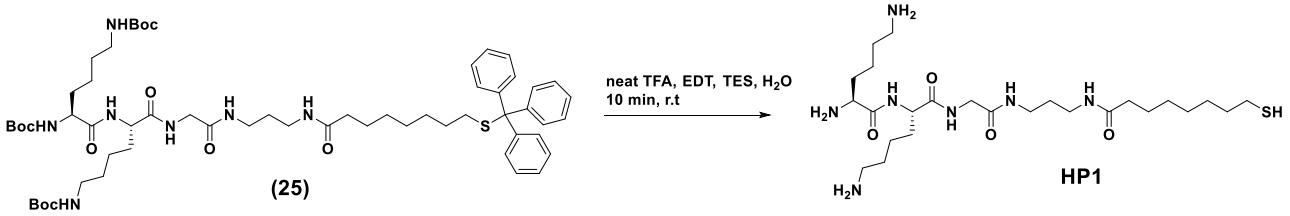

In a three-neck bottom round flask, compound **25** was dissolved in 1 mL od deoxygenated dichloromethane and stirred under an argon atmosphere at room temperature. Them, 1 mL of the deprotection cocktail (neat TFA/H_2O/EDT/TES; 94:2.5:2.5:1) was added and the reaction was left under stirring for 10 minutes.

Purification: the reaction mixture was brought to dryness under reduced pressure, being careful to use an activated carbon filter to trap the EDT. The resulted slightly yellow solid was obtained (0.01 g, q.t yield)

^{1}H-NMR (400 MHz, CD_3OD) δ: 1.23 – 2.01 (m, 23H), 2.11 – 2.25 (t, *J*= 6.8 Hz, 2H), 2.41 – 2.55 (t, *J*= 7.2 Hz, 2H), 2.89 – 3.02 (4H, m), 3.12 – 3.28 (m, 4H), 3.75 – 3.95 (m, 2H), 3.97 – 4.13 (m, 1H), 4.26 – 4.35 (m, 1H).

References

(1) Bidoggia, S.; Milocco, F.; Polizzi, S.; Canton, P.; Saccani, A.; Sanavio, B.; Krol, S.; Stellacci, F.; Pengo, P.; Pasquato, L. Fluorinated and Charged Hydrogenated Alkanethiolates Grafted on Gold: Expanding the Diversity of Mixed-Monolayer Nanoparticles for Biological Applications. *Bioconjug. Chem.* **2017**, *28* (1), 43–52. https://doi.org/10.1021/acs.bioconjchem.6b00585.

(2) Miranda, O. R.; Chen, H.-T.; You, C.-C.; Mortenson, D. E.; Yang, X.-C.; Bunz, U. H. F.; Rotello, V. M. Enzyme-Amplified Array Sensing of Proteins in Solution and in Biofluids. *J. Am. Chem. Soc.* **2010**, *132* (14), 5285–5289. https://doi.org/10.1021/ja1006756.

Ringraziamenti

Ringrazio il progetto di ricerca collaborativo BacHounds: Supramolecular nanostructures for bacteria detection (PRIN 2017) per aver contribuito al finanziamento della mia borsa di studio e di questo lavoro di tesi.

Al termine di questo percorso desidero anche ringraziare tutti coloro che hanno preso parte e contribuito alla realizzazione di questo progetto, sperando che in breve riesca a trasmettere tutta la mia gratitudine.

Primi tra tutti, ci tengo a ringraziare il Prof.re Paolo Pengo e il Prof.re Paolo Tecilla, per tutto il supporto e la costante disponibilità nel guidarmi e nel sostenermi, per la capacità di placare dubbi e incertezze, soprattutto nelle ultime fasi del mio percorso formativo. Ritengo preziosi i vostri consigli e farò tesoro di questa esperienza e di ciò che mi avete insegnato. Non ho la certezza di avervi trasmesso tutta la mia riconoscenza durante questi anni e per questo ci tengo a porla nero su bianco.

Ringrazio la Prof.ssa Lucia Pasquato, per avermi accolta nel suo gruppo di ricerca e reso possibile l'intero lavoro di ricerca, per avermi supportato in numerose occasioni, incoraggiandomi e spronandomi a dare il meglio.

Vorrei inoltre ringraziare il Prof.re Marco Montalti e la Dott.ssa Arianna Menichetti per aver reso possibile studi approfonditi per la caratterizzazione delle nanoparticelle, in particolare gli studi di emissione nel NIR, le analisi volte allo studio della natura del quenching da parte delle nanoparticelle nei confronti del polimero fluorescente e l'analisi delle costanti di affinità nanoparticelle/polimero. Un ringraziamento personale lo rivolgo ad Arianna, per l'incredibile gentilezza e disponibilità che ha dimostrato e per la pazienza con cui mi ha seguita e supportata fino alla fine.

Ringrazio la Prof.ssa Cristina Airoldi e il Prof.re Alessandro Palmioli per aver dato la possibilità a questo progetto di testare e dimostrare il suo fine ultimo, la sua applicabilità per una rapida identificazione di batteri, grazie agli studi di fluorescenza in presenza di diversi ceppi batterici condotti nei loro laboratori. Oltre a ciò, ringrazio per la cordialità e per la grande disponibilità

mostrata in ogni incontro. Colgo l'occasione per ringraziare Luca Moretti per la gentilezza e disponibilità con cui ha preso parte a questi esperimenti e contribuito allo studio.

Un ringraziamento particolare al Dr. Fabio Hollan e alla Dott.ssa Sara Drioli non solo per la costante disponibilità mostrata nel dare tutto l'aiuto e il supporto possibile, ma anche per la gentilezza e la solarità con cui mi hanno sempre accolta.

Infine, vorrei dedicare uno spazio speciale alle persone conosciute durante questo percorso che sono diventate punti di riferimento e fonte di sorriso sia dentro che fuori dal laboratorio. Non esprimerò a parole la fortuna e la gratitudine nell'avervi incontrato perché spero di averle dimostrate di persona e soprattutto di potere continuare a farlo.

Fuori dal contesto accademico, un piccolo ma doveroso pensiero a chi mi ha accompagnata in questo percorso pur essendo lontano e che, a prescindere dalla distanza fisica, è riuscito a trasmettere tutto il proprio supporto e amore come se mi fosse stato accanto per tutto il tempo. Grazie, con tutto il cuore.